COMMUNICATIONS
FROM THE
KONKOLY OBSERVATORY
OF THE
HUNGARIAN ACADEMY OF SCIENCES

MITTEILUNGEN
DER
STERNWARTE
DER UNGARISCHEN AKADEMIE
DER WISSENSCHAFTEN

BUDAPEST–SVÁBHEGY

No. 100.
(Vol. 12, Part 2)

THE INTERACTION OF STARS WITH THEIR ENVIRONMENT

Proceedings of the workshop and spring school
held at Visegrád, Hungary
23–25 May 1996

BUDAPEST, 1997

Editors:

Viktor L. Tóth
Department of Astronomy
Eötvös Loránd University
H-1083, Ludovika tér 2., Budapest, Hungary

Mária Kun and László Szabados
Konkoly Observatory of the Hungarian Academy of Sciences
P.O. Box 67, H-1525 Budapest XII, Hungary

ISBN 963 8361 37 9
HU ISSN 0238–2091
Felelős kiadó: Balázs Lajos
Nyomás és kötés: G-Print Bt.

Preface

For Earth-bound life interaction of stars with their environment is within reach. Our Sun has an effect on anyone who reads these proceedings. Solar–terrestrial interactions determine our weather and climate. Solar effects on the interplanetary medium result in the "space weather" which is getting more and more interesting for a wider audience. Similar interactions link the stars to the interstellar matter, and this way these processes play a key role in the formation and evolution of galaxies. These effects are directly or indirectly observed by measurements in all wavelengths from gamma-ray to radio. Modelling these processes requires tools and methods taken from particle physics, magnetohydrodynamics, celestial mechanics and various branches of mathematics, including statistics.

It is these aspects, kinds of measurements and tools that were reviewed during the "Interaction of Stars with their Environment – Advanced School and Workshop", at Visegrád in May 1996. The conference was organized by the Department of Astronomy of the Loránd Eötvös University (Budapest), the Konkoly Observatory of the Hungarian Academy of Sciences (Budapest), and the Astronomy Section of the L. Eötvös Physical Society.

Participants represented 15 countries (60% of them were students). Their contributions resulted in a successful meeting. We acknowledge the reviews, contributions and posters, and publish their written version in this book.

The meeting could not have been organized without the support from our sponsors: Loránd Eötvös University, Hungarian Academy of Sciences, OMFB, Europapier Hungaria, Humansoft, METLOG Instruments, Pepsi Cola FÁÜRT, Pilisi Parkerdő Rt., Csemege Julius Meinl, Douwe Egberts, Kékkúti Ásványvíz, Olajterv. Their generosity is gratefully acknowledged. Our thanks are extended to Visegrád citizens for their hospitality.

These proceedings could not have been published without the painstaking and enthusiastic work of Mr. Csaba Kiss. His help is highly appreciated.

The organizers and editors

Contents

1 Star Formation

2 Young Stars

3 Numerical Models

4 The Solar System

5 Galactic Processes

6 Pre-Main Sequence Stars

7 Main Sequence and Post-Main Sequence Stars

8 Supernova Remnants

List of participants

Nancy Ageorges (ESO, München, D)
ageo@astro.uni-jena.de

Vladimir Airapetian (CSC NASA GSFC, Greenbelt, USA)
vladimir@opal.gsfc.nasa.gov

Zsolt Bagoly (ELTE, Budapest, H)
zsolt@hercules.elte.hu

Lajos G. Balázs (Konkoly Observatory, Budapest, H)
balazs@ogyalla.konkoly.hu

István Ballai (Dept. of Astronomy, ELTE, Budapest, H)
ballai@innin.elte.hu

John Bally (Univ. of Colorado, USA)
bally@nebula.colorado.edu

Mary Barsony (Dept. of Physics, Univ. of California, Riv., USA)
fun@nusun.ucr.edu

Zoltán Barcza (Dept. of Meteorology, ELTE, Budapest, H)
bzoli@nimbus.elte.hu

Judit Bartholy (Dept. of Meteorology, ELTE, Budapest, H)
bari@nimbus.elte.hu

János Bartus (ELTE and Konkoly Obs., Budapest, H)
bartus@buda.konkoly.hu

Abuzeid Basheir (Dept. of Astronomy, ELTE, Budapest, H)
abu@innin.elte.hu

Zsolt Berend (Dept. of Astronomy, ELTE, Budapest, H)
berend@ogyalla.konkoly.hu

Peter Berczik (Main Astronomical Obs. UNAS, UKR)
berczik@mao.gluk.apc.org

Imre B. Bíró (ELTE and Astronomical Obs., Baja, H)
biro@innin.elte.hu

Tamás Borkovits (ELTE and Astronomical Obs., Baja, H)
borko@electra.bajaobs.hu

Árpád Csík (Dept. of Astronomy, ELTE, Budapest, H)
arpi@innin.elte.hu

Osman Demircan (Ankara University Obs., TR)
demircan@astro1.science.ankara.edu.tr

Luke Drury (Dublin Inst. for Advanced Studies, IRE)
ld@cp.dias.ie

John Dyson (Dept. of Physics, Univ. of Leeds, UK)
jed@ast.man.ac.uk

Emmanouella Fragoulopoulou (Sect. Astrophys. Athens Univ., GR)
elivan@atlas.uoa.ariadne-t.gr

Jose Franco (Inst. de Astronomia - UNAM, MEX)
pepe@astroscu.unam.mx

Mirjam Galicic (Dept. of Physics, Univ. Ljubljana, SLO)
mirjam.galicic@uni-lj.si

Vasili Gvaramadze (Abastumani Astrophysical Obs., Georgia)
vgvaram@astro.uni-bonn.de

Tibor Hegedüs (Astronomical Obs., Baja, H)
hege@electra.bajaobs.hu

Thomas Henning (Max-Planck Working Group, Jena, D)
henning@astro.uni-jena.de

Mika Juvela (Helsinki University Obs., SF)
mika.juvela@helsinki.fi

Csaba Kiss (Dept. of Astronomy, ELTE, Budapest, H)
pkisscs@innin.elte.hu

Carsten Kömpe (Uni-Sternwarte, Jena, D)
koempe@betty.astro.uni-jena.de

Ákos Körösmezey (KFKI Inst. for Particle and Nuclear Physics, Budapest, H)
akos@rmki.kfki.hu

Zsolt Kővári (ELTE and Konkoly Observatory, Budapest, H)
kovari@buda.konkoly.hu

Jacek Krelowski (Copernicus University, Toruń, PL)
jacek@astri.uni.torun.pl

Mária Kun (Konkoly Observatory, Budapest, H)
kun@ogyalla.konkoly.hu

Nikolaos Kylafis (Dept. of Physics, Univ. of Crete, GR)
kylafis@physics.uch.gr

Alexander Lapinov (Inst. of Applied Physics, Nizhny Novgorod, RUS)
lapinov@appl.sci-nnov.ru

David Luz (University of Lisbon, Dept. of Physics, Lisbon, P)
fastrofm@skull.cc.fc.ul.pt

Miklós Marik (Dept. of Astronomy, ELTE, Budapest, H)
marik@innin.elte.hu

Garrelt Mellema (Stockholm Observatory, Stockholm, S)
garrelt@astro.su.se

Tom Millar (UMIST, Manchester, UK)
tjm@ast.ma.umist.ac.uk

Attila Moór (Dept. of Astronomy, ELTE, Budapest, H)
moor@innin.elte.hu

Andrea Nagy (ELTE and Konkoly Observatory, Budapest, H)
nagya@buda.konkoly.hu

Antonella Natta (Arcetri Obs., Firenze, I)
natta@arcetri.astro.it

Ralph Neuhäuser (MPI für Extraterrestriche Phys., Garching, D)
rne@hpth03.mpe-garching.mpg.de

Silvana Nikolić (Belgrade Observatory, Belgrade, YU)
ENIKOLSI@ubbg.etf.bg.ac.yu

Atsuo T. Okazaki (Astronomical Inst. Univ. Amsterdam, NL)
okazaki@astro.uva.nl

Toshikazu Onishi (Dept. of Astronomy, Nagoya University, J)
ohnishi@alab6.a.phys.nagoya-u.ac.jp

Ferhat F. Özeren (Ankara University Observatory, TR)
gozlem-e@servis.net.tr

Werner Pfau (Uni - Sternwarte, Jena, D)
pfau@betty.astro.uni-jena.de

Paolo Padoan (Theoretical Astroph. Center, DK)
padoan@tac.dk

Paragi Zsolt (ELTE and FÖMI, Satellite Geodetic Obs., Penc, H)
paragi@novell.sgo.fomi.hu

Tom Ray (Dublin Inst. for Advanced Studies, IR)
tr@cp.dias.ie

Matthew Redman (Dept. of Phys.–Astro. Univ. of Manchester, UK)
mer@ast.man.ac.uk

Zsolt Sándor (Dept. of Astronomy, ELTE, H)
szsolt@innin.elte.hu

Nikolaos Sergis (Sect. Astrophys. of Athens University, GR)
elivan@atlas.uoa.ariadne-t.gr

László Szabados (Konkoly Observatory, Budapest, H)
szabados@buda.konkoly.hu

Gergely Szakály (Dept. of Astronomy, ELTE, Budapest, H)
szakaly@innin.elte.hu

Károly Szatmáry (Dept. of Experimental Physics, JATE, Szeged, H)
szatmary@physx.u-szeged.hu

Gábor Szécsényi-Nagy (Dept. of Astronomy, ELTE, Budapest, H)
szena@ludens.elte.hu

György Surek (METLOG Instruments, Budapest, H)
surek@innin.elte.hu

Károly Szegő (KFKI Inst. for Particle and Nuclear Physics, Budapest, H)
szego@rmki.kfki.hu

Gábor Tóth (Sterrekundig Instituut, Utrecht, NL)
toth@fys.ruu.nl

L. Viktor Tóth (Dept. of Astronomy, ELTE, Budapest, H)
lvtoth@innin.elte.hu

Nick Tothill (Queen Mary and Westf., Univ. London, UK)
N.F.H.Tothill@qmw.ac.uk

Malcolm Walmsley (I. Phys. Inst., University of Cologne, D)
walmsley@apollo.ph1.uni-koeln.de

Igor Zinchenko (Inst. of Applied Physics, Nizhny Novgorod, RUS)
zin@appl.sci-nnov.ru

Star formation

DENSE CORES AND STAR FORMATION

Malcolm Walmsley
Osservatorio Astrofisico di Arcetri
Largo E. Fermi 5, I-50125 Italy

Abstract

A summary is given of our present knowledge of the evolution and structure of dense cores in molecular clouds. The "inside-out" collapse model of star formation is summarized and recent tests of this model are discussed. Current approaches to determining ionization degree and other dense core parameters are briefly reviewed.

1 Introduction

Dense cores or clumps within molecular clouds are thought to be the immediate precursors of young newly formed stars. Thus a determination of their characteristics is equivalent to an estimate of the initial conditions for star formation. The molecular lines emitted by such regions are sensitive to the physical conditions within them and hence can be used as probes of quantities such as density and temperature. One can thus hope to obtain a reliable picture of the physical conditions pertaining immediately prior to the onset of collapse to form a star. This has been the main aim of much recent research into core properties using a variety of tracers (e.g. NH_3(1,1) , Benson and Myers 1989, Harju et al. 1993, and CS(1-0), Tatematsu et al. 1993). One typically finds regions of mass 1-100$M_\odot$, of temperature 10 K, of size 0.1 parsec, and of density 10^4 - 10^5 cm^{-3}. Thus the masses are sufficiently high to permit formation of stellar objects and the thermal pressures are higher than the average interstellar value.

Core characteristics have been reviewed by several authors (Myers 1987, Fuller and Myers 1987, Myers 1994, Walmsley 1995). Techniques for determining core density and core temperature have been considered by Walmsley (1987) and by Cernicharo (1991) while Wilson & Walmsley (1989) consider small scale molecular cloud structure in general. A useful reference is the volume "Clouds, Cores, and Low Mass Stars" (Edited by D.P. Clemens and R. Barvainis, Astron. Soc. Pacific Conference Series, Vol.65) where several contributions focus on the structures observed in regions of low mass star formation (see e.g. Fuller 1994, Mundy 1994).

The emphasis in the above cited works is on regions such as the Taurus complex where stars of order a solar mass or less are currently forming. The formation of O-B stars and in general of higher mass stars is clearly a more difficult problem. This is partly due to the greater distance of the nearest regions of high mass star formation and partly due to the fact that massive stars appear in general to form in clusters and associations rather than as single (or double) stars. This latter fact increases the likelihood that there occurs interaction between young recently formed stars and cores where stars are about to form. There are also observational differences between the studies of low mass and high mass stars. These arise from the fact that high mass stars heat and ionize their surroundings.

In this brief summary, I confine myself to the simpler case of low mass star formation and ignore the fascinating complexities of O-B star formation. However for the benefit of high–mass star formation "aficionados", I note that a useful discussion of high mass star formation is given in the review by Churchwell (1991) and some more recent work is summarized by Gaume (1994). In this work, I will discuss the formation of "isolated stars" if such a thing exists and in particular our knowledge of the physical conditions in the cores from which such stars form.

2 Tests of Inside-Out Collapse

Much recent discussion of low mass star forming regions has been based on the concept of "inside-out collapse" developed by Shu and his collaborators (see e.g. Shu, Adams, and Lizano 1987, Lizano and Shu 1989). This is based upon the idea that the starting point for collapse may in many cases be a structure whose characteristics resemble a singular isothermal sphere in hydrostatic equilibrium. Such a structure should have a $1/r^2$ density distribution about its center of mass and roughly speaking an observed column density distribution dropping off as $1/p$ where p is the projected distance from the center of the observed "core". The collapse that then ensues commences at the center and propagates at the sound speed towards the outside. At any moment in time, the structure consists of an "inside" which is collapsing with $v \sim r^{-0.5}$ and $n \sim 1/r^{1.5}$ and an "outside" which is still static. This propagation of the collapse from the center to the rim has given rise to the term "inside-out collapse". The applicability of this model to the real world is of course debatable (see e.g. Foster (1994) and Foster and Chevalier (1993)) and so one needs to find suitable tests in which the model predictions are confronted with observations. In the following, we summarize a few such tests which have been carried out to date.

2.1 Studies of the "Linewidth-size" relation

How can one study the evolution of dense cores prior to and in the immediate aftermath of the formation of a young star? There are no clear answers to this question but one popular approach has been to examine the distribution of cores in a linewidth–diameter diagram (see e.g. Caselli and Myers (1995) and references therein). In the first place, these parameters are relatively easy to measure in nearby regions such as Taurus and Orion. Secondly, irrespective of the precise mechanism leading to core collapse, it is clear that linewidth, which is a measure of velocity dispersion in the core, and size, which is related to the gravitational potential energy, are likely to be of critical importance for core

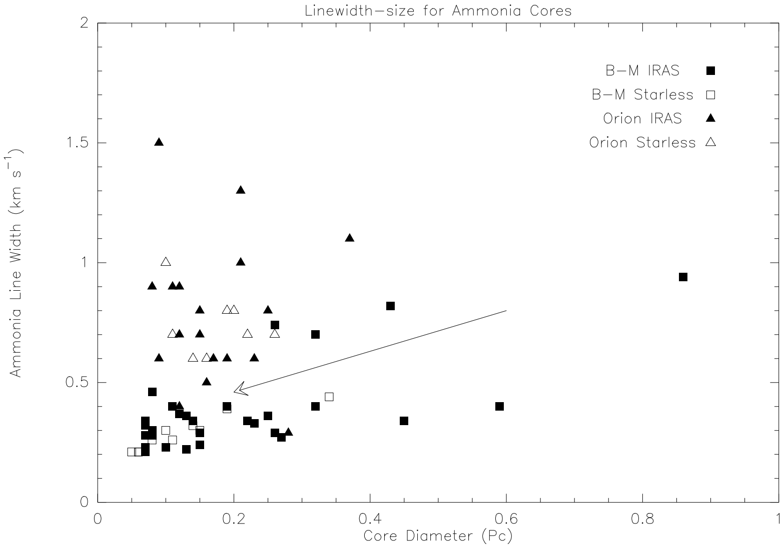

Figure 1: Linewidth versus core diameter based on the $NH_3(1,1)$ data of Benson and Myers (1989, filled squares associated with IRAS sources and empty squares starless cores) and of Harju et al. (1993, filled triangles Orion cores associated with IRAS sources and empty triangles starless Orion cores). The arrow shows how one might expect an evolutionary track to look prior to the switch–on of a star.

evolution. Any consideration of for example the virial theorem applied to the core will lead to a relationship between linewidth and size whose nature will depend upon (among other things) the mechanism or mechanisms causing the observed velocity dispersion. A summary of much of the recent work in this field is given by Fuller (1994). Here, I show one example of the results one obtains combining data from two ammonia surveys of nearby cores.

In Figure 1, I show a comparison of the results of two surveys in the $NH_3(1,1)$ transition (Benson and Myers 1989, Harju et al. 1993) towards clouds closer than 500 parsec. The Harju et al. data is for cores within the giant molecular cloud in Orion (distance 500 pc) whereas the Benson and Myers results concern cores associated with Taurus and other more modest molecular clouds (10^4 $M_\odot$ or less) rather closer to the earth ($<$ 300 pc). A distinction is also made in Figure 1 between "starless" cores and those associated with an embedded infrared (IRAS) source. Presumably, the latter are more evolved than the former. While the details of the evolution of a "starless" core are obscure (see below), one might certainly expect it to be contracting. Since velocity dispersion in all its forms opposes collapse, one might also expect pre–star–forming cores to evolve along tracks of decreasing linewidth. Thus a naive guess would be that an evolutionary track prior to star formation might look like the arrow of Figure 1. The behavior subsequent to star formation is even more speculative but Zhou et al. (1994) have suggested that vertical tracks in this diagram might be appropriate. Hence the linewidth should increase due to the input of kinetic energy stemming from collapse and from the outflows associated with newly formed stars while the size would initially be unaffected.

Unfortunately, the data do not provide clear support for this and similar models! It does seem that the starless cores have typically smaller linewidths than the cores with embedded infrared sources but there is no clear trend in the starless cores of the type depicted schematically by the arrow in Figure 1. What one does note is that the cores in the giant molecular cloud (Orion) have typically larger linewidths than those in the "mini molecular clouds" such as Taurus. This may be related to the fact that the "mini–clouds" do not seem to give rise to O-B stars.

However, more practical considerations may also be influencing the distribution of points on Figure 1. The linear resolution of the observations reported there was of the order of 0.1 parsec and that certainly renders suspect the distribution of points with core diameter less than this limit. Moreover, many cores have elliptical contours rendering the concept of size problematic. Finally, the "chemistry" of ammonia may be biasing the results and (for example) rendering the observed sizes suspect. Thus higher resolution observations in other tracers are warranted.

2.2 Dependence of the column density distribution on radius

A more direct approach to testing the inside–out collapse model is to examine the density distribution in observed cores and to compare with the predictions for an isothermal sphere. Clearly, the column density distribution as a function of radius is a measurable quantity if one can determine with any confidence the position of the core center. Then, one needs an observational tracer whose abundance is proportional to that of molecular hydrogen and one can measure the tracer column density as a function of offset from the center. With this in mind, Zhou et al. (1994) used the $C^{18}O$ column density distribution to analyze a small sample of cores whereas Ward-Thompson et al. (1994) examined the distribution of submillimeter dust emission. The results in both cases suggest that the "real" density distributions are less centrally peaked than $1/r^2$. A recent study by André et al. (1996) confirms this result for the core L1689B in the Ophiuchus complex although these authors find that the column density profile steepens to $1/p$ beyond $25''$ (0.02 pc). More refined models (Mouschovias 1995, Basu and Mouschovias 1995) involving magnetic field support may be needed to account for this.

2.3 Kinematical evidence for collapse

Once collapse has set in, the most fundamental question is whether direct kinematical evidence for infall exists. In a number of cases, such evidence has been found (e.g. Zhou et al. 1993, Wang et al. 1993, Wang et al. 1995, Myers et al. 1995). In a collapsing cloud, one expects that density, temperature, and the absolute value of the velocity should increase with decreasing distance from the central star. One can show that in an optically thick spectral line, such gradients will become apparent to an outside observer by means of a double-peaked profile whose *blue* (i.e. low velocity) peak is stronger than the *red* or high velocity peak. An example of this is shown in Figure 2 where I show both observed and theoretical profiles for one case where there is evidence that the protostar has been caught in the act of collapse (Zhou et al. 1993). Profiles of this type occur because in an optically thick transition, an external observer mainly sees gas at a depth corresponding roughly to unity optical depth (see Leung and Brown (1977), Zhou et al. (1993), Myers et al. (1995) for discussions). In a collapse situation, such gas is closer to the observer at velocities where the gas is red–shifted relative to the stellar velocity. It also turns out that for a velocity law of the form v_{infall} proportional to r^{-p}, the red–shifted gas is expected to be further from the embedded star and hence both less dense and cooler (see discussion of Zhou et al. 1993). The consequence of all this is that the red–shifted portion of the line is less intense than the blue–shifted part. As one can see, the agreement between model and data is qualitatively quite good although the blue–shifted peak of the more highly excited 225 GHz formaldehyde (H_2CO) line is considerably stronger than predicted by theory. Still, one can reasonably claim that this is direct evidence for infall. The details of the infall still however need elaboration.

One of the "details" for which one needs better understanding is that of the outflow. The embedded infrared source in B335 for instance is well known to have a bipolar outflow (in fact it is a class 0 source) whose orientation is roughly in the plane of the sky (see Hirano et al. 1992) and this may be responsible for the wings apparent in the 225 GHz spectrum shown in Figure 2. This outflow is likely to be in some manner a *consequence* of the inflow and understanding the mechanism of this process is certainly a challenge for the future. Presumably also, the outflow is not only caused by the inflow but reacts back upon it and perhaps is responsible for the cessation of infall. Such interactions presumably affect observations of the type seen in Figure 2. For the moment, the challenge is to find reliable methods of estimating both infall and outflow rates in order to compare the two.

3 Cores Prior to Collapse

One can estimate "core age" from the statistics of IRAS sources embedded in cores (Fuller and Myers 1987) and it turns out to be not greatly different to

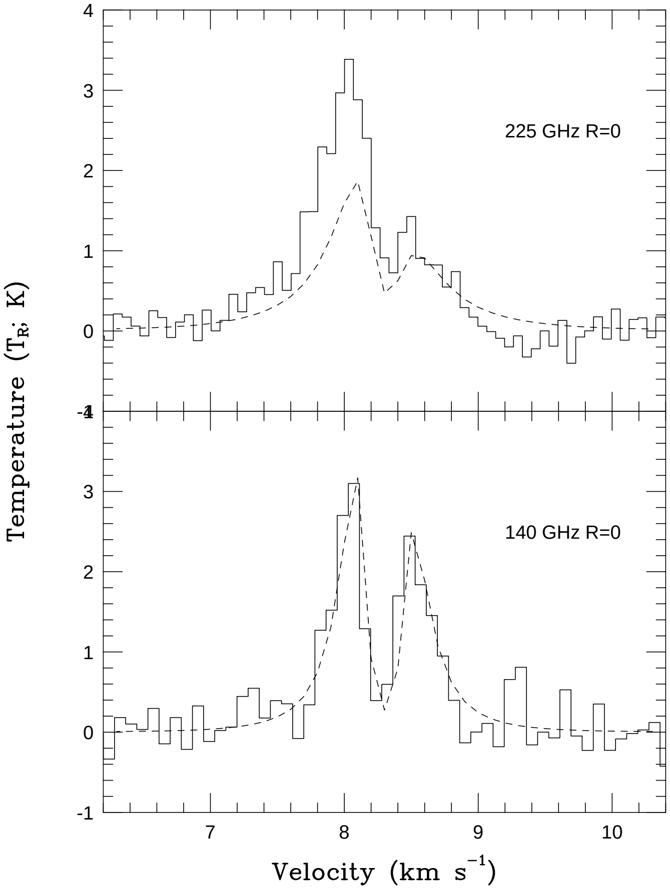

Figure 2: Comparison of model (dashed) and observed (full) profiles of the 140 GHz $2_{12} - 1_{11}$ H_2CO line (bottom panel) and the 225 GHz $3_{12} - 2_{11}$ H_2CO line (top panel) towards the embedded far infrared source in the dark Bok globule B335. The Figure is a corrected version of Fig. 10b from Zhou et al. (1993) (see erratum of Zhou et al. (1994))

the free-fall time (roughly 10^5 years for a density of 3×10^4 cm^{-3}) for these objects. This is short relative to molecular cloud lifetimes (perhaps 10^7 years) and implies that cores must be being formed continually. A consequence is that the mode of formation of the core is likely to leave its imprint upon core structure. The core has no time to "relax"! Moreover, collapse is not held up very long in the core stage. Because this is of some importance for the theory, I briefly review the Fuller-Myers argument here.

The probability that one finds an embedded infrared (IRAS) source associated with a core can be expressed as :

$$p = \frac{\tau_{clear}}{\tau_{wait} + \tau_{detect} + \tau_{clear}}$$

where τ_{clear} is the time taken between a star becoming detectable by IRAS and becoming optically visible (essentially the lifetime of a "class 1 source"), τ_{wait} is the time taken for a core to form a central star, and τ_{detect} is the time taken between the onset of collapse and the time at which observable FIR radiation is present. One can argue about most of the parameters in this equation but values of p in the range of 0.3 to 0.5 have been estimated from the core statistics (Beichman et al. 1986). On the other hand, τ_{detect} is almost certainly small and τ_{clear} is given by the lifetime of class 1 IRAS sources of order 10^5 years (see e.g. Kenyon et al. 1990). Thus it is difficult to avoid the conclusion that τ_{wait} (the lifetime of a "starless" core) is of order 10^5 years.

This causes some problems for theory in that it suggests that the timescales for disposing of magnetic field (assuming that this is the main force resisting collapse) is short. Thus, models with collapse caused by ambipolar diffusion of ions relative to neutrals need this to happen in at most "a few" times 10^5 years or not much more than a free fall time. The ambipolar diffusion timescale (Spitzer 1978, equation 13-57) is approximately $5 \times 10^{13} x_e$ years where x_e is the ionization degree n_e/n_H and thus one can conclude that a relatively low ionization degree (below 10^{-8}) is required by the statistics of infrared source core associations.

Making further progress in this field clearly then requires reliable estimates of both magnetic field and ionization degree. Unfortunately, it turns out to be difficult to measure the field in any direct fashion. Efforts made to date have mainly tried to make use of the Zeeman effect (see e.g. Crutcher et al. 1993) but measurements of this type are extremely difficult. The fundamental problem is that while the Zeeman splitting is most readily observable at low frequency, angular resolution is in general poor at long wavelengths. Most Zeeman experiments have involved the 21 cm line of atomic hydrogen or the 18 cm line of OH. The corresponding angular resolution is of the order typically of several arc minutes. On the other hand, the high density "cores" of interest have in general dimensions of the order of 0.1 parsec (1.7 arc min. at 200 pc) or less. Thus even in very nearby molecular clouds such as Orion (500 parsec), it is difficult to sample dense material (but see Myers and Goodman 1988a,b, Myers and Khersonsky 1995). An "educated guess" for many dense cores is that the magnetic field is around 30 microgauss but there is at least a factor of two uncertainty.

What can one say about measurements of the ionization degree? One can estimate it using the observed abundances of molecular ions such as HCO^+ and N_2H^+ which are linked via charge neutrality to the electron abundance and the ionization degree. Langer (1985) gives a useful summary of the early work in this field and outlines the uncertainties in the various methods of determining $n_e/n(H_2)$. The basic problem is that of accounting for the atomic ions which do not have rotational transitions and therefore cannot be directly measured. Current estimates of x_e are typically a few times 10^{-8} and thus correspond to longer ambipolar diffusion timescales than required by core statistics (see above). But there is considerable uncertainty in these numbers and the last word has certainly not been said. A recent study by de Boisanger et al. (1996) is a good example of a recent attempt to solve this problem (see also the work by Butner et al. 1995). It is worth noting also that estimates of the ionization degree based on theory (see e.g. Myers and Khersonsky 1995) give rise to even larger x_e and longer ambipolar diffusion timescales (see Myers and Khersonsky 1995 who estimate 10^7 - 10^8 years for TMC1-C). In fact, they are so long as to make ambipolar diffusion ineffective and would render much recent theoretical work irrelevant if confirmed.

4 Future Prospects

How is future research in the field of dense cores likely to develop? Predicting the future is dangerous and perhaps hopeless but nevertheless a great temptation. Thus, the following comments should be taken with considerable scepticism. As mentioned above, the most uncertain parameter for dense cores is typically the magnetic field. It is clear that any reliable estimate about the magnitude of the field in dense cores would be enormously important. However, there is no prospect of this situation changing in the near future and in this situation, the most probable development is that we obtain information of ever–increasing precision about the density and column density distribution in cores. This is likely to come for example from the new generation of bolometer arrays now available (SCUBA, SHARC) on the JCMT and CSO telescopes. In dense gas, millimeter dust emission is a tracer of the hydrogen column density distribution which is independent (largely) of the vagaries of interstellar chemistry. The available linear resolution will be of order 0.01 parsec which is much less than a Jeans length for the prevailing densities and temperatures. Thus, one will obtain information on core morphology at around the pivotal moment at which gravitational instability becomes operative. It will be interesting to compare such maps with those observed in molecular lines such as the formaldehyde transitions of Figure 2.

We can also expect advances in our knowledge of the "statistics" of dense cores. Given that a reasonable fraction of dense cores collapse to form protostars which subsequently evolve into pre–main–sequence objects, it is of importance to obtain a census of the number of dense cores in a given mass and size range. This requires unbiased surveys which in the past have been difficult to carry out. However, developments in receiver technology and, in particular, the development of focal plane arrays will change this situation and allow e.g. unbiased searches for ammonia cores. Of course, even without such receiver arrays, some statistical statements are possible. Tóth and Walmsley (1996) for example searched a reasonably large fraction of the L1251 cloud for "ammonia cores" and came to the conclusion that 40 percent of this cloud (by mass) was at densities above 10^4 cm^{-3}. This by itself has no great significance. A relatively small region was surveyed and it had been chosen because there was known to be dense gas present. Still, it should be possible to obtain estimates of this sort in the future for more representative samples and examine how the fraction of dense gas in molecular clouds varies as a function of position and cloud type. This presumably is a key number since it is the fraction of gas which is at densities such that solar mass cores are gravitationally bound which determines the star formation rate.

References

André P., Ward-Thompson D., Motte F., 1996, A&A 314, 625

Basu S., Mouschovias T. Ch., 1995, ApJ 453, 271

Beichman C.A. et al. 1986, ApJ 307, 337

Benson P.J. & Myers, P.C. 1989, ApJS 71, 89

Butner H.M., Lada E.A., Loren R.B. 1995, ApJ 448, 207

Caselli P., Myers P.C. 1995, ApJ 446, 665

Cernicharo J., 1991, p287 in *The Physics of Star Formation and Early Stellar Evolution*, (ed. Lada C.J., Kylafis N.D.), (publ. Kluwer Academic), NATO ASI Vol. 342

Churchwell E., 1991, p221 in *The Physics of Star Formation and Early Stellar Evolution*, (ed. Lada C.J., Kylafis N.D.), (publ. Kluwer Academic), NATO ASI Vol. 342

Crutcher, R.M., Troland, T.H., Goodman, A.A., Heiles, C., Kazès, I., Myers, P.C., 1993, ApJ 407, 175

de Boisanger C,, Helmich F.P., van Dishoeck E.F. 1996, A&A, 310, 315

Foster P. 1994, p105 in *Clouds, Cores, and Low Mass Stars*, edited by D.P. Clemens and R. Barvainis, Astron.Soc.Pacific Conference Series, Vol.65

Foster P.N., Chevalier R.A., 1993, ApJ 416, 303

Fuller G.A. 1994, p3 in *Clouds, Cores, and Low Mass Stars*, (Edited D.P. Clemens, R. Barvainis), Astron. Soc. Pacific Conference Series, Vol. 65

Fuller G.A., Myers P.C., 1987, p137 in *Physical Processes in Interstellar Clouds*, (ed. Morfill G.E., Scholer M.), D. Reidel, NATO ASI Series Vol. 210

Gaume R.A., 1994, p199 in *The Structure and Content of Molecular Clouds*, edited by T.L.Wilson and K.J.Johnston, publ. Springer Verlag, Lecture Notes in Physics 439

Harju, J., Walmsley, C.M., & Wouterloot J.G.A. 1993, AA Suppl., 98, 51

Hirano N., Kameya O., Kasuga T., Umemoto T. 1992, ApJ 390, L85.

Kenyon S.J., Hartmann L.W., Strom K.M., Strom S.E. 1990, AJ 99, 869.

Langer W.D. 1985 , p650 in *Protostars and Planets II*, edited by Black D.C., Mathews M.S., U. of Arizona Press.

Leung C.M., Brown R.L. 1977, ApJ 214, L73

Lizano, S., Shu, F.H. 1989, ApJ 342, 834

Mouschovias T.Ch. 1995, in *The Physics of Star Formation and Early Stellar Evolution*, edited by Lada C.J., Kylafis N.D., Kluwer Academic, NATO ASI Series C, Vol. 342.

Mundy L.G. 1994, p35 in *Clouds, Cores, and Low Mass Stars*, (eds. D.P. Clemens, R. Barvainis), ASP Conference Series Vol. 65

Myers P.C., 1987, p33 in *Star Forming Regions*, IAU Symposium 115, (eds. Peimbert M., Jugaku J.), D. Reidel

Myers P.C., 1994, p207 in *The Structure and Content of Molecular Clouds*, edited by T.L.Wilson and K.J.Johnston, Springer-Verlag, Lecture Notes in Physics 439

Myers P.C., Goodman A.A., 1988a, ApJ 326, L27

Myers P.C., Goodman A.A., 1988b, ApJ 329, 392

Myers P.C., Khersonsky V.K. 1995, ApJ 442, 186.

Myers P.C., Bachiller R., Caselli P., Fuller G.A., Mardones D., Tafalla M. & Wilner D.S., 1995, ApJ 449, L65

Shu F.H., Adams, F.C., Lizano, S., 1987, ARAA 25, 23

Spitzer L., 1978, *Physical processes in the interstellar medium*, publ. J.Wiley.

Tatematsu K. et al. 1993, ApJ 404, 603

Tóth L.V., Walmsley C.M. 1996, A&A 311, 981

Walmsley C.M., 1987, p161 in *Physical Processes in Interstellar Clouds*, (eds. Morfill, G.E., Scholer, M.) D. Reidel, NATO ASI Series Vol. 210

Walmsley C.M., 1995, Revista mexicana de astronomica y astrofisica (serie de conferencias) 1, 137.

Wang Y., Jaffe D.T., Evans N.J. II, Hayashi M., Tatematsu, K., Zhou, S. 1993, ApJ 419, 707

Wang Y., Evans N.J., Zhou S., Clemens D.P. 1995, ApJ 454, 217.

Ward-Thompson D., Scott P.F., Hills R.E., André P, 1994, MNRAS 268, 276

Wilson T.L., Walmsley, C.M. 1989, Astron. Astrophys. Rev., 1, 141

Zhou S., Evans N.J. II, Kömpe C., Walmsley C.M., 1993, ApJ 404, 232 (erratum : ApJ 421, 854).

Zhou S., Evans N.J. II, Wang Y., Peng R., Lo K.Y., 1994, ApJ 433, 131

A CLUSTER OF CLASS 0 PROTOSTARS IN SERPENS

M. Barsony
Physics Department, University of California, Riverside
Riverside, CA 92521 USA
e-mail: fun@nusun.ucr.edu

Abstract

We present new 12, 25, 60, and 100 μm HIRES-processed *IRAS* images of the nearby Serpens star-forming cloud core at FWHM resolutions of $\sim 30''$–$1'$. We use HIRES-processed point-source models of the *IRAS* emission to derive new flux values and flux upper limits for all the protostellar candidates in the Serpens core. Our fluxes (and flux upper limits) determine the spectral energy distributions (SED's) necessary to derive the dust temperature, circumstellar mass, bolometric luminosity, and evolutionary status of each protostellar candidate. Remarkably, we find that all five sources: FIRS1, SMM4, S68N, SMM2, and SMM3 studied by Hurt, Barsony & Wootten (1996) share the defining characteristics of Class 0 protostars, the short-lived (a few $\times$ 10^4 yr) earliest observable protostellar stage (André, Ward-Thompson & Barsony 1993, Barsony 1994).

1 Introduction

1.1 Class 0 Protostars

In order to study the process of star-formation, it is first necessary to locate and identify nearby examples of *protostars*. What exactly is a protostar? Several variants of the definition of a protostar exist in the literature:

- "When the mass [in a given volume of interstellar gas] exceeds a Jeans mass, one would expect the gas to collapse, forming a dense, prestellar cloud, or protostar." (Spitzer 1982)
- [A protostar is] "a young stellar object in the process of acquiring mass through the accretion of an infalling envelope." (Walker *et al.,* 1986).
- "an object deriving more than 1/2 its energy from the accretion of infalling material, rather than from either H-burning or the release of gravitational energy by quasi-hydrostatic contraction of a pre-main-sequence star." (Beichman *et al.,* 1986).

Although there is general agreement that the theoretical definition of a protostar is an object deriving most of its luminosity from the gravitational collapse of a dense, prestellar gas envelope, agreement over the observational characteristics of a protostar has been much harder to achieve.

We can generally divide attempts at the observational identification of protostars into the two general categories of spectroscopic or continuum observations.

The spectral line signature of infall has been fraught with controversy due to many complicating factors, which include radiative transfer effects, poor spatial resolution, and the presence of the theoretically unexpected, but observationally discovered bipolar molecular outflows emanating from the youngest identifiable protostars (*e.g.,* Wolf-Chase & Gregersen 1997; Gregersen *et al.*, 1997).

The classification and identification of the various pre-main-sequence evolutionary stages via continuum measurements first became possible as a consequence of the development of infrared detectors, covering the 2 μm–100 μm wavelength range. Since present-day sites of star-formation in molecular clouds contain $\approx 1\%$ by mass of dust, the dust in protostellar infall envelopes determines the shape (also known as the spectral energy distribution, or SED) of the emergent continuum flux as a function of wavelength by re-radiating any internally generated UV or visible radiation at infrared wavelengths.

The currently accepted classification scheme of young stellar objects, based on the shapes of their continuum SED's, was first proposed by Lada (1987), and has since been modified only slightly (André & Montmerle 1994). Using the definition of the 2.2μm–10μm spectral index, a:

$$a = \frac{dlog\,(\lambda F_{\lambda})}{d\,log\lambda}, \tag{1}$$

Class I sources have $a > 0$ and broader than blackbody SED's; Class II sources have $-2 < a < 0$ and SED's which peak in the near-infrared, but still radiate at levels above reddened stellar photospheres at mid- and far-infrared wavelengths; and Class III sources have $a < -2$ and SED's that resemble reddened photospheric emission. Based on the millimeter dust continuum emission properties of YSO's in the nearby, ρ Ophiuchi cloud core, it has been suggested that the demarcation between Class II and Class III sources be moved from $a = -2$ to $a = -1.5$ (André & Montmerle 1994). It was further proposed by Lada (1987) that these three infrared classes correspond to an evolutionary sequence from youngest (Class I) to oldest (Class III). Subsequent theoretical work led to the currently accepted picture of a Class I source as a few $\times$ 10^5 yr old highly embedded disk+protostellar core system surrounded by an extended infall envelope; a Class II source as a few $\times$ 10^6 yr old disk+protostellar core system (also known as a "classical T-Tauri star," or CTTS), and a Class III source as either a heavily reddened background object, or a few $\times$ 10^6 yr old or older pre-main-sequence star lacking any substantial disk component (also known as a "weak-lined T-Tauri star," or WTTS).

The observational identification of a protostar, based on its continuum spectral energy distribution, had to await the availability of sensitive, large-aperture, ground-based submillimeter telescopes (Chandler *et al.* 1990; André, Ward-Thompson & Barsony [AWB] 1993). The term "Class 0 protostar," was first coined by AWB to refer to objects still surrounded by infall envelopes containing at least half of the central object's final main sequence mass. These protostellar gas and dust infall envelopes are so optically thick that Class 0 objects remain undetected in the near-infrared and even in the mid-infrared (at IRAS sensitivities), therefore, they could not fit into the original infrared classification scheme of young stellar objects. The observational characteristics of Class 0 protostars as enumerated by Barsony (1994) are as follows:

- Undetected at $\lambda \leq 10\ \mu m$ (at IRAS sensitivities);
- High ratio of L_{submm}/L_{bol} (where L_{submm} is the luminosity radiated by the object at wavelengths longward of 350 μm and L_{bol} is the total luminosity of the object);
- A fairly narrow SED, resembling that of a single temperature blackbody at $T \leq 30$K;
- Presence of a molecular outflow.

The typical age of a Class 0 source is expected to be of order a few $\times\ 10^4$ yr. Given such a short lifetime, $\leq 1\%$ of a typical young, forming star cluster's population is expected to be in its Class 0 stage at any given time over the typical few million year formation time of a young stellar association (Fletcher & Stahler 1991a; 1991b).

1.2 The Serpens Core

The Serpens cloud core is a region of great interest for star formation studies because of its proximity (d = 310 pc; de Lara, Chavarria-K. & López-Molina 1991), its relatively compact angular extent (Strom, Vrba & Strom 1976), and the high density of young stellar objects it harbors (450 pc^{-3}) at all stages of pre-main-sequence evolution (Eiroa & Casali 1989; 1992, Casali, Eiroa & Duncan 1993). The Serpens core is unique in that it has been surveyed at both near-infrared and millimeter/submillimeter wavelengths (see Figure 1).

A promising method of finding new Class 0 candidates is by identifying strong, localized millimeter dust continuum emission peaks lacking near-infrared counterparts. A recent multi-transition H_2CO study of the millimeter continuum peaks SMM1/FIRS1, SMM2, SMM3, SMM4, and SMM9/S68N confirms the presence of central heating sources and substantial masses of circumstellar gas in each of these objects (Hurt, Barsony & Wootten 1996).

Since the peak emission of Class 0 protostars occurs at wavelengths of $\sim$ 100–200 μm, and the Serpens millimeter continuum peaks are separated by as little as $\approx 20''$, high-resolution far-infrared (FIR) data are required to produce the SED's of these sources to shed further light on their natures.

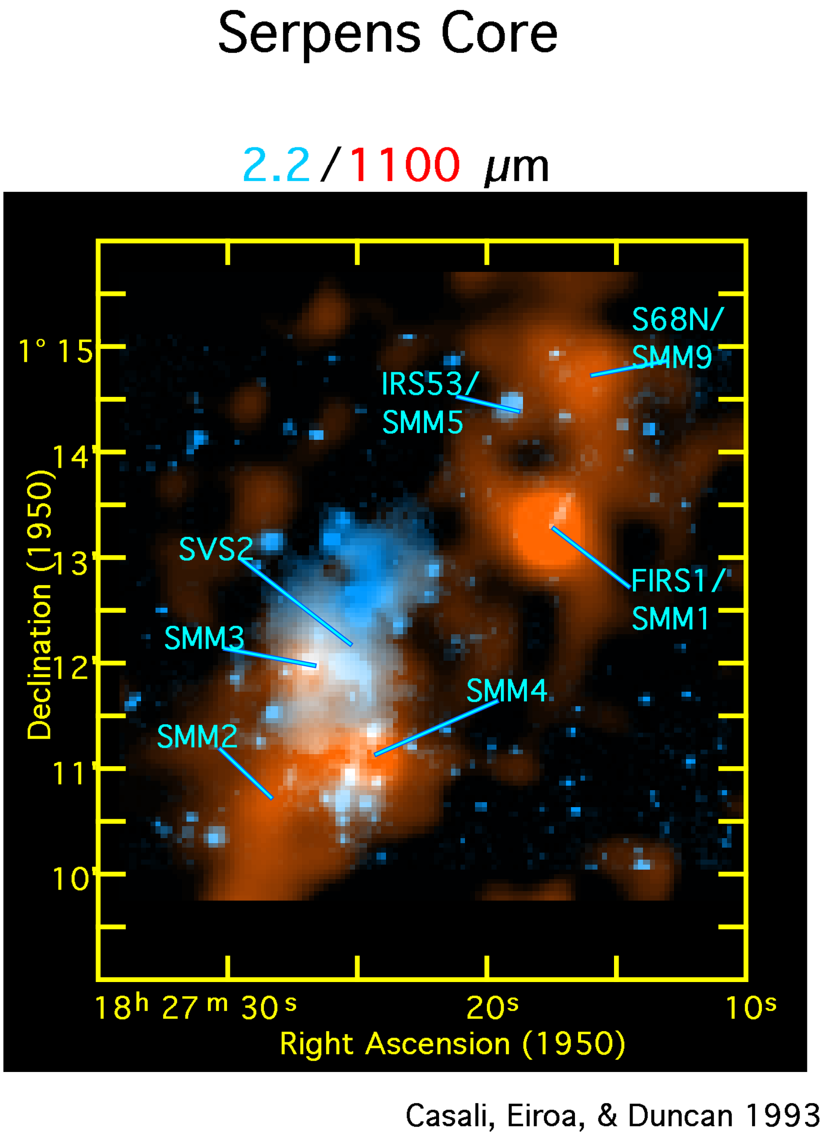

Figure 1: Image of the central 6′ × 5′ (corresponding to 0.54 pc × 0.45 pc at the source) region of the Serpens core, adapted from Casali, Eiroa & Duncan (1993). The 2 μm array camera image is light grey, whereas the 1.1mm continuum emission mapped with the James Clerk Maxwell Telescope is shown in darker grey. The five submillimeter continuum peaks lacking NIR counterparts, studied by Hurt, Barsony & Wootten (1996) are labelled, along with the two strong NIR sources, SVS2 & IRS53.

2 IRAS Data and HIRES Processing

The *Infrared Astronomical Satellite (IRAS)* was able to complete nearly three total sky surveys by scanning of its rectangular detectors at four different wavelengths. Detector responses were read out every $0.5'$ along the scan direction – each such data point is called a "footprint." At each wavelength, there were 2 subarrays of rectangular detectors, with 7 or 8 detectors per subarray. The average detector sizes (FWHM) were: $45'' \times 267''$, $45'' \times 279''$, $90'' \times 285''$, and $180'' \times 303''$, at 12 μm, 25 μm, 60 μm, and 100 μm, respectively. Several steps are involved in producing the best currently available images from the IRAS detector responses. First, the raw IRAS data are run through the LAUNDR program, which uses several one-dimensional flat-fielding and de-glitching techniques to bring the background level of adjacent tracks to a common level. An unwanted, troublesome artifact which results from imperfect detector calibrations across adjacent tracks is "striping." De-striping algorithms are now implemented in both the LAUNDR package, and in the image construction software, YORIC (Yetanother Optimal Resolution Image Constructor) to minimize this problem (Cao *et al.* 1996).

HIRES (HIgh-RESolution) processing of the *IRAS* data is implemented in the YORIC program which uses the Maximum Correlation Method (MCM) described by Aumann, Fowler & Melnyk (1990). At each iteration, YORIC creates simulated *IRAS* detector responses to an input image, compares these simulated responses to the actual detector responses recorded by *IRAS* in the area of sky to be simulated, and calculates correction factors for each image pixel (the default pixel size being $15''$) based on statistical correlations. The calculated multiplicative correction factors are then applied to the input image which becomes the next output image for further iterations of the algorithm.

Prior to the development of YORIC/HIRES, the images from the *IRAS* data were produced by FRESCO (Full-REsolution Survey COadd), which is essentially equivalent to one iteration of HIRES processing.

Figure 2 shows the FRESCO and HIRES images of the Serpens core.

The top panels show single-iteration FRESCO's that do not resolve the core. Images obtained at intermediate numbers of HIRES iterations are presented in the middle panels, and our final, adopted HIRES images are shown in the bottom panels. Default HIRES processing is generally carried out to 20 iterations at each wavelength, however it is clear that major improvements to image quality can be obtained at a much higher number of iterations, especially in the 60 μm and 100 μm maps. The final average point-source responses attained in these maps are $25'' \times 40''$ at 12 and 25 μm, $35'' \times 45''$ at 60 μm, and $50'' \times 60''$ at 100 μm, all with standard deviations of $\sim 20\%$.

Although the HIRES-processed images of the Serpens core are a significant improvement over the previously available FRESCO images of this region, the attained resolution is still insufficient to unambiguously resolve the protostellar candidates. In order to derive fluxes and flux upper limits for these objects, we

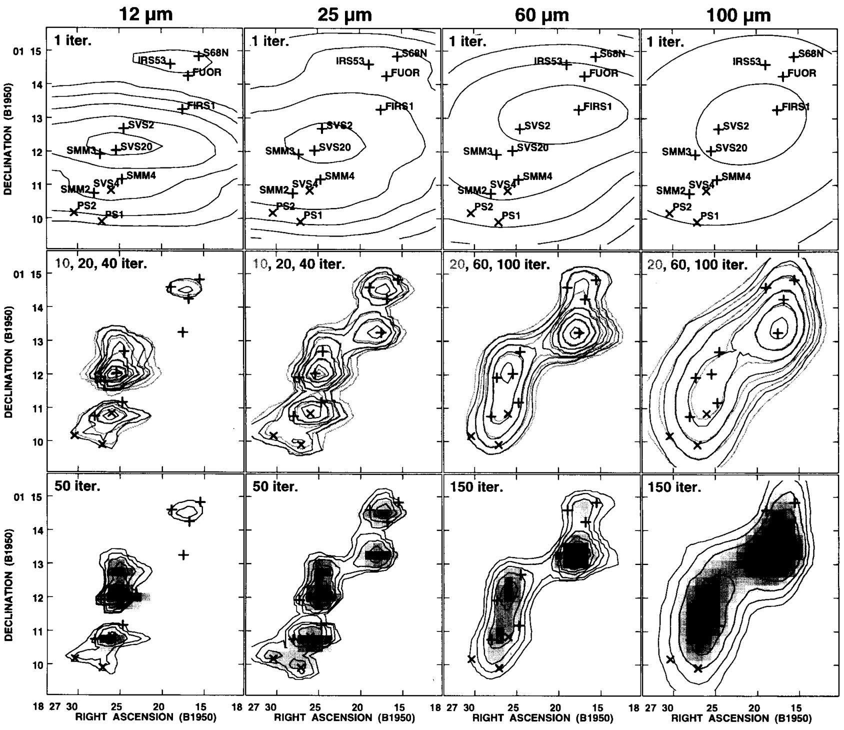

Figure 2: *IRAS* HIRES Serpens Core Images (adapted from Hurt & Barsony, 1996): We present 3 panels for each *IRAS* waveband at 12, 25, 60, and 100 μm. The top panels show the single iteration *IRAS* FRESCO images. The middle panels show in contours the results of differing levels of HIRES processing (lighter contours indicate fewer iterations). The bottom panels show our final adopted HIRES-processed "survey" images (*contours*) overlaid on the point-source "model" images (*greyscale*). All contours are separated by factors of 2 within the indicated ranges. At 12 μm: 1–16 MJy sr^{-1} (*top*), 5–640 MJy sr^{-1} (*middle & bottom*); at 25 μm: 1.5–24 MJy sr^{-1} (*top*), 10–640 MJy sr^{-1} (*middle & bottom*); at 60 μm: 20–320 MJy sr^{-1} (*top*), 50–3200 MJy sr^{-1} (*middle & bottom)*; and at 100 μm: 80–320 MJy sr^{-1} (*top*), 100–6400 MJy sr^{-1} (*middle & bottom*). The locations of the 12 point sources used to produce the "model" images described in the text are indicated by plusses and crosses. Crosses distinguish sources which were inferred to be present based on matching the "model" images to the "survey" images.

started with a point source model of the Serpens core, for which we specified the positions and fluxes for the dozen sources denoted by crosses or plus signs in Figure 2. The point-source model is HIRES-processed as if it were actual *IRAS* survey data, and the resulting point-source model maps were compared with the survey maps. The input source positions were acquired from observations at other wavelengths (either 2 μm or 1.1 mm), whereas the input fluxes were adjusted until the best agreement with the HIRES-processed survey data was achieved at each wavelength. The bottom panel of Figure 2 demonstrates the good agreement between the "survey" (*contours*) and final "model" (*grey scale*) maps. Fluxes obtained from aperture photometry of well-resolved sources in the "model" and "survey" maps agree to 5%. However, by having used the point source model, we know the input fluxes and flux upper limits to much higher accuracy than if we had depended on aperture photometry from the HIRES-processed survey data alone.

3 Results and Discussion

Our derived *IRAS* HIRES point source fluxes and/or flux upper limits at each waveband for the 12 point sources indicated in Figure 2 are listed in Table 1 of Hurt & Barsony (1996). We combined the available photometry for each candidate protostar, assumed 10″ source radii, except for SMM1/FIRS1, for which we assumed a 6″ source radius (McMullin *et al.* 1994) and fit modified blackbody curves to the data according to the equation:

$$F_\lambda = B_\lambda(T_d)(1 - e^{-\tau_\lambda})d\Omega \tag{2}$$

where F_λ is the observed flux at wavelength λ, $B_\lambda(T_d)$ is the value of the Planck function at wavelength λ for a dust temperature, T_d, $d\Omega$ is the source size, and the dust optical depth, τ_λ, was assumed to scale as $\lambda^{-1.5}$. Dust temperatures, T_d, and 250 μm optical depths, τ_{250}, were varied until a "best-fit" curve to the data was determined for each source. The bolometric luminosity of each object is then readily obtained by integrating the area under each blackbody fit. Circumstellar masses, M_c, were derived using the extrapolated 1.3mm fluxes, the derived dust temperatures, the known distance, and an assumed $\kappa_{1.3mm} = 0.01$ cm^2 gm^{-1} (Ossenkopf & Henning 1994):

$$M_c = \frac{F_\lambda d^2}{\kappa_\lambda B_\lambda(T_d)} \tag{3}$$

Several different criteria can be used to determine the proper classification of the Serpens protostellar candidates. One indicator of Class 0 status is the ratio of $L_{bol}/(10^3 \times L_{1.3mm})$. This ratio has values between 2–15 for Class 0 objects, and values from 30–200 for Class I objects (André, Ward-Thompson & Barsony 1993). The values of this ratio are ~ 4 for SMM4, ~ 7 for S68N/SMM9, ~ 10 for SMM2 and SMM3, and ~ 12 for FIRS1/SMM1.

Recently, an evolutionary status diagram in the L_{bol}–$L_{1.3mm}$ plane has been proposed for YSO's (Saraceno *et al.* 1996). For protostars,

$$L_{bol} = \frac{GM_*\dot{M}}{R_*} \quad (4)$$

which shows, that to a first approximation, for a constant mass accretion rate, the central core mass is proportional to the object's bolometric luminosity. (This also assumes the ratio M_*/R_* to be relatively constant during the protostellar phase, based on theoretical interiors models of fully convective central cores with deuterium burning – see Palla & Stahler 1993). Whereas the bolometric luminosity gives an indirect measure of the core mass, $L_{1.3mm}$ is an indirect measure of the envelope mass.

In Figure 3, we plot the Serpens protostars in such a diagram, along with known Class 0 and Class I sources.

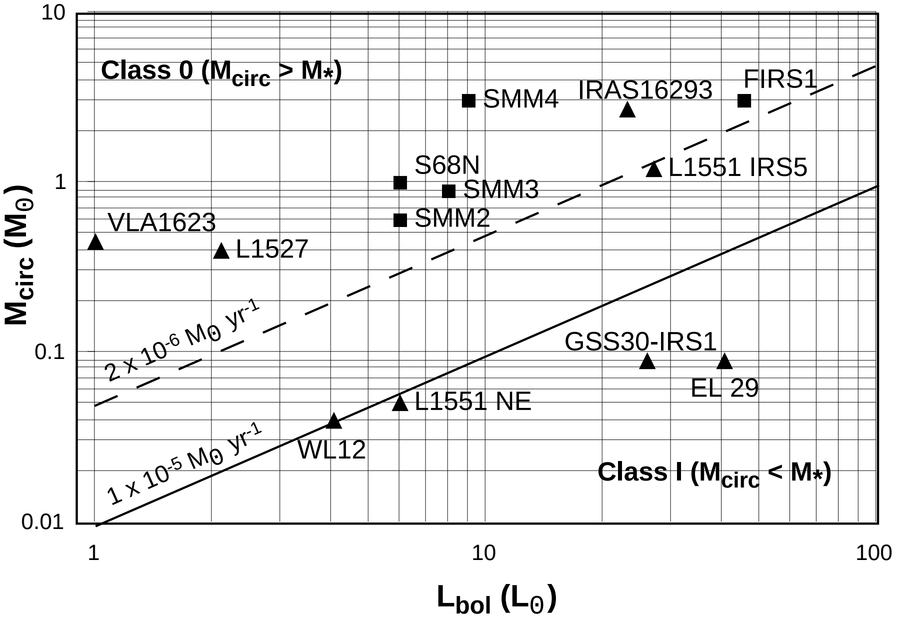

Figure 3: The Evolutionary Diagram for Embedded Sources: Class 0 sources have $M_{circumstellar} > M_*$, whereas $M_* < M_{circumstellar}$ for Class I sources (L_{bol} is directly related to M_*–see text). The two regions of the evolutionary diagram are divided by diagonal lines corresponding to constant mass accretion rates of $\dot{M} = 10^{-5}\ M_\odot$ yr^{-1} and $\dot{M} = 2 \times 10^{-6}\ M_\odot$, yr^{-1}, respectively.

The diagonal lines roughly divide the plane between Class 0 (above the diagonal) and Class I objects (below the diagonal) for assumed mass accretion rates of $\dot{M} = 10^{-5}$ $M_\odot$ yr^{-1} and $\dot{M} = 2 \times 10^{-6}$ $M_\odot$ yr^{-1}. The rationale for this division is that objects with higher inferred envelope masses than core masses are Class 0 protostars, whereas objects with larger core than envelope masses are Class I sources. It is clear from Figure 3 that all of the Serpens protostellar candidates, SMM1/FIRS1, SMM2, SMM3, SMM4, and S68N/SMM9 lie in the Class 0 region of this plane.

A final criterion for Class 0 status is the presence of outflow activity. FIRS1 is a famous outflow source (Curiel et al. 1993; Torrelles *et al.* 1992), SMM4 has a recently discovered CO outflow (White, Casali & Eiroa 1995), and S68N drives a bipolar molecular outflow recently discovered via CS J=2→1 mapping (Barsony et al. 1997). SMM2 and SMM3 have not yet been sufficiently carefully searched to definitively rule out the presence of outflow activity. Given the high source density in the region, such outflow searches may require millimeter interferometry, H_2 mapping in the near-infrared, or large-scale optical imaging through [SII] and nearby continuum filters (such as presented by J. Bally during this conference).

Acknowledgements

This work would not have been possible without the work of Dr. Robert Hurt, formerly of U.C. Riverside, and currently at the Infrared Processing and Analysis Center (*IPAC*). Consultations with Ms. JoAnn O'Linger, currently of U.C. Riverside, regarding the intricacies of *HIRES* processing and the successful incorporation of PostScript figures into a TEX document, were invaluable.

References

André, P., Ward-Thompson, D. & Barsony, M. [AWB], 1993, ApJ 406, 122

André, P. & Montmerle, T. 1994, ApJ 420, 837

Aumann, H.H., Fowler, J.W. & Melnyk, M. 1990, AJ 99, 1674

Barsony, M., 1994, in: Clouds, Cores, and Low-Mass Stars, Proceedings of the 4th Haystack Conference, eds. D. P. Clemens & R. Barvainis, ASP Conf. Ser. 65, Astronomical Society of the Pacific, San Francisco, p. 197

Barsony, M., Wootten, A.H., Hurt, R.L., Lowrance, P. & Kastner, J. 1997, in prep.

Beichman, C.A., Myers, P.C., Emerson, J.P., Harris, S., Mathieu, R., Benson, P.J. & Jennings, R.E. 1986, ApJ 307, 337

Cao, Y., Prince, T., Terebey, S. & Beichman, C.A. 1996, PASP 108, 535

Casali, M.M., Eiroa, C. & Duncan, W.D. 1993, A&A 275, 195

Chandler, C.J., Gear, W.K., Sandell, G., Hayashi, S., Duncan, W.D., Griffin, M.J. & Hazell, S. 1990, MNRAS 243, 330

Curiel, S., Rodriguez, L.F., Moran, J.M. & Cantó, J. 1993, ApJ 415, 191

de Lara, E., Chavarria-K., C. & López-Molina, G. 1991, A&A 243, 139

Eiroa, C. & Casali, M. M. 1989, A&A 223, L17

Eiroa, C. & Casali, M. M. 1992, A&A 262, 468

Fletcher, A. & Stahler, S.W. 1991a, ApJ 435, 313

Fletcher, A. & Stahler, S.W. 1991b, ApJ 435, 329

Gregersen, E.M., Evans, N.J. II, Zhou, S., Choi, M. 1997, ApJ 484, 256

Hurt, R.L., Barsony, M. & Wootten, A.H., 1996, ApJ 456, 686

Hurt, R.L. & Barsony, M. 1996, ApJL 460, L45

Lada, C.J., 1987, IAU Symp. 115: *Star-Forming Regions*, eds. M. Peimbert & J. Jugaku, Dordrecht: Reidel, p. 1

McMullin, J.P., Mundy, L.G., Wilking, B.A., Hezel, T. & Blake, G.A. 1994, ApJ 424, 222

Ossenkopf, V. & Henning, T. 1994, A&A 291, 943

Palla, F. & Stahler, S.W. 1993, ApJ 418, 414

Saraceno, P., André, P., Ceccarelli, C., Griffin, M. & Molinari, S. 1996, A&A 309, 827

Spitzer, L., 1982, in *Searching Between the Stars*, Yale University Press: New Haven, CT

Torrelles, J.M., Gómez, J.F., Curiel, S., Eiroa, C., Rodriguez, L.F. & Ho, P.T.P., 1992, ApJL 384, L59

Strom, S.E., Vrba, F. & Strom, K.M. 1976, AJ 81, 638

Walker, C.K., Lada, C.J., Young, E.T., Maloney, P.R., and Wilking, B.A. 1986, ApJL 309, L47

White, G.J., Casali, M.M. & Eiroa, C. 1995, A&A 298, 594

Wolf-Chase, G.A. & Gregersen, E. 1997, ApJL 479, L67

DENSE CORES IN REGIONS OF HIGH MASS STAR FORMATION

I. Zinchenko
Institute of Applied Physics, Russian Academy of Sciences
46 Uljanov str., 603600 Nizhny Novgorod, Russia
e-mail: zin@appl.sci-nnov.ru

Abstract

Results of the recent systematic studies of dense molecular cores in regions of high mass star formation are reviewed.

1 Introduction

There is an increasing interest in systematic studies of dense molecular cores in regions of high mass star formation (HMSF). In comparison with low mass star forming regions, extended samples of which have been observed in various molecular lines, only a few, rather arbitrarily selected cores associated with HMSF regions have been investigated in some detail (for a review see e.g. Walmsley & Güsten 1994).

Here we review first results of a project aimed at the systematic search for dense cores in regions of high mass star formation and their thorough investigation on the basis of multiline observations and numerical modelling.

2 Searching for HMSF cores

Systematic studies of HMSF cores require a representative sample. In order to compile it we need appropriate pointers and tracers of these objects.

High mass star formation is accompanied by several prominent phenomena. In particular, young massive stars create ultra-compact (UC) HII regions in their vicinity. At the later stages of the evolution more evolved HII regions are developed. Young stars are usually surrounded by rather thick dust envelopes which re-emit the stellar radiation in the far-infrared. Massive stars are rather luminous and are observed in this case as bright FIR sources. The physical conditions in the neighbourhood of high mass stars are favourable for the formation of molecular masers, in particular water masers. These phenomena provide us with the pointers when looking for dense molecular cores forming high mass stars.

There are several commonly accepted tracers of dense gas. These are mostly molecules with a relatively high abundance (which makes their detection easier) and a relatively high dipole moment so that they require enhanced density for effective excitation. One can also use higher transitions of these and other molecules because the critical density increases rapidly with frequency. However, molecular abundances can vary strongly which might lead to wrong conclusions. For example, in Figure 3 we present maps of S 255 in the CS $J = 2 - 1$ and NH_3 (1,1) lines which show significant difference in the distributions of these molecules though both of them are considered to be good tracers of dense gas. Therefore, we have to study the reasons of these abundance variations on the one hand and, on the other hand, it is necessary to use several species in order to obtain a reliable representation of investigated objects.

In recent years several comprehensive surveys of UC HII regions, bright FIR sources and H_2O masers in the lines of high density gas tracers have been performed. In particular, Bronfman et al. (1996) surveyed almost 1500 IRAS sources with the color characteristics of UC HII regions in the CS $J = 2-1$ line; Anglada et al. (1996) surveyed about 140 H_2O masers in the CS $J = 1 - 0$ and ammonia lines; Plume et al. (1992) surveyed H_2O masers in the CS $J = 7 - 6$ line, etc. These surveys are very useful for identifying dense molecular cores and their statistical studies. However, the sources usually are not mapped and therefore such important characteristics as mass, size, spatial structure and kinematics cannot be determined.

In 1992 the radio astronomical groups from the Helsinki University Observatory and Institute of Applied Physics (Nizhny Novgorod) started a CS survey of dense HMSF cores, in the northern sky at the Metsähovi and Onsala radio telescopes (Zinchenko et al. 1994, 1996) and in the southern sky at SEST (Zinchenko et al. 1995, Juvela 1996, Lapinov et al. 1996).

In Metsähovi 11 dense cores have been observed in the CS and $C^{34}S$ $J = 2-1$ lines and 6 of them have been mapped in the main isotope line. Two cores have been partly mapped in the $J = 1 - 0$ HCN line. In Onsala about 60 H_2O masers have been surveyed in the CS $J = 2 - 1$ line. The Onsala data have not been fully processed yet. A part of the cores was investigated in the (1,1) and (2,2) ammonia lines at the 100-m radio telescope in Effelsberg (Zinchenko et al. 1996). At SEST the observations have been performed towards non-stellar H_2O and OH maser sources (Braz & Epchtein 1983, Braz et al. 1989, Scalise et al. 1989). So far about 60 masers have been observed.

An important feature of these observations is that practically all detected sources have been mapped in the CS lines and observed also in the optically thin $C^{34}S$ lines. This enables determination of the basic physical parameters of the cores.

3 Basic physical properties

The CS cores have been detected at SEST in practically all of the survey directions. These directions were selected only on the basis of the maser activity. Thus, the detected sources represent a relatively uniform sample of HMSF cores.

Further we also use a subset of the total sample: cores located within 3 kpc from the Sun. They are less affected by the selection effect and might give unbiased representations of the statistical distributions.

In Figure 1 we present histograms of statistical distributions of the main physical parameters as derived from the CS data obtained at SEST: size, mean density, mass and CS mean line width (Zinchenko 1995). The thin lines in Figure 1 correspond to the whole sample and the heavy lines correspond to the 3 kpc subsample.

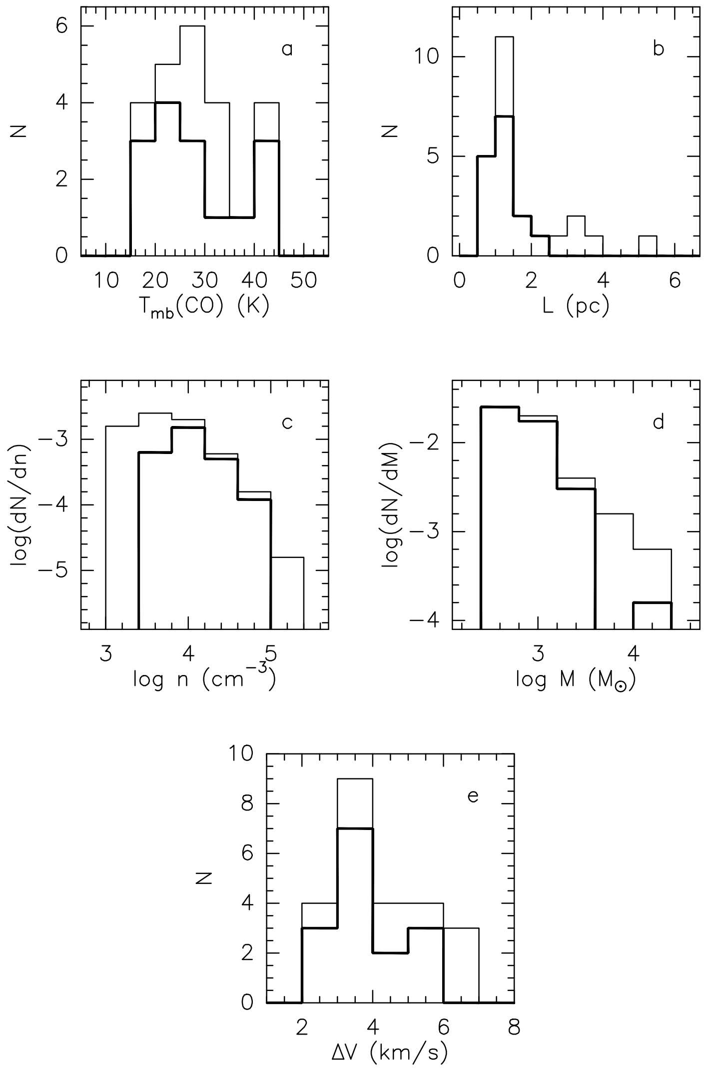

Figure 1: Histograms of the peak CO main beam brightness temperature (a), size (b), mean density (c), mass (d) and mean CS line width (e) distributions for the CS cores observed at SEST. The thin lines refer to the whole sample and the heavy lines refer to the 3 kpc subsample

We also plot in Figure 1 the histogram of the peak CO main beam brightness temperature distribution. It indicates the kinetic temperature in these regions. However, the kinetic temperature in the core interiors can deviate significantly from these values due to presumably high optical depths in this line and apparent foreground absorption in several cases.

An inspection of these histograms leads to the following conclusions:

The distribution of the core sizes peaks sharply at its lower edge. Most of the cores have sizes of $\sim 1.0-1.5$ pc. The mass spectrum for $M > 1000$ $\mathrm{M}_\odot$ can be fitted by the power law $dN/dM \propto M^{-\alpha}$. The exponent equals $\alpha \approx 1.2$ for the whole sample and $\alpha \approx 1.7$ for the 3 kpc subsample. The difference is explained as a natural result of the selection effect mentioned above. This selection effect should influence the mass spectrum presented in Figure 1d making it less steep at the high mass edge.

It is worth noting that the mean densities are rather low, frequently insufficient for effective excitation of the observed transitions. Density estimates in regions of line formation from multitransitional CS data give 2–3 orders of magnitude higher values. Therefore denser gas should exist in these objects.

In Figure 2 we plot the same core parameters (peak CO main beam temperature, size, density, mass and mean CS line width) as a function of the galactocentric radius. The Metsähovi data are added here too for the sake of comparison and to complement the data set of the analysis.

Figure 2 shows in particular that there is a trend to a systematic decrease of the mean density of the cores with increasing galactocentric distance. Such dependence of the mean density on R is probably consistent with the observed decrease in the HCN detection rate with increasing galactocentric distance for Sharpless clouds (Zinchenko et al. 1989).

In principle a dependence of the apparent mean density on R could be produced by a dependence of the $\mathrm{C^{34}S}$ relative abundance on the galactocentric distance because the mean densities have been derived from the $\mathrm{C^{34}S}$ column densities. In this case we can expect a similar dependence of the ratio of the mass derived from the same column densities to virial mass on R. However, there is no such dependence in the data. Thus, we conclude that possible variations of the $\mathrm{C^{34}S}$ abundance cannot explain the trend mentioned above. The dense gas in the cores seems to be in virial equilibrium.

4 Spatial and kinematic structure

The morphological (spatial and kinematic) appearances of the cores vary significantly. Almost half of the CS sources have apparently simple nearly spherical structure. There are elongated sources, possibly with smooth velocity gradients and multicomponent sources. This appearance is not determined by the distance to the source only. Some of the most remote cores have a rather complex spatial structure while other cores lying much closer are compact and do not demonstrate such complexity.

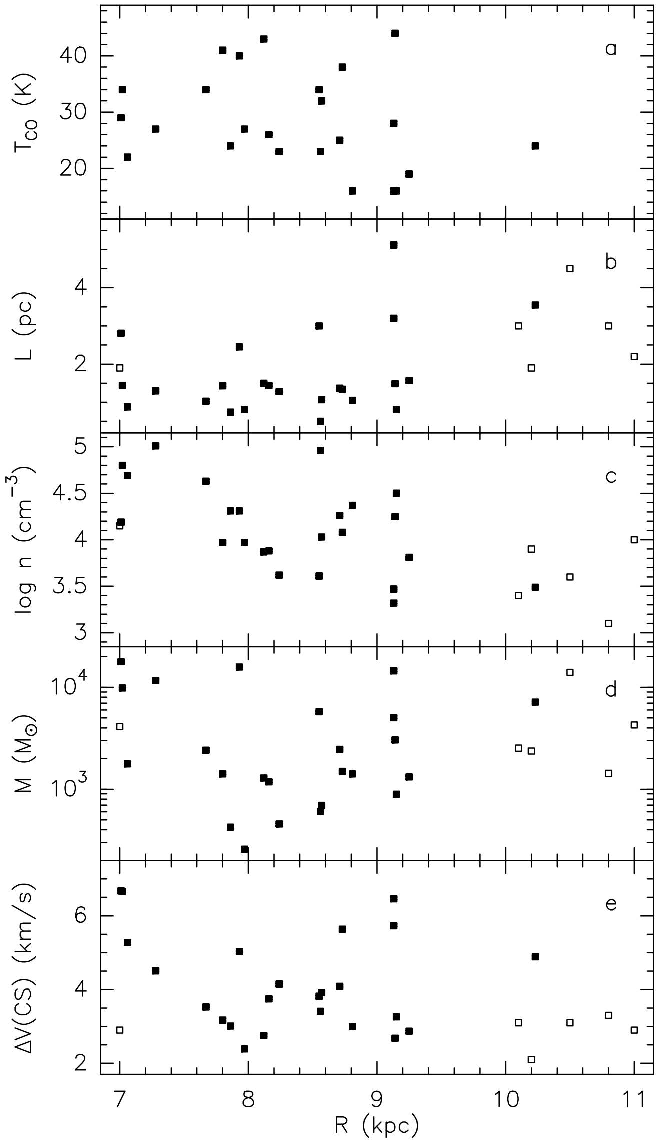

Figure 2: Dependences of the peak CO main beam brightness temperature (a), size (b), mean density (c), mass (d) and mean CS line width (e) on the galactocentric distances for the CS cores observed at SEST (filled squares) and Metsähovi radio telescope (open squares)

One of the most interesting examples is shown in Figure 3 (Zinchenko et al. 1996). The dense core associated with the HII region S255 has a highly elongated structure with a strong velocity gradient along the major axis. However, the images in the CS and in the NH_3 lines are significantly different. While the CS emission has a peak at the IRAS source position, the ammonia peaks are displaced to the north and to the south. Probably this difference is caused by the variations of the molecular abundances. It shows that one should be careful in interpreting the data since it is easy to come to very different conclusions about the source structure.

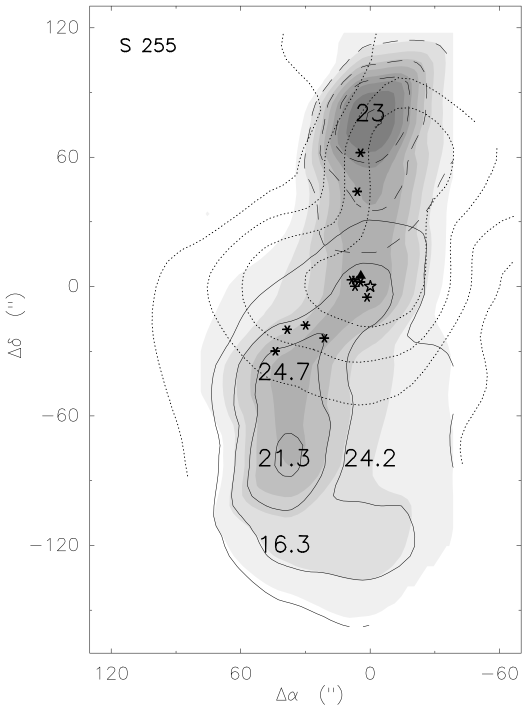

Figure 3: The integrated NH_3 (1,1) line intensity map of S255 (grey-scale). The $V_{\rm LSR}$ interval is from 4.8 to 10.8 $\rm km\,s^{-1}$. Solid and dashed contours correspond to the velocity intervals from 4.8 to 6.8 $\rm km\,s^{-1}$ and from 8.8 to 10.8 $\rm km\,s^{-1}$, respectively (contour levels start from 0.5 $\rm K\,km\,s^{-1}$ with 0.5 $\rm K\,km\,s^{-1}$ increment). The star shows the position of the IRAS point source. The triangle indicates the position of the H_2O maser. The asterisks mark the positions of near- and mid-IR sources. The numerical values show the kinetic temperature derived from the NH_3 (1,1) and (2,2) observations. The dotted contours correspond to the CS $J = 2-1$ map from Zinchenko et al. (1994)

For several cores with apparently spherical structure the line areas drop rather quickly with r, corresponding to $r^{-1.5}$ to r^{-2}. The effective optical depth in the lines at the core edges should not be high. If the CS excitation temperature is constant along the radius then the line area depends only on the column density (linearly). Then we would conclude that the mean gas density drops as fast as $r^{-2.5}$ to r^{-3} (for a constant CS abundance). Actually, in any case the CS will be excited less effectively at larger radii and the density gradient should be less steep than this. A numerical investigation of the radial density dependence requires multiline data.

The CS line widths decrease towards the core edges as well. In principle this could be due to decreasing optical depth and lower saturation broadening at the edges. However, in several cases the CS line width drops below the $C^{34}S$ line width (measured at the CS peak position). It might be that the optical depth in these $C^{34}S$ lines is also rather high. Otherwise we have to conclude that the nonthermal velocity dispersion decreases with the radius (this dispersion can be due to turbulent or systematic motions).

As mentioned above the data obtained imply strong density inhomogeneities in the cores. In particular, the densities in regions of line formation derived from the ratios of the $J = 7-6$ and $J = 2-1$ CS intensities are 2–3 orders of magnitude higher than the mean densities derived from the column densities. Another evidence comes from the comparison of the CS and $C^{34}S$ line widths and brightness temperatures. It shows that the CS line broadening is lower than predicted for an uniform LTE model with the terrestrial $[CS]/[C^{34}S]$ abundance ratio (Zinchenko 1995). These data can be explained in the framework of clumpy models or "core+envelope" model.

5 Prospects

Further investigations require (1) an extension of the list of such HMSF cores with comparable observational data available in order to obtain more reliable information on these statistics and dependences and (2) detailed multiline mapping of selected sources for better understanding their structure.

References

Anglada G., Estalella R., Pastor J., Rodriguez L., Haschick A., 1996, ApJ 463, 205

Braz M.A., Epchtein N., 1983, A&AS 54, 167

Braz M.A., Scalise Jr. E., Gregorio Hetem J.C., Monteiro do Vale J.L., Gaylard M., 1989, A&AS 77, 465

Bronfman L., Nyman L.-Å., May J., 1996, A&AS 115, 81

Juvela M., 1996, A&AS 118, 191

Lapinov A., et al., 1996, in preparation

Plume R., Jaffe D.T., Evans II N.J., 1992, ApJS 78, 505

Scalise Jr. E., Rodríguez L.F., Mendoza-Torres E., 1989, A&A 221, 105

Walmsley C.M., Güsten R., 1994, In: Wilson T.L., Johnston K.J. (eds.) *The Structure and Content of Molecular Clouds*, Lecture Notes in Physics 439, Springer-Verlag, Berlin, p. 164

Zinchenko I., 1995, A&A 303, 554

Zinchenko I., Lapinov A.V., Pirogov L.E., 1989, AZh 66, 1142 (SvA 33, 590)

Zinchenko I., Forsström V., Lapinov A., Mattila K., 1994, A&A 288, 601

Zinchenko I., Mattila K., Toriseva M., 1995, A&AS 111, 95

Zinchenko I., Henning Th., Schreyer K., 1996, A&A, submitted

MODELS AND OBSERVATIONS OF HOT MOLECULAR CORES

T.J. Millar and J. Hatchell
Department of Physics
UMIST, P.O. Box 88, Manchester M60 1QD, England

Abstract

We review the properties of hot molecular cores with specific reference to chemical modelling, in particular, for G34.3+0.15. We show that the hot core gas in this region has an age of 5×10^3–10^4 yrs and that the abundances of many molecules are consistent with formation in the gas-phase following evaporation of simple molecular ices from the grains. We report on a molecular line survey of a dozen hot cores and present detailed results for CH_3CN. We find, via a modified rotation diagram method which takes optical depth into account, that CH_3CN source sizes are small and that the fractional abundances so large that grain surface formation of this species seems to be required. We end with a discussion of current problems and future directions.

1 Introduction

Interstellar molecular clouds represent a wide spectrum of physical conditions and chemical compositions. For our purposes, we shall consider two types of cloud in which complex molecules have been observed. Cold, dense clouds, such as Taurus Molecular Cloud 1 (TMC-1) have $n(H_2) \sim 10^4$ cm^{-3}, $T \sim 10$ K and $A_v \sim 10$ mag. They are observed to be rich in large, linear unsaturated molecules such as the cyanopolyynes, HC_3N, HC_5N, HC_7N, HC_9N, C_nH(n=2-8), organo-sulphur species, C_2S, C_3S, and C_2O, C_3O and the carbenes H_2CCC and H_2CCCC. In addition, there are a large number of D-bearing molecules observed with D/H ratios in enhanced by factors of 10^3–10^4 over the cosmic D/H ratio of $\sim 1.5 \times 10^{-5}$ (Table 1). The fractional ionisation in these clouds is derived from measurements of molecular ions and is fairly small, $\sim 10^{-8}$, consistent with ionisation by low-energy cosmic-rays at a rate $\sim 10^{-17}$ ionisations per second per H-atom. Molecules of intermediate size, such as CH_3OH and CH_3CN, have fractional abundances $\sim 10^{-9}$. Essentially all of the observational evidence to date can be interpreted in terms of purely gas-phase chemical processes at low temperature – the latter being essential to account for the deuterium fractionation observed (see Millar et al. 1987, 1989, Millar and Herbst 1990, Millar 1992, Hasegawa and Herbst 1993, Herbst et al. 1994). Molecular hydrogen, on the other hand, needs to be produced on grain surfaces while the detection of infrared ice bands implies that some fraction, but not all, of the gas phase molecules freeze onto dust particles at low temperatures.

Hot molecular cores (HMCs) are small ($\lesssim 0.1$ pc), dense ($n(H_2) \sim 10^6$–10^8 cm^{-3}), hot ($T \sim 100$–300 K) and dark ($A_V \sim 10^3$ mag) clumps of gas in regions of massive star formation. Physically they appear to have been affected by nearby or internal star formation, either through direct heating or shock interaction. Chemically, they are known to be very different from cold clouds. They contain very large abundances of saturated molecules, including small species such as H_2O, NH_3, H_2S and CH_4, and large species such as CH_3OH, C_2H_5OH, C_2H_5CN and $(CH_3)_2O$, with abundances larger by a factor of at least 10^3 over those in cold clouds. Very few unsaturated hydrocarbon molecules are detected. Cyanoacetylene, HC_3N, is detected, often in vibrationally excited states, but larger cyanopolyynes are not. C_2H has been detected but no larger C_nH molecule. It may be that C_2H occupies a skin layer around a hot core and may not trace the hot dense gas in the volume of the core. Additionally, D fractionation is seen in many molecules, including HDO, NH_2D, DCN and HDCO with enhancements similar to those in cold clouds (Table 1). Indeed the fractional abundance of NH_2D in the Orion Hot Core is larger than that of NH_3 in TMC-1. Since fractionation is a very temperature-sensitive process (see Millar 1993; Millar et al. 1989), the chemical synthesis of deuterium must be occurring at cold temperatures, *not* at the gas kinetic temperature of the hot gas. Taken together with the abundance enhancements of saturated molecules, the implication is that significant processing has taken place on grain surfaces. In this sense, HMCs can be placed in an evolutionary picture of star formation. Cold, dense cores are at an early, or pre-collapse phase. The timescale for accretion of gas onto grain surfaces is $\sim 3 \times 10^9/(n/(\mathrm{cm}^{-3}))$ yr at 10 K, so that on a timescale of $\sim 10^6$ yr, the cold, unsaturated, but D-rich molecules freeze onto grains to form molecular-rich ices which can be detected by IR observations of protostellar sources. Once massive star formation occurs, heating or shock-induced processes liberate the mantle molecules into a hot, dense and essentially neutral gas – the latter is a result of cosmic-ray ionisation being less efficient at high density.

Table 1: Abundance ratios of D-bearing molecules to their H-bearing parents.

Molecule	TMC-1[1]	OMC-1[2]	Core[3]	Molecule	TMC-1[1]	OMC-1[2]	Core[3]
HDO			> 0.002	c-C_3HD	0.08		
DCO^+	0.015	0.002		C_4D	0.004		
N_2D^+	<0.045			DC_3N	0.06		
DCN	0.023	0.02	0.005	DC_5N	0.013		
DNC	0.015	0.01		CH_3OD			0.03
C_2D	0.01	0.045		CH_2DOH			0.04
NH_2D	<0.02		0.003	CH_2DCCH	0.054	<0.05	
HDCO	0.015	0.02	0.01 - 0.14	D_2CO			0.02

[1] TMC-1: Taurus Molecular Cloud 1, $T = 10$ K
[2] OMC-1: Orion Molecular Cloud 1, $T \sim 60$ K
[3] Core: Orion Hot Core, $T \sim 150$ - 200 K

Since the grain surface chemistry tends to form chemically stable molecules, the hot gas is stable for timescales of at least 10^3–10^4 yr. Eventually however, these parent species are destroyed to produce daughter molecules, some of which may also be very complex.

2 Chemical Models

The first models of HMCs were developed by Brown et al. (1988) who considered a three-phase scenario. In phase (1), they followed the chemistry and accretion of an initially atomic gas (with the exception of H_2) as it underwent collapse to high density. Since the accretion timescale ($\sim 10^6$ yr) was shorter than the timescale to reach a chemical steady-state, the accreted grain mantle was rich in atoms such as C, N and O. Phase (2) followed the hydrogenation of these atoms on the grain surface. Hydrogenation is always rapid, providing that there are sufficient H-atoms to collide with the dust. This requires a fractional abundance $\sim 10^{-3}$ which is met at low density and at early times. In this case all accreted C, N and O atoms are converted to CH_4, NH_3 and H_2O with abundances which agree well with observations of many hot cores. At higher density and later times, the H-atom abundance is less whilst the atoms are processed in the gas into stable molecules such as CO, N_2 and O_2. In this case these molecules accrete on to the grains, along with heavier species. In phase (3), Brown et al. followed the chemistry of the evaporated molecules in the hot gas and found that, with a rather limited chemistry, the molecules survived for at least 10^4 yr. Brown & Millar (1989 a,b) extended this work to include deuterium with essentially the same conclusions, and showed also that multiply deuterated molecules would be formed on the surface. Brown and colleagues concluded that observations of gas phase molecules in hot cores would give direct information on the composition of ice mantles in the cold phase. Since infrared observations cannot detect molecules whose abundances are $\overset{\sim}{<}$ 1–5% of the total number of molecules in the ice, whereas submillimeter observations of gas phase molecules are sensitive to abundances 10^6 times smaller, one can hope to use these observations to trace species in grain ices, and thus to constrain grain surface chemistry to a significant degree. This early hope has not yet been fully realised partly because more recent models of phase (3) have shown that chemical processing in the hot gas can be efficient for some species. On the other hand, such processing offers one the hope to develop a 'chemical clock' for HMCs – that is, to find molecules whose abundances are sensitive to the timescale following mantle evaporation.

3 Detailed Source Modelling

With the exception of the models discussed for the Orion hot cores by Charnley et al. (1992) and Caselli et al. (1993), there have been, until recently, no attempts to model more distant sources. Here we discuss models developed for another hot core, that associated with the ultracompact HII region, G34.3+0.15.

G34.3+0.15

This molecular cloud, at a distance of 3.8 kpc, has been studied through a 330–360 GHz spectral scan at the JCMT (Macdonald et al. 1996) and via multitransitional studies of CS (Hauschildt et al. 1995), NH_3 (Heaton et al. 1989), HCO^+ (Heaton et al. 1993) and C I/CO (Little et al. 1994) and, as a result, its chemical and physical parameters are relatively well determined. The molecular cloud has a three component structure, outlined in Table 2, with the densest and hottest component sitting at the head of a cometary H II region. The interaction between the H II region and the cloud appears to be liberating molecules to the gas. The JCMT spectral scan detected 338 lines from 35 species and rotation diagrams were used to obtain estimates of column density, N, and rotational temperature, $T_{\rm rot}$, for 13 species. The observations clearly show evidence of emission from all three components.

Table 2: Physical parameters adopted in the G34.3 model. The radial distance, r, is measured in pc.

Component	$n(H_2)$ (cm^{-3})	T (K)	Outer radius (pc)	$N(H_2)$ (cm^{-2})	A_V (mag)
Ultracompact core	2×10^7	300	0.01	6×10^{23}	640
Compact core	10^6	$30r^{-0.4}$	0.1	2.7×10^{23}	288
Halo	10^4r^{-2}	$30r^{-0.4}$	3.5	2.9×10^{23}	310

A detailed time- and depth-dependent chemical kinetic model has been constructed to investigate chemical evolution within the G34.3 cloud. Physical parameters for this three component model are given in Table 2. The chemical network is chosen so that one can follow the formation of molecules from atomic gas in the halo, and the breakdown of parent molecules liberated from grains in the hot cores of G34.3. The network contains 225 species and 2184 reactions. Models have been calculated at each of 22 radial positions over a period of 10^8 yr. In the cores, the initial state of the gas is molecular with abundances based on the observed and likely components of interstellar grain mantles. For the halo, all elements are atomic (with the exception of H_2) with total abundances given by summing the relevant abundances of species in the core. Thus for O I we set the initial fractional abundance in the halo as

$$f(\mathrm{O\,I}) = f(\mathrm{CO}) + f(\mathrm{H_2O}) + f(\mathrm{CH_3OH}) + f(\mathrm{H_2CO}) + 2f(\mathrm{O_2})$$

where the abundance on the right hand side of this equation refer to the initial fractional abundances in the core. This procedure ensures that the total elemental abundances are equal at every point in the cloud, and is consistent with a picture in which all heavy elements in the gas accrete onto grains in high density cores where they are synthesised to molecular form before evaporation into hot gas.

In order to compare with observations we combine abundances calculated for a specific time, $\mathrm{t}_{\mathrm{halo}}$, in the halo gas and those calculated for a different time, $\mathrm{t}_{\mathrm{core}}$, in the two inner hot cores, with the restriction that $\mathrm{t}_{\mathrm{halo}} > \mathrm{t}_{\mathrm{core}}$, since the cloud must be older than the age of the hot gas.

Parent molecules, that is those liberated from grains, get destroyed on timescales which are sensitive to the activation energy barrier for reaction with H atoms. For species with large barriers, for example H_2O, it takes much longer than 10^4 yr to destroy them while H_2S, which has $E_{\mathrm{A}} = 350$ K, is destroyed within 1000 yr after release in the hot, 300 K gas in the ultracompact core. By comparing observed and calculated column densities we derive ages of $t_{\mathrm{core}} \sim 3 \times 10^3$–$10^4$ yr and $\mathrm{t}_{\mathrm{halo}} \sim 10^5$ yr.

Some molecules can be clearly explained as daughter products. An example is HC_3N which is formed in abundance in the ultracompact core through reaction of parent C_2H_2 with CN and is consistent with the detection of vibrationally excited HC_3N in many hot core sources. Note that HC_3N has traditionally been associated as a tracer of **cold** molecular gas in interstellar clouds, but we find it to be produced easily in hot gas providing C_2H_2 is released from grain mantles. The larger cyanopolyynes are formed inefficiently since we do not consider that grain mantles can contain large unsaturated molecules such as diacetylene, C_4H_2.

Not all complex molecules appear to be daughter species. While $(CH_3)_2O$ probably is a daughter, the large observed abundances of C_2H_5OH (Millar et al. 1995) and CH_3CN (Olmi et al. 1996a,b; Hatchell et al. 1996) indicate that these may have formed on grain mantles. An observational test for parent/daughter species would be to investigate molecular abundance variations in a wide variety of hot cores. On timescales approaching 10^4 yr, parent abundances, with the exception of H_2S, are fairly insensitive to time compared to those of daughters. Full details of this model can be found in Millar et al. (1996).

4 Observational Surveys of Hot Cores

A desire to have a general model for the physics and kinematics of hot cores has led to surveys of the many molecular cores that are associated with ultracompact HII regions. Surveys have been carried out in a number of molecular lines (Churchwell et al. 1990, 1992; Cesaroni et al. 1991, 1992, 1994; Olmi et al. 1993). Ammonia and methyl cyanide have been popular choices as they trace dense gas and are good temperature indicators. Results indicate gas temperatures in excess of 100 K and densities of $\sim 10^7$ cm^{-3} in the central regions of the cores.

With a picture of the physical conditions in the hot cores emerging, we can begin to investigate observationally the chemistry by looking at a wider selection of molecules. Macdonald et al. (1996) carried out a spectral line survey of G34.3, and we have continued by looking at about a dozen sources in order to get an idea of the variation of conditions among these cores (Hatchell et al. 1996).

Observations were made using the James Clerk Maxwell Telescope (JCMT)[1] in September 1995. We tuned to four frequencies centred around H_2S 2(2,0)→2(2,1) (216.710 GHz), CH_3CN $J = 13 \rightarrow 12$ transitions (239.140 GHz), $C^{17}O J = 3 \rightarrow 2$ (337.061 GHz) and CH_3CN $J = 19 \rightarrow 18$ transitions (349.350 GHz). Counting both main and image (upper or lower) sidebands, we observed a total of ten 760 MHz-wide bands, which included more than 100 transitions of more than 20 molecules. Hot core sources are listed in Table 3 with the positions, distances (Cesaroni et al. 1991), and LSR velocities (from ammonia; Cesaroni et al. 1992; Olmi et al. 1993) used.

Table 3: Positions, velocities and distances for observed objects

Object	α_{1950} [h m s]	δ_{1950} [° ′ ″]	$v_{\rm LSR}$ [kms^{-1}]	d [kpc]
G9.62+0.19	18 03 16.2	−20 32 03	4.4	5.7
G10.30−0.15	18 05 57.9	−20 06 26	13.5	6.0
G10.47+0.03	18 05 40.3	−19 52 21	67.8	5.8
G12.21−0.10	18 09 43.7	−18 25 09	24.0	13.5
G13.87+0.28	18 11 41.8	−16 46 40	48.3	4.4
G29.96−0.02	18 43 27.1	−02 42 36	97.6	7.4
G31.41+0.31	18 44 59.4	−01 16 04	97.4	7.9
G34.26+0.15	18 50 46.1	−01 11 12	58.0	4.0
G43.89−0.78	19 12 02.8	−09 17 19	53.4	4.2
G45.12+0.13	19 11 06.2	−10 48 26	58.6	6.9
G45.45+0.06	19 12 00.1	−11 03 60	57.0	6.6
G45.47+0.05	19 12 04.4	−11 04 11	62.0	6.0
G75.78+0.34	20 19 52.0	−37 17 02	−0.1	4.1

Our observations included many lines of CH_3CN. Methyl cyanide is a symmetric top molecule that has rotational transitions involving energy states from tens to a few hundred kelvin above ground at submillimetre wavelengths, so it is used as a temperature tracer in dense molecular clouds. We detected methyl cyanide with a signal-to-noise ratio of more than two in seven sources: G9.62, G10.47, G12.21, G29.96, G31.41, G34.26 and G75.78. We failed to detect any in 600 seconds or more of integration on six sources: G10.30, G13.87, G43.89, G45.12, G45.45 and G45.47. Typical $J = 13 \rightarrow 12$ and $J = 19 \rightarrow 18$ spectra are shown in Figure 1. In the stronger sources, we also detected $CH_3^{13}CN$ lines. The ratio of the line intensities in $CH_3^{13}CN$ to their CH_3CN counterparts, of order 10, indicate a significant optical depth in the CH_3CN lines.

---

[1] The JCMT is operated by the Royal Observatory, Edinburgh on behalf of the SERC of the United Kingdom, the NWO of the Netherlands, and the NRC of Canada.

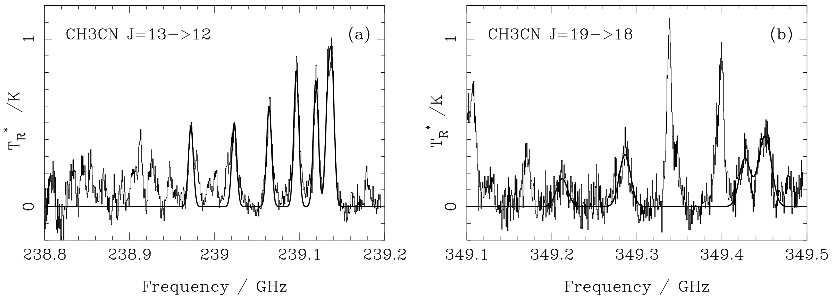

Figure 1: CH_3CN spectra towards G31.41. The observed spectra (thin lines) are overlaid with Gaussian fits to the CH_3CN lines. (a): $J = 13 \rightarrow 12$ spectrum with Gaussian fits to $K = 0 \ldots 6$ components. (b): $J = 19 \rightarrow 18$ spectrum with Gaussian fits to the $K = 0, 1, 2, 5$ and 6 components.

A Gaussian fitting procedure was used to estimate the line parameters. In each frequency band, we selected unconfused methyl cyanide lines with a signal-to-noise ratio of more than two. Each of the Gaussians was centred at the predicted line frequency and was constrained to have the same line width, resulting in a line width $\Delta\nu$ for each band and a peak line temperature T_L for each line within the band.

We analysed the gas excitation using the 'modified rotation diagram' (MRD) technique, a similar method to the standard rotation diagram method. MRD assumes the gas is thermalized but takes optical depth into account. This is necessary in these sources, where we know from the detection of $CH_3^{13}CN$ that the optical depth in CH_3CN is significant. A similar method was used by Olmi et al. (1996a). From an estimate of kinetic temperature T, methyl cyanide column density N_{CH_3CN} and source size θ_S, we can predict the intensity of each methyl cyanide line using the equation

$$T_L{}^{\mathrm{pred}} = \eta_C T (1 - e^{-\tau}), \qquad (1)$$

where η_C is the beam filling factor and τ is the optical depth at line peak (a function of T and N_{CH_3CN}) We use a least-χ^2 fit to choose the three parameters (T, N_{CH_3CN} and θ_S) that produce the closest match to the observed line intensities. We fit the model to the line intensities from the Gaussian fitting procedure. Figure 2 shows observed and modelled line temperatures as a function of upper state energy for G9.62. To estimate the uncertainties on the estimates of T, N_{CH_3CN} and θ_S, we use a standard Monte-Carlo technique.

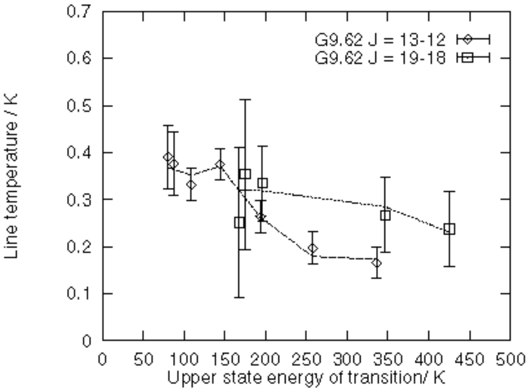

Figure 2: MRD model fit to CH_3CN $J = 13 \rightarrow 12$ and $J = 19 \rightarrow 18$ line temperatures in G9.62. The data are shown as points with errorbars; the model fits are overlaid as lines.

Temperature, column density and source size estimates for all sources are shown in Figure 3. The sources are arranged in order of the intensity of the $J = 13 \rightarrow 12$ $K = 2$ line, with stronger sources to the left. Uncertainties in the estimates from the CH_3CN $J = 19 \rightarrow 18$ data are larger than for the $J = 13 \rightarrow 12$, reflecting the better signal-to-noise ratio of the $J = 13 \rightarrow 12$ observations. The source sizes are well constrained for most sources. For the five strongest sources, both temperature and column density are usefully constrained by the $J = 13 \rightarrow 12$ transitions.

We find gas temperatures between 50 and 200 K and column densities of order 10^{17}cm^{-2}. The estimates for G10.47 and G31.41 are consistent with the interferometer results (Olmi et al. 1996a) and observations of vibrationally excited CH_3CN (Olmi et al. 1996b). Temperatures are generally higher than those estimated from lower-J transitions of CH_3CN and from ammonia (Olmi et al. 1993). Given that we have observed lines involving energy levels at 500 K above ground, we require the gas to be hot, and our results reflect this. Source sizes are small – 0.01 – 0.07 pc, comparable to or smaller than the associated ultracompact HII regions. The larger sources produce the more intense $J = 13 \rightarrow 12$ lines. The region emitting the higher-excitation $J = 19 \rightarrow 18$ transitions appears to be smaller, but we have no evidence (given our uncertainties) that it is hotter or denser. If the abundance of CH_3CN is similar to that in the OMC-1 hot cores ($\sim 10^{-8}$; Blake et al. 1987) then for a 0.05 pc source, hydrogen densities are implied to be $\sim 10^8$ cm^{-3}. It appears that CH_3CN is enhanced in these sources, possibly to a greater extent than in Orion.

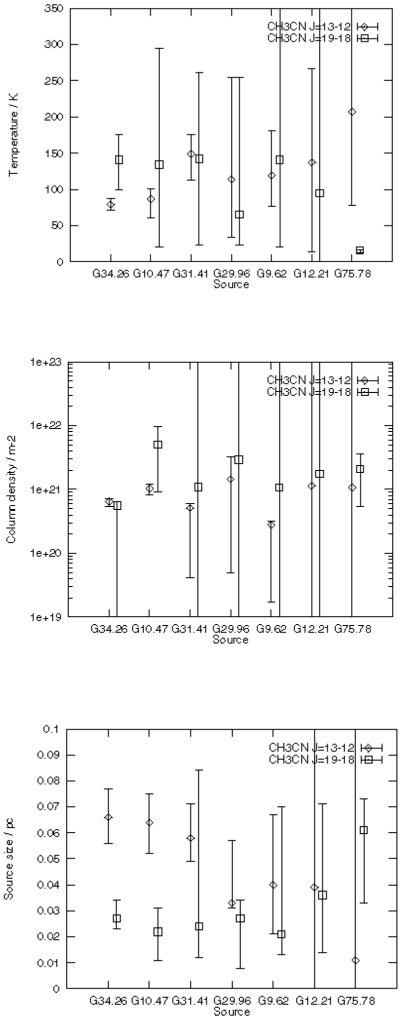

Figure 3 a, b, c: CH_3CN temperature, column density and source size. Errorbars are 1σ .

$C^{18}O$ and $C^{17}O$ emission trace quite different physical conditions from CH_3CN. This emission is predominantly from extended, cool gas surrounding the hot cores. The observations, with beamsizes of 14 and 21″ (for $J = 3 \rightarrow 2$ and $2 \rightarrow 1$ transitions), are not sensitive to hot, dense CO on the scale of the CH_3CN source sizes. Instead, the line emission is dominated by the cold, ambient cloud in which the cores form. We determine source sizes of 0.2 – 0.7

pc from CO, an order of magnitude greater than the methyl cyanide results. Excitation temperatures are 18–38 K. Column densities in the ambient cloud are 1–40 $\times 10^{23}$ cm^{-2}, assuming a $[H_2]/[C^{18}O]$ ratio of 1×10^7.

Another molecule observed in several of our sample sources is methanol. As for CH_3CN, we see emission from states that are several hundred kelvin above ground, and require high temperatures and densities for excitation. Like CH_3CN, CH_3OH is probably produced by processing on grain mantles and released into the gas phase by heating.

Three sources in the survey appear to have very similar chemical composition, namely G34.3, G10.47 and G31.41. In addition to CH_3OH and CH_3CN, which has levels up to 600 K above ground populated, they show 6 or 7 lines from the $J = 27 \rightarrow 26$ transition of C_2H_5CN and several transitions from the A- and E-states of $HCOOCH_3$, the latter from levels with $E_{\rm lower}$ below 200 K. Other species detected only in these sources include SiS, $^{13}CH_3OH$, $CH_3^{13}CN$ and vibrationally excited CH_3OH. Since high column densities and strong infrared radiation fields are needed to detect these species, these three sources appear to contain the densest and most highly excited gas with this gas being very close, probably within a few arcseconds, of an IR source. Other sources also contain hot gas. For example, transitions of CH_3CN which arise from levels 300 K above the ground state are detected also in G29.96, G9.62, G12.21 and G75.78.

Molecular transitions which trace lower excitation material are detected in all or nearly all sources. With the exception of G43.89, we detect the CH_3C_2H $J = 14 \rightarrow 13$ $K = 0$ and 1 components which arise from levels around 100 K above ground state. Low energy transitions from CCH, CH_3OH, SO and HNCO are detected in many sources. The $2_{2,0}$ - $2_{1,1}$ transition of H_2S, with an upper energy level at about 100 K, is detected in 6 sources, G34.3, G10.47, G31.41, G29.96, G9.62 and G75.78. Charnley (1996) has suggested that H_2S can be used to determine the age of hot core gas and it will be interesting to see if age rather than excitation is the reason for its non-detection in G12.21, G45.47, G10.3, G43.89 and G13.87.

Although the data have yet to be fully analysed, it is clear that hot molecular cores appear to have differing physical and chemical properties. G34.3, G10.47 and G31.41 appear to contain emission from the densest and most highly excited gas. All sources appear to have cooler, halo gas and much more work needs to be be done to separate out the core/halo contributions, and to investigate further excitation and chemical differences between sources.

5 Discussion and Conclusions

The chemical composition of hot molecular cores appears to be dominated, directly or indirectly, by the evaporation of molecular material from the ice mantles on interstellar dust grains. From a comparison of observations and theoretical models, one can conclude that the ices are not simply a repository for material accreted from cold gas – that is, their composition does not mirror the composition of cold gas in dark clouds. Instead, the mantles undergo a significant degree of chemical processing, principally hydrogenation but also deuteration and the formation of large molecules such as CH_3OH and C_2H_5OH. The details of this processing are still uncertain. It may involve radical production through ultraviolet processing and subsequent reaction, or quantum tunnelling of H and H_2 through activation energy barriers. Whatever the process, the detection of deuterium fractionation in hot cores implies that much of the processing takes place in a cold ice phase. Indeed it is probable that understanding the origin and interrelationship between deuterated species such as HDCO, D_2CO, CH_3OD and CH_2DOH will be the key to describing the chemistry of the molecular ice mantles. In the laboratory, it is already known that H_2CO and CH_3OH can be synthesised from CO through the addition of H atoms at 10 K (Hiraoka et al. 1994).

Since infrared studies of molecular ices, even those with ISO, are not sensitive to mantle components less than 1–5% that of the dominant molecule, H_2O, submillimeter observations of gas-phase molecules in hot cores allow one to probe the trace constituents of the ices, and thus can provide sensitive tests of models for surface chemistry. Such observations are also of importance in studying the star formation process. At high densities, one expects that cold gas, including CO, freezes onto grains and becomes unobservable through radio spectroscopy. In many instances the grain mantles are also unobservable because of the lack of a background continuum source. Although dust continuum emission can be detected from such 'protostars', this only gives information on the total mass of dust and gas, via a dust-to-gas ratio. One might therefore expect that there will be a phase in the formation of a star, which may last 10^5–10^6 yr, in which the star formation process becomes 'invisible' through the lack of a good observational diagnostic probe. Observational studies of hot molecular cores can help probe this hidden phase of star formation.

Despite our advances in understanding hot molecular cores much still remains to be done. We need to study the molecular composition of a wide variety of hot cores to look for systematic trends in abundances and excitation. The structure of the molecular cloud associated with G34.3+0.15 is complex and the same may be true in general of hot cores. We need multitransitional and interferometric studies of several molecules to determine physical and chemical structure and studies at offset positions to separate out core/halo contributions.

On the theoretical side, we need to investigate depth-dependent models in which the grain mantle composition may vary radially. Such effects may be expected if sublimation controls the nature of the molecules accreted, as argued by Caselli et al. (1993).

Although we have a lot of room-temperature laboratory data on which to base our models of hot gas phase chemistry, we have important gaps in our knowledge. Based on modelling we have asserted that certain molecules, for example C_2H_5OH and CH_3CN, are formed through surface chemistry. However, it is still very possible that we have not correctly identified the gas phase routes to these molecules and that solid state chemistry is a much simpler process than we envisage. In addition to experimental measurements of the rate coefficients of neutral-neutral reactions, we need to build more detailed physical models of grain mantles and cloud structures. We need also to investigate the removal of mantles by shock waves. In shocked regions the neutral gas will reach much higher temperatures than are possible due to thermal evaporation and the subsequent gas-phase chemistry may be qualitatively and quantitatively different from that described in this article. Hot molecular cores promise to be a useful probe into the star formation process, as well as possibly the best astrophysical example of fundamental low-temperature solid-state chemistry.

Acknowledgements

Astrophysics at UMIST is supported by a grant from PPARC. TJM would like to thank L. Viktor Tóth and the local organising committee for support and hospitality.

References

Blake, G.A., Sutton, E.C., Masson, C.R., Phillips, T.G., 1987, ApJ, 315, 621

Brown, P. D., Charnley, S.B., Millar, T.J., 1988, MNRAS, 231, 409

Brown, P. D., Millar, T. J., 1989a, MNRAS, 237, 661

Brown, P. D., Millar, T. J., 1989b, MNRAS, 240, 25P

Caselli, P., Hasegawa, T.I., Herbst, E., 1993, ApJ 408, 548

Cesaroni, R., Walmsley, C. M., Kömpe, C., Churchwell, E., 1991, A&A, 252, 278

Cesaroni, R., Walmsley, C. M., Churchwell, E., 1992, A&A, 256, 618

Cesaroni, R., Churchwell, E., Hofner, P., Walmsley, C. M., Kurtz, S., 1994, A&A, 288, 903

Charnley, S. B., 1996, ApJ, in press

Charnley, S. B., Tielens, A. G. G. M., Millar, T. J., 1992, ApJ, 399, L71

Churchwell, E., Walmsley, C. M., Cesaroni, R., 1990, A&AS, 83, 119

Churchwell, E., Walmsley, C. M., Wood, D. O. S., 1992, A&A, 253, 541

Hasegawa, T. I., Herbst, E., 1993, MNRAS, 261, 83

Hatchell, J. et al. 1996, A&A, in preparation

Hauschildt, H., Güsten, R., Schilke, P., 1995, in *The Physics and Chemistry of Interstellar Molecular Clouds*, eds. G. Winnewisser & G.C. Pelz, Springer Verlag, Berlin, in press

Heaton, B. D., Little, L. T., Bishop, I.S., 1989, A&A, 213, 148

Heaton, B. D., Little, L. T., Yamashita, T., Davies, S. R., Cunningham, C. T., Monteiro, T. S., 1993, A&A, 278, 238

Herbst, E., Lee, H.-H., Howe, D. A., Millar, T.J., 1994, MNRAS 268, 335

Hiraoka, K., Ohashi, N., Kihara, Y., Yamamoto, K., Sato, T., Yamashita, A., 1994, Chem. Phys. Letts., 229, 408

Little, L. T., Gibb, A. G., Heaton, B. D., Ellison, B. N., Claude, S. M. X., 1994, MNRAS, 271, 649

MacDonald, G.H., Gibb, A. G., Habing, R.J., Millar, T.J., 1996, A&AS, 119, 333

Millar, T. J., 1992, in *Astrochemistry of Cosmic Phenomena,* ed. P. D. Singh, Kluwer Academic Publishers, Dordrecht, p.121

Millar, T. J., 1993, in *Dust and Chemistry in Astronomy,* eds. T. J. Millar & D. A. Williams, IoP Publishers, Bristol, p.243

Millar, T. J., Bennett, A., Herbst, E., 1989, ApJ, 340, 906

Millar, T. J., Herbst, E., 1990, A&A, 231, 466

Millar, T. J., Leung, C. M., Herbst, E., 1987, A&A, 183, 109

Millar, T. J., Macdonald, G. H., Gibb, A. G., 1996, A&A, in prep

Millar, T. J., Macdonald, G. H., Habing, R. J., 1995, MNRAS, 273, 25

Olmi, L., Cesaroni, R., Walmsley, C. M., 1993, A&A, 276, 489

Olmi, L., Cesaroni, R., Walmsley, C. M., 1996a, A&A, 307, 599

Olmi, L., Cesaroni, R., Neri, R., Walmsley, C. M., 1996b, A&A, 315, 565

Young stars

REGIONS OF LOW-MASS STAR FORMATION

Werner Pfau
Astrophysikalisches Institut und Universitäts-Sternwarte
Schillergäßchen 2, D-07745, Jena, Germany

Abstract

The fundamental question of the relationship between the properties of the star-forming material and the resulting stellar population is addressed in general. Some detail is given on star formation in the Cha III cloud, the status of the isolated T Tauri stars, and on globules as places of star-forming activity.

1 Introduction

Table 1: Mean Characteristics of Interstellar Clouds

	GMC	Dark cloud	Bok globule
Complex			
Size [pc]	20 – 80	3 – 20	
Density [cm^{-3}]	100 – 300	50 – 300	
Mass [M$_\odot$]	$10^5 - 10^6$	$10^3 - 10^4$	
Kin. temp. [K]	7 – 30	8 – 12	
Examples	W51, W3, M17SW	Taurus, Perseus, ρ Oph complex	
Cloud			
Size [pc]	3 – 20	0.2 – 4	0.1 – 2
Density [cm^{-3}]	$10^3 - 10^4$	$10^2 - 10^4$	$10^3 - 10^5$
Mass [M$_\odot$]	$10^3 - 10^4$	5 – 500	2 – 100
Kin. temp. [K]	15 – 40	8 – 12	8 – 12
Examples	Orion OMC1, W33, W3A	HCL2, B5, L1495	B68, B335, CB17
Dense core			
Size [pc]	0.5 – 3	0.1 – 0.4	0.05 – 0.3
Density [cm^{-3}]	$10^4 - 10^6$	$10^4 - 10^5$	$10^4 - 10^6$
Mass [M$_\odot$]	$10 - 10^3$	0.3 – 10	0.5 – 10
Kin. temp. [K]	30 – 300	8 – 12	8 – 12
Dust temp. [K]		15 – 30	15 – 30
Examples	Orion Ridge	TMC1, TMC2	CB68 core

(collected by Launhardt, 1996)

Stars form in condensations within molecular clouds (MCs), the molecular cloud cores, after the onset of gravitational instability followed by the infall of cloud material to some gravitational centre. As to the details of this process there are still large uncertainties left. This is especially true for stars of high mass. Another fundamental question refers to the relation between the properties of the star-forming material and the resulting stellar population. As individual entities, MCs show a great complexity and their parameters cover a broad range. For typical characteristics see Table 1.

The cloud material often appears in elongated or even filamentary form with denser parts and young stellar objects at the outer ends (see, e.g., Figure 2 in Fukui & Mizuno, 1991, for the Taurus complex).

One important objective of research in the field is to relate cloud parameters to the star-forming activity going on there. So, besides measuring MC parameters, one has to carry out as complete and unbiased as possible multi-wavelength surveys for young stellar objects (YSOs) and pre-main sequence (PMS) stars, sometimes being deeply embedded within the cloud material. The task is difficult in that it is not yet clear which cloud parameters are crucial to star formation.

2 Associations

Table 2: List of T Associations and Relation to Nearby OB Associations

Designation	l [°]	b [°]	OB Ass.
IC 348	160	−17	Per OB2
Tau–Aur	(172	−16)	
B 30	192	−12	
Orion Nebula	209	−19	Ori OB1
B35	197	−11	
IC 446	201	00	
NGC 2264	203	02	Mon OB1
Cha T1	297	−15	
Cha T2	303	−14	
Lupus	(338	15)	
ρ Oph	(350	18)	Sco OB2
M 8	06	−01	
M 20	07	00	
R CrA	359	−17	R CrA
IC 5070	84	00	
NGC 7000	85	−01	
NGC 7023	104	14	
IC 5146	94	−05	Cyg OB7
Cep	(118	05)	Cep OB4

(Galactic coordinates of very extended regions in brackets)

In 1947 V. Ambartsumian coined the designation *association*, now OB association, for loose groupings of O- and B-type stars, massive stars found close to the plane of the Galaxy and in relation to giant dark clouds. Referring to concentrations of spectroscopically detected variable stars of the type T Tauri, P. N. Kholopov in 1951 introduced the designation *T association*. These PMS stars of low-mass are almost exclusively observed close to dark cloud regions, as well. Table 2 lists a selected number of T associations together with their counterparts of OB associations, if there is any.

That OB and T associations appear together is not a surprise. Intuitively we expect the formation of low-mass stars together with the high-mass ones. The surprising fact is rather that not in any case we find both types of associations together, and if this is the case, then low- and high-mass stars are not homogeneously mixed. Prominent examples are the Lynds dark cloud L 1641, which is dominated by young low-mass stars but forms only a minor part of the huge OB association Orion OB1, or the 1 pc diameter low-mass star cluster IC 348 within Perseus OB2, which measures about 50 pc across.

One possible way to discriminate between the stellar content of star-formation regions or parts of them is their *initial mass function*, IMF, i.e. the number of stars, N, at time of formation per unit interval of $lg\,M$, M being the mass expressed in solar masses, $M_\odot$ (see Figure 1). For masses above about 2 $M_\odot$ the IMF has the form

$$dN/d\,lgM \sim M^{-x}.$$

For stars with $M \geq 5\ M_\odot$ in the association Orion OB1, the exponent was determined by Brown et al. (1994) to be $x = 1.7 \pm 0.2$. A value close to this seems to be generally valid for stars of more than about solar mass in the solar vicinity, clusters and OB associations, and in external galaxies.

There is one important difference, however: the termination of stellar masses at the high-mass end increases with the total mass of the cloud complex the stars form from. At the low-mass end the mean behaviour is represented by $dN/d\,lgM \approx const.$ Peaks of slightly increased numbers of stars at 0.2 and 0.55 $M_\odot$ are probably real. As to the median mass there seems to be some variation between T associations. Whereas in the Taurus–Auriga region the mean mass of T Tauri stars is at 0.6 $M_\odot$, the larger value of about 1.1 $M_\odot$ is indicated for Orion (Larson, 1991). The MC condensations have column densities of $N(H_2) > 10^{22}$ cm^{-2}. They are opaque to optical radiation and the only means to study them are line observations of selected molecules and transitions. A large body of data has been collected up to now. For discussion we refer here to Vilas-Boas et al. (1994) and Ladd et al. (1994). If we arrange typical examples of star-forming regions in the form

Chamaeleon	Taurus–Auriga			
		Perseus	Orion B	Orion A
Lupus	ρ Ophiuchi			

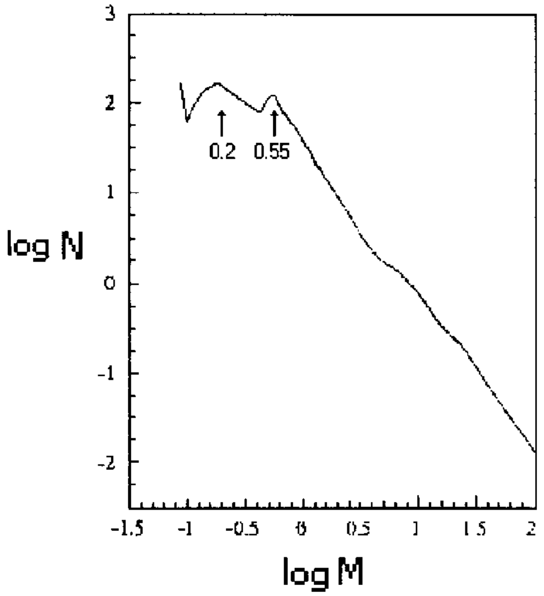

Figure 1: Initial mass function for constant star-formation rate (adapted from Basu & Rana, 1992)

and generalize the individual data, we find the trend of an increase in size, column density, and mass of cloud condensations and in the number of stars, the number of massive stars, and their clustering, when going from left to right. This picture is supported by the data, but it is also guided by the idea that a region of low total density, such as Chamaeleon, e.g., with its flat potential well can only form low-mass condensations and then in turn stars of relatively low mass only. On the other side, in places where the potential wells are deep, we might expect larger and denser cores. The resulting stellar population would then be characterized by low-mass stars being spatially more concentrated plus an additional number of high-mass stars, as it is demanded by the IMF. Examples might be stellar groups in Orion OB1.

The two pairs of regions arranged underneath each other on the left, show similarities in some respect and differences in other ones. The ρ Ophiuchi region, e.g., is dominated by embedded objects of Lada class I, whereas in Taurus–Auriga there are relatively more of class II, i.e., PMS stars.

An interesting aspect is the binary frequency among low-mass YSOs. It seems to be comparable in Chamaeleon, Lupus, near ρ Ophiuchi, and in the solar vicinity, but somewhat enhanced in Taurus–Auriga. With the only exception of Chamaeleon, binary or multiple systems seem to be equally abundant among WTTSs and CTTSs, in Chamaeleon duplicity appears with slightly higher probability for CTTSs (Brandner, 1996).

3 Low-mass young stellar objects

Important representatives of low-mass YSOs are the T Tauri stars. These are PMS stars, which originally were selected upon certain spectral characteristics, namely strong emission lines with sometimes complex profiles of hydrogen (Hα) and Ca II (H and K lines). With the *EINSTEIN* X-ray satellite, the first low-mass YSOs were detected, which lack the prominent spectral emission lines, but are outstanding in their, in most cases variable, X-ray emission. Simply from the presence of the emission lines we nowadays discriminate between the *classical* and the *weak-line* T Tauri stars, CTTSs and WTTSs, resp. Walter (1986) was among the first to emphasize the importance of non-classical T Tauri stars for the stellar content in star-forming regions. When complete samples are considered, one finds that the CTTSs concentrate with the density of the cloud material, the WTTSs, however, are much more widely distributed. A most powerful tool to survey extended regions on the sphere for X-ray sources is the ROSAT All-Sky Survey, RASS. For details and results see, e.g., the contribution by Neuhäuser & Sterzik (1997). Very recently the question of dispersed T Tauri stars and star formation was also addressed by Feigelson (1996).

In a multi-wavelength study we recently investigated the Cha III cloud as one of the parts of the low-mass star-forming region in Chamaeleon. The Chamaeleon region offers the advantages that it is more compact than the Taurus–Auriga region, with a distance of below 200 pc it is closer than Orion, and what is especially challenging, it separates into three parts, of which Cha III was considered to be inactive. As compared to other star-forming regions, even in comparison to Cha I and Cha II, the condensations in Cha III are of relatively low density and low mass only. They therefore appear suitable to probe the dependence of star formation on molecular gas parameters. We detected nearly 100 Hα emission line stars in a $5° \times 5°$ ESO-Schmidt field and 57 X-ray sources, 27 of them presumably WTTSs, in a deep ROSAT-PSPC field centred on the star T Cha. These are typical signs of recent star formation. For details I refer to Pfau et al. (1996).

To get insight into the spatial extent of star-forming regions off the areas of high extinction, Neuhäuser et al. (1995) conducted an RASS search south of the Taurus molecular clouds. They found WTTSs at positions up to 20° off the clouds. These stars might have formed at the places where we observe them now and became separated from the present molecular clouds when their local cloud material was used up and/or dispersed. There are others, however, which are far off, very young, and show a distinct radial velocity. These might have been ejected as run-away stars from multiple systems where they once had formed and gained their velocity from internal encounters (Sterzik & Durisen, 1995). Here again the question of duplicity among CTTSs and WTTSs is of great importance.

There are even more extreme cases of angular separation of T Tauri stars from molecular cloud regions. More than ten years ago Rucinski & Krautter (1983) directed attention to the star TW Hya. Being definitely of CTTS-type, it is located in a region of negligible gas density and more than 13° away from dark cloud material. Meanwhile, including our own contributions (Hoff, 1996), a whole little group of so called *isolated* T Tauri stars can be defined.

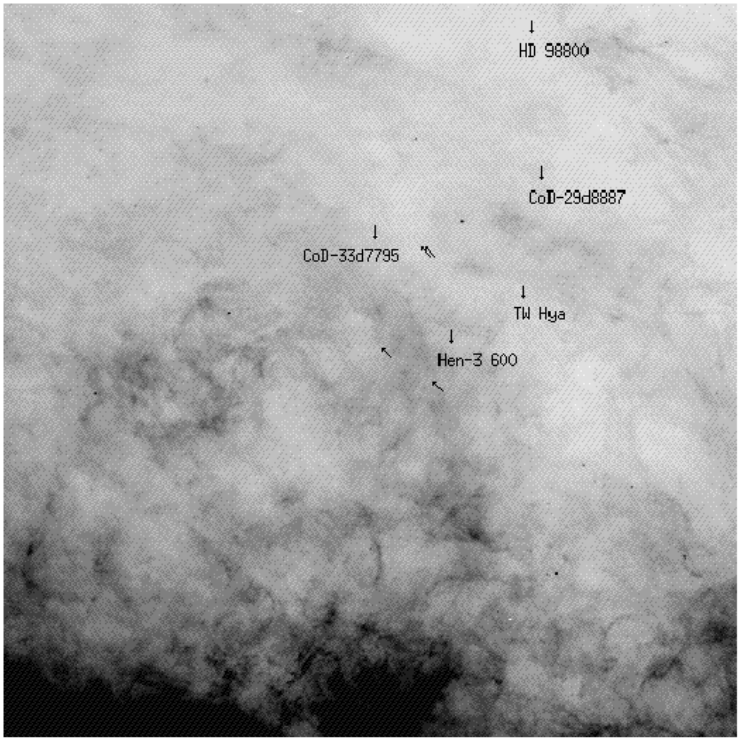

Figure 2: Nine isolated T Tauri stars are marked on the IRAS 100-μm map. A $30° \times 30°$ field centred at the galactic coordinates 285°, 20° is shown. The strong emission (here in black) at the bottom belongs to the constellations Vela and Centaurus.

Our pointed ROSAT PSPC observations revealed a number of X-ray sources in the vicinities of TW Hya and CoD$-29°8887$ (WTTS). From spectroscopic follow-up observations none of them turned out to be a PMS star (Hoff et al., 1996b). TW Hya and CoD$-29°8887$ are thus not locally accompanied by other low-mass YSOs. In order to check the possible presence of PMS candidates in a larger vicinity we used RASS data and searched $6° \times 6°$ fields around three of the isolated T Tauri stars. Together with follow-up observations this revealed a few additional isolated T Tauri stars (Figure 2, Hoff et al., 1996a). The distance of the objects is estimated to be between 50 and 100 pc. Together with the angular separation of several degrees, this means spatial separations of more than

5 pc between them. This satisfies their designation as being *isolated*. At the present stage of the investigation we tentatively explain this group of isolated T Tauri stars as the remnants of a past star-forming region very close to the sun. Its few members are scattered across an extended area on the sky and are difficult to detect.

4 Globules

Globules are very small and isolated molecular clouds of uncomplicated geometry. As a representative number, the catalogue by Clemens & Barvainis (1988) lists 248 objects with less than $10'$ angular diameter for the northern sky ($\delta > 30°$). A subgroup of the globules, the so called Bok globules, are relatively compact and of spherical form. As to their astrophysical properties they resemble the small dark clouds and in their substructures the dense cloud cores (see Table 1). As the latter ones, globules can be the places of formation of low- and intermediate-mass stars. Nearly 50% of the globules are associated with IRAS point sources. In their recent comprehensive study, Launhardt & Henning (1997) investigated the star-forming activity of Bok globules on the basis of NIR photometry and imaging, maps of the 1.3-mm dust emission, and molecular lines. As a result they conclude that 30 to 50% of the globules have masses below 5 $M_\odot$ and will probably never form stars of about solar mass. For another 30 to 50% they expect the presence of dense condensations in a pre-collapse phase. In 10 to 15%, stars of Lada classes −I, 0, and I have been detected, and further 10 to 15% show PMS stars (classes II and III). Part of the latter ones appear separated from the very cores and may have left the central region of the globule already.

In most of the cases close-by massive stars caused the dispersion of the surrounding molecular cloud material of lower density, so that the globule remained. Cometary globules are clear examples of the effect of erosion. With their intense radiation field the stellar neighbours then triggered star formation. The mean mass of all the identified stellar objects in globules amounts to 0.5 to 3 $M_\odot$.

References

Basu, S., Rana, N.C. 1992, ApJ 393, 373

Brandner, W. 1996, Doctoral Thesis, Würzburg

Brown, A.G.A., de Geus, E.J., de Zeeuw, P.T. 1994, A&A 289, 101

Clemens, D.B., Barvainis, R. 1988, ApJS 68, 257

Feigelson, E.D. 1996, ApJ 468, 306

Fukui, Y., Mizuno, A. 1991, Proc. IAU Symp. 147, *Fragmentation of Molecular Clouds and Star Formation*, Kluwer Dordrecht, p. 275

Hoff, W. 1996, unpublished

Hoff, W., Alcalá, J.M., Pfau, W., Sterzik, M.F. 1996a, Abstr. Ser. Astron. Ges. 12, 26

Hoff, W., Pfau, W., Henning, Th. 1996b, in preparation

Ladd, E.F., Myers, P.C., Goodman, A.A. 1994, ApJ 433, 117

Larson, R.B. 1991, Proc. IAU Symp. 147, *Fragmentation of Molecular Clouds and Star Formation*, Kluwer Dordrecht, p. 261

Launhardt, R. 1996, Doctoral Thesis, Jena

Launhardt, R., Henning, Th. 1997, A&A 326, 329

Neuhäuser, R., Sterzik, M.F., Torres, G., Martín, E.L. 1995, A&A 299, 13

Neuhäuser, R. & Sterzik, M. 1997, these proceedings p.369

Pfau, W., Hoff, W., Relke, H. 1996, A&AS submitted

Rucinski, S.M., Krautter, J. 1983, A&A 121, 217

Sterzik, M.F., Durisen, R.H. 1995, A&A 304, L9

Vilas-Boas, J.W.S., Myers, B.C., Fuller, G.A. 1994, ApJ 433, 96

Walter, F.M. 1986, ApJ 306, 573

ASTROPHYSICAL MASERS IN STAR-FORMING REGIONS

N. D. Kylafis[1,2] and K. G. Pavlakis[1,2]
[1] Univ. of Crete, Physics Dept., P.O. Box 2208, 710 03 Heraklion, Crete, Greece
and
[2]FORTH, P.O. Box 1527, 711 10 Heraklion, Crete, Greece

Abstract

The basic physics of astrophysical masers is briefly reviewed. First, a qualitative discussion of the basic concepts about masers is given. These are: Amplification, saturation, thermalization, beaming, variability, spectra and line widths. The difference between laboratory and astrophysical masers is then discussed, the basic requirements for the construction of a maser model are presented and the accuracy with which the various inputs are known is commented on. A qualitative discussion is given of the most common models, which are collisional and radiative. The use of OH masers as diagnostics of physical conditions in star-forming regions is discussed in the end.

1 Introduction

The subject of astrophysical masers is now more than thirty years old, and as a consequence, several good reviews have appeared in print. For the readers who want to enter the subject of astrophysical masers in a serious way, we recommend two reviews (one mainly theoretical, Elitzur 1982 and the other mainly observational, Reid & Moran 1988) and a book (Elitzur 1992).

In this short review, we avoid mathematical details and restrict ourselves to a qualitative discussion of astrophysical masers.

2 Basic concepts

The energy level diagram of a molecule consists of an infinite number of levels. Nevertheless, one need only consider a finite and relatively small number of energy levels in order to perform an accurate model calculation regarding a specific molecule. Even better, for the purposes of a qualitative discussion of masers, one can consider only two energy levels and treat the rest of them as a reservoir.

Let level 1 be the lower maser level and level 2 the upper one. The energy difference between the two levels is $\Delta E \equiv E_2 - E_1 = h\nu$, where ν is the frequency of the maser. Collisional and radiative transitions cause the molecules to circulate between the reservoir and the maser levels. Let n_1 and n_2 be the populations *per magnetic sublevel* of the two maser levels. The maser phenomenon occurs if, in steady state, the populations satisfy the condition $n_2 > n_1$. This is because, as a photon of frequency ν propagates, it is more likely to cause stimulated emission than to be absorbed.

2.1 Amplification

Consider radiation of frequency ν and intensity I propagating through molecules whose energy level diagram was discussed above. The change dI in the intensity that occurs as the radiation propagates by a length dl through the medium is

$$dI = -\kappa I dl \ , \tag{1}$$

where $\kappa \propto (n_1 - n_2)$ is the absorption coefficient corrected for stimulated emission. Here it is assumed for simplicity that the molecules do not emit radiation by spontaneous emission. Defining the optical depth τ by $d\tau \equiv \kappa dl$, one finds that the intensity as a function of optical depth is given by

$$I = I_0 e^{-\tau} \ , \tag{2}$$

where I_0 is the intensity of a background source that is incoming to the medium. If the populations of levels 1 and 2 are such that $n_1 > n_2$, then $\tau > 0$ and the radiation is attenuated as it propagates through the medium. This situation is typical in astrophysical environments and it leads to the formation of absorption lines. On the other hand, if $n_1 < n_2$, the optical depth is negative and the radiation is amplified. This is because a propagating photon is more likely to cause a stimulated emission than it is to be absorbed. Thus, one photon leads to two propagating in the same direction, two photons to four and so on. In other words, the amplification of the radiation is *exponential.*

As mentioned above, it was only for simplicity that spontaneous emission in the medium was neglected. In reality, such an emission always occurs and the radiation thus produced is also amplified. If there is no background source, as it is the case in most astrophysical masers, it is only the spontaneous emission that gets amplified.

2.2 Saturation

The exponential growth of the radiation intensity in a medium that exhibits inverted populations is truly fascinating. It is therefore important to investigate whether this exponential growth has any limits, assuming that the maser region is long enough. Since a stimulated emission event causes the transition of a molecule from the upper maser level to the lower, it is clear that stimulated emission tends to *reduce* the population inversion. At low intensities, the stimulated emission rate is relatively small and the population difference $n_1 - n_2$ remains essentially unaffected. As the intensity grows, so does the stimulated rate. Thus, a point is reached where the stimulated emission rate becomes comparable to the rate that causes the population inversion. At this point, *saturation* has set in because the rate of extraction of photons has reached its limiting value, which is the pumping rate (the rate of population inversion).

Increasing the volume of the emission region under saturation conditions will only increase the photon emission rate in proportion to the volume.

2.3 Thermalization

The establishment of inverted populations in a medium containing a certain kind of molecules is not as difficult as one might think. In fact, it is not an exaggeration to say that if the molecules are abused, they will most likely exhibit inverted populations in *some pair* of energy levels. One cannot easily predict which pair it will be, but inversion in some pair is almost certain. Common methods of abuse of molecules in astrophysical environments are a) collisions with other molecules, b) irradiation of the molecules and c) a combination of the above, which is the usual case. As an illustration, let us consider collisions with other molecules (e.g., H_2) as the cause of population inversion. If the density of H_2 molecules is low, the collision rate is low, the rate of population inversion is low and therefore the maser luminosity is correspondingly low. For low rates of abuse, the maser luminosity increases in proportion to the rate of abuse of the molecules. However, this proportionality has an upper limit. When the collision rate becomes very large, the collisional transitions of the molecules dominate all other transitions (see section 4.3 below), the molecules thermalize at the temperature of the H_2 molecules and the population inversion is destroyed. At thermalization, the level populations obey the Boltzmann distribution, namely

$$\frac{n_2}{n_1} = \exp(-\Delta E/kT) < 1 \ , \tag{3}$$

where T is the temperature of the H_2 molecules.

2.4 Beaming

The majority of the astrophysical masers *do not* emit isotropically. This effect can be understood as follows: Consider a maser region which is not spherically symmetric but instead it is elongated in some direction. The gain $|\tau|$ along the direction of elongation is larger than in directions perpendicular to it. Consequently, the intensity of the maser is largest along the direction of elongation. Thus, a departure from spherical symmetry introduces an anisotropy in the intensity.

Once an anisotropy in the intensity is established, it is further enhanced through the following process. Consider the maser photons that reach a certain point in the maser region from all possible directions. These beams of photons compete for the available pump photons there. The rate of stimulated emission caused by a given beam is proportional to its intensity. Therefore, the stronger beam wins and becomes even stronger. As a result, a non-spherically symmetric maser region results in maser emission in two opposite cones along the direction of elongation.

Radio observers measure the flux of photons that reach their telescope and, not knowing the degree of beaming, they make the assumption that the emission is isotropic. Thus, from the observed flux, an equivalent *isotropic* luminosity is quoted for the source. This procedure certainly overestimates the luminosity of a *maser spot*, but it gives the right value when one considers a region that contains many maser spots. This is because the cones of emission of the various spots have random orientations, but we only see the ones that are directed towards the earth.

2.5 Variability

All masers, even the very strong ones, are variable with the shortest timescale of variability of the order of l/c, where l is the length of the maser. This, of course, is not surprising because even a small change in the gain introduces a significant change in the intensity. Small changes in the gain can be caused either by changes in the aspect angle or by changes in the local physical parameters such as the density and the velocity field. For example, if the maser region is elongated, a small change in the aspect angle may result in a relatively large change in the intensity.

Despite the short timescale of variability, some maser spots can be followed for years. The lifetime of individual spots can be as large as one to two years for H_2O and more than ten years for OH masers. This relatively long lifetime has allowed studies of proper motion of the maser spots and through this the determination of their distance.

2.6 Spectra and line widths

The maser spectra observed in star-forming regions are fairly complex (see, e.g., Genzel and Downes 1977 for a collection of such spectra). H_2O maser spectra in star-forming regions extend over a frequency range corresponding to a velocity difference of a few tens km s^{-1} (typically less than 10 km s^{-1} for OH) and consist of many spikes. VLBI maps which resolve the maser region have shown that a spike arises from one or more distinct spots. The line width of a strong spike is typically a few times smaller than the width expected from the thermal motions of the molecules. This is expected because unlike a thermal line, a maser line grows exponentially (in the unsaturated regime) and therefore the full width at half maximum is smaller than thermal. As the line center saturates, the line wings continue to grow exponentially and the line width approaches the thermal one.

3 Laboratory versus astrophysical masers

Both laboratory and astrophysical masers are based on the same principle, namely, some transition exhibits inverted populations. Nevertheless, there are significant differences in the size and the technical characteristics of the two.

In laboratory masers, the maser region is typically ~ 1 m long (to astronomical accuracy). In order to have significant gain, the radiation is bounced between two mirrors, one of which is semi-transparent to allow the amplified radiation to escape. On the other hand, the astrophysical masers have significantly lower densities but gain lengths of order a few AU or larger. The absence of reflecting boundaries in astrophysical masers makes them single pass as opposed to multi pass in the laboratory ones. Furthermore, the fixed size of the laboratory masers introduces a mode selection, i.e., not all wavelengths can fit in the length of the maser. On the other hand, the astrophysical masers allow all possible wavelengths and they are broad band. Finally, laboratory masers emit coherent radiation, while the astrophysical ones emit non-coherent. This is because in astrophysical masers the beaming angle is fairly large and therefore a significant phase difference is introduced between two rays in the beam.

Because the radiative transfer in astrophysical masers is relatively simple (see section 5), the main theoretical effort has concentrated on inventing efficient pumping mechanisms and exploring the various parameter regimes.

4 Maser models

In what follows we discuss the requirements for the construction of a maser model and comment on how well we know the input parameters. We also give the basic equations that need to be solved and discuss qualitatively how collisional and radiative pumping works.

4.1 Requirements

In order to construct a maser model one needs the following:
a) The energy levels of the molecule that exhibits maser emission. These are generally well known.
b) The Einstein coefficients A_{ij} for the transitions from any upper level i to any lower level j. These also are well known, at least for the most common molecules.
c) The collision rates C_{ij} for transitions from any level i to any level j of the maser molecule. The colliding particles are the other molecules (e.g., H_2) in the region. These rates are only approximately known. Therefore, when maser models are constructed, it should always be kept in mind that the currently published collision rates may be revised.
d) The velocity field in the maser region. This is unknown and it is only guessed in maser models. Two types of velocity field have generally been assumed. In

one, the medium is static and the molecules obey a distribution of velocities (typically Gaussian). In the other, the medium exhibits a large velocity gradient, i.e., the macroscopic velocity differences are significantly larger than the thermal velocities of the molecules.
e) The geometry of the maser region is also unknown and in maser models a simple (typically spherical or cylindrical) geometry is assumed.

4.2 Basic equations

The set of equations that need to be solved consists of the statistical equilibrium equations for the level populations and the radiative transfer equations for the various line frequencies. For simplicity, we will assume that the molecules under study have only three, non-degenerate energy levels with energies E_1, E_2 and E_3 and corresponding populations n_1, n_2 and n_3. If only collisional and radiative transitions are taken into account, the steady state equations describing the level populations are

$$\begin{aligned}\frac{dn_3}{dt} &= -(A_{32}+A_{31})n_3 + R_{13}(n_1-n_3) + R_{23}(n_2-n_3) \\ &\qquad + C_{13}n_1 + C_{23}n_2 - (C_{32}+C_{31})n_3 = 0 \ , \qquad (4a)\\ \frac{dn_2}{dt} &= A_{32}n_3 - A_{21}n_2 - R_{23}(n_2-n_3) + R_{12}(n_1-n_2) \\ &\qquad + C_{12}n_1 + C_{32}n_3 - (C_{23}+C_{21})n_2 = 0 \ , \qquad (4b)\\ &\qquad n_1+n_2+n_3 = N \ , \qquad (4c)\end{aligned}$$

where N is the total number of maser molecules and R_{ij} are the radiative absorption rates corrected for stimulated emission. Generalization of these equations to any number of levels is straightforward.

If ν is the frequency of the transition from upper level j to lower level i and I_ν is the corresponding intensity, then the radiative transfer equation is given by

$$\frac{dI_\nu}{dl} = -\kappa_\nu I_\nu + \eta_\nu \ , \qquad (5)$$

where κ_ν is the absorption coefficient (which is a function of ν and $n_i - n_j$) and η_ν is the emissivity (which is a function of ν and n_j).

The system of equations (4) and (5) must be solved simultaneously.

4.3 Collisional and radiative pumping

Collisional pumping works as follows: The maser molecules are excited by collisions with the other particles (typically H_2) in the maser region. Their de-excitation is done both radiatively and collisionally. If the radiative de-excitations dominate the collisional ones, it is likely that some transition will exhibit inverted populations. However, when the collisions dominate both excitations and de-excitations, the molecules thermalize and the population inversion is destroyed. Equations (4), with only collision terms, yield the Boltzmann distribution for the level populations.

Radiative pumping works in a similar way. The excitation of the molecules is done with infrared radiation from an external source. The de-excitation is done via spontaneous and stimulated emission. In this "flow" of the molecules from level to level, it is likely that inverted populations will be established in some transition. If the external radiation dominates in the de-excitation, thermodynamic equilibrium is established at the temperature of the external radiation.

5 Masers as diagnostics of physical conditions

Significant progress has been made in our understanding of astrophysical masers. It has now reached the point where H_2O maser lines are predicted theoretically (Neufeld and Melnick 1991) and observed (Menten et al. 1990). Also, OH masers can now be used as diagnostics of the physical conditions in star-forming regions (Pavlakis and Kylafis 1996a, b, c; see also Cesaroni & Walmsley 1991). Here we restrict ourselves to this last aspect.

We have performed a detailed, systematic study of OH maser pumping in order to attempt to invert the problem and from the OH maser observations to infer the physical conditions in HII/OH regions. Our most important diagnostics are:

1) If the 4660 MHz line is seen, it means that $n_{\mathrm{H}_2} \sim 10^8$ cm^{-3}. If the 4751 MHz line is seen in the same spatial region, it confirms that $n_{\mathrm{H}_2} \sim 10^8$ cm^{-3}.

2) In the presence of a FIR radiation field, it is more likely to see the 1612 MHz line in the same spatial region with the 1665 MHz line than with the 1667 MHz one. When the 1612 MHz line is seen in the same spatial region with the 1665 MHz one, it means that $n_{\mathrm{H}_2} \sim 10^6$ cm^{-3}.

3) If both the 1665 MHz and the 1667 MHz lines are seen in the same spatial region, a FIR radiation field must be present and $n_{\mathrm{H}_2} \lesssim 10^6$ cm^{-3} there. The 1665 MHz line is typically the stronger of the two.

4) When the 1612 MHz line is observed, it means that $n_{\mathrm{H}_2} \gtrsim 10^6$ cm^{-3}.

5) Inversion of the 4766 MHz line means relatively small velocity gradients. We have found that this line is seen only for $V \lesssim 1$ km s^{-1} under all conditions we investigated.

6) The existence of the lines 1667 and 4766 MHz in the same spatial region, with the 1667 MHz one typically an order of magnitude brighter than the other, means $T_{\mathrm{H}_2} > 150$ K, $f_{\mathrm{ortho-H}_2} \gtrsim 0.5$ and relatively small velocities (typically $V < 1$ km s^{-1}).

7) In the presence of moderate velocity gradients ($V \sim 1$ km s^{-1}), if the 4766 MHz line is seen together with the 4751 MHz one in the same spatial region, then $f_{\mathrm{ortho-H}_2} \lesssim 0.5$. The 4766 MHz line is much stronger than the 4751 MHz one.

8) In the presence of moderate velocity gradients ($V \sim 1$ km s^{-1}), if the 4766 MHz line is observed together with the 1612 MHz one in the same spatial region, then $f_{\mathrm{ortho-H_2}} \gtrsim 0.5$.
9) In the presence of significant velocity gradients ($V \geq 2$ km s^{-1}), it is more likely to have the 1720 MHz line strongly inverted at $n_{\mathrm{H_2}} \sim$ few × 10^8 cm^{-3} than at $n_{\mathrm{H_2}} \lesssim$ few × 10^7 cm^{-3}.
10) As the FIR radiation field increases, the 1665 MHz line increases in intensity and is inverted in a larger range of densities.

This research has been supported in part by a grant from the General Secretariat of Research and Technology of Greece.

References

Cesaroni, R., & Walmsley, C. M. 1991, A&A, 241, 537

Elitzur, M. 1982, Rev. Mod. Phys., 54, 1225

Elitzur, M. 1992, *Astronomical Masers*, Kluwer, Dordrecht

Genzel, R., and Downes, D. 1977, A&AS, 30, 145

Menten, K. M., Melnick, G. J., Philips, T. G., and Neufeld, D. A. 1990, ApJ, 363, L27

Neufeld, D. A., and Melnick, G. J. 1991, ApJ, 368, 215

Pavlakis, K. G., and Kylafis, N. D. 1996a, ApJ 467, 292

Pavlakis, K. G., and Kylafis, N. D. 1996b, ApJ 467, 300

Pavlakis, K. G., and Kylafis, N. D. 1996c, ApJ, 467, 309

Reid, M. J., and Moran, J. M. 1988, in Verschuur G. L., Kellerman K. I., eds., *Galactic and Extragalactic Radio Astronomy*, Springer-Verlag, New York, p. 255.

HYDRODYNAMIC INTERACTIONS BETWEEN MASSIVE STARS AND THEIR ENVIRONMENTS

J.E. Dyson[1], T.W. Hartquist[2], R.J.R. Williams[1] and M.P. Redman[3]
[1]Department of Physics and Astronomy
University of Leeds, Leeds LS2 9JT England
[2]Max-Planck-Institut für extraterrestrische Physik
D-85740 Garching, Germany
[3]Department of Physics and Astronomy, University of Manchester
Manchester M13 9PL England

Abstract

It is becoming clear that a proper treatment of the interaction of stars with their environment must take into account the inhomogeneous nature of circumstellar material. Our ongoing study of this problem is revealing a rich variety of physical effects that have important implications for star-forming regions and the diffuse sources found within them. We describe the mechanisms by which mass is lost from dense clumps and formed into tails which have a range of lengths and shapes depending on the flow conditions. These considerations are applied to a model for ultracompact Hii regions (UCHiiR) in which, as a result of mass injection, the ionization front that is normally expected around a Hii region is replaced by a recombination front. The regions can reach a steady equilibrium, avoiding the well known lifetime problem for UCHiiR models. In another example, properties of the Wolf–Rayet nebula RCW 58 are explained by a mass-loaded model.

1 Introduction

Massive stars (initial main sequence masses, $M_\mathrm{i} \gtrsim 8\,\mathrm{M}_\odot$) possess powerful Lyman continuum radiation fields and hypersonic winds which together disrupt surrounding material. As they evolve, these stars are important sources of mass, momentum and energy for the interstellar medium at large. Massive stars start nuclear burning whilst still in their accretion phase; they are initially embedded in dusty accretion envelopes. Accretion is stopped by the combined action of the wind and radiation field, thus leading to an upper limit on the masses of stars (e.g. Kahn 1974). When these influences spread outside the accretion flow region, they modify the local environment. Conditions there do not reflect those which obtained when star formation took place; consequently, massive star formation is a badly understood process.

Mass loss changes the evolutionary paths of massive stars. Maeder (1984; 1990) showed that initially very high mass stars ($M_\mathrm{i} \gtrsim 60\,\mathrm{M}_\odot$) evolve from O stars to supernovae via stages in which they are successively blue supergiants, luminous blue variables (LBVs) and Wolf–Rayet stars. Lower mass stars ($25 \lesssim M_{\rm i}/\,{\rm M}_\odot \lesssim 60$) go through a red supergiant phase rather than an LBV stage. Fast and slow winds occur at different stages of the evolution, and the stellar luminosity and effective temperature also change dramatically with time, so there are many possible interactions between the stars and their ejecta (e.g. Dyson & Smith 1985).

Most studies of the interaction of the winds and radiation fields of stars with their surroundings are based on the assumption that the circumstellar gas is smoothly distributed. However, practically all diffuse sources of astrophysical interest are clumpy; these include such disparate objects as Wolf–Rayet and planetary nebulae, molecular clouds and active galactic nuclei. The most important distinction between flows initiated in clumpy and in smooth media is that in the former, there is mass, momentum and energy interchange at the interfaces betwen clumps and the diffuse flow, i.e. in boundary layers. The consequences are major (Hartquist & Dyson 1993). The interchange acts back on the dynamical and physical state of the global flow within which the clumps are embedded; conversely the global flow affects both the interchange process and the clumps themselves. Intermediate scale structures are found where material has left clumps and is in the process of assimilation into the global flow. These structures extend in the downstream global flow direction, i.e. they are 'tails'. On the smallest scales, the boundary layers themselves are of great interest but very badly understood. Hartquist & Dyson (1993) have argued that they can only be understood in the context of semi-empirical studies where suitable diagnostics exist. They suggested that chemically active boundary layers between stellar wind flows and dense clumps in molecular clouds probably provide the best combination of diagnostics and spatial resolution (cf. Charnley et al. 1990; Dyson et al. 1995; Rawlings & Hartquist 1996).

In this paper we will concentrate on the physical aspects of various flows in clumpy media. In Section 2 we discuss the mass injection process itself. In Section 3 we discuss the physics of ultracompact HII regions, and in particular we consider the structures of recombination fronts and of mass-loaded isothermal winds. In Section 4 we describe mass loaded flows in the context of a specific object, the Wolf–Rayet nebula RCW 58. Finally, in Section 5 we sum up and comment on areas of future work.

2 Mass Loss from Clumps

Clump material can be fed into a global flow by three different physical mechanisms: thermal evaporation (conduction), hydrodynamic ablation and photoevaporation (i.e. photoionization). Conductive evaporation has been studied extensively (e.g. Borkowski, Balbus & Fristrom 1990 and references therein). If the embedded clump, assumed spherical, is too small for radiative losses to affect the evaporation and too large for the conductivity to saturate at a value lower than that given by Spitzer & Härm (1953) (or for the evaporative flow to become transonic), the evaporation rate due to conduction is $2.75 \times 10^4\,\mathrm{g\,s^{-1}}T^{5/2}(R/1\,\mathrm{pc})$, where T is the temperature of the embedding medium and R is the cloud radius (Cowie & McKee 1977; McKee & Cowie 1977). Magnetic fields may decrease the effectiveness of conductive mass loss, but the level of this suppression is strongly dependent on the geometry of the field and on the detailed dynamics of the plasma.

Hydrodynamic ablation occurs when clumps are exposed to either supersonic or subsonic flows. The compression of a clump embedded in a supersonic flow continues until the clump pressure on the upstream-facing side of the clump becomes comparable to the ram pressure in the flow. The Bernoulli effect results in the pressure differences over the clump surface being comparable to the ram pressure. Expansion of the clump in the direction perpendicular to the flow direction occurs on a sound crossing time, as recent numerical calculations confirm (Stone & Norman 1992; Klein, McKee & Colella 1994). In magnetized media, the evaporation driven by ablation is somewhat reduced (MacLow et al. 1994).

There has been only one numerical simulation of the response of a non-magnetized clump to a subsonic flow (Klein et al. 1994); little information has been published about it, but the limited result seems to be in reasonable harmony with the arguments that are given immediately below. Hartquist et al. (1986) argued that the pressure difference over the clump surface in this case is equal to the clump thermal pressure multiplied by the square of the flow Mach number, M_{F}, measured in the clump frame. The expansion speed of the clump is equal to the internal sound speed in the clump multiplied by this same factor. These authors used a phenomenological approach to determine the dependence of the volume mass injection rate on the flow Mach number; they deduced a rate independent of M_{F} for supersonic flows and a rate proportional to $M_{\mathrm{F}}^{4/3}$ for subsonic flows.

Clumps photoionized by an external radiation field lose their heated surface layers through simple expansion provided that the surface pressure exceeds that of any surrounding material (Dyson 1968, 1994; Kahn 1969; Bertoldi & McKee 1990). If the external flow is supersonic, expansion will occur off that part of the clump surface facing in the downstream direction of the flow at approximately the sound speed in the ionized gas even if the ram pressure is comparable to the clump surface pressure (cf. Hartquist et al. 1986). Some additional mass-loss also will take place in the boundary layer between the shocked global flow gas, which is moving subsonically, and the clump surface. If the external flow is subsonic with a pressure equal to the clump surface pressure, mass-loss can occur only by the slow Bernoulli process as described above.

The whole question of mass-loss from clumps is complex and a proper treatment must include the effects of magnetic fields on ionization front properties and the thermal structure of the clump material. In the specific case of isothermal, non-magnetized, self-gravitating clumps, the surface pressure varies as $r^{-4/3}$, where r is the distance of the clump from the ionizing star (Dyson 1968). The ram pressure in a supersonic flow varies as r^{-2}; the relative importance of any suppression of expansion from the clump surface decreases with increasing distance from the star. The pressure structure in a subsonic flow depends on both the spatial variation and the Mach number dependence of the mass injection rate and strictly needs to be evaluated self-consistently. For the simplest possible case of a very subsonic flow at approximately constant pressure, the importance of suppression of expansion from a clump surface now increases with increasing distance from the star.

3 Ultracompact HII Regions (UcHIIR)

UCHIIR are small ($\approx 10^{17}\,\mathrm{cm}$) ionized regions of high root-mean-square electron density ($\langle n_e \rangle^{1/2} \approx 10^4\,\mathrm{cm}^{-3}$) found embedded deep within molecular clouds. They are thus associated with the early phases of massive star formation and in principle should give information about the star formation process. Arguments based on their numbers relative to the numbers of massive stars suggest a typical age of $t_{\mathrm{L}} \approx 10^5\,\mathrm{yr}$ (Wood & Churchwell 1989). This is short compared to the main sequence lifetimes of the massive stars but long in dynamical terms. Specifically, unless the ambient gas density around the site of star formation is exceptionally high ($\gtrsim 10^7\,\mathrm{cm}^{-3}$), 'classical' HII regions of similar age would have sizes about an order of magnitude greater than those actually observed (Dyson 1994). Severe demands are therefore put on dynamical models.

The most obvious way to circumvent this lifetime problem is shown schematically below:

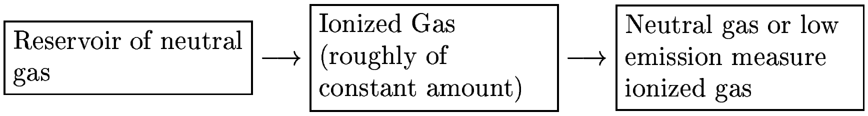

The morphologies of UCHIIR take several forms (Churchwell 1990). Some of these – but not all – show 'Strömgren' like properties: increasing size correlates with a decrease in the rms electron density (Kurtz, Churchwell & Wood 1994). These two factors indicate fairly convincingly that a range of models should be sought. Models which have been discussed in the literature and which are based on the schematic representation above include 'champagne flows' (Tenorio-Tagle, Yorke & Bodenheimer 1979) and 'self-evaporating' massive discs around massive stars (Hollenbach et al. 1994). By far the most attention in the literature has been given to the cometary models produced by bow-shocks in the interstellar gas ahead of moving stars with strong winds (Van Buren et al. 1990) where the reservoir is the molecular cloud gas up-stream of the bow-shocks. These models are discussed by Dyson, Williams & Redman (1995); Redman, Williams & Dyson (1996); Williams, Dyson & Redman (1996) (henceforth DWR, RWD, WDR respectively). A particular problem highlighted by them and by Dyson (1994) is that it is now well established that molecular clouds are extremely clumpy on scales down to the limit of resolution. This poses severe problems particularly for the cometary models.

However, it was suggested by Dyson (1994) and in DWR, RWD and WDR, that the clumpy natures of molecular clouds could be exploited to produce long-lived ionized regions. The basic premise is that the clumps act as *localised* reservoirs of neutral material which can be injected into the global HII region by the processes outlined in Section 2. (A rather similar model has also been proposed by Lizano et al. 1996). The significant point now is that because mass is continuously injected into the HII region, in a steady state, mass must also leave the HII region at a rate equal to the injection rate; the HII region is now bounded by a recombination front (RF) in contrast to an ionization front (IF) which bounds a classical expanding HII region. A RF can be held in a quasi-steady state either by the external pressure if the gas exits the RF subsonically, or by recoil pressure if the gas exits supersonically. Since the gas has been fully ionized before it exits from the HII region, it is likely that the hydrogen flowing out of the region is essentially in the form of atomic hydrogen; this is in distinction to the case of an ionization front bounded HII region in a molecular cloud where molecular hydrogen should lie just ahead of the IF (since the velocity of any shock ahead of an IF is not high enough to dissociate molecular hydrogen). In principle, this difference could provide a discriminant between RF and IF bounded models. We will here concentrate on some of the important physical aspects of these models and present morphological considerations elsewhere (Redman, Williams & Dyson – these proceedings, p 327).

The models given in DWR, RWD, WDR are based on the assumption of a smooth distribution of mass-loading centres in the global flow. In fact (Section 2), no matter what the actual injection mechanism is, mass is assimilated into the flow via tail-like intermediate scale structures. Hartquist, Dyson & Williams (1996) note that the adoption of smoothly distributed mass-source terms is probably valid only if the product of the number density of clumps, the lengthscale over which the global flow parameters vary and the effective cross section a tail structure presents to the global flow, is roughly unity or greater. Clearly it will be much easier to mass-load a flow if tails have reasonably wide opening angles and are not long and very thin. Tails behind clumps embedded in supersonic flows are likely to have wide opening angles and would, if visible, appear to be short and stubby (Dyson, Hartquist & Biro 1993). It is worth noting a caveat to this statement. If a clump has substantial substructure, individual bow-shocks form around each subclump; if the shocked gas can cool well (e.g. as the result of the mixing in of cold ablated clump gas with the shocked wind), the flows behind the subclumps are momentum driven and the net effect is to produce a long thin supersonic tail. Dyson & Hartquist (1994) proposed that such a model might account for the supersonic thin tail observed behind the galactic centre M supergiant, IRS7.

Dyson et al. (1993) showed that long thin tails are formed when a clump which loses mass subsonically is embedded in a very subsonic global flow. These authors in fact proposed that this type of interaction was responsible for the tails behind the well-known cometary globules in the Helix Nebula (NGC 7293), a highly evolved planetary nebula. Hartquist et al. (1996) did however note that a tail behind a clump in a subsonic flow might broaden out if viscous dissipation in the tail heated the tail sufficiently. They derived an upper limit on the density in a broad tail source; however this density would probably be comfortably exceeded by the density in the tail behind a clump in an UCHIIR. If photoevaporation from the clump surface is the dominant clump loss mechanism (Section 2), then the appropriate interaction is that between a supersonic source and a subsonic flow; in this case Dyson et al. (1993) showed that any tail structure would have a very wide opening angle. It is hard to draw general conclusions regarding the adoption of smoothly distributed mass-loading centres since as noted above, mass-loss from only the simplest possible clump structures has been investigated so far. This uncertainty of course affects any estimates of the spatial densities of the required mass-loading sources.

The structures of the recombination fronts are of considerable interest and the allowed transitions from the ionized side to the neutral side of RFs have major implications for UCHIIR models. The jump conditions holding across recombination fronts are similar to those holding across ionization fronts. The classic paper of Axford (1961) examines at length the possible transitions which can occur for IFs; this demands investigation of the IF structures themselves. Newman & Axford (1968) considered this problem for RFs and concluded that only subsonic-subsonic or supersonic-supersonic transitions were allowed. They ruled out the possibility of transonic solutions whereby a subsonic flow in the ionized gas could exit as a supersonic neutral flow. Completely subsonic UCHIIR bounded by a subsonic-subsonic RF are of course possible; however the confining external pressure is essentially the same as that required to confine a classical IF bounded region, and as already noted, this probably requires unreasonably high molecular cloud pressures. As is well known (cf. Williams & Dyson 1994), steady flows in regions of uniform mass loading pass though the sound speed at the edge of the mass-loading region, which here is the RF itself. The advantage of having gas leaving the UCHIIR sonically or supersonically is, of course, that the effectively ballistic exterior flow matches to the external pressure via a shock and much lower confining pressures are needed. This problem was resolved by Williams & Dyson (1996) who showed that Newman & Axford (1968) had inadvertently missed the small but important class of transonic solutions. These can be found through the exploitation of a generic instability in the integration of steady, sonic, near-isothermal flows. Great care is needed to integrate the flow equations between the isothermal and adiabatic sonic points which lie within the RF structures. Physically, mass-loading within the HII region takes the flow to the isothermal sound speed; the RF is needed to get the flow to the adiabatic sound speed. Subsonic UCHIIR which are transonic at the RF provide a range of very promising models (RWD).

RFs may also play an important role where 'classical' IFs are expected if the upstream gas is clumpy (or as a result of dense clumps generated by instabilities in the front). Dense neutral cores will slip past the advancing front into the ionized region. Even when the mass input is far smaller than required to stall the front entirely, as in the models of UCHiiR, the ionized region will expand more slowly than if there were no mass loading and will eventually start to lose ionized gas through an RF at its edge. Detailed diagnostics of the structures of the fronts, which differentiate between RFs and IFs, have still to be calculated. It is certain, at least, that the thickness of a transonic RF is about twenty times greater than that of an IF with the same characteristic density, and is roughly $(n/1\,\mathrm{cm}^{-3})^{-1}$ pc. The internal structures of such RFs may be observable in favourable circumstances.

An important class of model UCHiiR are around blue supergiant stars, which have extremely powerful winds. In these models the wind mass-loads from the clumps and this mass-loaded wind is, in fact, the UCHiiR itself (DWR). An important question is whether the mass-loaded wind can exit the region completely supersonically or whether it in fact shocks within the region (and then exits either subsonically or, more likely, transonically). Considerable differences exist in the predicted observational characteristics of UCHiiR between the shocked and unshocked cases (DWR, RWD). It is likely to be a good approximation to treat these mass-loaded winds as isothermal, i.e. they can radiate away the frictional energy dissipated as they slow down (Williams, in preparation). Williams, Hartquist & Dyson (1995) have analysed the dynamics of spherically symmetric, isothermal, mass-loaded winds. They showed than in many cases, such a wind will pass through a termination shock but that it can in fact shock at a speed much less than that of the initial stellar wind. (This weakness of the termination shock is also evident in the numerical simulations of the wind-blown Wolf–Rayet nebula RCW 58 performed by Arthur, Dyson & Hartquist (1994) – see also Section 4). Williams et al. (1995) commented on the relevance of this result to the question of the well-known radio quietness of wind blown bubbles; they argued that the dissipation of a great fraction of the winds' energy in a continuous flow results in less energy being available for cosmic ray acceleration which is restricted to the vicinity of the termination shock.

4 The Wolf–Rayet Nebula RCW 58

As a final example of the interaction of a massive star with its environment we consider the structure of the wind-blown Wolf–Rayet nebula RCW 58. This nebula is composed largely of stellar ejecta from the red supergiant phase preceding the present W–R phase of the exciting star (Smith et al. 1988). Much less than 1% of the integrated mechanical luminosity of the W–R stellar wind seems to have been converted into kinetic energy; enhanced radiative losses seem likely to have occurred (Smith et al. 1984). IUE absorption line data (Smith et al. 1984) show clearly that the structure of the wind-blown bubble around the star is substantially different from that expected for a classical energy driven bubble (e.g. Dyson 1989). In particular, the sense of the observed velocity-ionization potential (effectively temperature) correlation shows that these features must be formed in the shocked stellar wind. In order to produce both appropriate physical conditions there and the magnitude of the observed velocity-temperature slope, mass-loading must occur behind the stellar wind shock (Smith et al. 1984). Hartquist et al. (1986) gave a phenomenological description of the post-shock flow. The immediate post-shock flow, which initially behaves adiabatically, mass-loads and its Mach number increases towards unity where it remains until adiabatic expansion reduces the gas temperature to about 10^5 K. At this temperature, radiative cooling sets in suddenly, and the cooling timescale becomes much less than the mass-loading timescale. The gas cools without further mass-loading and it is in this region that the absorption features are produced and where the enhanced radiative losses take place.

This simple model explained very well the observed velocity-temperature correlation and the magnitude of the velocity-temperature slope. Arthur, Dyson & Hartquist (1994) constructed a spherically symmetric, time dependent numerical model of RCW 58. They were able to reproduce the observed nebular radius and the velocity spread of the absorbing gas which exists in the approximate temperature range 10^4–10^5 K. An intriguing result was that they also showed that once the Mach number of the adiabatic mass-loaded portion of the flow reached near unity, it remained there until radiative cooling set in, in accordance with the speculation of Hartquist et al. (1986). However the velocity-temperature correlation predicted did not match the linear form deduced from the data. They suggested that this discrepancy was due to their assumption of equilibrium cooling. More recent calculations (Arthur, Henney & Dyson 1996) which incorporate non-equilibrium cooling in fact produce good fits to both the velocity range and velocity-temperature relationship deduced from the data.

5 Conclusions

Most interactions between a massive star and its environment take place in a clumpy medium. Recent observational work has produced some spectacular images of the mass-loading centres around stars. O'Dell & Wen (1994) have used the HST to image possible proto-planetary disks in the Orion nebula, some of which have short tails. At higher resolution, O'Dell & Handron (1996) have produced detailed images of the cometary globules in the Helix nebula showing the tail shapes and evidence for dust absorption at the back of the cometary heads. For UCHiiR such direct imaging of the clumps is not yet possible. However, long-duration, multiple VLA configuration observations of SGR B2, an extensive star forming region near the galactic centre, show numerous UCHiiR, in some of which substructure is beginning to be discerned (Gaume et al. 1995; De Pree et al. 1995).

We have described how mass is removed from boundary layers around the clumps, incorporated into tails and added to a global flow. The interchange of mass, momentum and energy in the boundary layers feeds through to affect the structure and dynamics of the region influenced by the massive star. The details of this interchange await more sophisticated models of clumps.

We describe models of UCHIIR in which the ionized gas flow is mass loaded by clumps of molecular material which remain close to the central star. As the mass loading increases the density in the ionized region above that in a 'classical' HII region, the ionization front stalls and becomes a recombination front. The direction of the flow reverses (in the frame of the front) so that ionized gas is lost as it exits the region. We predict that outflows of HI should be seen around UCHIIR as a consequence of this. RWD speculated that the reason that the outflowing HI shocks around ordinary HII regions are not as thin or dense as expected from the structure of photodissociation regions (e.g. Kuchar & Bania 1993) is that they could in fact be neutral winds beyond recombination fronts.

The velocity and ionization structure of the wind-blown Wolf–Rayet nebula RCW 58, inferred from observational data, can be understood if mass loading occurs behind the shocked stellar wind and continues until radiative cooling sets in. This also explains the small kinetic energy of the shocked stellar ejecta.

Our models of this wide range of sources demonstrate how the effects of mass-loading are important if we are to understand the dynamics of astrophysical sources. The mass-loading process will become better understood as new high resolution observations begin to probe intermediate scale structures. Parallel to this, the poorly understood interaction between the intermediate and large scale structures must be included fully in theoretical models. Many important insights should be obtained by our continuing programme.

References

Arthur S.J., Dyson J.E., Hartquist T.W., 1994, MNRAS 261, 425

Arthur S.J., Henney W.J., Dyson J.E., 1996, A&A 313, 987

Axford W.I., 1961, Phil. Trans. R. Soc. London, A, 253, 301

Bertoldi F., McKee C.F., 1990, ApJ 354, 529

Borkowski K.J., Balbus S.A., Fristrom C.C., 1990, ApJ 355, 501

Charnley S.B., Dyson J.E., Hartquist T.W., Williams D.A., 1990, MNRAS 243, 405

Churchwell E., 1990, AAR 2, 79

Cowie L.L., McKee C.F., 1977, ApJ 211, 135

De Pree C.G., Gaume R.A., Goss W.M., Claussen M.J., 1995, ApJ 451, 284

Dyson J.E., 1968, A&SS 1, 388

Dyson J.E., 1989, in: IAU Colloquium 121, *Structure and Dynamics of the Interstellar Medium*, Tenorio-Tagle G., Moles M., Melnick J. (eds), Springer Verlag, Berlin, p149

Dyson J.E., 1994, in: Lecture Notes in Physics 431, *Star Formation and Techniques in Infrared and mm-wave Astronomy*, Ray T.P., Beckwith S.V. (eds), Springer Verlag, Berlin, p93

Dyson J.E., Smith L.J., 1985 in: *Cosmical Gas Dynamics*, Kahn F.D. (ed), VNU Science Press, Utrecht, p173

Dyson J.E., Hartquist T.W., 1994, MNRAS 269, 447

Dyson J.E., Hartquist T.W., Biro S., 1993, MNRAS 261, 430

Dyson J.E., Hartquist T.W., Malone M.T., Taylor S.D., 1995, Rev. Mex. Astron. Astrofis. (Conference Series) 1, 119

Dyson J.E., Williams R.J.R., Redman M.P., 1995, MNRAS 277, 700

Gaume R.A., Claussen M.J., De Pree C.G., Goss W.M., Mehringer D.M., 1995, ApJ 449, 663

Hartquist T.W., Dyson J.E., 1993, QJRAS 34, 57

Hartquist T.W., Dyson J.E., Pettini M., Smith L.J., 1986, MNRAS 221, 715

Hartquist T.W., Dyson J.E., Williams R.J.R., 1996, A&SS 235, 1165

Hollenbach D., Johnstone D., Lizano L., Shu F., 1994, ApJ 428, 654

Kahn F.D., 1969, Physica 41, 172

Kahn F.D., 1974, A&A 37, 149

Klein R.I., McKee C.F., Colella P., 1994, ApJ 420, 213

Kuchar T.A., Bania T.M., 1993, ApJ 414, 664

Kurtz S., Churchwell E., Wood D.O.S., 1994, ApJS 91, 659

Lizano S., Cantó J., Garay G., Hollenbach D., 1996, ApJ 468, 739

MacLow M.-M., McKee C.F., Klein R.I., Stone J.M., Norman M.L., 1994, ApJ 433,757

Maeder A., 1984, in: IAU Symposium 105, *Observational Tests of the Stellar Evolution Theory*, Maeder A., Renzini A. (eds), Reidel, Dordrecht, p229

Maeder A., 1990, A&AS 84, 139

McKee C.F., Cowie L.L., 1977, ApJ 215,213

Newman R.C., Axford W.I., 1968 ApJ 151, 114

O'Dell C.R., Wen Z., 1994, ApJ 394, 194

O'Dell C.R., Handron K.D., 1996, AJ 111, 1630

Rawlings J.M.C., Hartquist T.W., 1996, ApJ (submitted)

Redman M.P., Williams R.J.R., Dyson J.E., 1996, MNRAS 280, 661

Smith L.J., Pettini M., Dyson J.E., Hartquist T.W., 1984, MNRAS 211, 679

Smith L.J., Pettini M., Dyson J.E., Hartquist T.W., 1988, MNRAS 234, 625

Spitzer L., Härm R., 1953, Phys. Rev. 89, 977

Stone J.M., Norman M.L., 1992, ApJ 390, L17

Tenorio-Tagle G., Yorke H.W., Bodenheimer P., 1979, A&A 80, 100

Van Buren D., MacLow M.-M., Wood D.O.S., Churchwell E., 1990, ApJ 353, 570

Williams R.J.R., Dyson J.E., 1994, MNRAS 270, L52

Williams R.J.R., Dyson J.E., 1996, MNRAS 279, 987

Williams R.J.R., Hartquist T.W., Dyson J.E., 1995, ApJ 446, 759

Williams R.J.R., Dyson J.E., Redman M.P., 1996, MNRAS 280, 667

Wood D.O.S., Churchwell E., 1989, ApJS 69, 831

Numerical models

NON-LTE RADIATIVE TRANSFER IN CLUMPY MOLECULAR CLOUDS

M. Juvela
Helsinki University Observatory, Tähtitorninmäki
P.O.Box 14, SF-00014 University of Helsinki, Finland

Abstract

We have developed a program that can be used to solve the radiative transfer problem in one-, two- and three-dimensional model clouds with Monte Carlo simulation. The program includes some minor modifications to the traditional Monte Carlo scheme. These changes can, in some cases, significantly speed up the simulation and enable efficient calculations of clouds with high optical depths.

The three-dimensional model clouds consist of cubic cells. Since the velocity, temperature and density can be independently specified for each cell, this also enables the study of clouds with clumpy density structure.

We describe the principles of the simulation program and present some preliminary results from our studies where the CS and $C^{34}S$ spectra observed in southern massive star-forming regions are compared with the model calculations.

1 Introduction

The density distribution of interstellar molecular clouds is known to be very clumpy at all observable size scales. These density fluctuations influence the radiative transfer properties of the clouds and must be taken into account if the observed spectra are to be compared with model calculations.

Realistic models must contain a full three-dimensional description of the density distribution. Since we also want to experiment with different velocity and temperature fields, Monte Carlo simulation seems to be the best way of solving the radiative-transfer problem. The simulation provides information about the interaction between the radiation field and the gas. This enables us to solve the new level populations from the equilibrium equations and the iteration continues until the changes in the population levels become insignificant.

For years Monte Carlo simulation has been used for radiative transfer calculations in simple one-dimensional model clouds (e.g. Bernes 1979) but lately the method was extended also to three-dimensional cloud models (Park & Hong 1995). We have developed a new similar program that can be used to study both one-dimensional, spherically symmetric model clouds as well as three-dimensional clouds divided into cubic cells.

We have made observations of several transitions of the molecules CS and $C^{34}S$ in southern massive star forming cores (Juvela 1996). The cores show very different line ratios and line intensities. One common feature is the general lack of strong self-absorption features which is difficult to explain unless a low volume filling factor is assumed. The aim of our study is to derive a qualitative picture of the density distribution in such cores by comparing observations with the three-dimensional models.

2 The creation of the model clouds

For the model calculations one must first set the values of density, kinetic temperature, microturbulence and velocity in each cell. These quantities remain constant throughout the calculations.

The model clouds may have two kinds of turbulence. Microturbulence determines, together with the thermal line broadening, the intrinsic line-width of the cells. Macroturbulence describes the random velocities of the cells themselves. In addition, there may also be systematic macroscopic motions, e.g. infall or rotation.

For generating the clumpy density distribution we have used three methods. The first method takes a density distribution $\mathrm{n}\sim\mathrm{r}^{-\alpha}$ and sets the density in randomly selected cells to some lower value. This gives a simple way to change the volume filling factor without changing the shape of the large scale density distribution. The two other methods are based on the structure tree statistics (Houlahan & Scalo 1992) and fractal models (Hetem Jr. & Lépine 1993). Both methods are derived from the observed properties of the molecular clouds and are not directly linked with theoretical hydrodynamic models.

The structure tree statistics describes the cloud as a hierarchical system of clumps. The creation of the cloud starts with one big clump and proceeds recursively as some number of sub-clumps are generated within each clump. The density distribution of a clump is identical with that of the parent with the size scaled down and the density multiplied with some constant. In our models the clumps have a density distribution $(r/R)^{\alpha}$, where r is the distance from the centre of the clump, R the size of the structure and α a free parameter.

Molecular clouds show similar structure on different size scales (see e.g. Dickman et al. 1990; Falgarone et al. 1991) and this fractal nature of the clouds seems to extend at least down to 0.01 pc. The fractal dimension of most interstellar clouds is close to 1.3 (Dickman et al. 1990). We have created fractal density distributions in the model clouds using the method of Hetem and Lépine (1993). The algorithm starts by dividing a cubic cloud into eight sub-cubes with the mass of the cloud divided between these according to random numbers. The procedure is repeated recursively on all sub-cubes. In order to force the density to increase towards the centre of the cloud we have used a variation in which after each division the densest of the eight sub-cells is moved closest to the centre and the least dense cell furthest away (see Hetem & Lépine 1993). The algorithm has only one free parameter, α. The fractal dimension only weakly depends on α, while the distribution of cell densities is more affected with smaller

α producing clouds with fewer cells with relatively high densities.

3 The radiative transfer program

Our program takes a description of the model cloud, solves the equilibrium populations of the molecule and calculates the spectra as they would appear to an observer.

The program contains two methods for the radiative transfer simulations. The first one is the traditional Monte Carlo simulation. Packets of model photons are created in randomly selected location within the clouds and are followed until they exit the cloud. As the packet goes through a cell the number of absorption events is added to local counters. The absorbed photons are removed from the photon packet which continues its way into the next cell.

In the other method the photon packets are always started at the surface of the model cloud. At this stage the packets contain only background photons. As the packet enters the cloud, absorbed photons are removed in the usual manner and the absorption counters are updated. However, part of the photons emitted by the cell are also added to the photon packet as it moves into the next cell. The packet is updated only at cell boundaries while in the traditional Monte Carlo the emission events take place in random locations. This means that in this second method the photons absorbed within the emitting cell must be treated explicitly. Instead of simulating many emission events along the photon path within the cell (as a kind of Monte Carlo integration) the integral of emitted and absorbed photons is calculated explicitly. This is much faster since fewer photon packets are needed in order to achieve the desired accuracy. This should be particularly important in the study of clumpy clouds where the density contrasts of even adjacent cells can be large.

The whole simulation process is based on random numbers. In real interstellar clouds the number of emitted photons is much higher than the number of photon packets that can be simulated. Therefore also the fluctuations in the simulated radiation field will be larger and this will lead to undesirable random errors in the results. For this reason, we have mainly used quasi-random numbers instead of the normal pseudo-random numbers. Compared with normal random numbers the quasi-random numbers have a more uniform distribution.

4 The analysis of CS observation

We have observed CS and $C^{34}S$ transitions 2–1, 3–2, 5–4 and 7–6 in over 30 southern ($\delta < -28°$) cores (Juvela 1996). In addition to one-point measurements most cores have also been mapped at least in CS(3–2), CS(5–4) and $C^{34}S$(2–1). This dataset is a good starting point for multitransition modeling and will also provide some information about the spatial distribution of the dense gas.

As an example, we show in Figure 1 the results from one-dimensional and three-dimensional cloud models compared with the CS spectra observed in the core G 348.73-1.04. In Figure 1a the model cloud has a spherically symmetric density distribution with n$\sim r^{-1.5}$. The model cloud is divided into 20 spheres of equal thickness. The density decreases from 1.1×10^{5}cm^{-3} in the centre to 1.1×10^{3}cm^{-3} at the edge, only 18″ from the cloud centre. Although the kinetic temperature T_K was set to almost 100 K the calculated intensity of the higher transitions is still too weak. On the other hand, also the angular size of the model cloud is too small.

In Figure 1b are the corresponding spectra calculated from a three-dimensional model cloud with fractal density distribution. The model consists of $36\times36\times36$ cells and the densities of the cells range from zero to 3.0×10^{6}cm^{-3}. The model cloud has lower kinetic temperature than the one-dimensional model, T_K=60 K. The diameter of the cloud is also larger (68″) since the effective volume filling factor is less than 1.0. Although the fit is considerably better, the model still predicts too small emission in the off-positions. This may indicate that the core still has a lower volume filling factor.

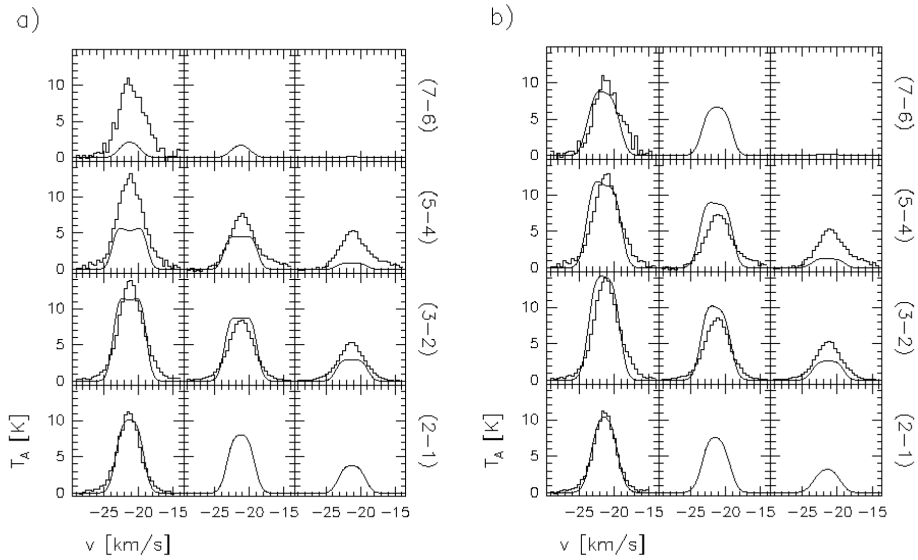

Figure 1: The CS spectra J=2–1, J=3–2, J=5–4 and J=7–6 observed in the core G 348.73-1.04 (histograms) compared with spectra calculated with two different models (solid lines). In frame **a** the model cloud has a spherically symmetric density distribution and in frame **b** the density distribution is generated using a fractal model. For both frames the leftmost spectra are observed towards the cloud centre, the next spectra are observed 20″ and the rightmost 40″ from the cloud centre.

5 Conclusions

Monte Carlo has proved to be both a flexible and an accurate method for solving the radiative transfer problem. Thanks to the rapid development in computer technology even more realistic three-dimensional cloud models can nowadays be studied without supercomputers.

We have made model calculations of three-dimensional clouds with clumpy density distributions. The comparison of CS and $C^{34}S$ observations with the models gives support to the existence of large density variations and low volume filling factors in massive star-forming cores.

References

Bernes, C. 1979, A&A, 73, 67

Dickman, R.L., Horvath, M.A., Margulis, M. 1990, ApJ, 365, 568

Falgarone, E., Phillips, T.G., Walker, C.K. 1991, ApJ, 378, 186

Hetem Jr.,A., Lépine, J.R.D 1993, A&A, 270, 451

Houlahan, P., Scalo, J. 1992, ApJ, 393, 172

Juvela, M. 1996, A&AS 118, 191

Park, Y.-S., Hong, S.S. 1995, A&A, 300, 890

NUMERICAL SIMULATIONS OF MAGNETOHYDRODYNAMIC FLOWS

G. Tóth
Astronomical Institute, Utrecht University
Postbus 80000, 3508 TA Utrecht, The Netherlands
toth@fys.ruu.nl, http://www.fys.ruu.nl/~toth

Abstract

This review deals with the numerical simulation of magnetohydrodynamic flows. A general overview of the different numerical techniques compares their advantages, disadvantages and points to the appropriate application areas. Some specific schemes, and their implementation in the Versatile Advection Code are discussed in more detail.

1 Introduction

There can be several reasons to do hydrodynamic and magnetohydrodynamic (MHD) computer simulations.

In astronomy, in contrast with physics, the observer usually cannot influence the object of the investigation, in other words, one cannot do experiments, only observations. Analytical calculations and numerical simulations provide the only substitute for experiments. Due to the complexity of the physical phenomena analytical calculations are limited to the simplest cases and many approximations have to be made. Numerical simulations have their own limitations too, but they can be used together with observations and analytical calculations in a complementary way which can lead to a deeper understanding of the examined phenomena.

Even in cases when experiments can be performed, computer simulations may turn out to be more efficient and less expensive. This is the situation in aerospace engineering, where wind tunnel experiments are replaced by simulations for economical reasons. In fact, most of the modern numerical hydrodynamic schemes were invented and developed by researchers working in the aerospace industry. Magnetohydrodynamics has fewer engineering applications than hydrodynamics, although the thermonuclear fusion research also requires computer simulations of magnetised plasma.

Finally, computer scientists and the computer industry are always searching for applications that can prove the usefulness of their software and hardware. The memory and CPU required by three-dimensional MHD calculations are still a great challenge even for the latest parallel super computers. Massively parallel computers, on the other hand, require new numerical algorithms to be developed.

2 Equations

The magnetised plasma can be described by the following primitive variables: the mass density ρ, velocity $\mathbf{v}$, pressure p, and magnetic field $\mathbf{B}$, which are all functions of time and three (if no simplifying symmetry assumption is made) spatial coordinates. For ideal MHD the resistivity η is zero, while in resistive MHD $\eta > 0$ is not negligible at least in some parts of the flow. The units for the magnetic field are chosen so that the magnetic permeability $\mu = 1$.

The MHD equations can be expressed in various mathematical forms, however, for numerical models the conservative form is often preferred: the equations explicitly represent the conservation of mass, momentum, total energy, and induction of magnetic field. The conservative variables are ρ, the momentum density $\rho\mathbf{v}$, the total energy density e, and $\mathbf{B}$. This is especially important if *weak solutions* containing discontinuities are of interest.

In terms of these variables the partial differential equations of resistive MHD are

$$\begin{aligned}
\frac{\partial\rho}{\partial t} + \nabla\cdot(\mathbf{v}\rho) &= 0 && (1)\\
\frac{\partial\rho\mathbf{v}}{\partial t} + \nabla\cdot(\mathbf{v}\rho\mathbf{v} - \mathbf{B}\mathbf{B}) + \nabla p_{tot} &= -(\nabla\cdot\mathbf{B})\mathbf{B} && (2)\\
\frac{\partial e}{\partial t} + \nabla\cdot(\mathbf{v}e + \mathbf{v}p_{tot} - \mathbf{B}\mathbf{B}\cdot\mathbf{v} - \mathbf{B}\times\eta\mathbf{J}) &= -(\nabla\cdot\mathbf{B})\mathbf{B}\cdot\mathbf{v} && (3)\\
\frac{\partial\mathbf{B}}{\partial t} + \nabla\cdot(\mathbf{v}\mathbf{B} - \mathbf{B}\mathbf{v}) + \nabla\times(\eta\mathbf{J}) &= -(\nabla\cdot\mathbf{B})\mathbf{v} && (4)
\end{aligned}$$

where the total pressure, total energy density, and current density are

$$\begin{aligned}
p_{tot} &= p + \mathbf{B}^2/2 && (5)\\
e &= p/(\gamma-1) + \rho v^2/2 + \mathbf{B}^2/2 && (6)\\
\mathbf{J} &= \nabla\times\mathbf{B} && (7)
\end{aligned}$$

for an ideal gas with adiabatic index γ.

The *initial condition* should satisfy

$$\nabla\cdot\mathbf{B} = 0 \qquad (8)$$

The exact solution of the MHD equations (1)–(4) keeps $\nabla\cdot\mathbf{B} = 0$ indefinitely, thus the terms on the right hand sides of equations (2)–(4) should always remain zero. In multidimensional numerical calculations, however, the discretisation errors may produce a finite divergence of the magnetic field unless the scheme is specifically designed to keep the discretised form of $\nabla\cdot\mathbf{B}$ zero. It was found by Powell (1994) that writing the MHD equations in the above form together with a modified Riemann solver is stable unlike the usual form in which these "corrective source terms" are dropped. Tóth and Odstrčil (1996) found that

Powell's source terms are beneficial for the flux-corrected transport (FCT) and total variation diminishing Lax-Friedrich (TVDLF) schemes as well. Note, that these terms are not in a conservative form, but they are usually small. Other methods to eliminate errors in $\nabla\cdot\mathbf{B}$ will be discussed in section 5.

In general a system of conservation laws with some extra source terms can be written as

$$\partial_t\vec{U} + \partial_i\vec{F}_i(U) = \vec{S}(U) \tag{9}$$

where $\vec{U}$, $\vec{F}_i$, and $\vec{S}$ contain the conservative variables, the fluxes, and the source terms respectively, and ∂_i represents the spatial derivative in direction i, and a summation is implied over $i = 1, 2, 3$.

3 Discretisation in Space

In this section a very concise overview of the different approaches towards spatial discretisation is given. The interested reader may look at standard text books (e.g. Fletcher 1991) describing the standard discretisation techniques and read some more recent articles (e.g. Lele 1992, Yee 1996, and Lowrie et al. 1995) on the relatively new compact schemes.

3.1 Finite Differences

The simplest discrete representation of spatial derivatives is by finite differences. The variables are given as point-wise values U_i at locations x_i. Difference formulas of a given order of accuracy can be derived from Taylor expansion around the grid points. The advantage of finite differences is its simplicity, it can be implemented easily and efficiently. The main disadvantage is that there is no guarantee for conservation of quantities on non-uniform grids.

3.2 Finite Volume

In the finite volume discretisation space is divided into grid cells, and the cell-averages $V_i^{-1}\int_{V_i} U$ are known for each cell. The differential equations are discretised in their integral form, i.e. the fluxes through the cell interfaces are added to and subtracted from the cell-averages. This method automatically leads to a conservative discretisation on arbitrary structured or unstructured grids. The disadvantage of finite volumes is in the difficulty to go higher than second order spatial accuracy and the relatively complicated representation of second derivatives in space.

3.3 Finite Elements

In the finite elements method the nodal values U_i are given at the x_i points (nodes), while at other locations U is represented by localised interpolating polynomials, i.e. the solution consists of finite elements. The discretisation of the partial differential equations happens by the weighted residuals method. The advantage of the finite element discretisation lies in its systematic approach to high-order accuracy on arbitrary grids by use of high order interpolation polynomials. On the other hand it is rather complicated, and even with explicit time integration schemes it requires the inversion of huge linear systems. Discontinuities are also a problem for standard finite element methods.

3.4 Pseudo-Spectral Methods

A further step from the local description towards a global description is representing U by a linear combination of some orthogonal functions, e.g. by its Fourier components. Again the method of weighted residuals can be applied to obtain the discretised equations. In practice non-linear terms in the equations have to be evaluated in physical space since the corresponding convolutions in Fourier space are very expensive. This combination of spectral and physical space is called the pseudo-spectral method. The transformation between these two discrete sets of variables can be efficiently done by fast Fourier transforms (FFT). Pseudo-spectral methods can be extremely accurate with only a few modes representing U, this is referred to as *exponential convergence*, since the discretisation error decreases exponentially with the increasing number of modes. Disadvantages of this method include the problems with satisfying arbitrary boundary conditions, and accurate representation of discontinuous solutions.

3.5 Compact Schemes

In the computational fluid dynamics research there is a new trend of developing compact schemes with high order accuracy, but localised description of data. There are several approaches to obtain such a scheme: Padé discretisation of derivatives (implicit finite differences); using the multi-dimensional information around a grid point rather than extending the stencil in one spatial direction (multi-D finite difference); or storing higher order moments of U in the grid cells (generalisation of finite volume, or discontinuous finite elements). Although these schemes are very promising they are still in an experimental stage at the moment.

4 Discretisation in Time

4.1 Explicit

In explicit schemes the fluxes and the sources are calculated at the n-th time level and their contribution is added to the current values of U. The general conservation law (10) can be discretised in time as

$$\vec{U}^{n+1} = \vec{U}^n + \Delta t[-\partial_i \vec{F}_i(\vec{U}^n) + \vec{S}(\vec{U}^n)] \tag{10}$$

This is a first order approximation in Δt, but it is easy to form higher order Runge-Kutta or predictor-corrector type schemes.

Explicit time integration is simple and fast, and it is easily parallelised for parallel computers. The main disadvantage is that the time step Δt is limited by numerical stability requirements. For the MHD equations the stability condition requires that the time step is shorter than the crossing time of the grid cells by the fast magnetosonic wave, $\Delta t < \Delta x / c_{fast}$. For resistive MHD an additional constraint is the diffusion time, $\Delta t < (\Delta x)^2/\eta$. In cases when fast waves are really present and the time evolution should be accurately simulated, the stability limitation coincides with the accuracy limitation, since one cannot calculate the interaction of fast waves without representing them at the discrete time levels in each cell they are passing through.

In some time–accurate calculations, however, the fast waves that set the limit on the time step are not actually present at all, thus the accuracy would not require short time steps, and the explicit scheme may be very inefficient. This is also the case in steady state calculations, where the transients leading to the final state are of no interest.

4.2 Implicit

Stability of the time integration can be achieved by implicit time integration

$$\vec{U}^{n+1} = \vec{U}^n + \Delta t[-\partial_i \vec{F}_i(\vec{U}^{n+1}) + \vec{S}(\vec{U}^{n+1})] \tag{11}$$

Note that the fluxes and the sources are evaluated at the next time level. This simple scheme is only first order accurate in time, but that can be improved easily for time–accurate calculations.

While the stability of the implicit time discretisation is a great improvement over explicit schemes, one has to solve the implicit equations for the unknown $\vec{U}^{n+1}$. Usually a Newton-Raphson method is used which requires inversion of the $[I - \Delta t \partial(\partial_i \vec{F}_i)/\partial \vec{U}]$ matrix. In 1D there are efficient direct solvers, while in multidimensional cases iterative and multigrid methods need to be used. This can be costly both in terms of CPU and storage requirements.

4.3 Semi-implicit

Semi-implicit methods try to combine the stability of implicit methods with the efficiency of explicit methods. The idea is to treat only that part of the equations implicitly, which causes the stability problems. For example, in resistive MHD when the diffusion time $(\Delta x)^2/\eta$ becomes the limiting time for Δt, one can treat the resistive terms implicitly, i.e. calculating them at the next time level, while all the other terms explicitly. There is a lot gained relative to the fully implicit method: the size of the matrix to be inverted decreased since only $\mathbf{B}$ and e are implicit, the matrix elements are much simpler, and the structure of the matrix is symmetric and diagonally dominated, which is much easier to solve with iterative methods than the advection dominated fully implicit problem. The only problem with semi-implicit methods is that they are equation and problem dependent.

5 How to keep $\nabla \cdot \mathbf{B} = 0$

The MHD equations have a special property which does not occur in the hydrodynamic equations, namely the requirement that the magnetic field should remain divergence free. This is automatically satisfied in 1D simulations, but the standard discretisation methods do not guarantee that in multi-dimensional simulations. There are several ways to deal with this problem.

The simplest approach is to increase the spatial resolution until the divergence of $\mathbf{B}$ becomes small and the solution starts to converge. This may not work if the scheme is unstable due to the errors in $\nabla\cdot\mathbf{B}$, which is the case for some Riemann type solvers. The non-conservative source terms on the right hand sides of equations (2)–(4) with a modified Riemann solver (Powell 1994) eliminate the instability, but not the error. For some problems the use of Powell's source terms seems to be sufficient, the errors in $\nabla\cdot\mathbf{B}$ remain small, and the conservation of quantities is satisfactory. In other problems, especially for long time integrations, the error may grow to unacceptable values.

Another way to keep $\nabla\cdot\mathbf{B}$ exactly zero is to rewrite the MHD equations by using the *vector potential* $\mathbf{A}$ instead of $\mathbf{B} = \nabla \times \mathbf{A}$. The disadvantage of this approach is that the order of spatial derivatives increases by one, which reduces the order of accuracy by one; the equations became complicated in 3D, and the boundary conditions on the vector potential may not be physically intuitive.

For finite difference schemes the *constrained transport* method by Evans and Hawley (1988) offers a simple and efficient solution by using staggered grids. The magnetic field components are represented on the cell interfaces, while density, momentum and energy in the cell centers. Unfortunately this arrangement excludes finite volume discretisation, and Riemann solver based shock-capturing schemes.

The most general fix to the problem is the *projection scheme* originally proposed by Brackbill and Barnes (1980), which is a correction to the magnetic field after the time step is completed by some arbitrary numerical scheme. The name comes from the idea that the $\mathbf{B}$ field is projected to a divergence free $\mathbf{B}'$ field which is as close as possible to $\mathbf{B}$. To achieve this, one needs to solve a Poisson equation for the potential ϕ

$$\nabla^2\phi = \nabla\cdot\mathbf{B} \tag{12}$$

and then to correct the magnetic field to $\mathbf{B}' = \mathbf{B} - \nabla\phi$. It is easy to show that the correction does not affect the vector potential, the current density or the integrated magnetic flux. In fact one can prove that $\int dx(\mathbf{B}' - \mathbf{B})^2$ is minimal with the constraint $\nabla \cdot \mathbf{B}' = 0$. In summary the projection scheme is the smallest possible correction that removes the unphysical part of the numerical solution without affecting the physically meaningful quantities. The price to pay for these nice properties is the Poisson problem, but that can be solved efficiently with either direct or iterative solvers. It is also important to apply the boundary conditions to $\mathbf{B}'$, and to choose good boundary conditions for the Poisson equation.

6 Implementation and Testing

In the previous sections a great number of options are listed for both space and time discretisation. It is not practical to implement all these schemes and just see which one works best for the problem we want to solve. Instead, one needs to go through a number of steps to make a choice.

First, the class of problems to be solved should be considered. Even if at the beginning it seems that we are interested in doing a single simulation only, unavoidably we will want to solve other related problems later, especially with all the efforts put into the software development. The selected class of problems should be written in a general mathematical form, e.g. like equation (9). Using general notation in the software is preferred, since the different variables can be handled in a uniform manner, and changes to the equation can be done easily.

In the selection of the discretisation technique several things should be taken into account. The geometry of the computational domain determines if a Cartesian grid is sufficient, or the more general structured, or even unstructured grids are necessary. If we expect discontinuities in the solution only shock capturing methods should be used, while smooth solutions can be best approximated with high order methods. The time scales determine if explicit time integration schemes are efficient or not. The hardware to be used depends on the size of the problem and of course on the availability of super computers. If parallel machines are needed, the numerical techniques need to parallelise well.

Before one starts to develop a new code from scratch it is worthwhile to check whether an existing code can be used. It is possible that there already is a working software which needs only minor modifications to solve our problems. Of course, codes written for special problems by other researchers are usually difficult to get, to understand, and to modify. Another option is to use a general software that covers the problems we want to solve. There are a few such general MHD codes publicly available, like the ZEUS code by Stone and Norman (1992) at *http://zeus.ncsa.uiuc.edu:8080/lca_home_page.html*, and the Versatile Advection Code (VAC) by Tóth (1996a) at *http://www.fys.ruu.nl/~toth*.

New or modified codes should be thoroughly tested on simple problems with known solutions before an attempt is made to do the simulations we are interested in. The results of the simulations should be checked against physics (e.g. conservation of quantities not built explicitly into the numerical scheme), against other numerical methods (if available), and most importantly, against grid refinement, i.e. *the solution should converge as the spatial and temporal resolution is increased.*

7 Versatile Advection Code

7.1 Software

The general purpose VAC software is being developed by the author since 1994. The philosophy behind VAC is using a single versatile software with options and switches for various problems, rather than developing a different method or version for each problem separately. The advantage of such a general approach is a reduction of overall time for software development, easier maintenance, compatibility of different parts, automatic extension of new features to all existing applications. The price of the general approach is some added complexity in the source code.

VAC is written in a dimension independent notation which is translated by a special-purpose preprocessor (Tóth 1996b) to Fortran 90, and it can be further translated to Fortran 77. The preprocessor and the translator to Fortran 77 are written in the Perl language. The Perl interpreter is freely available from the net, and is already installed on most UNIX systems. The Fortran 90 code expresses data parallelism clearly, which is important for parallel computers. An automatic translation to high performance Fortran (HPF) is under development. VAC has been installed and is being used on a number of workstations (DEC, SGI, IBM, SUN), on the vector super computer Cray C90, and it has been tested for scaling properties on the parallel Connection Machine CM5.

The source code is divided into smaller units, called modules. Some modules have several versions, for example the VACPHYS module which contains the equation specific information: fluxes, sources, the eigenvalues and eigenvectors for the approximate Riemann solver, etc. Each system of equations is specified by its respective VACPHYS.EQUATION module. The boundary conditions and the initial conditions are often problem specific, these special subroutines are collected in the VACUSR.PROBLEM modules. This is the only part of the source code which the user is expected to modify, and it can be written in the dimension independent notation as well as Fortran 90 or Fortran 77.

The documentation, about 100 pages, is written in hypertext markup language (HTML), which can be viewed and/or printed from the standard web browsers, e.g. Netscape or Mosaic. There is a user interface written in Perl, which lets the user to configure, edit, compile, and run VAC, and visualise results through the same web browser. Of course, one can do all these steps from the UNIX shell as well. The manual pages and a demo version of the interface can be looked at the author's home page. The latest version of VAC was distributed to 16 users.

7.2 Equations

VAC aims to solve a set of conservation laws with source terms of the form equation (9).

At the moment five VACPHYS.EQUATIONS modules are implemented: the simple transport equation for test purposes, the Euler equations of compressible hydrodynamics with adiabatic or full energy equation, and the resistive MHD equations with isothermal or full energy equation (1)–(4). Source terms for external gravity, heat conduction, and viscosity can be included and modified as library subroutines. Other source terms can be defined in a user written subroutine in the VACUSR module.

All equation-modules are written in the dimension independent notation, thus the number of spatial dimensions $1 \leq D \leq 3$ and the number of components $D \leq C \leq 3$ for the vector variables (e.g. the momentum and the magnetic field) may have 6 different combinations.

7.3 Geometry

The equations can be solved on a 1, 2 or 3D structured grid with conservative finite volume discretisation. A structured grid can be thought of as a continuous mapping from a Cartesian mesh. Structured grids include Cartesian, polar and spherical grids as trivial examples, but they can be used in more complicated geometries as well. In 1D and 2D both slab and cylindrical symmetry may be assumed for the ignored dimension(s).

Boundary conditions are implemented by two layers of ghost cells around the mesh. The values in the ghost cells are updated in every time step, thus the discretised equations can be applied to the cells inside the physical mesh without making special cases for the edges. This way the boundary conditions are fully specified in the subroutines updating the ghost cells, and the boundary conditions become independent of the choice of the numerical schemes. For each boundary and each variable the type of the boundary can be defined. At present there are seven predefined boundary types: *periodic, symmetric, antisymmetric, fixed, fixed-gradient* and *continuous.* The continuous boundary condition is an approximate representation of an open boundary by putting the gradients normal to the boundary to zero in the ghost cells. The fixed-gradient type is similar, except that the gradient can be different from zero. Time dependent or more complicated boundary conditions can be realised via the `special` boundary type which results in a call of a user defined subroutine.

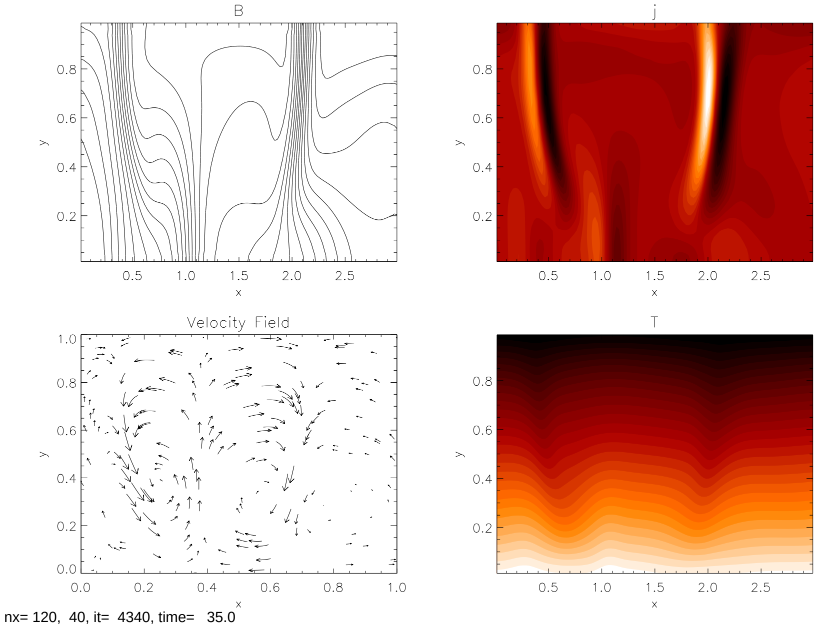

Figure 1: Magneto-convection. See explanation in Section 7.5.

7.4 Numerical Schemes

At present four algorithms are available for solving the differential equations. The Flux Corrected Transport scheme (FCT), two Total Variation Diminishing schemes with a Roe-type Riemann solver (TVD and TVD-MUSCL), and a Lax-Friedrich type TVD scheme (TVDLF) with no Riemann solver. See the article by Tóth and Odstrčil (1996) for a description of these schemes and the references provided there.

All these schemes are explicit, second order in space and time, and they are able to simulate shocks and other discontinuities as well as smooth flows. Multidimensional equations are solved either by Strang type dimensional splitting, or by adding the fluxes from all directions at the same time. Source terms may be included in a time split fashion or added at the same time as the fluxes.

The well-known FCT schemes solve each equation separately. Artificial diffusion is added only where it is needed for numerical stability. The FCT schemes are good in resolving contact discontinuities, they can handle shocks well, but close to the discontinuities some numerical noise might be generated. The TVD schemes on the other hand are very efficient in maintaining monotone profiles by appropriately limiting the slopes of the variables. The TVD schemes with the approximate Riemann solver can resolve discontinuities as well as or better than FCT without the spurious oscillations, but the Riemann solver is specific to the equation, and the TVD and TVD-MUSCL schemes are not as robust as the TVD Lax-Friedrich scheme, which does not need a Riemann solver at all. The TVDLF scheme is somewhat more diffusive than the other two.

The projection scheme to eliminate divergence **B** is also implemented, as well as Powell's MHD Riemann solver and the corrective source terms.

7.5 Simulations

The code has been extensively tested (Tóth and Odstrčil 1996) on standard numerical tests. It is currently used in several research projects, with applications ranging from accretion disks, and atmospheres of magnetised stars to solar magnetic flux tubes, coronal holes, prominences, and reconnection.

As a fairly complex and spectacular example, a simulation of magneto-convection is shown. This simulation has originally been done by Hurlburt and Toomre (1988), and it was implemented for VAC by R. Keppens. The resistive MHD equations (1)–(4) are solved with external gravity, thermal conduction, and viscosity source terms. The lower and upper boundaries are solid walls of different temperatures, the left and right boundaries are periodic. Initially the stratified gas is in hydrostatic balance, and there is a uniform vertical magnetic field. A small perturbation in the velocity is added. Due to the thermal convection the perturbation grows and after some transients convection cells are formed with circular motion. The magnetic field is expelled from the convection cells, and strong flux sheets are formed between the cells.

Figure 1 shows the magnetic field, the current density, the velocity field and the temperature distribution in the transient stage. The figure is a single frame from the animation which can be produced by the IDL procedure *animate* provided with VAC.

7.6 Development

VAC is a constantly evolving software. Currently the main effort of is put into developing implicit and semi-implicit time integration schemes. Another target is to run the code on massively parallel computers other than the CM5. An automatic translation tool will be developed that can add the parallel HPF directives to the code automatically. First the explicit schemes should become parallelisable, later the implicit algorithms as well.

8 Conclusion

Numerical simulation of MHD flows is not a simple problem. There is no one "perfect" numerical scheme that could solve, or which would be optimal for, all possible problems. It is important to know the available methods, their strengths and weaknesses, before one starts to write a program. Due to the complexity of the numerical algorithms it may be worthwhile to use or modify existing software. This allows the researcher to concentrate on the simulations and not on the software development. Numerical codes and the results of the simulations should always be thoroughly tested and verified. On the other hand, well designed numerical simulations can provide a wealth of information on the physical processes which we could otherwise only observe.

Acknowledgements

The project of Massive Parallel Processing Applied to Magnetohydrodynamics is funded by the Dutch Science Foundation (NWO), and it is done in a collaboration with the FOM Institute for Plasma Physics, the Mathematics Department at Utrecht, and the Center for Mathematics and Computer Science (CWI) at Amsterdam. The author is also supported by the Hungarian Academy of Sciences (OTKA grant F 017313).

References

Brackbill J. U., Barnes D. C., 1980, J. Comput. Phys. 35, 426

Evans C. R., Hawley J.F., 1988, ApJ 332, 659

Fletcher C. A. J., 1991, Computational Techniques for Fluid Dynamics, Springer, Berlin

Hurlburt N. E., Toomre J., 1988, ApJ 327, 920

Lele S. K., 1992, J. Comput. Phys. 103, 16

Lowrie R. B., Roe P. L.S. K., van Leer B., 1995, AIAA paper 95-1658

Powell K. G., 1994, ICASE Report No 94-24, Langley, VA

Stone J. M., Norman M. L., 1992, ApJS 80, 753

Tóth G., 1996a, Astrophys. Lett. & Comm. 34, 245

Tóth G., 1996b, The LASY Preprocessor and its Application to General Multi-Dimensional Codes, submitted for publication to J. Comput. Phys.

Tóth G., Odstrčil D., 1996, Comparison of some Flux Corrected Transport and Total Variation Diminishing Numerical Schemes for Hydrodynamic and Magnetohydrodynamic Problems, accepted for publication by J. Comput. Phys.

Yee H. C., 1996, Explicit and Implicit Compact High-Resolution Shock-Capturing Methods I: Formulation, accepted for publication by J. Comput. Phys.

INTERSTELLAR SHOCK–CLOUD COLLISIONS: NEW METHODS FOR COOLING

A. Horváth, Jr.[1,2] and Cs. Kiss[1]
[1] Dept. of Astronomy, Loránd Eötvös University
Ludovika tér 2., H-1083, Budapest, Hungary
[2] Széchenyi István College, Győr, Hungary

Abstract

The study of interactions of low velocity shocks with molecular clouds represents an important and interesting class of astro-hydrodynamical calculations, because these studies help understand the first step of triggered star formation. Because of the complexity of equations describing these processes, numerical calculations are needed.

In this work we present some results of a hydrocode which is able to follow the processes after the collision between the cloud and the shock front. The main result of this paper is focused on two new methods for calculating the effect of radiative cooling in optically thin approximation. The new methods are more accurate and need less CPU-time than the usually applied methods.

1 The hydrocode

Our numerical model is based on Zeus 2D hydrocode (Stone & Norman 1992). In our calculations we take into account the forces of the gas pressure, the radiative cooling in optically thin approximation; in the present version gravitational forces are neglected. Our model uses real gas equation of state, which means a mixture of H and He atoms and H_2 molecules (Monaghan & Lattanzio 1989, Horváth 1997). As it was shown (Horváth & Tóth 1995), chemical processes can affect the dynamical evolution significantly. In the high density region of the cloud ($\rho > 10\,m_{\mathrm{H}}\mathrm{cm}^{-3}$) we use a cooling function which includes H_2 and CO cooling as well (Hollenbach & McKee 1979). We assumed cylindrical symmetry.

2 New methods for cooling calculations

Cooling has a very imporant role in the shock-cloud collisional processes, because high density regions can be created in this way. Unfortunately, there are a lot of difficulties in calculating the effect of radiative cooling.

The main problem is that the characteristic time of the cooling is usually much shorter than the dynamical timescales. In the words of numerical analysis this means that the cooling term is a stiff term in the differential equations of these processes. The usual way for solving these problems is to split the equations into stiff and non-stiff parts and solve the stiff part separately. The methods used for solving the stiff part must be very stable and accurate for large timesteps, because the whole system is solved with the same integration step, which is in the order of dynamical timescales. We will concentrate on this stiff part of the code in this paper.

We can write the stiff term in the following form:

$$\frac{du}{dt} = \Phi(u, \rho) \tag{1}$$

where u is the energy density, ρ is the mass density, Φ is a function which describes the radiative energy changes. The Φ function consists of two terms: the cooling term (Monaghan & Lattanzio 1989) and a $Z \cdot \rho$ outer heating term, where Z is a constant.

In the beginning of the time-step we have a u_i value for energy density and we want to get the new u_{i+1} value after a Δt timestep.

The commonly used methods for solving this stiff term of the cooling are the classical implicit Euler and Crank–Nicolson methods (Press et al. 1992). Here we describe two new methods which proved to be more adequate for cooling calculations.

The first is the "interpolation method". Its novelty is to interpolate the function Φ with a linear function between the energy density at the beginning of time-step and the equlibrium value. The linearized differential equation is analytically solvable. This way we get the following equation:

$$u_{i+1} = u_e + (u_i - u_e)\mathrm{exp}\left(-\frac{\Phi(u_i, \rho)}{u_e - u_i}\Delta t\right)$$

where u_e is the energy density in the equilibrium, i.e. $\Phi(u_e, \rho) = 0$.

This method has the very important property that the energy density tends to the equlibrium value if we increase the timestep to the infinity, so it is stable for arbitrarily large timesteps. On the other hand, it is an explicit method, this way no iteration needed, therefore the interpolation method needs less CPU-time than the Crank-Nicolson's method (see the test results below).

The other new method is a "semi-analytic" one. One can easily show that the analytic solution of (1) is

$$u_{i+1} = F^{-1}\left(F(u_i, \rho) + \Delta t\right)$$

where

$$F(u, \rho) = \int_{u^*}^{u} \frac{1}{\Phi(u', \rho)}\, du'$$

where u^* is an arbitrary value.

The semi-analytic method is based on this formula. We have to make a large interpolation array of the function F once at the beginning of the calculations. During the calculations we can get the new u_{i+1} values only by one interpolation, an addition and an inverse interpolation. All these steps need a very small amount of CPU-time, and after it we get the exact solution of (1) within the interpolation and the initial integration error.

We remark that there are some small technical difficulties in choosing u^* and making the interpolation array which are not discussed in this paper.

3 Numerical tests

First we tested the numerical methods separately from the whole hydrocode. We present the graphs of the relative errors in Figure 1.

We measured the CPU-usage too. In the case of "semi-analytic" method this does not contain the time of making the interpolation array. We can do this, because in a hydrocode we have to build this array at the beginning only once, while we use it in every timestep for every cell, which means 10^6–10^9 cooling steps.

Figure 1 **a** and **b**: Relative errors at $\rho = 100\, m_{\rm H}{\rm cm}^{-3}$ as a function of the logarithm of temperature and timestep. Test with two classical methods: with implicit Euler integration (left) and with Crank–Nicolson method (right)

Figure 1 **c** and **d**: The same as Figure 1 **a**, **b** but with the new interpolation (left) and new semi-analytic method (right).

We can say that the "interpolation method" has the same accuracy as the Crank–Nicolson's and is more accurate than the implicit Euler method. The "semi-analytic" method is the best in accuracy: its error is two or three orders of magnitude smaller than for the others.

We measured the CPU-times of these methods. The classical methods had approximately the same CPU-usage. The "interpolation method" was approximately three times faster than the classical ones, while the "semi-analytic" was 10–30 times faster.

4 Applications

We included the new methods to our hydrocode described in Horváth & Tóth (1995). Through these studies we hope to be able to apply our model for calculating the parameters of individual objects, like for example the *Khavtassi 15* non-starforming dark cloud.

References

Hollenbach D. and McKee C. 1979, ApJS 41, 555

Horváth A. Jr. 1997, in prep.

Horváth A. Jr. and Tóth L.V. 1995, ApSS 233, 169

Monaghan J.J. and Lattanzio J.C. 1989, *A Simulation of the Collapse and Fragmentation of Cooling Molecular Clouds,* Lawrence Livermore National Laboratory.

Press W.H., Flannery B.P., Teukolsky S.A., Vetterling W.T. 1992, *Numerical Recipes in C*, Cambridge University Press

Stone J.M. and Norman M.L. 1992, ApJS 80, 819

The Solar System

INTERACTION OF THE SOLAR WIND WITH THE LOCAL INTERSTELLAR MEDIUM

P. Király
KFKI Research Institute for Particle and Nuclear Physics
H-1525 Budapest P.O.Box 49, Hungary

Abstract

The next frontier of space physics is the study of the interface region between the solar cavity, dominated by the supersonic solar wind, and the more or less undisturbed very local interstellar medium. The neutral component of the interstellar gas and the high-energy cosmic ray ions penetrate deep into the inner solar system, while low-energy ions are much more efficiently excluded. Instruments on the outbound Voyager and Pioneer spacecraft show several signs of their approach towards the termination shock of the solar wind, but the position and properties of the shock are still uncertain. Recent results on backscattered UV light, anomalous cosmic rays, pick-up ions, cosmic ray modulation, and the 3-dimensional structure of the solar cavity are discussed.

1 Introduction

Our local star, the Sun, interacts with its interstellar environment primarily through the solar wind, the magnetized supersonic plasma streaming out of the solar corona in all directions. While this interaction is much less violent than those of active stars, it may provide a good prototype for a large number of main-sequence stars. Recent remote-sensing and in-situ plasma observations promise a better understanding of the interaction of the Sun with the very local interstellar medium. The new data, however, also require more refined models than previously thought.

The heliosphere is the domain of space strongly influenced by the Sun and filled with plasma of predominantly solar origin. It consists of the supersonic and subsonic regions of the solar wind, separated by a termination shock. The subsonic region is sometimes called the 'inner heliosheath'. The solar wind plasma is separated from the ionised component of the streaming interstellar medium by the heliopause. The elongated heliosphere is surrounded by the heliosheath (or outer heliosheath), the interstellar plasma streaming past the heliopause, diverted by the outward pressure of the solar wind plasma and magnetic field. If the relative motion of the partially ionised interstellar gas is supersonic (and superalfvenic), as appears now likely, then a further discontinuity appears in the streaming interstellar plasma, namely the bow shock. The bow shock is strongest in the direction of the nose of the heliosphere, from where the interstellar wind arrives, and gradually weakens towards the tail.

While most of the mass of the solar system is concentrated in the Sun and planets, their combined volume is negligible relative to that of the heliosphere. For energetic charged particles propagating in the heliosphere, plasma structures are much more important than high-density planets, even if those dilute structures are not immediately visible. For researchers involved in space sciences, the solar system is better described by the analogy of a jet of water falling on a dinner plate than by the conventional picture of massive balls following Keplerian orbits around a central object (Axford and Suess, 1994). Magnetic field from the rotating solar corona is convected outwards by the solar wind, forming Archimedean spiral structures on both sides of the wavy heliospheric current sheet separating fields of opposite polarities. In some respects, the outer heliospheric discontinuities are reminiscent of those at the earth magnetosphere, but their sizes are about 10^5 times larger. Compared to interstellar distances, however, the characteristic size of the heliosphere of about 100 AU (astronomical units), is still small: it is less than 0.1 per cent of the distance to the nearest star. Even if a relatively long heliotail exists, its length should not surpass a few per cent of the typical interstellar distance. Thus the bulk of interstellar plasma is hardly influenced by the weak outflows from ordinary stars like the Sun. Interaction of solar plasma with the interstellar medium is, on the other hand, crucial from the point of view of the structure of the boundary region of the heliosphere.

The heliospheric boundary region has also some relevance for the Earth environment. The anomalous component (AC) of cosmic rays, which is thought to be accelerated at the heliospheric termination shock, provides an important energetic ion component of the terrestrial magnetosphere, forming newly discovered radiation belts. Mechanisms of trapping and decay of those particle populations can provide important information about magnetospheric structure. A better understanding of AC transport into and within the magnetosphere is important for heliospheric physics, because it helps monitoring the time variation of various species of the interplanetary AC. The comparison of the anomalous component measured in the outer solar system and in the Earth magnetosphere can provide information on propagation in the intervening regions. Magnetic reconnection at the heliospheric and magnetospheric boundary may have some analogous features, but differences are also important.

2 Heliospheric missions

The Pioneer and Voyager deep space probes, launched in the 1970's, have completed their fruitful planetary exploration programme and are now approaching the termination shock of the supersonic solar wind. Both Pioneer 10 and Voyager 1 are now at distances of more than 60 AU from the Sun, and most of their instruments are in good shape. Voyager 2 is also performing well, but its distance is still under 50 AU. Pioneer 11 is the only member of the family that has now practically gone out of operation, because its energy supply is too low. On 30 September 1995 NASA terminated daily communications with that spacecraft (COSPAR Bulletin, December 1995), following the recommendations of a Heliospheric Missions Review Panel earlier that year (Axford et al., 1995). The three remaining spacecraft cover both heliospheric longitude and latitude reasonably well. Pioneer 10 is the only spacecraft of the three that is moving towards the heliospheric tail, and also the one closest to the ecliptic. Its expected loss due to insufficient power will much reduce the coverage of the outer heliosphere. Unfortunately power is running out faster than expected, and one important cosmic ray detector had to be shut down in May 1996. The two Voyagers will, however, hopefully survive until 2015 or even 2020, and will provide the first in situ information about the termination shock, the heliopause, and perhaps about the interstellar medium as well.

Important missions of interest for global heliospheric studies also operate in the inner heliosphere. Ulysses was launched in 1990, and has now just completed its passes both over the south and north poles of the Sun. It is the first mission to cover solar polar regions, and the results reveal the 3-dimensional structure of the heliosphere at low solar activity. A continuation of the mission will result in polar passes around the turn of century, near the time of maximum solar activity. Another important mission of heliospheric relevance is SAMPEX (Solar, Anomalous, and Magnetospheric Particle Explorer), launched in 1992 to a low earth orbit. This small but successful mission has provided a lot of information on the anomalous component of cosmic rays penetrating into and trapped in the earth magnetosphere. An extension of that mission until the decay of its orbit due to atmospheric drag, expected for January 2002, will ensure the monitoring of anomalous cosmic ray intensities over almost a complete solar cycle.

The heliospheric missions mentioned above were reviewed at NASA by an international panel in March 1995 (Axford et al., 1995). Most of the principal investigators of the four missions presented their plans for extended data collection and evaluation. The panel made recommendations for the continuation and modification of the research program and for administrative changes. Although some recommended changes have already been implemented (such as the termination of regular daily reception of Pioneer 11 data), others are still worked on. It has been strongly emphasised by the panel that there is no hope to have another deep-space heliospheric fleet in place for decades, therefore it is imperative that present potential for the exploration of our connection to the galaxy should be fully utilised.

3 Components of the local interstellar medium

The very local interstellar medium (VLISM) that feeds neutral gas into the heliosphere and influences the shape and structure of the heliospheric boundary region is known to be partially ionised, although its degree of ionisation is still uncertain. The charged component of the medium with frozen-in magnetic fields is excluded from the heliosphere. The neutral component, however, carries some imprint of the state of the undisturbed VLISM, and remote sensing by electromagnetic waves adds further information on both components. For a detailed recent review of our interstellar environment see Frisch (1995).

The solar system is in a low-pressure interarm region of the galaxy. On the 100 pc scale, the Sun is surrounded by a bubble of dilute hot coronal gas, probably originating from a supernova explosion. It contains several clouds and systems of clouds or cloudlets of higher density and lower temperature. More locally, the Sun is near the edge of a warm interstellar cloudlet called the local cloud or 'local fluff'. It extends to not more than a few pc, and may be an evaporative extension of the 'squall line', a structure of denser clouds in the direction of the galactic centre. Gas in the anticentre direction is more dilute and more uniform. The velocity of the local fluff in the heliocentric system is about 26 km/s, streaming from the approximate direction of the galactic centre. It is also of some significance that the velocity vector of the cloud is close to the solar ecliptic plane. Doppler shifts of EUV, UV, and optical absorption lines towards nearby stars are consistent with the velocity vector of the neutral gas penetrating into the heliosphere, although other velocity components are also seen towards more distant stars. The better the spectral resolution, the more inhomogeneous the solar environment appears. The densities of the dominant components cannot be directly determined from absorption lines, but some more accessible lines of minor atoms and ions suggest ionisation equilibrium.

The state of observations is more favourable for the neutral component of the interstellar gas than for the ionised one. Neutral atoms can enter the heliosphere with relative ease, until they are ionised by solar UV radiation or by charge exchange with fully stripped solar wind ions. The penetrating neutrals (mainly H and He) resonantly backscatter solar UV line radiation, and their abundance, temperature, and velocity can be reasonably well determined from the spectral and directional distribution of that 'interplanetary glow'. Although temperatures and bulk velocity vectors for the H and He components show somewhat discordant values, the difference is now well understood in terms of the different strengths of their interaction with solar UV lines and with heliospheric boundary regions. While the entry of H into the heliosphere is hampered by the pressure of solar Lyman alpha radiation and by charge exchange with solar wind ions, He enters the heliosphere with practically unchanged velocity, density and temperature. Direct measurement of penetrating interstellar He atoms by the Ulysses GAS instrument has eliminated most discrepancies and contributed to a better definition of the parameters of the local interstellar medium. The asymptotic velocity has been determined as 26 ± 1 km/s, the direction of the gas flow in the solar ecliptic system as 72 ± 2.4 degree (longitude) and -2.5 ± 2.7 degree (latitude), the temperature as 6700 ± 1500 K (Witte et al., 1993).

Energetic cosmic rays also penetrate the heliosphere, and their anisotropy may carry information on the average direction of the interstellar magnetic field in neighbourhoods extending to several times their Larmor radii. In a good approximation, the directional distribution of cosmic rays arriving from distant sources is expected to be axially symmetric around the local magnetic field. It was pointed out a long time ago that the phase of first harmonic sidereal cosmic ray anisotropy was approximately constant up to energies of about 10^{14} eV, compatible with the constancy of the interstellar magnetic field in a region of 0.1 pc or more. That result was interpreted as being compatible with the uniformity of gas flow in the local cloud region (Király et al., 1979). More recent results on cosmic ray anisotropy support that view, but also suggest that the anisotropy is only partly due to interstellar effects, while at lower energies it is also influenced by the heliotail.

4 Derivatives of the neutral component

Once ionised, interstellar atoms penetrating the heliosphere are picked up by magnetic fields frozen into the solar wind, and are swept outwards towards the heliospheric termination shock. Only the neutral component of the local interstellar gas, i.e. atoms with high first ionisation potential can contribute to pick-up ions. Although pick-up ions interact with magnetic field fluctuations, they do preserve their identity to some extent, partly due to being singly ionised, and partly because their velocity distribution differs from that of solar wind ions. Thermalization is a very slow process, also hampered by adiabatic energy losses. The distribution of freshly ionised pick-up ions is a ring in velocity space that gradually extends to a shell or partial shell distribution. Some acceleration is also observed at low ecliptic latitudes. As Ulysses observations prove, formation of the shell distribution by pitch-angle scattering is slower at high ecliptic latitudes (see Gloeckler et al., 1995), and practically no acceleration is seen. Beyond 20 to 30 AU, the pressure of pick-up protons dominates over both magnetic and thermal pressures in the solar wind. Depending on the distance to the termination shock, the number density of pick-up protons may be 10 to 20 per cent of the solar wind protons at the shock. Pick-up protons should substantially modify shock structure and also cause a decrease of the solar wind speed in the distant heliosphere.

Pick-up ions are, by a not yet fully understood mechanism, preferentially accelerated at the termination shock to several or several tens or even hundreds of MeV/n, and some fraction of them returns to the inner solar system as the anomalous component (AC) or anomalous cosmic rays. They dominate the energy spectra of some elements at those energies during minimum solar activity periods not only in the outer heliosphere, but also at 1 AU. Their penetration into the inner heliosphere is facilitated by the large mass per charge ratio. This does not apply to anomalous hydrogen, which can be found only in the outer solar system, and has only been recently identified unequivocally (cf. Christian et al., 1995). The increase of the anomalous component from one solar minimum period to the next is an indication of the approaching termination shock. Also, lower energy particles are expected to appear as the residual modulation decreases.

In the inner solar system anomalous O, He, N, Ne, Ar, and recently also C ions have been detected. It is not quite clear, however, whether they all have been fully accelerated at the termination shock, or for some of them (e.g. for C) there is also a contribution from acceleration at other shocks of smaller extent (e.g. travelling shocks, corotating shocks). The general tendency of increase with increasing solar distance shows, however, that the predominant source of anomalous cosmic rays lies beyond the present positions of the outer heliospheric spacecraft. A truly galactic origin of singly ionised atoms appears to be excluded by the small ($< 1pc$) mean free path for stripping of a second electron in the local galactic environment. It is an important very recent development, however, that AC ions of energies above 20 MeV/n observed by SAMPEX instruments at earth usually carry multiple charges, due to electron stripping in the process of acceleration at the termination shock (Mewaldt et al., 1996). That may provide a clock for the acceleration process, indicating acceleration times of the order of 1 year.

A good measurement of the spatial distribution of pick-up ions and of anomalous cosmic rays in the heliosphere would be a good test of theoretical ideas. The comparison of upstream–downstream asymmetries with calculations for different elements would be particularly efficient (Fichtner et al., 1994). Present observations are not precise enough for such detailed comparisons. The majority of anomalous cosmic rays is expected to be carried downstream by the heliospheric tail. That component cannot be directly measured, but the energetic neutral atoms (ENA) resulting from charge exchange of energetic ions with neutral atoms are in principle detectable locally. Such future observations may provide an ideal way of remote sensing distant heliospheric structures. A somewhat similar measurement of neutral He atoms by the Ulysses GAS experiment (Witte et al., 1993) has already provided the first high-precision direct information on the interstellar wind.

Geomagnetically trapped heavy anomalous cosmic rays (O, N, Ne, and possibly C) are more or less fully stripped, but their position in the magnetosphere (L-shell) and pitch-angle distribution clearly show their origin (e.g. Selesnick et al., 1995). Measurements by the polar-orbiting spacecraft SAMPEX at about 600 km altitude can almost simultaneously detect the trapped component (at low L shells) and the interplanetary component (in polar regions). The ratio of the average intensity of anomalous trapped oxygen at $L = 2$ to that coming directly from interplanetary space was found to be about 200 at $E = 16 MeV/nucleon$. Abundances of other elements are lower, and enhancement factors are also energy dependent. In addition to a reliable monitoring of interplanetary intensities, trapping probabilities and decay lifetimes in the magnetosphere can also be inferred.

5 Position and structure of the inner shock and heliopause

In a naive magnetohydrodynamic approximation, the region dominated by the supersonic solar wind is influenced only by solar processes, and no action should propagate upstream, towards the Sun. Thus there should be no direct information about the position and properties of the termination shock, until one of the outer heliospheric spacecraft actually reaches the shock. In real life, there are several upstream propagating effects, such as electromagnetic waves, suprathermal and energetic ions, high-velocity electrons, some plasma waves, neutral atoms, cosmic rays. The expected imprint of the termination shock and of the heliopause on those upstream information carriers is, however, model-dependent. Theoretical estimates based on solar wind and interstellar medium parameters have even larger uncertainties. Thus, in spite of considerable efforts and some initial results, the position and structure of the discontinuities, and the time of the expected (first) encounter of Voyager 1 (and possibly of Pioneer 10) with the termination shock are still somewhat uncertain, although some consensus appears to emerge.

A good summary of expectations on the location of the termination shock, based on a critical review of contributions to a specialised symposium, was given by M.A. Lee (1993). As a best bet, he suggested 80 AU for the upstream shock distance, but with large error bars. The uncertainties extend farther towards higher values, although that asymmetry is partially due to the observational fact that the termination shock had not been crossed yet. The more than three years elapsed since then also eliminated some low estimates. Dynamical calculations based on directly measured solar wind and interstellar neutral gas properties, as well as on indirect estimates on the local interstellar magnetic field and on the degree of ionisation of the VLISM yield more uncertain values than those based on directly measured messengers of the termination shock. Such useful messengers include the upstream-downstream asymmetry of the Lyman alpha glow, the radial and time dependence of cosmic ray modulation, as well as pressures and gradients of the anomalous component. Most estimates were based on Voyager and Pioneer data.

In response to variations in the dynamic pressure of the solar wind, the positions of outer heliospheric discontinuities are expected to change both with the phase of the solar cycle and with heliographic latitude. Temporal changes also influence the number of times a given spacecraft is going to cross the termination shock. The shock is expected to move with a radial speed often exceeding that of the spacecraft, at least in the declining phase of the solar cycle (Whang et al., 1995). The dynamic pressure (and therefore also the shock distance) is found to be anticorrelated with the sunspot number, thus the minimum shock distance is expected around solar maximum. Whang et al. (1995) use an 1991 global merged interaction region (GMIR) sweeping outward through the solar wind together with the subsequent, 1992-93 detection of a radio emission event from the outer heliosphere to determine the heliopause distance as about 150 AU, assuming that the radio emission comes from that region. They also give an estimate for the average position of the termination shock as 66 AU, reaching 75 AU at minimum and 58 AU at maximum solar activity. Accepting those estimates, Voyager 1 would cross the termination shock around 1988, in the early rising phase of solar activity, and probably there would be no second encounter with the shock. In calculating the average shock distance of 66 AU the pick-up component was taken into account, but somewhat arbitrary assumptions were made about the interstellar magnetic field. The pick-up component was found to substantially reduce the Mach-number of the shock.

The structure of the distant heliosphere can be strongly modified by the degree of ionisation of the interstellar medium, by the direction and strength of the local interstellar magnetic field, and by resonance charge exchange, pick-up ion, AC, interplanetary magnetic field, and cosmic ray effects. Fractional ionisation and resonance charge exchange effects in the upstream and downstream directions have been handled recently in detailed model calculations by Baranov and Malama (1995). Complementary views on the magnetic structure of the outer heliosphere and of the heliotail have been presented by Nerney et al. (1993) and by Washimi (1993). In the former, the importance of field-line reconnection on the heliopause is emphasised. It arises from interaction of the interstellar field with alternate stripes of oppositely directed magnetic fields, 'painted' onto the heliopause by the expansion of the nearly ecliptic substagnation region of the termination shock. As the upstream direction of the interstellar flow is close to the ecliptic, interplanetary fields change sign twice per solar rotation in the substagnation region, which maps onto the surface layer of the heliotail. Unipolar regions are mapped into deeper layers, and the change of direction there should occur only once per solar cycle. In the latter reference, the authors emphasise the dynamical effects of the shocked interplanetary fields. In their model, the outflow of subsonic solar wind occurs along the solar rotation axis, and the flows are first collimated, before being bent towards the downstream direction of the interstellar wind. Of course both models use different simplifying assumptions. Fully self-consistent model calculations of the outer heliosphere and of the transition region to the interstellar wind are not yet available.

6 Conclusions

Exploration of the outer heliosphere and of the very local interstellar medium is an interdisciplinary pursuit. Astrophysicists can provide important contributions there, along with astronomers dealing with X-ray and UV studies, interplanetary plasma physicists, cosmic ray physicists and researchers of terrestrial magnetospheric physics. Outer and some inner heliospheric spacecraft and even magnetospheric missions and ground-based observations supply a steady flow of relevant data. Interest in the transition region between the familiar supersonic solar wind and the undisturbed interstellar medium will increase as the Voyagers approach and pass the termination shock around or after the turn of the century.

Acknowledgements

The author wishes to express his acknowledgements to NASA for invitation to the Heliospheric Missions Science Review Panel and for financial support. Organisers of the present workshop are acknowledged for their interest and help. This research was also supported by the Hungarian national grant OTKA-T-016952.

References

Axford, W.I. and Suess, T., 1994, EOS 75, 587

Axford, W.I., Lee, M.A., Adams, J.H., Fishman, G.J., Fuselier, S.A., Hall, D.T., Király, P. and Squibb, G., *Exploring our Connection to the Galaxy*; Report of the Heliospheric Missions Science Review Panel, May 1995.

Baranov, V.B., and Malama Y.G., 1995, J. Geophys. Res., 100, 14755

Christian, E.R., Cummings, A.C. and Stone, E.C., 1995, in Proc. *24th International Cosmic Ray Conference*, 4, 816, Rome

Fichtner, H., Fahr, H.J., Grzedzielski, S., Rucinski, D. and Sreenivasan, S.R., 1994, Astron. Astrophys., 284, 599

Frisch, P.C., 1995, Space Sci. Rev., 72, 499

Gloeckler, G., Fisk, L.A., and Schwadron, N., 1995, in Proc. *24th International Cosmic Ray Conference*, 4, 443

Király, P., Kóta, J., Osborne, J.L., Stapley, N.R. and Wolfendale, A.D., 1979, Lettere al Nuovo Cim., 24, 249

Lee, M.A., 1993, Adv. Space Res., 13, 283

Mewaldt, R.A., Selesnick, R.S., Cummings, J.R., Stone, E.C., von Rosenvinge, T.T., 1996, ApJ 466, L43

Nerney, S., Suess, S.T. and Schmahl, E.J., 1993, J. Geophys. Res., 98, 15169

Selesnick, R.S., Cummings, A.C., Cummings, J.R., Mewaldt, R.A., Stone, E.C. and von Rosenvinge, T.T., 1995, J. Geophys. Res., 100, 9503

Washimi, H., 1993, Adv. Space Res., 13, 227

Whang, Y.C., Burlaga, L.F., and Ness, N.F., 1995, J. Geophys. Res., 100, 17015

Witte, M., Rosenbauer, H., Banaszkiewicz, M. and Fahr, H., 1993, Adv. Space Res., 13, 121

ASYMMETRIC EMERGING FLUX LOOPS AND THE ROTATION RATE OF SUNSPOT GROUPS

A. Bashir[1,2] and M. Marik[1]
[1] Eötvös Loránd University, Department of Astronomy
Budapest, Ludovika tér 2, H-1083 Hungary
[2]Garyonis University, Physics and Astronomy Department
P. O. Box 9480, Benghazi, Libya

Abstract

From the analysis of the rotation rate of the middle point between the main spots of a given number (49) of sunspot groups taken from the *Greenwich Photoheliographic Results* for the years 1964-1976 that cover the solar cycle no. 20, it is proved that the magnetic flux loops emerging from bipolar sunspot groups are asymmetric.

1 Introduction

Bipolar sunspot groups are generally formed by so-called emerging magnetic flux loops, that come out from sublayers of the photosphere (Zwaan, 1985). As the loop is emerging, the spots of opposite polarity are moving apart. This movement is asymmetric compared to the surrounding photosphere, because the loop is tilted eastward (van Driel-Gesztelyi and Petrovay, 1990; Petrovay et al., 1990). Namely, the preceding spots *(p)* move westward (in the direction of rotation) much faster than the following spots *(f)* move eastward (opposite direction of rotation). So, if we observe the proper motion of the main spots we find the following: in the first few days of their development, the spots move apart faster than in the case of the last few days before they decay (rotation of young sunspot groups) (see Balthasar and Wöhl, 1980 and Ternullo, Zappala, and Zuccarello, 1981) because in the decaying time the loop is stable. In this work we try to prove this hypothesis (the asymmetry of flux loops) by investigating the rotation rate of sunspot groups using the middle point between the preceding and the following spots.

2 Data and Method

The present work is based on the *Greenwich Photoheliographic Results (GPR)* data for the years 1964-1976 that cover the solar cycle no. 20. Our intention was to choose only the sunspot groups and others with small spots around them requiring that the minimum life-time of the sunspots should be at least six days. This condition gives us a chance to obtain the rotation rate of the middle point between the main spots of the sunspot groups once from the first three days when the loops start to emerge, and secondly, the rotation rate of the middle point of the last three days before the groups decay when the loops are stable. In this way we could observe the difference between the rotation rate of the middle point and the Carrington rotation rate in both cases. From among data points for the given period, we could select 49 data points which were used for this task. The middle point is measured as the mean longitude of the sunspot group and the data points were analysed by a least squares procedure. A plot of the difference in rotation rate $\Delta\omega$ between the middle points and the Carrington rotation against the heliographic latitudes is constructed for both cases.

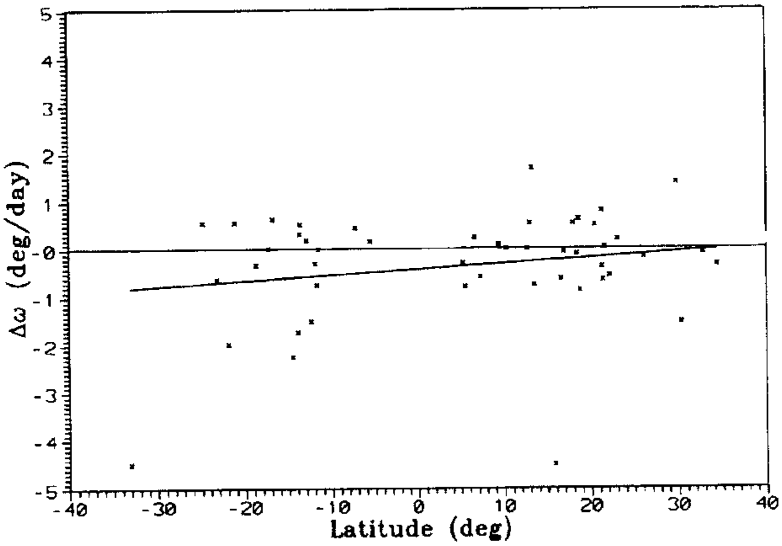

Figure 1: The difference ($\Delta\omega$) in rotation rate between the rotation of the middle point between the main spots of the sunspot groups and the Carrington rotation (zero line) is shown in this graph by the solid line for the first three days of the sunspot groups' life-time.

3. Results

The difference in rotation rate between the middle point and the Carrington rotation rate is given in *degrees/day.* In Figure 1 $\Delta\omega$ represents this difference for the case of the first three days of development. Each cross in the graph reflects the mean rotation rate of the middle point of each sunspot group compared with the Carrington rotation rate *(zero line).* It is clear from this graph that the line that presents the difference in the rotation is under the zero line which means that the middle point is rotating more slowly than the Carrington rotation, and this is true because the loops in this stage are asymmetric and their emerging moves the following spots *(f)* backwards away from the preceding spots *(p).* Now in Figure 2 we have the same parameters but for the last three days before the groups decay, when the loops are stable (stop emerging). In this graph the line shows us practically the same rotation as the Carrington rotation and this is also true because in this stage as the loops are stable the middle points should be stable too. From both these graphs we conclude that our results support the theory of the asymmetric flux loops in the active regions.

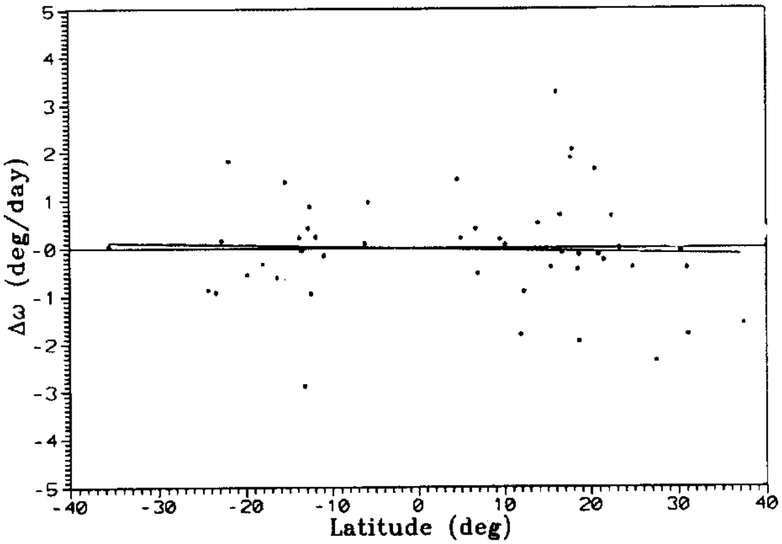

Figure 2: The same as Figure 1 but for the last three days of the sunspot groups' life-time.

References

Balthasar, H., and Wöhl, H. 1980, A&A 92, 111

Petrovay, K., Brown, J.C., van Driel-Gesztelyi, L., Fletcher, L., Marik, M., Stewart, G. 1990, Solar Phys. 127, 51

Ternullo, M., Zappala, R. A., and Zuccarello, F. 1981, Solar Phys. 74, 111

van Driel-Gesztelyi, L. and Petrovay, K. 1990, Solar Phys. 126, 285

Zwaan, C. 1985, Solar Phys., 100, 397

Galactic processes

INTERACTIONS OF MASSIVE STARS WITH THEIR PARENTAL CLOUDS

J. Franco[1], G. García-Segura[1] and T. Plewa[2]
[1]Instituto de Astronomía–UNAM
Apdo. Postal 70-264, 04510 México D. F., México
[2]Max-Planck-Institut für Astrophysik, Garching, Germany

Abstract

Here we discuss the interaction of massive stars with their parental molecular clouds. A summary of the dynamical evolution of HII regions and wind-driven bubbles in high-pressure cloud cores is given. Both ultracompact HII regions and ultracompact wind-driven bubbles can reach pressure equilibrium with their surrounding medium. The structures stall their expansion and become static and, as long as the ionization sources and the ambient densities remain about constant, the resulting regions are stable and long lived. For cases with negative density gradients, and depending on the density distribution, some regions never reach the static equilibrium condition. For power-law density stratifications, $\rho \propto r^{-w}$, the properties of the evolution depend on a critical exponent, w_{crit}, above which the ionization front cannot be slowed down by recombinations or new ionizations, and the cloud becomes fully ionized. This critical exponent is $w_{crit} = 3/2$ during the expansion phase. For $w > 3/2$ the gas expands supersonically into the surrounding ionized medium, and there are two regimes separated by $w = 3$. For $3/2 < w \leq 3$, the slow regime, the inner region drives a weak shock moving with almost constant velocity through the cloud. For $w > 3$, the fast regime, the shock becomes strong and accelerates with time. Finally, the evolution of slow winds in highly pressurized region is described briefly.

1 Introduction

Young stars display vigorous activity and their energy output stirs and heats the gas in their vicinity. Low-mass stars provide a small energy rate and affect only small volumes, but their collective action can provide partial support against the collapse of their parental clouds, and could regulate some aspects of the cloud evolution (e.g., Norman & Silk 1980; Franco & Cox 1983; Franco 1984; McKee 1989). In contrast, stars with initial masses above 8 $M_{\odot}$, massive stars, inject large amounts of radiative and mechanical energy from their moment of birth until their final explosion as a supernova. In the general, low-density, interstellar medium of a gaseous galaxy, the combined effects of supernovae, stellar winds, and HII region expansion destroy star-forming clouds, produce the hottest gas phases, create large expanding bubbles, and are probably responsible for both stimulating and shutting off the star formation process at different scales (e.g., Cox & Smith 1974; Salpeter 1976; McKee & Ostriker 1977; Franco & Shore 1984; Cioffi & Shull 1991; Franco et al. 1994; Silich et al. 1996). Thus, the collection of OB associations in gaseous galaxies represents a rich energy source which may be controlling the general structure of the interstellar medium, and the star formation rate (e.g., Mueller & Arnett 1976; Gerola & Seiden 1978; Franco & Shore 1984; Dopita 1988; see reviews by Tenorio-Tagle & Bodenheimer 1988, Franco 1991, 1992, Ferrini 1992, and Shore & Ferrini 1994).

The strong UV radiation field from massive stars creates large photoionized, HII regions. Young HII regions have large pressures and, when the pressure of the surrounding medium is low, they expand fast and drive a strong shock wave ahead of the ionization front. Expanding HII regions ionize and stir the parental cloud and, when the ionization front encounters a strong negative density gradient, they create fast "champagne" flows and can also generate cometary globules and elephant trunks (e.g., Tenorio-Tagle 1982; Yorke 1986; Franco et al. 1989, 1990; Rodriguez-Gaspar et al. 1995; García-Segura & Franco 1996). These flows are generated by the pressure difference between the HII region and the ambient medium, and they are responsible for the disruption of the cloud environment (e.g., Whitworth 1979; Elmegreen 1983; Larson 1992; Franco et al. 1994). Individual HII regions are bright objects and they are used as tracers of the active star formation sites in external galaxies (e.g., Osterbrock 1989).

Stellar winds and supernova explosions, on the other hand, being powerful sources of mechanical energy generate overpressured regions which drive shock waves into the ambient medium (see reviews by Ostriker & McKee 1988, and Bisnovatyi-Kogan & Silich 1995). The resulting wind-driven bubbles and supernova remnants, either from a single progenitor or from an entire association, are believed to generate most of the structuring observed in a gaseous galactic disk (e.g., Reynolds & Ogden 1978; Cowie et al. 1979; Heiles 1979; McCray & Snow 1979). Actually, many observed structures in the Milky Way and in external galaxies have been ascribed to this stellar energy injection (e.g., Heiles 1979, 1984; Brinks & Bajaja 1986; Deul & Hartog 1990; Palous et al. 1990, 1994). These bubbles may create fountains or winds at galactic scales (e.g., Shapiro & Field 1976; Chevalier & Oegerle 1979; Bregman 1980; Cox 1981; Heiles 1990; Houck & Bregman 1990), and their expanding shocks have also been suspected of inducing star formation (e.g., Herbst & Assousa 1977; Dopita et al. 1985). Thus, stellar activity creates a collection of cavities with different sizes, and can be viewed as an important element in defining the structure and activity of star-forming galaxies. Galaxies, however, are open systems and their properties are also defined by the interactions with neighboring galaxies. Here we describe only the effects of the stellar energy injection in high-density, high-pressure, regions.

2 The parental clouds and massive stars

Molecular clouds have complex density and velocity distributions, and are composed of a variety of high-density condensations. In our Galaxy, they have non-thermal turbulent velocities, reaching up to about 10 kms^{-1}, and fairly strong magnetic fields, of up to tens of mG (e.g., Myers & Goodman 1988). The *average* densities for molecular cloud complexes is between 10^2 and 10^3 cm^{-3}, but the high-density condensations have average densities of about $\sim 10^6$ cm^{-3} and may even reach values in excess of 10^8 cm^{-3} (e.g., Bergin et al. 1996; Akeson et al. 1996; see review by Walmsley 1995). These high density condensations, or cloud cores, are the actual sites of star formation, and the initial shape and early evolution of the resulting HII regions depend on the corresponding core density distributions and pressures. Theoretical studies on the collapse of clouds indicate that rotating and magnetized cores evolve into flattened (disk-like) structures (e.g., Bodenheimer & Black 1978; Cassen et al. 1985), but nonrotating and nonmagnetic cases remain spherically symmetric with power-law density distributions (e.g., Larson 1974). Isothermal spheres in hydrostatic equilibrium have a density distribution $\rho \sim r^{-2}$, and the distribution evolves towards $r^{-3/2}$ during the free-fall collapse. The pressures at the centers of these cores are fairly large, and can reach values of about 5 or 6 orders of magnitude above the pressures at the cloud boundaries (see García-Segura & Franco 1996).

Recent observational studies are revealing the structure of the dense star forming regions (see review by Walmsley 1995), and provide the average parameters of the core density distributions. Radio observations of cloud cores and dark clouds, along with visual extinction studies in nearby star forming clouds, indicate internal density distributions ranging from r^{-1} to r^{-3} (e.g., Arquilla & Goldsmith 1985; Chernicaro et al. 1985; Gregorio Hetem et al. 1988; see also Myers 1985). A reasonable mean value for the observationally derived power-law distributions is $\rho \sim r^{-2}$. The typical sizes of the massive high-density cores are about $r_c \sim 0.1$ pc (see Walmsley 1995), and the observationally derived core masses are in the range of 10 to 300 $\mathrm{M}_\odot$ (e.g., Snell et al. 1993). The observed properties of ultracompact HII regions (UCHII), on the other hand, indicate that the exciting stars (one or several massive stars) are embedded in dense and warm cores, with densities between 10^4-10^7 cm^{-3} and temperatures of about 10^2 K (e.g., Churchwell 1990; Cesaroni et al. 1994; Kurtz et al. 1994; Hofner et al. 1996; Hurt et al. 1996). The early stages of HII region evolution, then, occur inside these dense cloud cores.

2.1 HII region expansion at constant densities

Beginning with Strömgren (1939) and Kahn (1954), the expansion and evolution of HII regions has been studied with analytical and numerical models (see Yorke 1986; Osterbrock 1989; Franco et al. 1989, 1990). For a constant photon flux and uniform ambient densities, the evolution has well defined formation and expansion phases. During the formation phase, the UV photon field creates an ionization front that moves through the gas. Its speed is reduced (by geometrical dilution and recombinations), approaching a value of about twice the speed of sound in the ionized gas in, approximately, one recombination time. At this moment, which marks the end of the formation phase, the HII region reaches the initial Strömgren size, and the pressure gradient across the ionization front begins to drive the expansion of the ionized gas. The expansion is supersonic with respect to the surrounding gas and creates a shock wave that accelerates and compresses the ambient shocked medium. The ionization front sits behind the shock front during the rest of the evolution, and most of the shocked gas is accumulated in the interphase between the two fronts. If either the ionization or the shock front encounters a strong negative density gradient (say, the edge of the cloud) and overruns it, then the HII region enters into its champagne phase. Numerical models indicate that there also appears a strong instability that can fragment the shocked shell, and may explain the existence of cometary globules and the highly irregular morphologies of ionized nebulae (see García-Segura & Franco 1996).

2.1.1 The formation phase

Assuming a self-gravitating spherical cloud with a molecular density distribution that includes a central core, with radius r_c and constant density n_c, and an isothermal envelope with a power-law density stratification $n_{H_2}(r) = n_c(r/r_c)^{-2}$ for $r \geq r_c$. The total pressure at the core center is

$$P(0) = P_0 = \frac{2\pi G}{3}\rho_c^2 r_c^2 + P(r_c) = \frac{8}{5}P(r_c) \simeq 2 \times 10^{-7}\ n_6^2 r_{0.1}^2 \quad \text{dyn cm}^{-2}, \tag{1}$$

where G is the gravitational constant, $P(r_c)$ is the pressure at the core boundary $r = r_c$, $n_6 = n_c/10^6$ cm^{-3}, and $r_{0.1} = r_c/0.1$ pc. Note that the corresponding molecular mass is

$$M_c \simeq \left(\frac{\pi P_0}{G}\right)^{1/2} r_c^2 \sim 10^2\ P_7^{1/2} r_{0.1}^2 \quad \mathrm{M}_\odot, \tag{2}$$

where $P_7 = P_0/10^{-7}$ dyn cm^{-2}. A star located at the cloud center and producing F_* ionizing photons per unit time creates an spherical HII region. The gas in the HII region is fully ionized and the ion density is simply twice the molecular density, $n_i = 2n_{H_2}$. The initial Strömgren radius generated by such a star is

$$R_s = \left[\frac{3\ F_*}{4\pi(2n_c)^2\alpha_B}\right]^{1/3} \simeq 2 \times 10^{-3} F_{48}^{1/3} n_6^{-2/3} \alpha_0^{-1/3} \ \text{pc}, \tag{3}$$

where α_B is the hydrogen recombination coefficient to all levels above the ground level, $\alpha_0 = \alpha_B/2.6 \times 10^{-13}$cm^3 s^{-1}, $F_{48} = F_*/10^{48}$ s^{-1}, and $n_6 = n_c/10^6$ cm^{-3}. Thus, $R_s < r_c$ and the initial HII region is well contained within the core, and the formation phase follows the well known constant density evolution described above. Note that for a dusty cloud, the initial radius is even smaller and is given by the transcendental equation $R_{S,\mathrm{dust}} \simeq R_S\ e^{-\tau/3}$ (Franco et al. 1990), where the optical depth due to dust absorption is $\tau = \int_0^{R_S,\mathrm{dust}} \sigma_{\mathrm{dust}} n_0 dr$, and σ_{dust} is the average dust absorption cross-section per gas particle. This approximation agrees to better than 10% with detailed radiative transfer calculations (Díaz et al. 1996).

The formation phase is completed in a recombination time, and the pressure in the ionized region drives a shock into the molecular ambient medium. The HII region now begins its expansion phase. The equilibrium temperature in the photoionized region, $T_i \sim 10^4$, is achieved in a relatively short time scale. The advance of the ionization front is controlled by recombinations in the photoionized gas, and the expansion proceeds in a nearly isothermal fashion. Neglecting the external pressure, the main features of the expansion in a constant density medium can be derived with the thin shell approximation (see reviews Ostriker & McKee 1988, Bisnovatyi-Kogan & Silich 1995, and García-Segura & Franco 1996). Also, the pressureless expansion in density stratifications can be solved with simple approximations to the shock front conditions (Franco et al. 1989, 1990). The evolution including the external pressure, however, cannot be solved in a closed analytical form, but one can derive limits to the main expected features. Obviously, detailed numerical simulations provide an adequate description of the evolution in this and more complicated cases.

2.1.2 The expansion phase

The evolution can be easily derived by assuming the existence of a thin shell with mass M, containing all the swept-up ambient gas. This approximation can be applied to HII regions when the fraction of mass eroded by the ionization front from the shell is small. This is true for constant, increasing, or mildly decreasing density stratifications, but is not applicable for strongly decreasing gradients because the shell is easily eroded by photoionization (Franco et al. 1990). Here we consider the constant density case and the thin shell approximation can be used without restrictions. Neglecting magnetic fields and self-gravity, the equation of motion of the shell, located at a distant R from the central star, is

$$4\pi R^2 (P_i - P_0) = \frac{d}{dt}(Mv), \tag{4}$$

where P_i is the internal pressure, P_0 is the external pressure, and v is the shell velocity. Assuming that the shell radius can be written as a power-law in time, $R = R_0 \zeta^\beta$ (where R_0 is the initial radius of the region, $\zeta = (t_0 + t)/t_0$, and t_0 is a reference initial time), with constant R_0 or β (i.e., neglecting the existence of terms with $\dot{R}_0$ and $\dot{\beta}$), the right hand side of the equation becomes

$$\frac{d}{dt}(Mv) = \left(\frac{4\beta - 1}{3\beta}\right) 4\pi \rho_0 R^2 v^2. \tag{5}$$

The assumption of a constant β, as we will see below, does not hold for cases with $P_0 > 0$, but the present approximations can still be applied in a piece-wise fashion (i.e., one can use them in segments, changing the values for R_0 and t_0).

The equation of motion can then be written as

$$P_i - P_0 = \rho_0 v^2 \frac{(4\beta - 1)}{3\beta}, \tag{6}$$

and the shell evolution is given by

$$\frac{dR}{dt} = \left[\frac{3\beta}{(4\beta - 1)} \frac{(P_i - P_0)}{\rho_0}\right]^{1/2}. \tag{7}$$

Thus, one can write the formal solution to the equation of motion simply as

$$R - R_0 = \int_1^{\zeta} \left[\frac{3\beta}{(4\beta - 1)\rho_0} (P_i - P_0)\right]^{1/2} t_0 \, d\zeta. \tag{8}$$

This formal solution can be applied to HII regions, wind-driven bubbles, and SN remnants (see below). Obviously, the integration is not straightforward unless $P_0 = 0$, or the pressure difference, $P_i - P_0$, can be written as an explicit function of either R or t. In general this is not possible, but one can *always* check the behavior at early and late times, when the external pressure can be neglected and when the internal and external pressures become comparable. Here we illustrate the behavior in both cases.

2.1.3 Pressure equilibrium

For the case of expanding HII regions, using $R_0 = R_S$ as the initial Strömgren radius, we can set the solution for the expansion simply as

$$R_{HII}(t) = R_S \zeta^{\beta}. \tag{9}$$

The average ion density inside the HII region at any given time is given by

$$\langle n_i \rangle = \left[\frac{3\, F_\star}{4\, \pi\, \alpha_B}\right]^{1/2} R_{HII}^{-3/2}, \tag{10}$$

and the corresponding internal pressure is

$$P_i = \left(\frac{3\, k^2 T_i^2 F_\star}{\pi\, \alpha_B}\right)^{1/2} R_{HII}^{-3/2}. \tag{11}$$

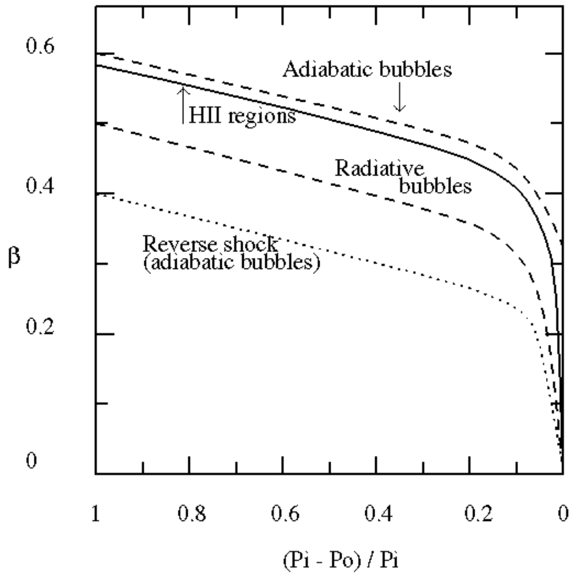

Figure 1: The evolution of the exponent β as a function of the normalized pressure difference $(P_i - P_0)/P_i$.

The region, then, evolves as

$$R_{HII} = R_S + \int_1^{\zeta} \left(\frac{3\beta}{(4\beta - 1)\rho_0} \left[\left(\frac{3\; k^2 T_i^2 F_\star}{\pi \alpha_B R_S^3 \zeta^{3\beta}} \right)^{1/2} - P_0 \right] \right)^{1/2} t_0 \; d\zeta. \qquad (12)$$

At early times, when $P_0/P_i \ll 1$, the integration with constant β gives $R_{HII} \propto \zeta^{1-3\beta/4}$. Thus, our initial assumption for the power-law implies that $\beta = 1 - 3\beta/4$, and one gets $\beta = 4/7$. The solution, then, is now written as

$$R_{HII} = R_S \left[1 + \frac{7}{4} \left(\frac{8\; k\; T_i}{3\mu_H} \right)^{1/2} \frac{t_0}{R_S} (\zeta^{4/7} - 1) \right]. \qquad (13)$$

Defining $c_i \simeq (8\; k\; T_i/3\mu_H)^{1/2}$, and recalling the initial definition of the power-law $\zeta^{4/7} = R_{HII}/R_S$, the reference time is simply given by $t_0 = (4/7)(R_S/c_i)$. Thus, as expected, one recovers the well known law for HII region expansion in a pressureless medium with a constant density

$$R_{HII} \simeq R_S \left(1 + \frac{7}{4} \frac{c_i t}{R_S} \right)^{4/7} . \qquad (14)$$

Using this explicit time dependence, the internal pressure decreases as

$$P_i = P_{i,0}\left(1+\frac{7}{4}\frac{c_i t}{R_S}\right)^{-6/7}, \tag{15}$$

where $P_{i,0}$ is the pressure at $t=0$.

The expansion continues until $P_i \to P_0$, and the internal pressure tends to a constant value. In this limit, the time dependence in the formal solution vanishes, giving $3\beta/2 \to 0$. These limits show that, for a constant density medium, β evolves as a function of the pressure difference from $4/7$ to zero. Figure 1 shows the evolution of β, as a function of the normalized pressure difference $(P_i - P_0)/P_i$, for HII regions and wind-driven bubbles (García-Segura & Franco 1996). The exponents were derived from high-resolution numerical simulations performed in one dimension for the evolution inside high density cores. Figure 2 shows the evolution of an HII region in a high-density core with $P_7 = 1$.

When pressure equilibrium is reached, the ion density is simply given by

$$n_{i,\mathrm{eq}} = \left(\frac{P_0}{2kT_i}\right) \simeq 3.6\times10^4 P_7 T_{\mathrm{HII},4}^{-1} \ \ \mathrm{cm}^{-3}, \tag{16}$$

where $P_7 = P_0/10^{-7}$ dyn cm^{-2}, and $T_{\mathrm{HII},4} = T_i/10^4$ K. The equilibrium radius of the H II region, then, corresponds to a Strömgren radius at this equilibrium density

$$R_{\mathrm{S,eq}} \approx 2.9\times10^{-2}\ F_{48}^{1/3}\ T_{\mathrm{HII},4}^{2/3}\ P_7^{-2/3} \quad \mathrm{pc}, \tag{17}$$

where $F_{48} = F_\star/10^{48}$ s^{-1}.

For high-pressure cores with $r_c \sim 0.1$ pc, the photoionized regions can reach pressure equilibrium without breaking out of the core. The resulting sizes are similar to those of the ultracompact class (see Dyson et al. p.239 in this volume), and indicate that UCHII can be explained by simple pressure equilibrium. This is in agreement with the recent results reported by Xie et al. (1996), that show the smaller UCHII are embedded in the higher pressure cores. Also note that the equilibrium values with $P_7 = 1$, $T_{\mathrm{HII},4} \sim 1$, and $F_{48} \sim 1$, are *very similar* to the average sizes and electron densities in UCHII (see Figure 151 of Kurtz et al. 1994). The apparent longevity problem of UCHIIs is rooted in the notion that young HII regions should grow fast and reach the expanded state on a relatively short time-scale. This statement is false, however, if the external pressure is large and halts the expansion at a small radius: *in pressure equilibrium, UCHIIs are stable and long lived.*

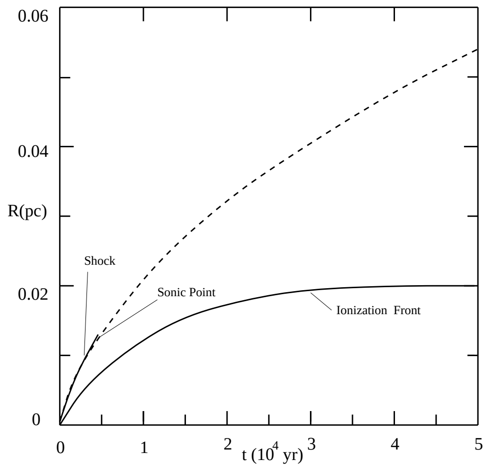

Figure 2: The evolution of an HII region, with $F_{48} = 1$, in a high-pressure core, with $P_7 = 1$.

2.2 HII evolution in decreasing density gradients

If a star is born at a distance smaller than $R_{S,\mathrm{eq}}$ from the core boundary, the speeds of the ionization and shock fronts are modified by the negative density gradient. The gas of the HII regions is accelerated in supersonic flows and no static solution, in pressure equilibrium exists (e.g., Tenorio-Tagle 1982; Franco et al. 1989, 1990). Thus, under these conditions the ultracompact stage is indeed a transient phase. Here we assume isothermal clouds with $\rho \propto r^{-2}$, but one can easily find the solutions for the general power-law case, $\rho \propto r^{-w}$ (see Franco et al. 1990). For $R_s \geq r_c$, the initial ionization front reaches the core radius with a speed

$$U_c \simeq 90\ \alpha_0\ n_3\ r_{17} \left[\left(\frac{R_s}{r_c}\right)^3 - 1\right] \mathrm{km\ s}^{-1}, \tag{18}$$

and in a time scale

$$t_c \simeq 130\ \alpha_0^{-1} n_3^{-1}\ \ln\left[\frac{1}{1-(r_c/R_s)^3}\right]\ \mathrm{yr}, \tag{19}$$

where $r_{17} = r_c/10^{17}$ cm. Afterwards, the ionization front enters the density gradient and its speed becomes

$$U_{if} = \frac{U_c}{(R_s/r_c)^3 - 1} u(w), \tag{20}$$

with

$$u(w) = \begin{cases} (r_c/r_i)^{2-w} \left[(R_s/r_c)^3 + 2w\beta - 3\beta\,(r_i/r_c)^{1/\beta}\right] & \text{for } w \neq 3/2, \\ (r_c/r_i)^{1/2} \left[(R_s/r_c)^3 - 1 - 3\ \ln\,(r_i/r_c)\right] & \text{for } w = 3/2, \end{cases} \tag{21}$$

where r_i is the location of the front, and $\beta = (3 - 2w)^{-1}$. This defines a critical exponent, corresponding to the maximum density gradient that is able to stop the ionization front,

$$w_f = \frac{3}{2}\left[1 - \left(\frac{r_c}{R_s}\right)^3\right]^{-1}, \tag{22}$$

and above which no initial HII radius exists. Note that for $R_s/r_c > 2$ the critical value becomes $w_f \simeq 3/2$. Obviously, the concept of a critical exponent is not restricted to power-law stratifications and can also be applied to other types of density distributions, for instance, exponential, gaussian, and sech^2 profiles (see Franco et al. 1989).

For $w \neq 3/2$, the initial HII region radius can be written as

$$R_w = g(w) R_s, \tag{23}$$

with

$$g(w) = \left[\frac{3 - 2w}{3} + \frac{2w}{3}\left(\frac{r_c}{R_s}\right)^3\right]^\beta \left(\frac{R_s}{r_c}\right)^{2w\beta}, \tag{24}$$

where R_s is the Strömgren radius for the density n_c. The solution for $w = 3/2$ is

$$R_{3/2} = r_c \exp\left\{\frac{1}{3}\left[\left(\frac{R_s}{r_c}\right)^3 - 1\right]\right\}. \tag{25}$$

After the formation phase has been completed in clouds with $w \leq w_f$, the HII region begins its expansion phase. For simplicity, we assume that the shock evolution starts at $t = 0$ when R_w is achieved. Given that the expansion is subsonic with respect to the ionized gas, the density structure inside the HII region can be regarded as uniform and its average ion density at time t is

$$\rho_i(t) \simeq \mu_i \frac{(9 - 6w)^{1/2}}{3 - w}(2n_c) R_s^{3/2} R^{-3/2}(t), \tag{26}$$

where μ_i is the mass per ion, and $R(t)$ is the radius of the HII region at the time t. For $w \leq 3/2$, the radius can be approximated by

$$R(t) \simeq R_w \left[1 + \frac{7 - 2w}{4}\left(\frac{12}{9 - 4w}\right)^{1/2} \frac{c_i t}{R_w}\right]^{4/(7-2w)}, \tag{27}$$

where c_i is the sound speed in the ionized gas. The ratio of total mass (neutral plus ionized), $M_s(t)$, to ionized mass, $M_i(t)$, contained within the expanded radius evolves as

$$\frac{M_s(t)}{M_i(t)} \simeq \left[\frac{R(t)}{R_w}\right]^{(3-2w)/2}. \tag{28}$$

This equation indicates: i) for $w < 3/2$, the interphase between the ionization front and the leading shock accumulates neutral gas and its mass grows with time to exceed even the mass of ionized gas, and ii) for $w = 3/2 = w_{crit}$, the two fronts move together without allowing the formation and growth of a neutral interphase. Note that the decreasing ratio predicted by equation (28) for $w > 3/2$ is physically meaningless and it only indicates that the ionization front overtakes the shock front (and proceeds to ionize the whole cloud). Thus, regardless of the value of the critical exponent for the formation phase, w_f, the expansion phase is characterized by a critical exponent with a well defined value, $w_{crit} = 3/2$, which is independent of the initial conditions. Furthermore, this critical exponent $w_{crit} = 3/2$ is not affected by dust absorption (see Franco et al. 1990).

For $3/2 < w < w_f$, the ionization front overtakes the shock and the whole cloud becomes ionized. In this case, the pressure gradient simply follows the density gradient. The ionized cloud is set into motion, but the expanded core (now with a radius identical to the position of the overtaken shock) is the densest region and feels the strongest outwards acceleration. Then, superimposed on the general gas expansion there is a wave driven by the fast growing core (the wave location defines the size of the expanded core), and the cloud experiences the so-called "champagne" phase. This core expansion tends to accelerate with time and two different regimes, separated by $w = 3$, are apparent: a *slow* regime with almost constant expansion velocities, and a *fast* regime with strongly accelerating shocks. The slow regime corresponds to $3/2 < w < 3$ and the core grows approximately as

$$r(t) \simeq r_c + \left[1 + \left(\frac{3}{3-w}\right)^{1/2}\right] c_i t, \tag{29}$$

where for simplicity the initial radius of the denser part of the cloud has been set equal to r_c, the initial size of the core. For $w = 3$ the isothermal growth is approximated by

$$r(t) \simeq 3.2 r_c \left[\frac{c_i t}{r_c}\right]^{1.1}. \tag{30}$$

For $w > 3$, the fast regime, the shock acceleration increases with increasing values of the exponent and the core expansion is approximated by

$$r(t) \simeq r_c \left[1 + \left(\frac{4}{w-3}\right)^{1/2} \left(\frac{\delta + 2 - w}{2}\right) \frac{c_i t}{r_c}\right]^{2/(\delta+2-w)}, \tag{31}$$

where $\delta \simeq 0.55(w-3) + 2.8$.

2.3 Wind-driven bubbles

The evolution of the cavity created by a stellar wind, a wind-driven bubble, can also be derived with the thin shell approximation described above. The thermalization of the wind creates a hot shocked region enclosed by two shocks: a reverse shock that stops the supersonic wind, and an outer shock that penetrates the ambient gas. The gas processed by each shock is separated by a contact surface, the contact discontinuity. The kinetic energy of the wind is transformed into thermal energy at the reverse shock producing a hot gas (e.g., Weaver et al. 1977). For the case of a strong wind evolving in a high-density and dusty molecular core, the properties of the cooling are poorly known, but the shocked ambient gas cools down very quickly and a thin external shell is formed on time-scales of the order of years. Thus, the ambient gas is collected in a thin shell by the outer shock during most of the evolution. The case of the shocked stellar wind is less clear because the cooling time there can be substantially longer than in the shocked ambient gas, and it is difficult to define when the thin shell is formed behind the reverse shock. Thus, one can simply derive the limits for the evolution of the reverse shock in both the adiabatic and radiative modes.

The density in a steady wind, with a constant mass loss, decreases as

$$\rho_w = \frac{\dot{M}}{4\pi r^2 v_\infty}, \tag{32}$$

where $\dot{M}$ is the stellar mass-loss rate, and v_∞ is the wind speed. The pressure in the shocked wind region is defined by the wind ram pressure, $\rho_w v_\infty^2$, at the location of the reverse shock and is given by

$$P_i = \frac{\dot{M} v_\infty}{4\pi R_{rs}^2}, \tag{33}$$

where R_{rs} is the radius of the reverse shock.

2.3.1 Adiabatic case

For an adiabatic bubble evolving in a constant density medium and powered by a constant mechanical luminosity, $L_{\rm w}$, the thermal energy of the shocked wind region grows linearly with time, $E_{th} = 5\,L_{\rm w}t/11$ (Weaver et al. 1977). The shocked ambient medium is concentrated in the external thin shell and the the bubble radius, R_b is the radius of the contact discontinuity. The thermal pressure of the bubble interior changes as $P_i = (5L_{\rm w}t)/(22\pi R_b^3)$. This pressure is equal to that given by equation (33), and the locations of the reverse and outer shocks are related by mass conservation

$$R_{rs} = R_b^{3/2} \left(\frac{11 \dot{M} v_\infty}{10 L_{\rm w}\, t} \right)^{1/2}. \tag{34}$$

The solution for R_b, then, also provides the evolution of the reverse shock. The initial radius in this case is very small, and we simply set $R_b = R_0(t/t_0)^\beta$, where R_0 now represents the bubble radius at some reference time t_0. Again, as in the HII region case, the formal solution is

$$R_b = \int_0^t \left[\frac{3\beta}{(4\beta - 1)\rho_0} \left(\frac{5L_{\rm w} t^{1-3\beta} t_0^{3\beta}}{22\pi R_0^3} - P_0 \right) \right]^{1/2} dt. \tag{35}$$

At early times, $P_i \gg P_0$ and P_0 can be neglected in the above equation. The exponent is then defined by $\beta = 1 + (1 - 3\beta)/2$, giving the well known adiabatic expansion in a medium with constant density $R_b \propto L_{\rm w}^{1/5} \rho_0^{-1/5} t^{3/5}$. The position of the reverse shock (equation 34), then, evolves as $R_{rs} \propto t^{2/5}$. With this time dependence, the internal pressure drops as $P_i \propto t^{-4/5}$. At later times, when $P_i \to P_0$, the bubble reaches quasi-equilibrium with the ambient gas and the growth is $R_{b,\rm eq} \propto (L_{\rm w}/P_0)^{1/3} t^{1/3}$. In pressure equilibrium, the radius of an *adiabatic* bubble grows at a slow rate, but *no steady state* solution exists during this stage. The final radius of the reverse shock is simply given by the balance between the external and the wind ram pressures. The wind density at equilibrium is $\rho_{w,\rm eq} = P_0/v_\infty^2$, and the location of the reverse shock is

$$R_{rs,\rm eq} = \left[\frac{\dot{M}\, v_\infty}{4\,\pi\, P_0} \right]^{1/2} \simeq 2.3 \times 10^{-2} \left[\frac{\dot{M}_6\; v_{\infty,8}}{P_7} \right]^{1/2} \quad \text{pc}, \tag{36}$$

where $\dot{M}_6 = \dot{M}/10^{-6}$ M$_\odot$ yr^{-1}, and $v_{\infty,8} = v_\infty/10^8$ cm s^{-1}. Using mass conservation in the shocked wind region, $M_{sw} = \dot{M}t$, the quasi-equilibrium radius of an *ultracompact* wind-driven bubble is given by

$$R_{b,\rm eq} = R_{rs,\rm eq} \left(1 + \frac{3L_w t}{8\pi P_0 R_{rs,\rm eq}^3} \right)^{1/3}. \tag{37}$$

Clearly, for adiabatic bubbles, β goes from 3/5 at early times to 1/3 at late times.

2.3.2 Radiative case

Once radiative losses become important, the hot gas looses its pressure and the bubble collapses into a simple structure: the free-expanding wind collides with the cold shell and the gas is thermalized and cools down to low temperatures in a cooling length. At this moment, the shell becomes static at the radius $R_{rs,\rm eq}$.

If the bubble becomes radiative before the final radius, $R_{rs,\rm eq}$, is reached, the shell is pushed directly by the wind pressure. For this radiative bubble case, the formal solution is

$$R_b = \int_0^t \left[\frac{3\beta}{(4\beta - 1)\rho_0} \left(\frac{\dot{M}\, v_\infty t_0^{2\beta}}{4\pi R_0^2 t^{2\beta}} - P_0 \right) \right]^{1/2} dt. \tag{38}$$

The early times solution, with $P_i \gg P_0$, gives the relation $\beta = 1 - \beta$, and one recovers the well known solution for radiative bubbles $R_b \propto t^{1/2}$ (e.g., Steigman et al. 1975). The ram pressure now evolves as $P_i \propto t^{-1}$. At late times, one gets $\beta \rightarrow 0$ and the shell reaches the final equilibrium radius (eqn. 36). Thus, the exponent in this case evolves from 1/2 to 0. Note that if the bubble starts on an adiabatic track and becomes radiative before pressure equilibrium is achieved, the exponent varies from 3/5 to 1/2, and then to zero. Figure 3 illustrates the evolution of an ultracompact wind-driven shell in a high-pressure core.

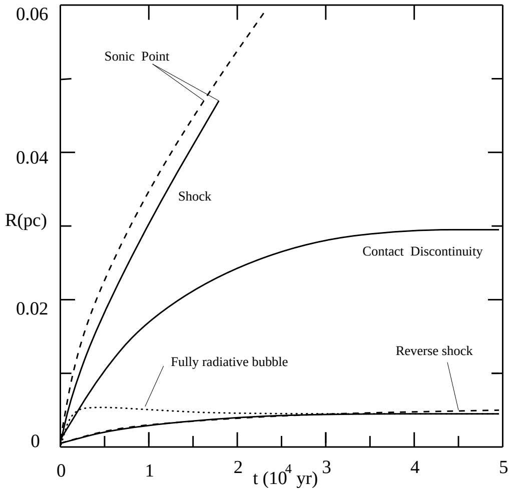

Figure 3: The evolution of an ultracompact wind-driven bubble, with $\dot{M}_6 = 1$ and $v_{\infty,8} = 1$, in a high-pressure core, with $P_7 = 1$.

3 Discussion

3.1 Young stars

The history of the pressure in a star forming region, then, follows a somehow simple scheme. The initial properties and pressure of the gas in a star forming cloud is defined by self-gravity. Once young stars appear, their energy input modifies the structure and evolution of the cloud. This is particularly true for massive stars, their radiative and mechanical energy inputs are even able to disrupt their parental clouds. In the case of the dense cloud cores, the sizes of either HII regions or wind-driven bubbles are severely reduced by the large ambient pressure (García-Segura & Franco 1996). In fact, the pressure equilibrium radii of ultra-compact HII regions are actually indistinguishable from those of ultra-compact wind-driven bubbles, and they could be stable and long lived. Actually, Xie et al. (1996) have recently found evidence indicating that the smaller UCHII seem to be embedded in the higher pressure cores.

The situation is completely different when the stars are located near the edge of the cloud core. The resulting HII regions (and also wind-driven bubbles) generate supersonic outflows. Cases with $w > w_{crit}$ lead to the champagne phase: once the cloud is fully ionized, the expansion becomes supersonic. For spherical clouds with a small constant-density core and a power-law density distribution, r^{-w}, outside the core, there is a critical exponent ($w_{crit} = 3/2$) above which the cloud becomes completely ionized. This represents an efficient mechanism for cloud destruction and, once the parental molecular cloud is completely ionized, can limit the number of massive stars and the star formation rate (Franco et al. 1994). For a cloud of mass M_{GMC}, with only 10% of this mass concentrated in star-forming dense cores, the number of newly formed OB stars required for complete cloud destruction is

$$N_{OB} \sim 30 \frac{M_{GMC,5} n_3^{1/5}}{F_{48}^{3/5} (c_{i,15} t_{MS,7})^{6/5}}. \tag{39}$$

where $M_{GMC,5} = M_c/10^5$ $\mathrm{M}_\odot$, $n_3 = n_0/10^3$ cm^{-3}, $c_{i,15} = c_i/15$ km s^{-1}, and $t_{MS,7}$ is the main sequence lifetime in units of 10^7 yr. This corresponds to a total star forming efficiency of about ~ 5 % (larger average densities and cloud masses can result in higher star formation efficiencies).

Summarizing, photoionization from OB stars can destroy the parental cloud on relatively short time scales, and defines the limiting number of newly formed stars. The fastest and most effective destruction mechanism is due to peripheral, blister HII regions, and they can limit the star forming efficiency at galactic scales. Internal HII regions at high cloud pressures, on the other hand, result in large star forming efficiencies and they may be the main limiting mechanism in star forming bursts and at early galactic evolutionary stages (see Cox 1983).

3.2 Slow winds from evolved stars

The evolution of evolved stellar winds in high-pressure regions is discussed in Franco et al. (1996), and here we just repeat the relevant parts. As the cloud is dispersed, the average gas density decreases and the newly formed cluster becomes visible. The individual HII regions merge into a single photo-ionized structure and the whole cluster now powers an extended, low density, HII region. The stellar wind bubbles now can grow to larger sizes and some of them begin to interact. As more winds collide, the region gets pressurized by interacting winds and the general structure of the gas in the cluster is now defined by this mass and energy input (Franco et al. 1996).

Given a total number of massive stars in the cluster, N_{OB}, and their average mass input rate, $\langle \dot{M} \rangle$, the pressure due to interacting adiabatic winds is

$$P_i \sim \frac{N_{OB} \langle \dot{M} \rangle c_i}{4\pi r_{clus}^2} \sim 10^{-8} \frac{N_2 \langle \dot{M}_6 \rangle c_{2000}}{r_{pc}^2} \quad \text{dyn cm}^{-2}, \tag{40}$$

where $r_{pc} = r_{clus}/1$ pc is the stellar group radius, $N_2 = N_{OB}/10^2$, $\langle \dot{M}_6 \rangle = \langle \dot{M} \rangle / 10^{-6}$ $M_\odot$ yr^{-1}, and $c_{2000} = c_i/2000$ km s^{-1} is the sound speed in the interacting wind region. This is the central pressure driving the expansion of the resulting superbubble before the supernova explosion stage. For modest stellar groups with relatively extended sizes, like most OB associations in our Galaxy, the resulting pressure is only slightly above the ISM pressure (i.e., for $N_2 \sim 0.5$ and $r_{pc} \sim 20$, the value is $P_i \sim 10^{-11}$ dyn cm^{-2}). For the case of rich and compact groups, as those generated in a starburst, the pressures can reach very large values. For instance, for the approximate cluster properties in starbursts described by Ho (1996), $r_{pc} \sim 3$ and $N_2 > 10$, the resulting pressures can reach values of the order of $P_1 \sim 10^{-7}$ dyn cm^{-2}, similar to those due to self-gravity in star forming cores. At these high pressures, the wind of a red giant (or supergiant) cannot expand much and the bubble reaches pressure equilibrium at a relatively small distance from the evolving star. Thus, the large mass lost during the slow red giant wind phase is concentrated in a dense circumstellar shell.

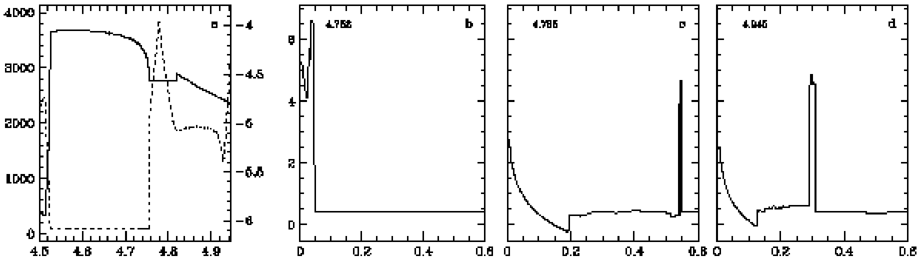

Figure 4: Wind-driven bubble from an evolved $35\,M_\odot$ star in a high pressure medium. **a)** Left scale: terminal wind velocity (km s^{-1}); right scale: mass loss rate ($M_\odot$ yr^{-1}); horizontal scale: time (millions of yr). **(b)-(d)**: Evolution of the wind-driven bubble. The gas density (cm^{-3}) is plotted on a logarithmic scale versus the radial distance (pc). Evolutionary times (upper-left corner of each panel) are given in million years.

Figure 4 shows the evolution of a wind-driven bubble around a $35\,M_\odot$ star. Figure 4a shows the wind velocity and mass-loss rate (dashed and solid lines, respectively: García-Segura, Langer & Mac Low 1996). The simulations are done only over the time spanning the red supergiant and Wolf–Rayet phases, and assume that the region is already pressurized by the main sequence winds from massive stars.

We have used the AMRA code, as described by Plewa & Różyczka (1996). During the RSG phase the wind-driven shell is located very close ($R \approx 0.04$ pc) to the star due to a very low ram-pressure from the wind (Figure 4b). Later on (Figure 4c), the powerful WR wind pushes the shell away from the star to the maximum distance of $R \approx 0.54$ pc. Still later, when the wind has variations, the shell adjusts its position accordingly, and reaches the distance $R \approx 0.3$ pc at the end of simulation (Figure 4d). It must be stressed that the series of successive accelerations and decelerations of the shell motion during the WR phase will certainly drive flow instabilities and cause deviations from the sphericity assumed in our model. The role of these multidimensional instabilities in the evolution of the shell is currently under study (with 2-D and 3-D models), and the results will be presented in a future communication. Regardless of the possible shell fragmentation, however, when the star explodes as a supernova, the ejecta collides with a dense circumstellar shell. This interaction generates a bright and compact supernova remnant, with a powerful photoionizing emission (e.g., Terlevich et al. 1992; Franco et al. 1993; Plewa & Różyczka 1996), that may also be a very strong radio source, like SN 1993J (see Marcaide et al. 1995). If the shell is fragmented, the ejecta–fragment interactions will occur during a series of different time intervals, leading to a natural variability in the emission at almost any wavelength (see Cid-Fernandes et al. 1996). This type of interaction is also currently under investigation, and further modeling will shed more light on the evolution of SN remnants in high-pressure environments.

JF and GGS acknowledge partial support from DGAPA-UNAM grant IN105894, CONACyT grants 400354-5-4843E and 400354-5-0639PE, and a R&D Cray research grant. The work of TP was partially supported by the grant KBN 2P-304-017-07 from the Polish Committee for Scientific Research. The simulations were performed on the CRAY Y-MP of the Supercomputing Center at UNAM, and on a workstation cluster at the Max-Planck-Institut für Astrophysik.

References

Akeson, R. L., Carlstrom, J. E., Phillips, J. A. & Woody, D. P. 1996, ApJL 456, L45

Arquilla, R. & Goldsmith, P. F. 1985, ApJ 297, 436.

Bergin, E., Snell, R. & Goldsmith, P. 1996, ApJ 460, 343

Bisnovatyi-Kogan, G. S. & Silich, S. A. 1995, RevModPhys 67, 661

Bodenheimer, P. & Black, D. C. 1978, in *Protostars and Planets I*, ed. T. Gehrels, (Tucson: Univ. Arizona Press), 288

Bregman, J. N. 1980, ApJ 236, 577

Brinks, E. & Bajaja, E. 1986, A&A 169, 14

Cassen, P., Shu, F. H. & Terebey, S. 1985, in *Protostars and Planets II*, ed. D. C. Black & M. S. Matthews (Tucson: Univ. Arizona Press), 448

Cesaroni, R., Churchwell, E., Hofner, P., Walmsley, M. & Kurtz, S. 1994, A&A 288, 903

Chernicaro, J., Bachiller, R. & Duvert, G. 1985, A&A 149, 273

Chevalier, R. A. & Oegerle, W. 1979, ApJ 227, 39

Churchwell, E. 1990, A&AR 2, 79

Cid-Fernandes R., Plewa T., Różyczka M., Franco J., Tenorio-Tagle G., Terlevich R. & Miller W., 1996, MNRAS 283, 419

Cioffi, D. E. & Shull, J. M. 1991, ApJ 367, 96

Cowie, L. L., Songaila, A. & York, D. G. 1979, ApJ 230, 469

Cox, D. P. 1981, ApJ 245, 534

Cox, D. P. 1983, ApJL, 265, L61

Cox, D. P. & Smith, B. W. 1974, ApJL, 189, L105

Deul, E. & Hartog, R. H. 1990, A&A 229, 362

Díaz, R. I., Franco, J. & Shore, S. N. 1996, in preparation

Dopita, M. 1988, *Supernova Remnants and the ISM, IAU Coll. 101*, ed. R. Roger & T. Landecker, (Cambridge Univ. Press: Cambridge), 493

Dopita, M. A., Mathewson, D. S. & Ford, V. L. 1985, ApJ 297, 599

Elmegreen, B. G. 1983, MNRAS 203, 1011

Ferrini, F. 1992, in *Evolution of Interstellar Matter and Dynamics of Galaxies*, ed. J. Palous, W. B. Burton & P. O. Lindblad, (Cambridge: Cambridge Univ. Press), 304

Franco, J. 1984, A&A 137, 85

Franco, J. 1991, in *Chemical and Dynamical Evolution of Galaxies*, ed. F. Ferrini, J. Franco & F. Matteucci, (Pisa: ETS Editrice), 506

Franco, J. 1992, in *Star Formation in Stellar Systems*, ed. G. Tenorio-Tagle, M. Prieto & F. Sanchez, (Cambridge: Cambridge Univ. Press), 515

Franco, J. & Cox, D. P. 1983, ApJ 273, 243

Franco, J., García-Segura, G. & Plewa, T. 1996, in preparation

Franco, J., Miller, W., Cox, D., Terlevich, R., Różyczka, M. & Tenorio-Tagle, G. 1993, RMexA&A 27, 133

Franco, J., Plewa, T. & García-Segura, G. 1996, in *Starburst Activity in Galaxies*, ed. J. Franco, R. Terlevich & A. Serrano, RMexA&A (Conf. Series), p.172

Franco, J. & Shore, S. N. 1984, ApJ 285, 813

Franco, J., Shore, S. N. & Tenorio-Tagle, G. 1994, ApJ 436, 795

Franco, J., Tenorio-Tagle, G. & Bodenheimer, P. 1989, RMxA&A 18, 65

Franco, J., Tenorio-Tagle, G. & Bodenheimer, P. 1990, ApJ 349, 126

García-Segura, G. & Franco, J. 1996, ApJ 469, 171

García-Segura, G., Langer, N., & Mac Low, M.-M. 1996, A&A 316, 133

Gerola, H. & Seiden, P. 1978, ApJ 223, 129

Gregorio Hetem, J. C., Sanzovo, G. C. & Lepine, J. D. R. 1988, A&ASupp, 76, 647

Heiles, C. 1979, ApJ 229, 533

Heiles, C. 1984, ApJS 55, 58

Heiles, C. 1990, ApJ 354, 483

Herbst, W. & Assousa, G. E. 1977, ApJ 217, 473

Ho, L. 1996, in *Starburst Activity in Galaxies*, ed. J. Franco, R. Terlevich & A. Serrano, RMexA&A (Conf. Series), p. 5

Hofner, P., Kurtz, S., Churchwell, E., Walmsley, M. & Cesaroni, R. 1996, ApJ 460, 359

Houck, J. C. & Bregman, J. N. 1990, ApJ 352, 506

Hurt, R. L., Barsony, M. & Wooten, A. 1996, ApJ 456, 686

Kahn, F. D. 1954, BAN 12, 187

Kurtz, S., Churchwell, E. & Wood, D. O. S. 1994, ApJS 91, 659

Larson, R. B. 1974, FundCosmicPhys 1, 1

Larson, R. B. 1992, in *Star Formation in Stellar Systems*, ed. G. Tenorio-Tagle, M. Prieto & F. Sanchez, (Cambridge: Cambridge Univ. Press), 125

Marcaide, J. M. et al. 1995, Science 270, 1475

McCray, R. & Snow, T. P. Jr. 1979, ARA&A 17, 213

McKee, C. F. 1989, ApJ 345, 782

McKee, C. F. & Ostriker, J. P. 1977, ApJ 218, 148

Mueller, M. & Arnett, W. D. 1976, ApJ 210, 670

Myers, P. C. 1985, in *Protostars and Planets II*, ed. D. C. Black & M. S. Matthews, (Tucson: Univ. Arizona Press), 81

Myers, P. C. & Goodman, A. A. 1988, ApJ 326, L27

Norman, C. & Silk, J. 1980, ApJ 238, 158

Osterbrock, D. E. 1989, *Astrophysics of Gaseous Nebulae and Active Galactic Nuclei*, (Mill Valley: Univ. Science Books)

Ostriker, J. P. & McKee, C. F. 1988, RevModPhys, 60, 1

Palous, J., Franco, J. & Tenorio-Tagle, G. 1990, A&A 227, 175

Palous, J., Tenorio-Tagle, G. & Franco, J. 1994, MNRAS 270, 75

Plewa, T. & Różyczka, M. 1996, in *Starburst Activity in Galaxies*, ed. J. Franco, R. Terlevich & A. Serrano, RMexAA (Conf. Series), p. 232

Reynolds, R. J. & Ogden, P. M. 1978, ApJ 224, 94

Rodriguez-Gaspar, J. A., Tenorio-Tagle, G. & Franco, J. 1995, ApJ 451, 210

Salpeter, E. E. 1976, ApJ 229, 533

Shapiro, P. R. & Field, G. B. 1976, ApJ 205, 762

Shore, S. N. & Ferrini, F. 1994, FundCosmicPhys, 16, 1

Silich, S., Franco, J., Palous, J. & Tenorio-Tagle, G. 1996, ApJ 468, 722

Snell, R., Carpenter, J., Schloerrb, F. P. & Strutskie, M. 1993, in *Massive Stars: Their Lives in the Interstellar Medium*, ed. J. P. Cassinelli & E. B. Churchwell, ASP (Conf. Series) 35, 138

Steigman, G., Strittmatter, P. A. & Williams, R. E. 1975, ApJ 198, 575

Strömgren, B. 1939, ApJ 89, 526

Tenorio-Tagle, G. 1982, in *Regions of Recent Star Formation*, ed. R. S. Roger & P. E. Dewdney, (Dordrecht: Reidel)

Tenorio-Tagle, G. & Bodenheimer, P. 1988, ARAA 26, 145

Terlevich, R., Tenorio-Tagle, G., Franco, J. & Melnick, J., 1992 MNRAS 255, 713

Walmsley, M. 1995, RMexAA (Conf. Ser.) 1, 137

Weaver, R., McCray, R., Castor, J., Shapiro, P. & Moore, R. 1977, ApJ 218, 377

Whitworth, A. 1979, MNRAS 186, 59

Xie, T., Mundy, L. G., Vogel, S. N. & Hofner, P. 1996, ApJ 473, L13

Yorke, H. W. 1986, ARAA, 24, 46

STAR FORMATION IN FORMING GALAXIES

P. Berczik & S. G. Kravchuk
Main Astronomical Observatory
Ukrainian National Academy of Sciences
Golosiiv, Kiev-022, 252650, Ukraine
e-mail: berczik@mao.gluk.apc.org

Abstract

We present results of SPH (Smoothed Particle Hydrodynamics) simulations of the collapse and subsequent evolution of the isolated, initially constant-density perturbation in cosmologically motivated situation. The protogalaxy perturbation made of dark and baryonic matter in a 10:1 ratio is taken initially in solid-body rotation and in Hubble flow. The model includes gasdynamics, radiative processes, star formation and supernova feedback.

The results show that the accounting for chaotic motions and the time lag between initial development of suitable conditions for star formation and star formation itself provides the realistic description of the process of galaxy formation and evolution. It is also shown that the gas consumption problem accompanying the standard modelling of the process of galaxy formation and dynamical and chemical evolution seems to be a model artifact.

1 Introduction

The main purpose of this paper is to follow the Star Formation (SF) in forming galaxies. First of all attention is paid to the initial SF burst at early stages of protogalaxy evolution and following behaviour of gas component in just formed galaxy. In modelling we use modified SPH method. In this sense this is a continuation of well-known works by Katz (1992) and Katz & Gunn (1991). Our version of SPH code with individual time step in detail is described by Berczik & Kolesnik (1993). The standard SPH code was altered and supplemented by an algorithm accounting for SF and supernovae (SN) feedback.

Novelty of our approach is as follows:

- energy criterion for SF accounting for chaotic velocities in interstellar matter (ISM),
- time lag between initial development of suitable conditions for SF and SF itself,
- self-consistent determination of SF efficiency.

Our aim was to demonstrate the dynamical sequences produced by this modified approach. We succeeded in obtaining, with reasonable accuracy, typical spiral and elliptical galaxies. Gas and stellar content variation, their distribution over the galaxy disk and the main dynamical properties of disk and halo components are also reproduced satisfactorily.

2 Initial conditions

As the initial protogalaxy model, we take a rotating, overdense homogeneous sphere of gas and dark matter of radius $R = 100$ *kpc* relevant for CDM–scenario. The mass of the baryonic matter is taken to be $M_{gas} = 10^{11}\ M_{\odot}$ and the mass of the dark component is set equal to $M_{DM} = 10^{12}\ M_{\odot}$.

The SPH calculations are carried out for $N_{gas} = 515$ gas particles and $N_{DM} = 515$ dark matter particles. The smoothing lengths are chosen in such a way that each gas particle has $N_B = 5$ neighbours within h_i and the minimum h_i is set equal to 1 *kpc*. We place the centers of particles initially on a homogeneous grid inside a sphere of radius R. The Courant's number C_n determining time step δt_i (see Berczik & Kolesnik 1993) is set equal to 0.1.

The initial velocity field is defined through the initial angular velocity $\mathbf{\Omega}_0(x, y, z)$ and constant of Hubble flow $H_0 = 75\ km/s \cdot Mpc^{-1}$:

$$\mathbf{V}_0(x, y, z) = [\mathbf{\Omega}_0(x, y, z) \times \mathbf{r}] + H_0 \cdot \mathbf{r}. \tag{1}$$

The initial angular velocity for the first model is $\mathbf{\Omega}_0 = (0,\ 0,\ 0.3) \cdot \Omega_{cir}$ and $\mathbf{\Omega}_0 = (0,\ 0,\ 0.03) \cdot \Omega_{cir}$ for the second model. Here the $\Omega_{cir} = V_{cir}/R$ and $V_{cir} = \sqrt{G \cdot (M_{gas} + M_{DM})/R}$.

The spin parameter of such rotating system is defined (Peebles 1969) as:

$$\lambda = \mid \mathbf{L}_0 \mid \cdot \sqrt{\mid E_0^{gr} \mid} / (G \cdot (M_{gas} + M_{DM})^{5/2}). \tag{2}$$

Here $\mathbf{L}_0$ is the total initial angular momentum and E_0^{gr} is the total initial gravitational energy of the protogalaxy. For the system, whose angular momentum is acquired through the tidal torque of the surrounding matter, the standard spin parameter (Zurek et al. 1988, Eisenstein & Loeb 1995) range between $\lambda \approx 0.01 \div 0.08$. In present work, we study the two rotating models with $\lambda \approx 0.08$, the "rapid" model, and $\lambda \approx 0.01$ is the "slow" model.

The initial temperature of the gas is set equal to $T_0 = 10^4\ K$. To follow its subsequent thermal behavior in numerical simulations we use the approximated form of standard cooling function for an optically thin plasma with a primordial composition in ionization equilibrium and set the absolute cutoff temperature to $10^4\ K$ according to Katz & Gunn (1991).

3 Star Formation in SPH

Provided that we are only concerned with the first order effects, we use the most reasonable simplified way of treating SF with SPH. We assume that each particle consists of the gas and star component, e.g., $m_i \equiv m_i^{gas} + m_i^*$. Initially for all particles $m_i^* \equiv 0$ (see also Mihos & Hernquist 1994, Berczik 1995).

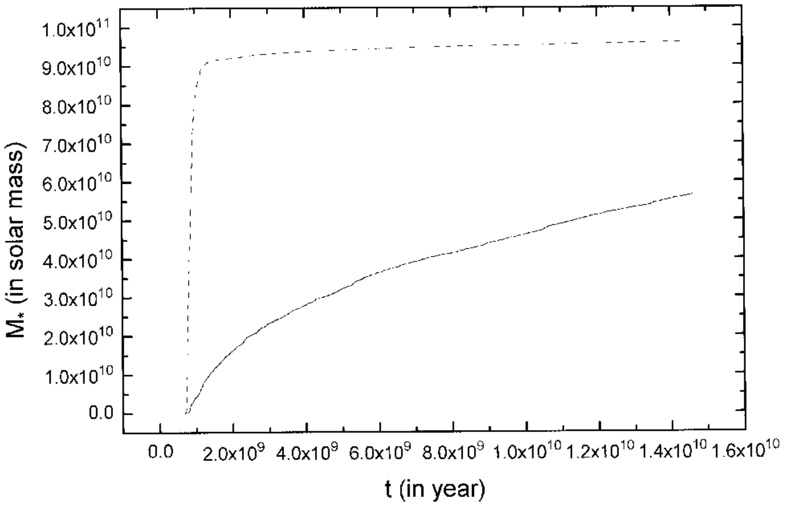

Figure 1: The evolution of galaxy total stellar mass $M_*(t)$ (mass in $M_\odot$, time in *year*). The solid line corresponds to the "rapid" model, the dashed line to the "slow" model.

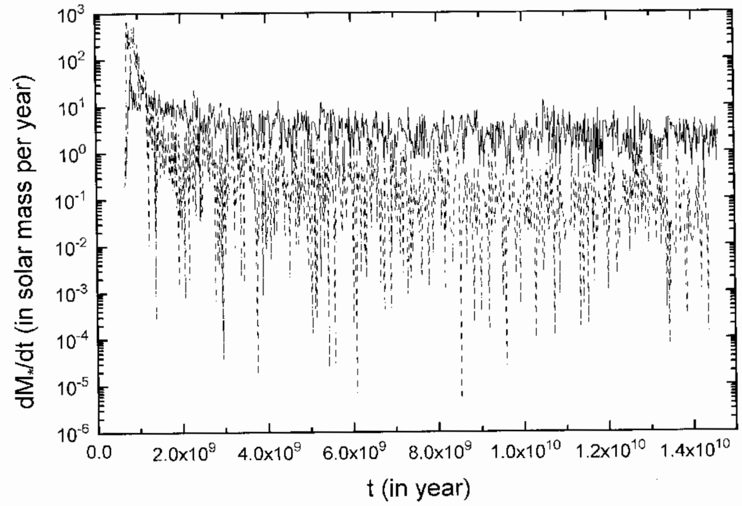

Figure 2: The evolution of the global star formation rate (SFR) $dM_*(t)/dt$ (SFR in $M_\odot/year$, time in *year*). The solid line corresponds to the "rapid" model, the dashed line to the "slow" model.

In the gas the SF can start if the absolute value of the particle's gravitational energy exceeds the sum of its thermal energy and energy of chaotic motions e.g., $\mid E_i^{gr} \mid \quad \geq E_i^{th} + E_i^{ch}$. We think that this condition is necessary. It seems reasonable that the chosen gas particle will produce stars only if the above condition holds over the time interval exceeding its free-fall time $t_{ff} = \sqrt{3 \cdot \pi / 32 \cdot G \cdot \rho}$. Using it we, therefore, exclude transient structures, that are destroyed by the tidal action of surrounding matter.

When the collapsing particle i has been defined we update the m_i^{gas} and m_i^* (see e.g., Friedli & Benz 1995) accounting for that ϵ fraction of gas is converted into stars according to the initial mass function (IMF). In our calculation we define ϵ as:

$$\epsilon = 1 - (E_i^{th} + E_i^{ch}) / \mid E_i^{gr} \mid . \tag{3}$$

Following Katz (1992), to treat the ISM response on SN explosions we assume that the explosion energy is converted totally into the thermal energy of the gas particle i if (see Friedli & Benz 1995):

$$\Delta E_i^{SN} = R^{SN} \cdot \epsilon \cdot m_i^{gas} \cdot \Delta E_{SN}^{mean}. \tag{4}$$

Here the R^{SN} is the number of SN created per unit mass of stars formed. The ΔE_{SN}^{mean} is the mean energy produced by one SNII. In our calculations we use the values: $\Delta E_{SN}^{mean} = 10^{44}\ J$ and $R^{SN} \approx 0.002\ M_\odot^{-1}$ (see Friedli & Benz 1995).

Therefore the updating specific internal energy of i-th particle after SN is:

$$u_i := u_i + \frac{\Delta E_i^{SN}}{m_i^{gas}} = u_i + \frac{R^{SN} \cdot \epsilon \cdot \Delta E_{SN}^{mean}}{(1 - \epsilon)}. \tag{5}$$

4 Conclusion

Using the modified star formation algorithm we were able to follow the process of galaxy formation and its subsequent evolution over the period about $15 \cdot 10^9$ *year*.

In the case of the "rapid" model, our final configuration is a three-component system that resembles a typical spiral galaxy: a disk consisting of stars and gas, a spheroidal component consisting of stars, and an extended dark matter halo. By chance, in spite of being richer in gaseous content our final model shows a close resemblance to the characteristics of our own Galaxy, that provides an independent checking of model assumptions.

In the case of the "slow" model, we have the structure typical of elliptical galaxy: the triaxial galaxy made of stars and the extended dark halo.

Figure 1 shows the variation of the total stellar mass $M_*(t)$ with time and Figure 2 shows the time variation of the global star formation rate (SFR) $dM_*(t)/dt$ for both models.

Finally we summarize the main results of this work.

- We propose a new SF algorithm for SPH modelling which avoids the problem of gas consumption typical of previous simulations.
- By numerical simulation of the protogalaxy over the period of $15 \cdot 10^9$ *years* we obtain a system of stars and gas with typical characteristics of spiral and elliptical galaxies. It is to be noted that the main dynamical parameter which determines the type of the forming galaxy is its initial angular momentum.

Acknowledgements

Peter Berczik would like to acknowledge the International Science Foundation for financial support of this work under grants No. UC 9000 and UC 9200.

References

Berczik P., Kolesnik I.G., 1993, Kinematika i Fizika Nebesnykh Tel 9, No. 2, 3

Berczik P., 1995, in COBE Workshop Proceedings, Ed. E. Dwek, American Institute of Physics Conference Proceedings 348, 174

Eisenstein D.J., Loeb A., 1995, ApJ 439, 520

Friedli D., Benz W., 1995, A&A 301, 649

Katz N., 1992, ApJ 391, 502

Katz N., Gunn J.E., 1991, ApJ 377, 365

Mihos J.C., Hernquist L., 1994, ApJ 437, 611

Peebles P.J.E., 1969, A&A 155, 393

Zurek W.H., Quinn P.J., Salmon J.K., 1988, ApJ 330, 519

SCALE HEIGHT OF MIRA VARIABLES

Zs. Berend[1], J. Hron[2], L.G. Balázs[3], F. Kerschbaum[2]
[1]Loránd Eötvös University, Dept. of Astronomy,
Ludovika tér 2., H-1083 Budapest, Hungary
[2]Institut für Astronomie, Universität Wien
Türkenschanzstr. 17., A-1180 Wien, Austria
[3]Konkoly Observatory, P. O. Box 67.,
H-1525 Budapest XII., Hungary

Abstract

We estimated the scale height of intermediate and short period Miras making use of the maximum likelihood method. The available sample contains 1394 Mira variables. We divided these variables according to their periods. Our selection criterion was: $|b| > 30^0$ because the interstellar absorption is practically negligible in this region at $\lambda = 12\ \mu m$. 85 intermediate period and 140 short period Miras have been left after the selection, their estimated scale heights are 260 pc and 590 pc respectively.

1 Introduction

Miras are pulsating red giants of high luminosity, lying on the asymptotic giant branch of the H-R diagram. In this phase of evolution they are characterized by heavy mass loss ejecting significant amount of dust into the interstellar medium.

It would be interesting to know how much interstellar dust comes from such long period variables. A good testing of this idea would be to compare the distribution of interstellar dust with that of Miras in the Galactic disk. If they correlate with each other, then these variable stars may give a significant contribution to the production of interstellar dust, if they do not, then one has to consider other processes responsible for it.

2 Discussion

Assuming an exponential distribution for the spatial density knowledge of the scale height of the population is nessecary in order to know the distribution of the given population. We have elaborated a procedure for the estimation of scale height based on the maximum likelihood method.

Let us consider the following function:

$$L = \tilde{A}(m_1, l_1, b_1; z_0)\tilde{A}(m_2, l_2, b_2; z_0)\ldots\tilde{A}(m_n, l_n, b_n; z_0), \tag{1}$$

where $\tilde{A}$ is the spatial density function of stars depending on distance and direction referring to a given spectral type, m_i, l_i, b_i are the apparent magnitude and galactic coordinates of stars of the sample and z_0 is the exponential scale height of the population, and the unknown parameter of the likelihood function.

This function takes its maximum at some $\tilde{z}_0 = \tilde{z}_0(m_i, l_i, b_i)$. This $\tilde{z}_0$ value is considered to be the estimation of the real scale height value. The likelihood function (1) gives the probability density of obtaining the available sample in the course of the sampling of $\tilde{A}(m, l, b; z_0)$. This means, that the z_0 value is estimated by that special $\tilde{z}_0$ value, which if it were the real value of our parameter, then exactly the given sample would be the most likely one among the possible samples of n elements.

If $\tilde{z}_0$ is the maximum likelihood estimation of the z_0 parameter, then asymptotically

$$2(L_{max} - L_0) \approx \chi^2 ,$$

where L_{max} is the maximum of the likelihood function (1), and L_0 is the value taken at the real parameter, and χ^2 has the degree of freedom of the number of parameters estimated. The 1 σ confidence interval of the estimated parameters can be obtained by subtracting 0.5 from the likelihood function at maximum and drawing a horizontal line at that point (see Figure 2a,b). The two extremities of the confidence area will be where this line intersects the curve. This value can be reduced by increasing the number of elements of the sample.

We have written a programme estimating scale height making use of the outlined process. Firstly we tested the programme with simulated data. We generated the samples by Monte Carlo method, and the scale heights estimated were all consistent with the values used for simulation within 1 σ.

We tested the method also with genuine data. The available sample contains the periods, the galactic coordinates and the 12 μm fluxes of 1394 Miras. The method needs apparent magnitudes, therefore we converted the 12 μm fluxes into magnitudes (Rucinski, 1985).

Table 1:

Period (day)	*Number of Stars*
P > 400	190
300 ≤ P ≤ 400	471
P < 300	733

The distribution of these variables in the galactic coordinate system is shown in Figure 1a. Miras can be classified into populations according to their periods, and each population represents a different subsystem of the Galactic disk. We separated the variables in the sample into three groups: long, intermediate and short period Miras (see Table 1). The long and intermediate period Miras belong to the so-called “thin disk” and have a smaller scale height than the short period ones, which populate the “thick disk” (Gilmore & Reid 1983).

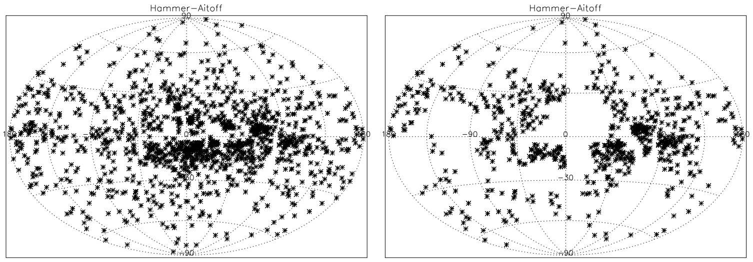

Figure 1: a) 1394 Mira variables b) 733 short period Mira variables

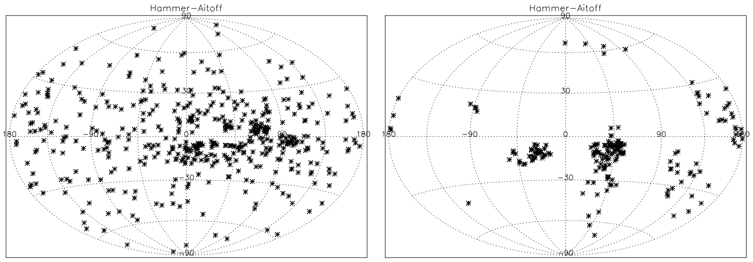

Figure 1: c) 471 intermediate period Mira variables d) 190 long period Mira variables

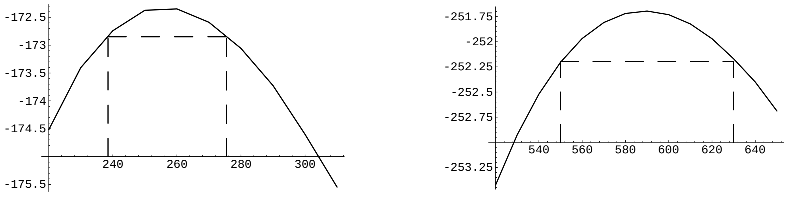

Figure 2: The likelihood functions
a) intermediate period Miras b) short period Miras

Examining the distribution of the 3 subpopulations (see Figure 1b,c,d) we recognized that the sample consisting of long period Miras is extremely incomplete and shows a patchy surface distribution. That is why subsequently we were dealing only with the other two subpopulations. Another selection criterion, *viz.* $|b| > 30^0$ is necessary because the interstellar absorption is difficult to estimate at low latitudes, but we may assume that it is negligible in this region at $\lambda = 12\,\mu m$. 85 intermediate period and 140 short period Miras have been left after the selections. It is hard to estimate the completeness of the sample, since it is an unknown function of the direction. For the calculation of the maximum of the likelihood functions we used numerical methods. We increased the z_0

parameter by 10 pc from a chosen initial value, and we calculated its likelihood function value at every step with numerical integration. The point at which the value of the likelihood function is the highest is considered to be the estimated scale height of the given population. The likelihood functions obtained by this method are shown in Figure 2a,b. The regions surrounded by dashed lines represent the 1 σ confidence intervals. The resulting scale height values are shown in Table 2. These results correspond within 1 σ with the values obtained by Jura & Kleinmann (1992) by means of other methods.

Table 2: Results

Type	*Scale Height (pc)*
short period Miras	590
intermediate period Miras	260

It is known from the literature that the scale height of the interstellar dust is approximately 100 pc. This shows, that there is no direct correlation between the two distributions.

Acknowledgements

This work was partly financed by the project No.49 of the Austrian–Hungarian Technical & Scientific cooperation.

References

Gilmore, G. & Reid, N. 1983, MNRAS 202, 1025

Jura, M. & Kleinmann, S. G. 1992, ApJS 79, 105

Rucinski, S. M. 1985, AJ 90, 2321

TOWARDS THE IDENTIFICATION OF THE CIRCUMSTELLAR DUST FEATURE AT 13μm

C. Kömpe[1], J. Gürtler[1], B. Begemann[2], J. Dorschner[2]
Th. Henning[2], H. Mutschke[2], and R. Nass[3]
[1] Universitäts-Sternwarte, Schillergäßchen 2, D-07745 Jena, Germany
[2] MPG-Arbeitsgruppe “Staub in Sternentstehungsgebieten”
Schillergäßchen 3, D-07745 Jena, Germany
[3] Institut für Neue Materialien, Im Stadtwald, D-66123 Saarbrücken, Germany

Abstract

The IRAS LRS data of many O-rich evolved stars show an emission feature at 13 μm. Al_2O_3 has been proposed in the literature as the carrier of this band. We compared the average profile from 51 objects with profiles computed from laboratory data of amorphous and crystalline Al_2O_3. We found that (1) the 13 μm band could not be fitted by amorphous Al_2O_3, (2) the 13 μm band could probably be fitted by a suitable distribution of spherical and ellipsoidal grains of crystalline α-Al_2O_3, and (3) the strength of the 10-μm silicate feature correlates well with the strength of the 13 μm feature making silicate a possible carrier of this band.

1 Introduction

The infrared spectra of many evolved stars with oxygen-rich envelopes show an emission band at 13 μm close to the silicate feature at 10 μm. This 13 μm feature can be clearly seen in the IRAS LRS data; the spectrum of the variable star V Eri is shown in Figure 1 as an example. However, the carrier of this feature has not yet been identified. From the absence of the 13 μm band in carbon-rich envelopes, one may conclude that the feature could be produced by vibrations of an oxygen bond, possibly Al–O. From several Al-containing compounds that have been suggested so far, only Al_2O_3 has received some attention in the literature; we are therefore concentrating on this compound. From condensation theory it is expected that Al_2O_3 particles that form in circumstellar envelopes should have an amorphous rather than a crystalline structure. The main goal of this study is thus to investigate if amorphous Al_2O_3 could be the carrier of the 13 μm emission band by comparing an observational profile with theoretical spectra based on laboratory data. We will also discuss silicates as an alternative carrier of the 13 μm band. A more detailed account of this study will be published elsewhere (Begemann et al. 1997).

2 The observational 13 μm band profile

We have used the IRAS LRS database that provides many spectra of evolved stars showing the 13 μm band to derive an average feature (see Figure 1). First,

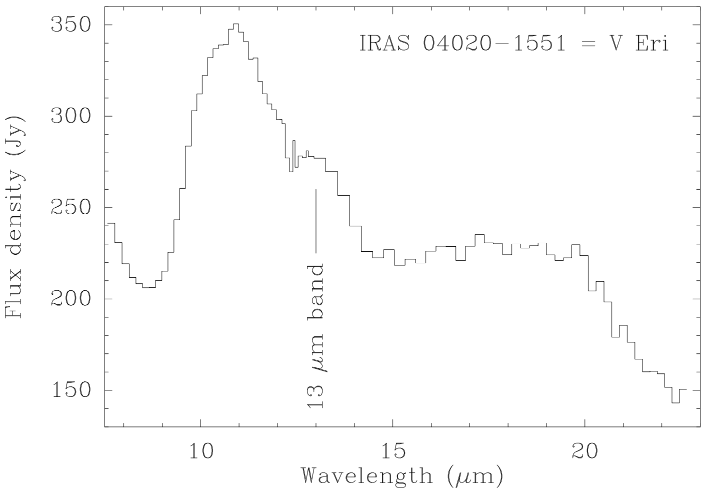

Figure 1: The 13 μm feature is illustrated by the IRAS Low Resolution Spectrum (LRS) of the variable star V Eri. This source is included in the sample of 51 objects used in our study.

we selected all those spectra from the IRAS LRS catalogue which are likely to show the 10-μm feature in emission according to the IRAS spectral classification and which have a flux density $\geq$ 100 Jy at 12 μm. From these, we choose 51 spectra having a distinct 13 μm feature suitable for extraction from the underlying emission. The 13 μm band was then extracted from all spectra by fitting a polynomial to the underlying emission and an average profile was calculated. The average 13 μm band is shown in Figure 2. Its shape could be fitted quite well by a Lorentz profile (not shown here) typical of bands in solids.

2.1 The case for Al_2O_3

Theoretical profiles of the 13 μm band are obtained by Mie calculations using appropriate optical constants of the dust grain material. In the case of Al_2O_3, we have considered two types of material: amorphous and crystalline Al_2O_3.

2.1.1 Amorphous Al_2O_3

The optical constants of amorphous Al_2O_3 were determined in our laboratory. In order to do this, samples of amorphous Al_2O_3 were prepared by a sol-gel technique. The amorphous nature of the Al_2O_3 compound was checked by X-ray and nuclear magnetic resonance (NMR) spectroscopy. Finally, the optical constants were derived from infrared transmission spectra using effective medium theory. The theoretical profile calculated using the optical constants is shown in Figure 2. The comparison of the observational and theoretical profiles clearly show that their peak positions do not coincide at all. One thus has to conclude that amorphous Al_2O_3 cannot be the carrier of the 13 μm band.

2.1.2 Crystalline Al_2O_3

In this case, the optical constants of α-Al_2O_3 were taken from the literature (Barker 1963). Theoretical profiles were calculated for two grain shapes: spherical grains and a continuous distribution of ellipsoids (CDE); the profiles are shown in Figure 2. The positions of the theoretical profiles coincide quite well with that of the observational profile, but not their widths. However, we believe that a suitable grain shape distribution combineing spherical and ellipsoidal grains could also give the observational width. α-Al_2O_3 should therefore be considered a good candidate for the carrier of the 13 μm band.

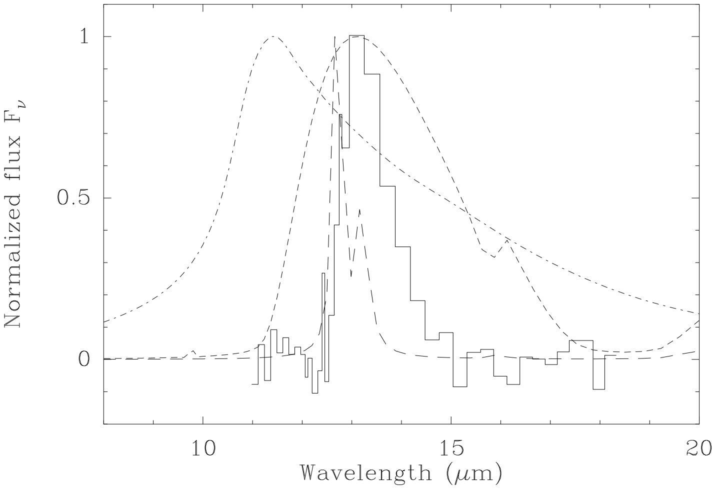

Figure 2: Comparison of the average 13 μm profile (solid line) with the results of theoretical Mie calculations based on the optical data of amorphous Al_2O_3 (dash-dotted line) and those of α-Al_2O_3 for spherical grains (long dashes) and for a continuous distribution of ellipsoids (short dashes).

2.2 The case for silicates

It has been suggested in the literature that the 13 μm feature could also be related to silicates. Vardya et al. (1986) are the first who attributed this band to an "Al/Ca silicate". In this silicate, Si is partially substituted by Al, and vibrations of Al–O bonds are thought to produce the 13 μm feature. If the observed 13 μm band is indeed due to vibrations within the silicate structure, then the strength of this feature is expected to correlate with that of the well known 10-μm silicate band. We have plotted these band strengths against each other and found indeed a good correlation (Figure 3). A natural explanation for this correlation is the assumption of a silicate origin of the 13 μm band.

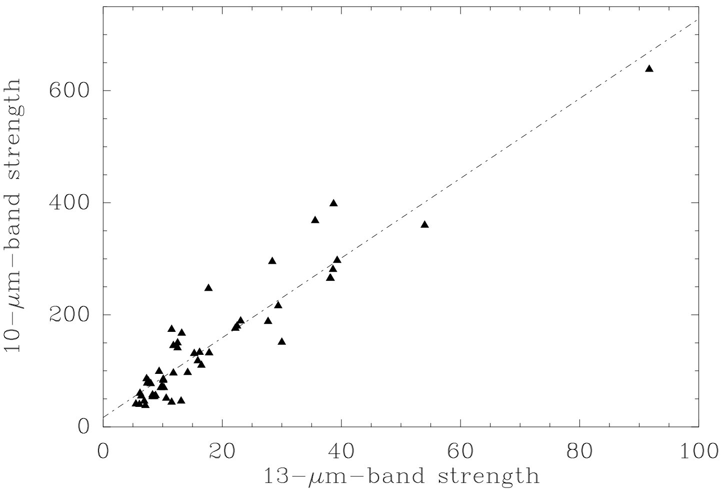

Figure 3: Correlation of the strength of the silicate dust feature at 10 μm and that of the 13 μm feature. Shown are the data (triangles) of the 51 sources of our sample and a least squares line fit.

3 Summary

The main goal of this study was to investigate if amorphous Al_2O_3 could be the origin of the feature at 13 μm seen in the infrared spectra of many evolved stars. The identification with Al_2O_3 had been suggested in the literature, and condensation theory indicates that it should be amorphous rather than crystalline. We determined an average profile of the 13 μm band from the IRAS LRS data of 51 evolved stars and compared this observational profile with a theoretical profile based on the optical constants of amorphous Al_2O_3. Samples of this material were prepared in our laboratory and the optical constants determined. However, the comparison of the observational and the theoretical profiles rules amorphous Al_2O_3 as the carrier of the 13 μm band out. In addition, we have done a similar comparison for crystalline α-Al_2O_3 using optical constants from the literature. In this case, observation and theory are compatible if one assumes a suitable distribution of the grain shapes. Another important result is that the 13 μm feature might also be identified with silicate. This is supported by our finding that the strengths of the 10 μm silicate band and that of the 13 μm feature correlate quite well. We thus end this study with two possible carriers of the 13 μm band: crystalline α-Al_2O_3 and silicate.

References

Barker Jr., A. S. 1963, Phys. Rev. 132, 1474

Begemann, B. et al. 1997, ApJ 476, 199

Vardya, M.S., de Jong, T., Willems, F. J. 1986, ApJ 304, L29

MASS-LOADED MODELS OF ULTRACOMPACT H II REGIONS

M.P. Redman[1], R.J.R. Williams[1,2] and J.E. Dyson[2]
[1]Department of Physics and Astronomy
University of Manchester, Manchester M13 9PL, UK
[2]Department of Physics and Astronomy
University of Leeds, Leeds LS2 9JT, UK

Abstract

Recent observations of the ultracompact H II regions generated by newly formed massive stars show an extremely complicated local environment. We have proposed that a significant fraction of ultracompact H II regions are the result of the interaction of the wind and ionizing radiation from a young massive star with the clumpy molecular cloud gas in its neighbourhood. Mass loss from the neutral clumps allows the compact nebulæ to be long-lived. Simple spatial distributions of the clumps within the ionized region allow the occurrence of subsonic and supersonic flows, with shocks or smooth transitions between them. Many of the commonest observed morphologies for these objects can be explained by these models. In particular, cometary morphologies can be reproduced by a gradient in the number density of mass loading centres across the region, as would be expected towards the edge of a dense molecular core.

1 Introduction

Surveys of ultracompact H II regions (UCH II R) in the radio have led to the suggestion that the ionized gas in these objects usually has one of a few simple morphologies (Kurtz et al. 1994; Wood and Churchwell 1989). These are cometary, core-halo, shell, irregular/multiple peaked and spherical/unresolved. Most recent theoretical and observational effort has been directed towards the cometary class. Gaume et al. (1995) have produced high resolution observations that show that some cometary regions are actually better described as 'arc-like' because the faint tails hook back around the nebula. They are more akin to the shell types than regions such as G34.3 + 0.2, the prototypical cometary UCH II R.

If UCH II R are small 'classical' H II regions, one expects them to expand quickly out of the ultracompact phase. However, the number of UCH II R counted in the surveys is far higher than would be expected if this were correct. Any description of UCH II R must be able to address this 'lifetime paradox' (Wood and Churchwell 1989).

We have modelled UCH II R in terms of the interaction between a massive star and neutral clumps in its immediate environment. We show here how this model can be used to explain the longevity of UCH II R and reproduce many of the morphologies described above.

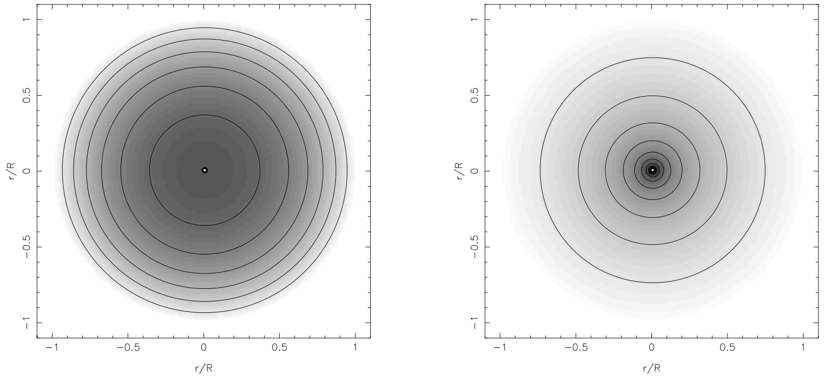

Figure 1: Emission measure plots for subsonic flows with constant $\dot{q}$, (left) and $\dot{q} \propto r^{-3/2}$ (right). The star is at the origin.

2 Model

The clumpy nature of molecular clouds on all length scales is well established. Recent high resolution work is beginning to reveal an extremely complicated local environment in the vicinity of UCHIIR and models that do not address this are beginning to look inappropriate.

In a series of papers (Dyson, Williams and Redman 1995; Redman, Williams and Dyson 1996; Williams, Dyson and Redman 1996) we have developed a model where the wind and UV radiation field from a massive star interact with neutral clumps in the ionized gas to set up a quasi-steady mass loaded flow. Crucially, the region is no longer bounded by an ionization front (IF) but by a recombination front (RF). The size of the region is no longer directly related to its age; rather it is a measure of the degree of mass loading within the region – the region will remain compact so long as there are sufficiently many clumps.

We assume smoothly distributed mass addition and solve the mass and momentum equations for different spatial distributions of clumps.

3 Results

Where mass-loading dominates a weak stellar wind (e.g. for B stars), the wind shocks close to the star and the flow remains subsonic to the recombination front (although it can be transonic here). In Figure 1 emission measure plots are shown for constant mass loading rate $\dot{q}$ and for $\dot{q} \propto r^{-3/2}$. Uniform and centre-brightened morphologies are produced. The line profiles are not shown as they are observationally indistinguishable from a thermally broadened Gaussian.

The powerful wind of an O star can create a flow that, although deceler-

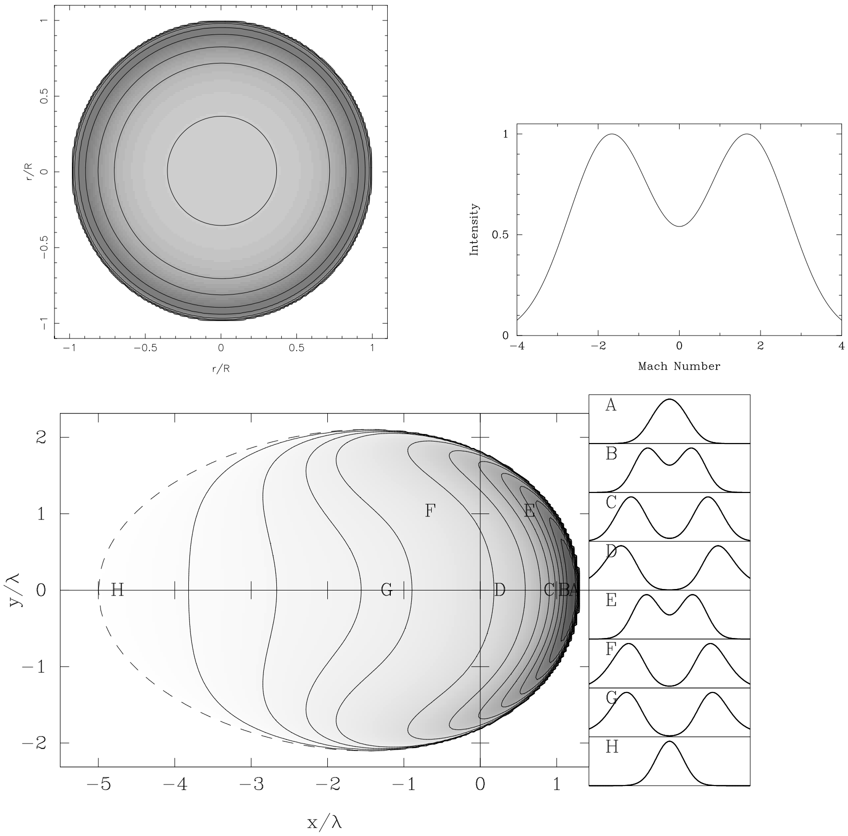

Figure 2: Supersonic flows. In the upper-left panel the emission measure image for constant $\dot{q}$ is shown, and in the upper-right a line profile from a line of sight close to the centre. In the lower panel, $\dot{q}$ increases from left to right. The emission measure image is shown with line profiles given for labelled points.

ating, remains supersonic out to the recombination front. Two situations are depicted in Figure 2. For constant $\dot{q}$ the shell morphologies are reproduced. If $\dot{q}$ increases in the positive x direction, as might be found near to a dense molecular core, a cometary morphology is produced. If $\dot{q}$ increases more slowly, arc-like shapes are also found. In both cases, for lines of sight that pass close to the central star, broad double-peaked line profiles result. Furthermore, the flow recombines and exits at about Mach 2 so high speed HI outflows should be seen.

4 Conclusions

We have shown that by considering the interaction of a massive star with its clumpy surroundings, the lifetime problem can be accounted for and many of the observed morphologies reproduced (the irregular/multiple peaked UCHIIR are probably due to emission from individual clumps). Lizano et al. (1996) have also investigated a mass loaded model. Their approach is different in that it uses a specific model for the globules and has a mass injection rate which is a function of time.

By treating the very special case of self-gravitating isothermal clumps (c.f. Kahn 1969), the space density of clumps that may be required is $\sim 10^5 - 10^6 \mathrm{pc}^{-3}$ (Dyson et al. 1995). This however is very uncertain and more realistic models of clumps are required.

A detailed comparison of these models with observational data is now in progress.

References

Dyson J. E., Williams R. J. R., Redman M. P., 1995, MNRAS 277, 700

Gaume R. A., Claussen M. J., De Pree C. G., Goss W. M., Mehringer D. M., 1995, ApJ 449, 663

Kahn F. D., 1969, Physica 41, 172

Kurtz S., Churchwell E., Wood D. O. S., 1994, ApJS 91, 659

Lizano S., Cantó J., Garay G., Hollenbach D. 1996, ApJ 468, 739

Redman M. P., Williams R. J. R., Dyson J. E., 1996, MNRAS 280, 661

Williams R. J. R., Dyson J. E., Redman M. P., 1996, MNRAS 280, 667

Wood D. O. S., Churchwell E., 1989, ApJS 69, 831

Pre–Main Sequence stars

INFALL IN YOUNG STARS

Antonella Natta
Osservatorio Astrofisico di Arcetri
Largo Fermi 5, I-50125 Firenze, Italy

Abstract

I discuss in this paper three examples of gas infall in pre-main sequence stars and in very young main-sequence stars. Although the fraction of mass accreted by the star in these later phases is small in comparison to earlier phases of star formation, by investigating the origin and properties of the infalling matter we can address a number of problems, from the properties of accretion disks to the early phases of the formation of solar systems.

1 Introduction

Residual infall of circumstellar matter onto the central star is by now a well known phenomenon in a variety of young stars. The rate of accretion is much smaller than in the earliest phases of star formation, by at least two orders of magnitude. Although the fraction of mass accreted by the star in these later phases is small, by investigating the origin and properties of the infalling matter we can address a number of interesting problems, from the properties of accretion disks to the early phases of the formation of solar systems.

In this paper I will discuss three examples. In all cases, the evidence of infalling matter comes from spectroscopy, i.e. from observations of red-shifted absorption components in various lines of hydrogen and metals. The first example is that of T Tauri stars (TTS), where the infalling matter is interpreted as coming from the circumstellar accretion disk. The second is that of the main-sequence star β Pic, where the infalling matter results from the evaporation of star-grazing bodies, planetesimals or proto-comets. The third example is that of a special group of pre-main sequence stars of intermediate mass, called UX Ori-type stars, which appear to be in an intermediate state between the previous two.

2 T Tauri stars

TTS are known to show red-shifted absorption components in various lines of the Balmer series and in some metal resonance lines, for example the D lines of Na I at 5900 Å. Recent studies (Edwards 1995) estimate that they are seen in about 60% of classical TTS. Very often, blue-shifted and red-shifted absorption are observed simultaneously and at similar velocities, of the order of 100-200 km s^{-1} (see, for example, Krautter et al. 1990).

These observations have recently found a natural explanation in the framework of magnetospheric accretion models. These models assume that the central star is surrounded by an accretion disk. If the star has a strong magnetic field (of the order of 1000 gauss), the inner parts of the disk (approximately up to the corotation radius, i.e. few stellar radii) are disrupted; some fraction of the matter accreting along the disk will reach the stellar surface along the magnetic field lines, while the rest will be ejected from the system (Camenzind 1990; Königl 1991; Shu et al. 1994; Najita and Shu 1994; Gullbring 1994). These models follow with some modifications the original work of Gosh and Lamb (1979a,b) on accretion in white dwarfs.

The models developed by Shu and collaborators make some quantitative predictions, that can be compared with the observations. The first is the simultaneous occurrence of infall and outflow, with rates $\dot{M}_w \sim 0.1\dot{M}_{ac}$, where $\dot{M}_w$ is the rate of mass-loss and $\dot{M}_{ac}$ the mass accretion rate in the disk. Estimates of these two quantities have been obtained by Hartigan et al. (1995). Both suffer from large uncertainties and show a spread over at least three orders of magnitude, but the distribution of the ratio $\dot{M}_w/\dot{M}_{ac}$ clearly peaks at values of order 0.01 (cf. Fig.1). Thus, there is here a discrepancy between models and observations which deserves further investigation.

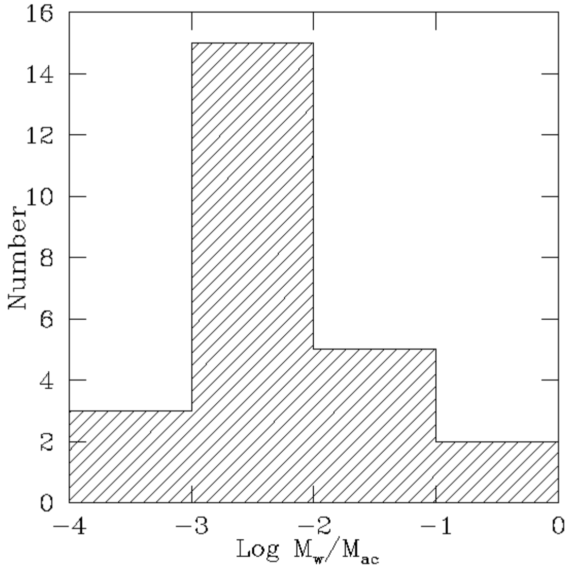

Figure 1: Distribution of the ratio $\dot{M}_w/\dot{M}_{ac}$ in the sample of 29 TTS studied by Hartigan et al. (1995).

Another general prediction of magnetospheric accretion models is the truncation of the inner disk at a few stellar radii. This affects the spectral energy distribution of the system in the near infrared. Kenyon et al. (1996) show that the expected pattern is consistent with the observations.

Hartmann et al. (1994) claim that most of the emission lines in TTS form in the infalling gas and show that the observed profiles of the Balmer lines are in fact roughly consistent with this hypothesis. In this view, the outflow is seen only in the blue-shifted, rather narrow and often not very deep absorption components observed in a large number of TTS (Kuhi 1978). These models assume an *ad hoc* temperature profile in the gas columns, which, however, seems reasonable when compared to the results of temperature calculations in magnetic accretion funnels by Martin (1996). Variability studies of H_α (Johns & Basri 1995a,b) confirm that several different regions contribute to this line. In one case, SU Aur (see also Petrov et al. 1996), the observed variability pattern is roughly consistent with magnetospheric accretion models, but in general it is much more complex.

Studies of the veiling and of TTS photometric variability, which is in this scenario attributed to the emission of hot spots at the base of the infalling gas columns, appear to be consistent with the models (Gullbring 1994).

Finally, in these models the star is strongly coupled, via its magnetic field, to the disk. The effect of this coupling is to impede the spin up of the contracting star. This mechanism can explain the double-peaked distribution of the angular velocity of TTS (Edwards et al. 1994; Bouvier et al. 1993), which is otherwise difficult to interpret.

In summary, magnetospheric accretion models appear a very promising framework for the understanding of the activity of TTS and of a number of their properties. A further check of their reality requires a measurement of the stellar magnetic field. This is a formidable problem, and only one measure of the field in a weak line TTS is at present available (Basri et al. 1992). In this one case, $B \sim 1000$ gauss.

3 Infall in a young main-sequence star: β Pic

β Pic is a young main-sequence star of about 1.8 $M_\odot$ (spectral type A5), very near to us (D=18 pc). It has a circumstellar disk, which has been directly imaged at various wavelengths (Smith & Terrile 1984; Lagage & Pantin 1994) and which is responsible for the small infrared excess at wavelengths longer than about 8μm (Knacke et al. 1993). The disk has a surface brightness profile at 10μm which flattens toward the central star, suggesting that its inner parts have been cleared by the formation of a large planetary body (Lagage & Pantin 1994; see also Gillett 1986). The disk is very likely not the primary accretion disk which is associated with the earlier phases of star formation, but a secondary disk, formed by the disintegration of larger bodies, planetesimals or proto-comets (Backman & Paresce 1993).

Several metal lines (but not the hydrogen lines, which have photospheric profiles) show red-shifted absorption features. Their velocities range from ~40 to ~200 km s^{-1}, and they are highly variable, with typical time scales of few hours or a day. This phenomenon is observed in low excitation lines, such as the

H and K lines of Ca II, but also in some higher ionization species, such as C IV and Al III. This phenomenology has been studied in great detail by Beust and collaborators (see, for example, Beust et al. 1994 and references therein). Their interpretation is that the absorption is produced in gaseous halos formed by the evaporation of solid bodies (planetesimals or proto-comets) on star-grazing orbits. In order to explain the frequency and intensity of the absorption features, one has to assume that swarms of such bodies (more than 100 yr^{-1} with size larger than 1 km) are on star-grazing orbits, due to the dynamical perturbing action of a much larger body, such as a massive planet.

At present, β Pic is probably the best example of a very young planetary system, and provides the best laboratory to test our ideas on the early stages of the solar system itself.

4 UX Ori-type stars: an intermediate case?

Stars in this group are probably relatively old pre-main sequence stars, which appear to be in a transition phase between accretion and full disruption and dissipation of their entire disks, an epoch in which planetary bodies are perhaps being formed. They are younger than β Pic, but probably older, in evolutionary terms, than classical TTS.

The prototype is the star UX Ori, with a spectral type of A2 and a mass of 3.3 $M_\odot$ (cf. Grinin et al. 1994; Grady et al. 1995). The stars in this group have spectral type in the range from A to G; they are characterized by large visual photometric variability, attributed to variable extinction by clouds of dust surrounding the star in a disk-like geometrical configuration (Grinin et al. 1991; Herbst et al. 1994) In general, these stars are not associated with optical nebulosities or large scale molecular emission, nor with IR companions, i.e., they have moved away from their parent molecular cloud. At the same time, UX Ori-type stars show some of the classical features of pre-main sequence stars, such as strong H_α in emission (Grinin & Rostopchina 1996) and large IR excess (they have all been detected by IRAS; Weintraub 1990), which has been interpreted as due to a circumstellar accretion disk (Hillenbrand et al. 1992). The disk masses, however, are quite small. Of a sample of about 30 UX Ori-type stars (selected from Herbst et al. 1994 and Grinin and Rostopchina 1996), 16 (mostly in Taurus and Chamaeleon) have been observed at 1.3 mm by various authors (Beckwith et al. 1990; Hillenbrand et al. 1992; Henning et al. 1993; Mannings 1994; Osterloh & Beckwith 1995); the derived masses are $< 0.02\ M_\odot$ in 12 out of 16 stars. Such values are significantly smaller than the median disk masses in Herbig AeBe stars and classical T Tauri stars (Hillenbrand et al. 1992; Osterloh & Beckwith 1995).

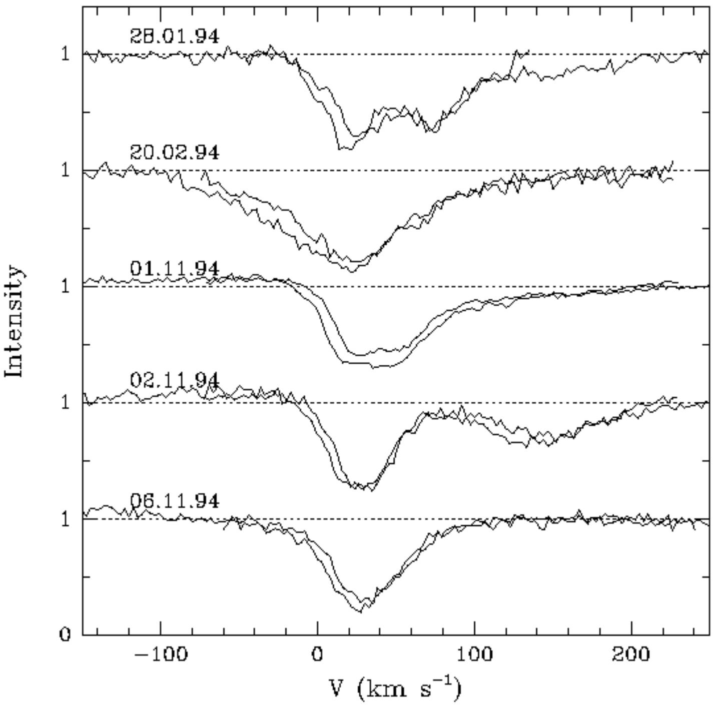

Figure 2: Na D line profiles for BF Ori at different epochs. The two components of the doublet have been overlapped and shown as a function of the velocity displacement from the line center. Note the red-shifted absorption components at epochs 28.01.94, with redshift ~80 km s^{-1}, and 02.11.94, with redshift ~140 km s^{-1}. From Grinin et al. (1996a).

Some UX Ori-type stars show evidence in their optical spectra of matter infalling into the star with high velocity ($\sim$ 100-200 km s^{-1}) (Grinin et al. 1994, 1996a; Grady et al. 1995). Fig. 2 shows, for example, a sequence of spectra of BF Ori in the region of the Na D lines. Sorelli et al. (1996) have studied the physical conditions required to produce a red-shifted absorption component similar to what is observed. The velocity shift of ~100-200 km s^{-1} indicates a formation region very close to the star (roughly <10 stellar radii), where Na, which has an ionization potential of only 5.14 eV, is very quickly ionized by the strong and hot stellar radiation field. They find that the redshifted absorption lines can only form in small (typical size $L \sim 10^{11}$ cm, about the stellar radius), dense, infalling gas clumps and consider two possibilities for their origin. The first is that, as in the magnetospheric accretion models of TTS, the absorption features form in columns of infalling gas. They find that the redshifted

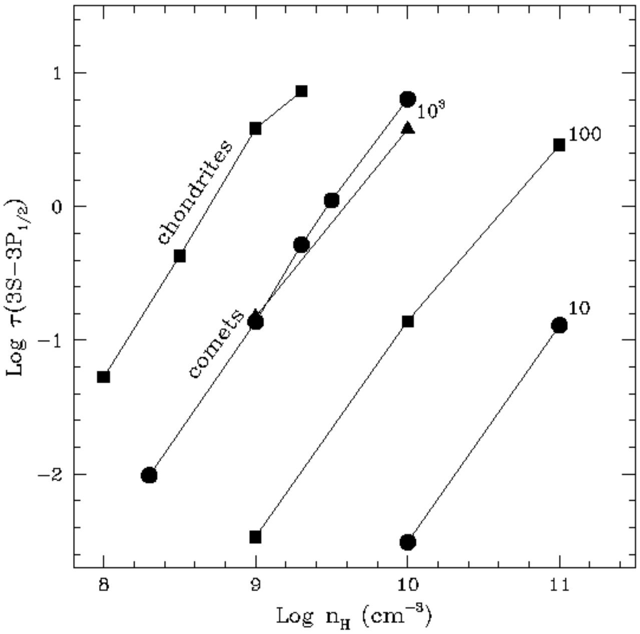

Figure 3: Optical depth in the stronger of the Na D lines as a function of the cloud density. Each curve is labelled with the metallicity index m. $m = 1$ indicates solar chemical composition; when $m > 1$, the abundance of all elements heavier than helium increases by m with respect to the solar values. In all cases the size of the cloud is 10^{11} cm and the distance from the star is $D = 10$ $R_\star$ (see Sorelli et al. (1996) for a complete description of the model).

absorption lines can only form in small (typical size $L \sim 10^{11}$ cm, about the stellar radius), dense, infalling gas clumps and consider two possibilities for their origin. The first is that, as in the magnetospheric accretion models of TTS, the absorption features form in columns of infalling gas. In this case, the gas chemical composition is solar and a clump density $n_H \gtrsim 3 \times 10^{12}$ cm^{-3} is required. These conditions can be produced at the base of a column of gas falling into the star from a circumstellar accretion disk along magnetic lines. In this case, an accretion rate $\dot{M}_{ac} \gtrsim 3 \times 10^{-7}$ $M_\odot$ yr^{-1} and a stellar magnetic field of about 600 gauss are required.

A second possibility is that, as in β Pic, the Na D red-shifted absorption features are produced by evaporating solid bodies. In this case, the chemical composition of the gas is very different from solar, highly enriched in metals and with very little residual hydrogen. Sorelli et al. find that, as the gas metallicity increases, less dense clouds are required to fit the Na D observations (cf. Fig. 3). In the extreme case of a gas cloud resulting from the evaporation of CIchondrite meteorites, it is $n_H \gtrsim 5 \times 10^8$ cm^{-3}, $L \sim 10^{11}$ cm. The mass of the cloud is therefore of the order of 10^{20} gr, and the parental body must have a radius of at least 20 km. The fragmentation and evaporation of such bodies, and the following dynamical evolution of the evaporated gas, have been discussed by Grinin et al. (1996b).

The lack of conclusive evidence on the evolutionary age of UX Ori-type stars requires further investigation, in particular more detailed studies of the properties of their circumstellar disks and of the region of formation of the double-peaked H_α which is commonly associated with these stars (Grinin & Rostopchina 1996).

References

Backman, D.E., & Paresce, F. 1993, in *Protostars and Planets III* ed. G. Levy and J. Lunine (Tucson: University of Arizona Press), p.1253

Basri, G., Marcy, G.W. & Valenti, J.A. 1992, ApJ, 390, 622

Beckwith, S.V.W., Sargent, A.I., Chini, R.S. & Güsten, R. 1990, AJ 99, 924

Beust, H., Vidal-Madjar, A., Ferlet, R. & Lagrange-Henry, A.M., 1994, Astr. Space Sci. 212, 147

Bouvier, J., Cabrit, S., Fernandez, M., Martin, E.L. & Matthews, J.M. 1993, A&A, 272, 176

Camenzind, M. 1990, Rev. in Mod. Astron. 3, 234

Edwards, S. 1995, Rev.Mex.A.A. (Serie de Conferencias), 1, 309

Edwards, S., Hartigan, P., Ghandour, L. & Andrulis, C. 1994, AJ, 108, 1056

Gillett, F.C. 1986, in *Light on Dark Matter*, ed. F.P. Israel, (Dordrecht: Reidel), p.61

Gosh, P. & Lamb, F.K. 1979a, ApJ, 232, 259

Gosh, P. & Lamb, F.K. 1979b, ApJ, 234, 296

Grady, C.A., Pèrez, M.R., Thé, P.S., Grinin, V.P., de Winter, D., Johnson, S.B. & Talavera, A. 1995, A&A, 302, 472

Grinin, V.P., Kiselev, N.N., Minikulov, N.Kh., Chernova, G.P. & Voshchinnikov, N.V. 1991, Ap. Sp. Sci., 186, 283

Grinin, V.P., Kozlova, O.V. & Rostopchina, A.N. 1996a, A&A, 309, 474

Grinin, V.P., Natta, A. & Tambovtseva, L.V. 1996b, A&A 313, 857

Grinin, V.P. & Rostopchina, A.N. 1996, Astron. Rep., 40, 171

Grinin, V.P., Thé, P.S., de Winter, D., Giampapa, M., Rostopchina, A.N., Tambovtseva, L.V., van den Ancker, M.E. 1994, A&A 292, 165

Gullbring, E. 1994, A&A 287, 131

Hartigan, P., Edwards, S. & Ghandour, L. 1995, ApJ 452, 736

Hartmann, L., Hewett, R. & Calvet, N. 1994, ApJ 426, 669

Henning, T., Pfau, W., Zinnecker, H. & Prusti, T. 1993, A&A 276, 129

Herbst, W., Herbst, D.K., Grossman, E.J. & Weinstein, D. 1994, AJ 108, 1906

Hillenbrand, L.A., Strom, S.E., Vrba, F.J. & Keene, J. 1992, ApJ 397, 613

Johns, C.M. & Basri, G. 1995a, AJ 109, 2800

Johns, C.M. & Basri, G. 1995b, ApJ 449, 341

Kenyon, S., Yi, I. & Hartmann, L. 1996, ApJ 462, 439

Knacke, R.F., Fajardo-Acosta, S.B., Telesco, C.M., Hackwell, J.A., Lynch, D.K. & Russell, R.W. 1993, ApJ 418, 440

Königl, A., 1991, ApJ 370, L39

Krautter, J., Appenzeller, I. & Jankovics, I. 1990, A&A 236, 416

Kuhi, L.V. 1978, in *Protostars and Planets I*, T. Gehrels (ed.), (Tucson: University of Arizona Press), p.708

Lagage, P.-O. & Pantin, E. 1994, Nature 369, 628

Mannings, V. 1994, MNRAS 271, 587

Martin, S.C. 1996, ApJ 470, 537

Najita, J. & Shu, F. 1994, ApJ, 429, 808

Osterloh, M. & Beckwith, S.V.W. 1995, ApJ, 439, 288

Petrov, P.P., Gullbring, E., Ilyin, I., Gahm, G.F., Tuominen, I., Hackman, T. & Lodén K. 1996, A&A 314, 821

Shu, F., Najita, J., Ostriker, E., Wilking, F., Ruden, S. & Lizano, S. 1994, ApJ, 429, 781

Smith, B.A. & Terrile, R. 1984, Science, 226, 1421

Sorelli, C., Grinin, V.P. & Natta, A. 1996, A&A, 309, 155

Weintraub, D.A. 1990, ApJS, 74, 575

UNIVERSALITY OF THE STELLAR INITIAL MASS FUNCTION

P. Padoan[1], Å.P. Nordlund[1,2] and B.J.T. Jones[3]
[1]Theoretical Astrophysics Center
Juliane Maries Vej 30, DK-2100 Copenhagen, Denmark
[2]Astronomical Observatory
Juliane Maries Vej 30, DK-2100 Copenhagen, Denmark
[3]Imperial College of Science, Technology and Medicine
Blackett Laboratory, Prince Consort Road, London SW7 2BZ, UK

Abstract

A model is developed for the origin of the stellar IMF, that contains a dependence on the average physical parameters (temperature, density, velocity dispersion) of the large scale site of star formation. The model is based on recent numerical experiments of highly supersonic random flows (Nordlund & Padoan 1996).

The statistical properties of the density field arising from the numerical experiment are in excellent agreement with those of the density field in dark clouds, as inferred from stellar extinction determinations, using a new method (Padoan, Jones & Nordlund 1996).

It is shown that a Miller–Scalo like IMF is naturally produced by the model for the typical physical conditions in molecular clouds. A more "massive" IMF in starbursts is also predicted.

1 Introduction

Star formation is a central problem of astrophysics and cosmology. It is very difficult to interpret observations of galaxies, or to predict their evolution, without any theoretical idea about the process of star formation.

Most theoretical attempts to predict the IMF have been based on the idea of gravitational fragmentation. This idea is a direct consequence of linear gravitational instability: in a system with very small density and velocity fluctuations, gravitational instability causes the collapse of structures larger than a critical mass, that is the mass for which the thermal energy of the gas is comparable with its gravitational energy. During the collapse, if cooling is efficient, the critical mass becomes smaller, and substructures can collapse inside the collapsing object.

The next level of complexity is to still maintain the idea of a critical mass for gravitational instability, but using a distribution of the values of the physical parameters for its definition. The distribution of the physical parameters should be as close as possible to the actual distribution in the star forming system, so that the complexity of the nonlinear velocity and density field is bypassed using a statistical approach.

A further step is that of arguing that several ways of injecting and transferring kinetic energy in star forming systems exist, like gravity, magnetic fields, fluid turbulence, supernovae and HII regions, winds from young stars, tidal fields, thermal and magnetic instabilities, galactic shear. All these sources of energy contribute to the generation of random motions, that, mediated by fluid turbulence, establish universal flow statistics.

When cooling is very efficient, the most important of such statistics is the density distribution. Once this is determined, the critical mass for gravitational instability can be defined along that distribution, resulting in a distribution of collapsing objects, or protostars (Padoan 1995).

In the present work, we make use of recent numerical and observational results that allow us to describe the density distribution in supersonic random flows (such as the ones in molecular clouds), and therefore to derive the mass distribution of protostars.

Almost all previous physical models for the origin of the stellar IMF are inconsistent with the presence of supersonic random flows in the star formation sites, which is well documented by molecular emission line observations, and must be responsible for the presence of a complex system of interacting isothermal shocks in the gas.

2 The density field in random supersonic flows

In this section we give a statistical description of the density field that emerges from randomly forced supersonic flows. Such motions are present in dark clouds, where stars are formed.

The statistical description is based on numerical experiments, but it is also confirmed by stellar extinction observations in dark clouds.

2.1 Random supersonic flows in numerical experiments

Nordlund and Padoan (1996) have recently discussed the importance of supersonic flows in shaping the density distribution in the cold interstellar medium (ISM).

They have run numerical simulations of isothermal flows randomly forced to high Mach numbers. Their experiments are meant to represent a fraction of a giant molecular cloud, where in fact such random supersonic motions are observed. Most details about the numerical code and the experiments are given in Nordlund & Padoan (1996); here we only summarize the main results.

The physical parameters of the simulated system are: $\sigma_v = 2.5km/s$, $T = 10K$ (therefore rms Mach number about 10), $M = 4000M_\odot$, $L = 6pc$, where L is the linear size of the periodic box.

It is found that the flow develops a complex system of interacting shocks, and these are able to generate very large density contrasts, up to 5 orders of magnitude, $\rho_{max}/\rho_{min} \approx 10^5$. In fact, most of the mass concentrates in a small fraction of the total volume of the simulation, with a very intermittent distribution. The probability density function of the density field is well approximated by a log-normal distribution:

$$p(lnx)dlnx = \frac{1}{(2\pi\sigma^2)^{1/2}} exp\left[-\frac{1}{2}\left(\frac{lnx - \overline{lnx}}{\sigma}\right)^2\right] dlnx \tag{1}$$

where x is the relative number density:

$$x = n/\overline{n} \tag{2}$$

and the standard deviation σ and the mean $\overline{lnx}$ are functions of the rms Mach number of the flow, $\mathcal{M}$:

$$\overline{lnx} = -\frac{\sigma^2}{2} \tag{3}$$

and

$$\sigma^2 = ln(1 + \mathcal{M}^2\beta^2) \tag{4}$$

or, for the linear density:

$$\sigma_{linear} = \beta\mathcal{M} \tag{5}$$

where $\beta \approx 0.5$. Therefore, the standard deviation grows linearly with the rms Mach number of the flow.

It is also found that the power spectrum, $S(k)$, of the density distribution is consistent with a power law:

$$S(k) \propto k^{-2.6} \tag{6}$$

where k is the wavenumber.

The fact that the standard deviation of the linear density field, σ_{linear}, grows linearly with the rms Mach number of the flow can be easily understood. In fact the density contrast behind an isothermal shock is proportional to $\mathcal{M}^2$, that is the square of the Mach number, but the dense shocked gas occupies only a fraction $\mathcal{M}^{-2}$ of the original volume. Since the standard deviation is a volume average, the two effects result in a linear growth of σ_{linear} with $\mathcal{M}$. This is in fact the result, if one computes σ_{linear} for the simple case of a single strong, isothermal, plane shock, that sweeps all the mass of the system.

2.2 Random supersonic flows in dark clouds

An observational counterpart of the numerical experiments on supersonic random flows has been recently indicated by Padoan, Jones & Nordlund (1996), reinterpreting the observational results by Lada et al. (1994).

Lada et al. performed infrared stellar extinction measurements, through the dark cloud IC5146 in Cygnus. They obtained values of extinction for more than a thousand stars, sampled the observed area with a regular grid, and measured the mean and the dispersion of the extinction determinations in each bin of the grid. They found that the dispersion grows with the mean extinction.

This result is an indication that the absorbing material in the dark cloud has a structure well below the resolution of the extinction map. Padoan, Jones, & Nordlund (1996) have shown that an intermittent 3-D distribution in the cloud, in particular a log-normal distribution, explains in a natural way the growth of dispersion with mean extinction. They have also shown that the observational data can be used to constrain the value of the standard deviation and of the spectral index (power law power spectrum) of the 3-D density distribution. The observational constraints are in good agreement with the numerical predictions.

Therefore, both numerical results and observations show that the random supersonic flows, present in dark clouds, result in a very intermittent density distribution, well described by a log-normal statistics. Both the values of the standard deviation and of the spectral index of such distribution are predicted numerically and confirmed observationally.

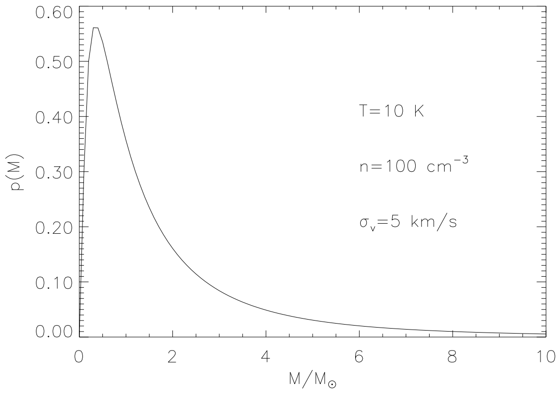

Figure 1: A linear plot of the theoretical MF. The linear shape is characterized by a maximum, with an exponential cutoff for smaller masses. The exponential cutoff is an important feature, because could be identified in the observations, without ambiguities due to uncertainties in the mass–luminosity relation.

3 The derivation of the stellar IMF

A simple way to define a mass distribution of protostars is that of identifying each protostar with one local Jeans' mass. In this way the protostar MF is simply a Jeans' mass distribution. Since the gas is cooling rapidly, the temperature is uniform, and the Jeans' mass distribution is just determined by the density distribution.

The concept of the 'local' Jeans' mass is meaningful in our scenario for molecular clouds (MCs), because random supersonic motions (cascading from larger scale) are present, and are responsible for shaping the density field. Strong density enhancements, that is to say the local convergence of the flow, are due to nonlinear hydrodynamical interactions, rather than to the local gravitational potential. We therefore suggest a description of star formation where random motions are first creating a complex and highly nonlinear density field (through isothermal shocks), and gravity then takes over, when each 'local' Jeans' mass (defined with the local density) collapses into a protostar.

The statistics of the density field is not sufficient in general to predict the protostar MF. Some extra knowledge on the topology of the density field is necessary.

For example, the distribution of mass in a complex system of interacting shocks can be hierarchical. The mass distribution in MCs is also found to be hierarchical over a very large range of scales (Scalo 1985; Vázquez-Semadeni 1994). This brings a considerable difficulty when trying to define a mass distribution of cores inside MCs (Myers, Linke and Benson 1983; Blitz 1987; Carr 1987; Loren 1989; Stutzki and Güsten 1990; Lada, Bally and Stark 1991; Nozawa et al. 1991; Langer, Wilson and Anderson 1993; Williams and Blitz 1993), and indeed any mass distribution estimated from molecular emission line maps is ill-defined, if the hierarchical structure is not taken into account.

The main uncertainty in the Jeans' mass distribution, derived as a transformation of the density distribution, is related to the density fluctuations that are smaller than their Jeans' mass. If many fluctuations are smaller than their Jeans' mass, the transformation of density into Jeans' mass overestimates the number of collapsing protostars with that mass.

In order to check whether this is an important source of error in predicting the protostar MF, we need to understand the topology of the density field.

It has often been noticed that molecular clouds have a filamentary morphology. In our numerical simulations of random supersonic flows (Nordlund & Padoan 1996), up to rms Mach number 10, we also find a density field characterized by filaments and knots. The thickness of these structures, l, is expected to be:

$$l \approx L\mathcal{M}^{-2/D}$$

where $\mathcal{M}$ is the rms Mach number of the velocity dispersion on the scale L, and $D = 1, 2, 3$, in the case of 1, 2 or 3 dimensional compressions respectively. This is due to the fact that most density enhancements are produced by isothermal shocks with Mach number $\mathcal{M}$. The exact choice of the scale L of the random motions is not important, because the typical scaling law of velocity dispersion found in the ISM is $\sigma_v \propto L^{1/2}$. For typical values in molecular clouds the thickness is in the range $l = 0.02 - 0.5$ pc. The density in these sheets and filaments is also increased, with respect to the mean density in the cloud, and therefore the Jeans' length is decreased, with respect to the Jeans' length for the mean density of the cloud. The condition that the thickness of the structures is larger than their local Jeans' length, l_J, that is $l/l_J > 1$, is then given by:

$$\frac{L}{L_J} > \mathcal{M}^{2/D-1}$$

where L_J is the Jeans' length for the mean density on the scale L. The condition is always satisfied in molecular clouds, especially for $D = 2$ or $D = 3$, that are the values suggested by the numerical experiments.

We conclude therefore that the transformation of the density field into the distribution of Jeans' masses gives an estimate of the mass distribution of collapsing objects, that is not in error by more than a few percent.

The density distribution per unit volume is given by equation (1). If we multiply that function with the relative density x, we get the density distribution per unit mass, that is the mass fraction at any given density:

$$f(x)dx = xp(x)dx \tag{7}$$

The fraction of the total mass in collapsing structures of mass $< M$ is the integral of the distribution $f(x)$ over relative densities $x > x_J$:

$$\int_{x_J}^{\infty} f(x)dx$$

where x_J is the Jeans' density for the mass M. The Jeans' mass distribution is the derivative along mass of the previous integral:

$$F(M_J) = f(x_J)\frac{dx_j}{dM_J} \tag{8}$$

The Jeans' mass can be written as:

$$M = M_J = 1M_{\odot}Bx^{-1/2} \tag{9}$$

where:

$$B = 1.2\left(\frac{T}{10K}\right)^{3/2}\left(\frac{\overline{n}}{1000cm^{-3}}\right)^{-1/2} \tag{10}$$

is the average Jeans' mass, that is the Jeans' mass for the average relative density $x = 1$.

Here we use the simplest definition of Jeans' mass: without turbulent pressure or rotation, because the gas has just been shocked and is dissipating its kinetic energy in a short time; without magnetic pressure, because we will discuss the effect of the magnetic field in such random flows in subsequent papers (our numerical experiments are in fact solving the MHD equations).

Using equations (1), (7), (8), (9), and (10) we get the protostar MF:

$$F(M)dM = \frac{2B^2}{(2\pi\sigma^2)^{0.5}} M^{-3} exp\left[-\frac{1}{2}\left(\frac{2lnM - A}{\sigma}\right)^2\right] dM \tag{11}$$

where M is in solar masses, and:

$$A = 2lnB - \overline{lnx} \tag{12}$$

A linear plot of the protostar MF is shown in Figure 1, for $T = 10K$. One recognizes a long tail at large masses and an exponential cutoff at the smallest masses, inherited from the log-normal distribution of density. This shape is an important result, because most models for the origin of the stellar IMF are not able to reproduce the cutoff at the smallest masses, which should be present in any reasonable IMF.

In the coming sections we will discuss the dependence of the MF on the average physical parameters of the star forming gas, and we will then compare our results with the observations.

4 The dependence of the IMF on the physical parameters

The protostar MF depends on the density distribution that arises from random supersonic motions, through a complex system of interacting shocks, and on the definition of the Jeans' mass. The first dependence brings into the MF the dependence on the average temperature, T, and velocity dispersion of the flow, σ_v, through the rms Mach number of the flow, which is the only parameter of the density distribution in random supersonic flows. The dependence on the Jeans' mass translates into a dependence of the MF on the average density, n, and on the temperature. Therefore our model for the MF may be applied to different sites of star formation, identified by their mean values of density, temperature and velocity dispersion.

In Figures 2, 3, and 4, we have plotted mass distributions for different values of the physical parameters. We have chosen to plot the exponent of the power law approximation of the MF, rather than the actual MF. The exponent is defined as:

$$X = \frac{\partial ln(F(lnM))}{\partial lnM} = \left(\frac{2A}{\sigma^2} - 3\right) - \frac{4}{\sigma^2} lnM \tag{13}$$

The Salpeter MF has $X = -1.35$, and the Miller–Scalo MF has $X = -1.0 - 0.43 lnM$ (Miller & Scalo 1979), where M is in solar masses.

The most probable stellar mass per logarithmic mass interval, that is the stellar mass that contributes most to the MF, is defined by $X(M_{max}) \equiv 0$, along the curves $X(M)$ plotted in the figures.

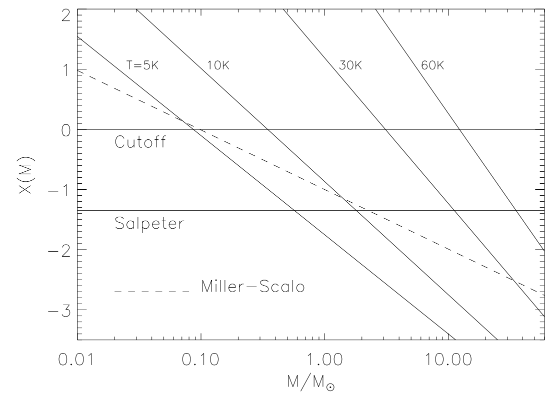

Figure 2: The power law exponent of the theoretical MF is plotted versus the mass, for different temperatures. The Miller–Scalo MF (dashed line) is also plotted for comparison. The Salpeter's value $X = -1.35$ and the cutoff value $X = 0$ are also shown. The Miller–Scalo exponent is fitted by low temperatures at low masses, and by high temperature at large masses. The mean density and velocity dispersion have been taken to be $n = 1000 cm^{-3}$, and $\sigma_v = 2.5 km/s$, typical of molecular cloud cores.

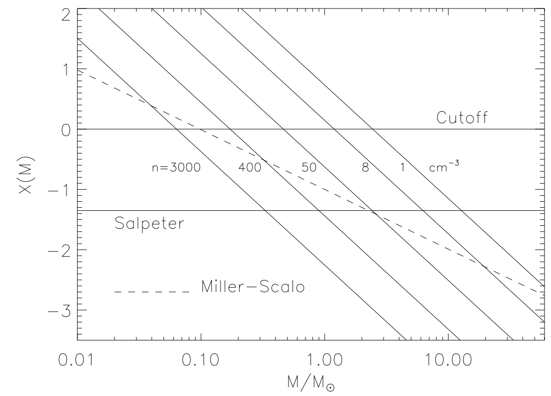

Figure 3: The same as in Figure 2, but for different values of density. The temperature and velocity dispersion have been taken to be $T = 10K$, and $\sigma_v = 2.5 km/s$. The exponent $X(M)$ varies with mass always faster than in the Miller–Scalo, which is an indication that the Miller–Scalo emerges from a mixed population of stars, formed in clouds with different temperatures.

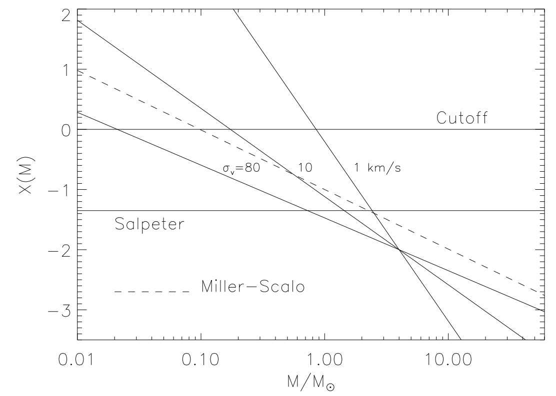

Figure 4: The same as in Fig. 2, but for different velocity dispersions. The temperature and density have been taken to be $T = 10K$, and $n = 1000cm^{-3}$. Very large velocity dispersions, probably typical of large primordial clouds (protogalaxies and protoglobular clouds) can fit very well the Miller–Scalo, even for a single temperature.

In Figure 2 we see that a growing T produces a flattening of the MF at large masses, and a growth of M_{max}, that is the typical stellar mass. The effect of the growth of density is illustrated in Figure 3; its effect is the opposite of the effect of the temperature. Figure 4 shows the dependence on velocity dispersion.

Note that, although the effect of temperature and density is qualitatively as expected from the definition of the Jeans' mass, the effect of T on the MF is more complicated than through the Jeans' mass, because T also affects the density distribution, through the Mach number.

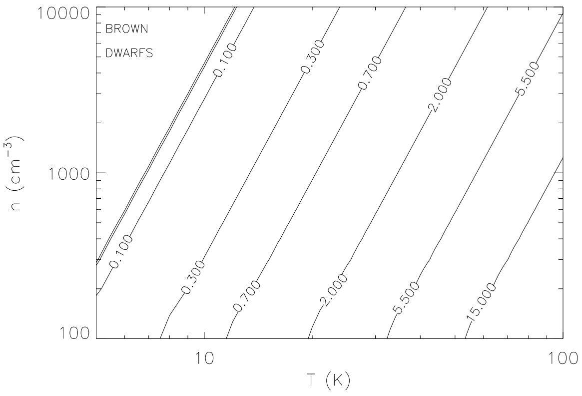

Figure 5: Lines of constant value of the cutoff, or typical stellar mass, in solar masses, on the plane density–temperature. The velocity dispersion is $\sigma_v = 3.0km/s$, typical of molecular clouds.

We will now discuss the variation of the position of the cutoff (or of the typical stellar mass) with the physical parameters.

5 The typical stellar mass

The main result of a theory of star formation should be the prediction of the typical stellar mass. From this point of view, all models resulting in a power law MF are not successful, because power laws are featureless.

In this work we have shown that the random supersonic motions present in molecular clouds produce a protostar MF with an exponential cutoff at the smallest masses, just below the most probable protostellar mass, M_{max}.

The position of the maximum in the MF is given by imposing

$$X(M_{max}) \equiv 0$$

in equation (13). By using the definition of A from (12), of σ from (4), and of M_J from (9) and (10), we get:

$$M_{max} = 1M_{\odot}Be^{\left(-\frac{1}{2}\sigma^2\right)} \tag{14}$$

where $1M_{\odot}B$ is the average Jeans' mass, that is the Jeans' mass for the average density. Therefore:

$$M_{max} = 0.2M_{\odot}\left(\frac{n}{1000cm^{-3}}\right)^{-1/2}\left(\frac{T}{10K}\right)^{2}\left(\frac{\sigma_v}{2.5km/s}\right)^{-1} \tag{15}$$

We can read the result as a modified Jeans' mass. The modification is quite important. In fact this modified Jeans' mass is more sensitive to temperature than the traditional Jeans' mass, and is also quite sensitive to the velocity dispersion σ_v.

This result is not surprising, because it looks like the Jeans' mass at constant external pressure (Spitzer, 1978, p.241), if turbulent ram pressure is considered. Nevertheless this is an important result because it has been obtained from a realistic statistical description of random supersonic flows, that allows the prediction of the whole shape of the MF.

Another way to interpret the modified Jeans' mass is to use equation (14), and substitute the standard deviation of the logarithmic density distribution, σ, with the linear standard deviation, σ_{linear}, from equations (4) and (5). We obtain:

$$M_{max} = \frac{1M_{\odot}B}{\sigma_{linear}} \tag{16}$$

where σ_{linear} is about one half of the rms Mach number of the flow (cf equation (5)), and B is the Jeans' mass for the mean density, in solar masses. Therefore we may conclude that *the most probable Jeans' mass is equal to the Jeans' mass* *for the mean density divided by half of the rms Mach number.* As an example, a typical molecular cloud with rms Mach number about 10, and Jeans' mass of the mean density about $1M_\odot$, has a most probable Jeans' mass of $0.2M_\odot$.

In Figure 5 , we show contours of constant M_{max}, on the plane $n-T$, for $\sigma_v = 3km/s$, typical of molecular clouds.

6 The observed IMF

We show in this section that the model predicts a Miller–Scalo IMF for the solar neighborhood, if a temperature distribution is used, and a more "massive" IMF for $T \geq 40$, that is probably typical of the starbursts and of the warmest molecular clouds.

6.1 The MF in the solar neighborhood and in open clusters

In Figure 6 the theoretical MF for $T = 10K$ (dashed line) is compared with the Miller–Scalo MF (MSMF) (dotted line). The shape of the theoretical MF is different from the shape of the MSMF. In fact, for the typical parameters of MCs, or of MC cores, the MF is always narrower than the MSMF. On the other hand, the models with low T (say $5K$) give the correct slope for low masses, while the models with high T (say $40K$) give the correct slope for the large masses.

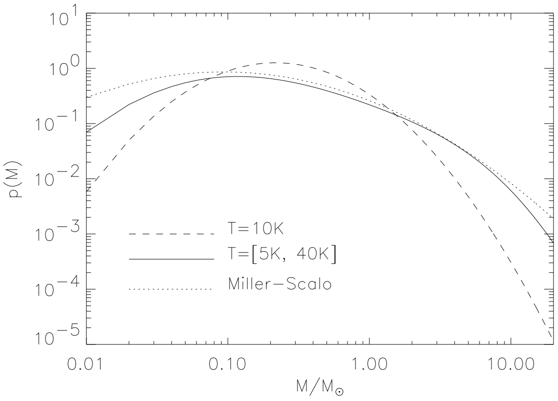

Figure 6: Log-log plot of the theoretical MF (dashed line), for a temperature $T = 10K$. The Miller–Scalo MF is plotted for comparison (dotted line). The single temperature MF cannot be made to fit the Miller–Scalo. Once the theoretical MF is generated from a distribution of temperatures, in the range $5-40K$ (continuous line), it is practically coincident with the Miller–Scalo.

Therefore the MSMF can be reproduced only if the solar neighborhood stars are assumed to be born in clouds with temperatures in the range $5-40K$, which is a reasonable assumption, since these temperature values are measured in cloud cores. It is likely that the solar neighborhood stars are a mixed population coming from different cloud cores, or even from different giant molecular cloud complexes, with temperatures in the range observed in present day molecular clouds.

To illustrate the origin of a MF that contains a mixed population, coming from clouds with different temperatures, we integrate our theoretical MF along a temperature distribution, $g(T)dT$:

$$F_{mixed}(M)dM = \int_T F(M,T)dMg(T)dT$$

Figure 6 shows the result of the temperature integration (continuous line). The temperature distribution has been taken to be $g(T) \propto T^{-1}$, which means that there are more cold clouds than warm ones.

One can see that the temperature integration improves the shape of the single temperature MF, making the theoretical MF practically coincident with the MSMF.

We may therefore conclude that the MSMF is predicted by the model, as long as most of the solar neighborhood stars are formed in molecular clouds similar to the ones that are the sites of present day star formation, with temperatures between $5K$ and $40K$.

The MSMF is consistent with the Salpeter MF (1955), and with subsequent determinations such as Garmany, Conti & Chiosi (1982), Humphreys & McElroy (1984), Vanbeveren (1984), Van Buren (1985), Rana (1987).

Very recent observational works are again all consistent with a Miller–Scalo MF, both in the field and in open clusters.

As for the open clusters, Rieke, Ashok & Boyle (1989) and Williams et al. (1995) found that the MF in the ρ Ophiuchi cluster is practically flat at about $0.1M_{\odot}$; Kroupa, Gilmore & Tout (1992) found that the MF in NGC 2362 is indistinguishable from the solar neighborhood MF; the same conclusion was reached by Phelps & Janes (1993), who studied 23 open clusters in our Galaxy, and by Will, Bomans & De Boer (1995) for NGC 1818, in the Large Magellanic Cloud.

As for the field stars, the works by Tinney, Mould, & Reid (1992), Tinney (1993), and Kroupa (1995) are all consistent with a MF which is almost flat at about $0.1M_{\odot}$, and the works by Kroupa (1995) and Basu & Rana (1992) are consistent with a Miller–Scalo MF.

In summary, it is apparent that all the observational determinations of the MF in the solar neighborhood, both in the field and in open clusters, up to about $10M_{\odot}$, are consistent with the theoretical predictions of the present work.

6.2 More massive stars: OB associations

To study the MF of stars more massive than $\sim 10M_{\odot}$, it is necessary to observe young stellar systems, such as OB associations. Recent examples of determinations of MF in OB associations, both in the Galaxy and in the Magellanic Clouds, are the works by Grondin, Demers, & Kunkel (1992), Parker & Garmany (1993), Hill et al. (1994), Hill, Madore & Freedman (1994), Massey, Johnson, & DeGioia-Eastwood (1995).

The results of these works are far from coherent, especially if the reported exceedingly small errors of the MF slopes are adopted. The mass function slopes vary from $X = -1.0$ to $X = -2.5$ (Salpeter $X = -1.35$), for masses in the approximate interval $10 - 70M_{\odot}$. Massey and collaborators tend to give average values close to $X = -1.1$, for both the Galaxy and the Magellanic Clouds, while Hill and collaborators prefer values close to $X = -2.0$. Given the uncertainties in the calibrations necessary to produce the observational H-R diagram, in the stellar evolutionary tracks used for the conversion of luminosity into mass, and in the adopted age of the associations, the average slopes determined by the two groups are not inconsistent with each other.

The main points are:

- The general agreement on the fact that there is no difference between the MF in OB associations in the Galaxy and the MF in OB associations in the Magellanic Clouds. (The same conclusion is reached by Blaha & Humphreys (1989).)
- The presence of a significant scatter in the slopes of the MFs of different OB associations, determined by the same authors.

The second point indicates that some physical parameter is responsible for the formation of different MFs in different associations.

Now, going back to the model, we see that these observational results are indeed predicted, if it is assumed that OB associations emerge from clouds that are slightly warmer than the clouds where small stars are formed. This is in fact known to be the case. It has already been shown above that the MSMF (Miller–Scalo MF), which is a global MF, can be reproduced with a mixed population of stars, formed in the temperature interval $5 - 40K$. In the case of the OB associations, we are selecting only the population formed in the warmest clouds, with temperatures between $30K$ and $60K$.

In fact, as illustrated by Figure 3, with typical density and velocity dispersion of molecular clouds, the exponent of the MF at $30M_{\odot}$ goes from $X = -1.0$ to $X = -2.5$ (as in the observations), in the temperature range from $T = 60K$ to $T = 30K$ respectively.

6.3 Starbursts and 30 Doradus

It has been claimed by many authors, on both theoretical and observational grounds, that the IMF in starburst regions is more "massive" than in the solar neighbourhood.

It has been found that the models of the stellar populations in starbursts suggest a MF with the low-mass cutoff at a few solar masses (e.g. Doane & Mathews 1993; Rieke et al. 1993; Doyon, Joseph & Wright 1994).

These "massive" MFs are in agreement with our theoretical prediction. In fact, a value of $4M_\odot$ is predicted for the cutoff in the MF, for $T \approx 60K$, which is reasonable in environments with strong UV and X-ray radiation fields, and with enhanced (even by a factor 100) cosmic ray flux.

A local example of a starburst event is the main core of 30 Doradus, R136a. Malumuth and Heap (1994) determined the LF for the stellar population in the center of 30 Doradus, and found a MF with the slope $X = -0.9$, in the very center, and $X = -1.8$, for stars outside R136a. The slope $X = -0.9$ is the flattest ever found in OB associations in the Magellanic Clouds.

This is to be expected in fact, since R136a is the site with the most intense star formation in the Magellanic Clouds, and therefore one of warmest regions. $X = -0.9$ is just the value predicted by the model for $T = 60K$, or slightly warmer (Figure 3).

6.4 Globular clusters

Several authors have determined the MF in globular clusters. Examples are Fahlman et al. (1989), Piotto et al. (1990), Richer et al. (1990, 1991), Ferraro & Piotto (1992).

The main observational problems are the small mass interval that can be observed with ground based instruments, and the uncertainties in theoretical models for stars smaller than $\sim 0.3M_\odot$.

Recent HST observations of the globular cluster NGC 6397 (Paresce, De Marchi, & Romaniello 1995) indicate that the LF is not as steep as previously claimed with ground based observations (Fahlman et al. 1989). Moreover, new evolutionary tracks for small stars show that the LF is consistent with a flat MF (d'Antona & Mazzitelli 1996), that is with an exponent $X = 0$ (Salpeter $X = -1.35$).

Since the observed stars have masses in the interval $0.1 - 0.6M_\odot$, we can conclude that the exponential cutoff in the MF has to be close to $0.1M_\odot$, and that we are close to being able to observe it.

Padoan, Jimenez & Jones (in preparation) have studied the hypothesis of a primordial origin of GCs, by applying the present model of star formation to protoglobular clouds of a few $10^8 M_\odot$ in baryons. In their model the GCs originate from the star formation process in the core of the large cloud, at density $n \approx 10^4 cm^{-3}$ and temperature $T \approx 100K$ (due to H_2 cooling), while most of the halo stars are the stars formed in the rest of the protoglobular cloud, which does not result in a bound system. For the halo stars the parameters are $n = 250 cm^{-3}$ and $T = 100 K$. The assumed velocity dispersion is some fraction of the virial velocity, $\sigma_v \approx 50 km/s$.

It is found that the GC MF matches very well the Miller–Scalo MF. In particular, the exponent of the MF, in the interval $[0.1, 0.6] M_\odot$, is $X = [0.5, -0.5]$, in agreement with the most recent results on the MF in NGC 6397, mentioned above.

The halo stars are formed at a lower density, and are therefore more massive. Their typical mass is $0.8 M_\odot$, which means that stellar counts in the halo should exhibit a cutoff below a mass of about $0.08 M_\odot$. The exponent of their MF is $X = -1.9$ at $30 M$, while it is $X = -2.7$ for the GC stars, and $X = -2.5$ for the MSMF.

7 Discussion

In the present work we suggest that most stars, both very massive and very small, are formed as a consequence of turbulent fragmentation, that is the fragmentation due to a complex system of strong interacting shocks, emerging from a field of random supersonic motions. On the other hand, turbulent fragmentation is only a large scale process; the details of the evolution of single protostars into main sequence objects may be totally different for stars of different masses (indeed the time-scales must be very different). In other words, with the present work we do not contradict any result, or even speculation, concerning the formation of single stars (eg. Shu, Adams, & Lizano 1987; Mouschovias 1991, Basu & Mouschovias 1995): we just give the distribution of protostellar objects, that is not easily predicted by modeling the evolution of a single protostar (cf Adams & Fatuzzo 1996). In fact the complexity of the ISM is such that star formation on large scale must be a stochastic process, that can be described only with a statistical approach.

A purely statistical description of the origin of the IMF has been given by several authors, as an attempt to model the process of gravitational fragmentation (eg. Auluck & Kothari 1954; Kruszewski 1961; Kiang 1966; Reddish 1962, 1966; Fowler & Hoyle 1963; Belserene 1970; Larson 1972; Elmegreen & Mathieu 1983; Zinnecker 1984; Di Fazio 1986).

Other works tried to relate the MF of molecular cloud cores with the stellar MF (see Zinnecker et al. (1993) for a discussion).

Most of the physical models for the origin of the IMF have been based on the concept of opacity-limited fragmentation (Silk 1977ab, Yoshii & Saio 1985, 1986).

In all cited models, the presence of random supersonic motions in the clouds is not taken into account. Models where such motions are considered in a semi-empirical way are Myers & Fuller (1993) and Silk (1995). The effect of turbulent motions are also considered by Arny (1971), as a source of internal pressure, and by Hunter & Fleck (1982), as a source of compression.

Takebe, Unno & Hatanaka (1962) assumed, like in the present work, that the mass function is set by the distribution of the Jeans' mass in the cloud, but, missing a physical model for the cloud structure, they inferred this from the IMF.

The present work is an improvement on Padoan (1995). In that paper the scenario of turbulent fragmentation is described in detail, while here we focus on the derivation of the MF of protostars. These works are the first attempts to derive the stellar MF, taking into account the presence of a complex system of interacting strong shocks in the star forming gas, which is the inevitable consequence of the observed random supersonic motions. In fact the shocks are responsible for shaping the density field in the clouds.

Such an approach has been made possible only very recently, thanks to the numerical study of randomly forced highly supersonic flows (Nordlund & Padoan 1996), and to the recognition of their observational counterpart (Padoan, Jones & Nordlund 1996).

The dependence of the MF of protostars on the physical parameters of the ISM brings a very interesting question: why are some clouds warmer than others and able to form massive stars? Are they warmer from the beginning, or are they heated by the massive stars?

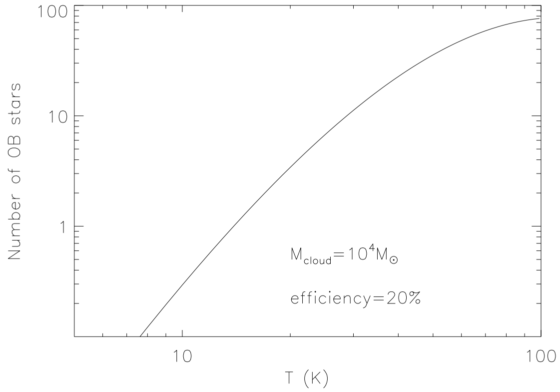

Figure 7: Number of OB stars found in a cloud of $10^4 M_\odot$, if 20% of the cloud mass is transformed into stars. The Larson's relations have been used to fix density and velocity dispersion, while the temperature has been taken to be $10K$.

To answer this question we must recall the stochastic nature of the star formation process. In Figure 7 we plot the number of OB stars found in a cloud of $10^4 M_\odot$, as a function of T, if 20% of the cloud is turned into stars. The number is given by the integration of the theoretical MF for different temperatures, from $5K$ to $100K$. One can see that, even a relatively large cloud with such a high star formation efficiency is not forming any single OB stars, if its temperature is less than $15K$. If the temperature is $20K$, 3 OB stars may be formed. The process of star formation may continue for about 10^7 years, and these massive stars, since they are only a few, may be born in the very beginning, or in the very end of the whole period of star formation, or even never. A few OB stars may also be born in clouds as cold as $10K$, given the stochastic nature of the process.

When OB stars are formed, the cloud gets warmer, and becomes able to form more OB stars. The final result of this positive feedback can be a rather warm cloud, with many massive stars, and with a relatively flat MF.

We can therefore speculate that warm clouds, like Orion, forming massive stars, are just the natural evolution of colder clouds, like Taurus, that managed to get a few OB stars to start with, by pure chance, because of the stochastic nature of the process of star formation.

Most theoretical models for the IMF have failed in proposing a physical mechanism for the cutoff in the IMF. In the present model the cutoff is inherited, as the whole shape of the MF, from the distribution of the density field. We stress that the density field has not been built ad hoc to produce a nice MF of protostars. Rather, we have noticed that sites of star formation (dark clouds) are shaken by supersonic random motions, that must cause a complex system of strong isothermal shocks. We have therefore studied, with numerical simulations, the density field emerging from this kind of flows, and we have found a log-normal distribution. This is remarkable because the Miller–Scalo MF is also a log-normal distribution. Then we have identified a new way to constrain the 3-D density field in dark clouds, using stellar extinction determinations, and found again the same result as in the numerical simulations (Padoan, Jones, & Nordlund 1996).

We therefore propose that the stellar IMF is determined primarily by the random supersonic motion of the cold molecular gas.

The prediction for the cutoff in the present model is very reasonable. In fact the general picture where random motions are sources of compression, through shocks, is consistent with the result that the cutoff is similar to a Jeans' mass with constant external pressure, where the turbulent ram pressure is considered (eq.13).

An important characteristics of the theoretical protostar MF discussed in this work is the fact that the growth in mass of the cutoff, or typical stellar mass, occurs together with the flattening of the MF at large masses. For example, we expect that OB associations with very flat MF have probably few or no stars less massive than $2-3M_{\odot}$, although they might have a population of small stars, born when no OB stars were yet formed in the neighborhood. In the case of starbursts, there is observational evidence for the absence of stars smaller than about $4M_{\odot}$, which means that the MF must also be very flat, compared with the Miller–Scalo MF.

8 Summary and conclusions

In the present work we have proposed a new physical model for the origin of the stellar IMF. The model is based on a new statistical description of star formation on large scale, that focuses on the importance of the well documented presence of random supersonic flows in the sites of star formation.

Very recent numerical and observational results, concerning the density distribution that arises from random supersonic motions, are implemented in the theoretical model for the MF of protostars. The main results of the present work are the following:

- The MF is quantified without free parameters, with its dependence on the mean temperature, density and velocity dispersion of the star forming gas.
- The shape of the protostar MF has a single maximum, a long tail of massive stars, and an exponential cutoff below the maximum. Such a shape is inherited directly from the density distribution in random supersonic flows.
- The typical protostellar mass is $M_{max} \approx 0.2 M_{\odot} \left(\frac{n}{1000 cm^{-3}}\right)^{-1/2} \left(\frac{T}{10K}\right)^{2} \left(\frac{\sigma_v}{2.5 km/s}\right)^{-1}$, and $M_{max} \approx 0.1 M_{\odot} \left(\frac{T}{10K}\right)^{2}$, using the ISM scaling laws.
- A Miller–Scalo IMF is predicted for the solar neighborhood stars, if they are formed in molecular clouds, similar to the ones observed in the sites of present day star formation, with temperature in the range $5K - 40K$.
- Globular clusters are expected to have a MF very similar to the Miller–Scalo, with a typical stellar mass of $0.1 M_{\odot}$.
- Starburst regions should have flatter IMF, with a more massive cutoff, because of their higher mean temperature.

The effect of the magnetic field in the present statistical approach is under study, and will be presented in a separate paper.

Acknowledgements

This work has been supported by the Danish National Research Foundation through its establishment of the Theoretical Astrophysics Center. P. P. thanks Raul Jimenez, John Peacock, Derek Ward-Thompson and Francesco Lucchin for stimulating discussions.

References

Adams, F. C. & Fatuzzo, M. 1996, ApJ 464, 256

Arny T., 1971, ApJ 169, 289

Auluck, F. C. & Kothari, D. S. 1954, Nature, 174, 565

Basu, S. & Rana, N. C. 1992, ApJ, 393, 373

Basu, S. & Mouschovias, T. C. 1995, ApJ, 452, 386

Belserene, E. P. 1970, Observatory, 90, 239

Blaha C. & Humphreys R.M., 1989, AJ 98, 1598

Blitz, L. 1987, in Physical Processes in Interstellar Clouds, ed. E. Morfill and M. Scholer (Reidel Publ. Comp.), 35

Carr, J. S. 1987, ApJ, 323, 170

Charlot, S., Ferrari, F., Mathews, G. J. & Silk, J. 1993, ApJ, 419, L57

Coles, P. & Lucchin, F. 1995, Cosmology, (Wiley)

d'Antona, F., Mazzitelli, I. 1996, ApJ 456, 329

Di Fazio, A. 1986, A&A 159, 49

Doane, J. S. & Mathews, W. G. 1993, ApJ 419, 573

Dobashi, K., Yonekura, Y., Mizuno, A. & Fukui, Y. 1992, AJ 104, 1525

Doyon, R., Joseph, R. D. & Wright, G. S. 1994, ApJ 421, 101

Elmegreen, B. G. & Mathieu, R. D. 1983, MNRAS 203, 305

Fahlman, G. G., Richer, H. B., Searle, L. & Thompson, E. B. 1989, ApJ 343, L49

Ferraro, F. R. & Piotto, G. 1992, MNRAS, 255, 71

Fowler, W. A. & Hoyle, F. 1963, Roy. Obs. Bull., 11, 1

Garmany, C.D., Conti, P.S. & Chiosi, C. 1982, ApJ 263, 777

Grondin, L., Demers, S. & Kunkel, W. E. 1992, AJ, 103, 1234

Hill, R. J., Isensee, J. E., Cornatt, R. H., Bohlin, R. C., O'Connell, R. W., Roberts, M. S., Smith, A. M. & Stecher, T. P. 1994, ApJ, 425, 122

Hill, R. J., Madore, B. F., & Freedman, W. L. 1994, ApJ, 429, 204

Humphreys, R.M. & McElroy, D.B. 1984, ApJ 284, 565

Hunter, J. H. Jr. & Fleck, R. C. Jr 1982, ApJ, 256, 505

Kiang, T. 1966, Zs. Ap., 64, 426

Kroupa, P. 1995, ApJ, 453, 358

Kroupa, P., Gilmore, G. & Tout, C. A. 1992, AJ, 103, 1602

Kruszewski, A. 1961, Acta Astr. 11, 199

Lada, E. A., Bally, J. & Stark, A. A. 1991, ApJ, 368, 432

Lada, C. J., Lada, E. A., Clemens, D. P. & Bally, J. 1994, ApJ, 429, 694

Langer, W. D., Wilson, R. W. & Anderson, C. H. 1993, ApJ, 408, L45

Larson, R. B. 1972, Nature 236, 21

Loren, R. B. 1989, ApJ 338, 902

Malumuth, E. M. & Heap, S. R. 1994, AJ, 107, 1054

Massey, P., Johnson, K. E., DeGioia-Eastwood, K. 1995, ApJ 454, 151

Miller, G. E, & Scalo, J. M. 1979, ApJS 41, 413

Mouschovias, T. C. 1991, ApJ 373, 169

Myers, P. C., Linke, R. A., & Benson, P. J 1983, ApJ 264, 517

Myers, P. C., & Fuller, G. A. 1993, ApJ 402, 635

Nordlund, Å. P., Padoan, P. & Jones, B. J. T. 1996, submitted to ApJ

Nordlund, Å. P. & Padoan, P. 1996, submitted to Phys. Fluids

Nozawa, S., Mizuno, A., Teshima, Y., Ogawa, A. & Fukui, Y. 1991, ApJS, 77, 647

Padoan, P. 1995, MNRAS 277, 377

Padoan, P., Jones, B. J. T. & Nordlund, Å. P. 1996, submitted to ApJ

Paresce, F., De Marchi, G. & Romaniello, M. 1995, ApJ 440, 216

Phelps, R. L. & Janes, K. A. 1993, AJ 106, 1870

Piotto, G., King, I. R., Capaccioli, M., Ortolani, S. & Djorgovski, S. 1990, ApJ 350, 662

Rana, N.C. 1987, A&A 184, 104

Reddish, V. C. 1962, Sci. Progr. 50, 235

Reddish, V. C. 1966, in Vistas in Astronomy Vol.7, ed. A. Beer (Oxford: Pergamon), 173

Richer, H. B., Fahlman, G. G., Buonanno, R. & Fusi Pecci, F. 1990, ApJ 359, L11

Richer, H. B., Fahlman, G. G., Buonanno, R., Fusi Pecci, F., Searle, L. & Thompson, I. B. 1991, ApJ 381, 147

Rieke, G. H., Ashok, N. M. & Boyle, L. P. 1989, ApJ 339, L71

Rieke, G. H., Loken, K., Rieke, M. J. & Tamblyn, P. 1993, ApJ 412, 99

Salpeter, E.E. 1955, ApJ 121, 161

Scalo, J. M. 1985, in Protostars and Planets II, ed. D. C. Black and M. S. Mathews (Tucson: University of Arizona Press), 349

Shu, F. H., Adams, F. C. & Lizano, S. 1987, Ann. Rev. A&A 25, 23

Silk, J. 1977a, ApJ 214, 152

Silk, J. 1977b, ApJ 214, 718

Silk, J. 1995, ApJ 438, L41

Spitzer, L.Jr. 1978, Physical processes in the interstellar medium (Wiley)

Stutzki, J. & Güsten, R. 1990, ApJ, 356, 513

Takebe, H., Unno, W. & Hatanaka, T. 1962, Pub. Astr. Soc. Japan 14, 340

Tinney, C. G. 1993, ApJ 414, 279

Tinney, C. G., Mould, J. R. & Reid, I. N. 1992, ApJ, 396, 173

Vanbeveren, D. 1984, A&A 139, 545

Van Buren, D. 1985, ApJ 294, 567

Vázquez-Semadeni, E. 1994, ApJ 423, 681

Will, J., Bomans, D. J. & De Boer, K. S. 1995, A&A 295, 54

Williams, J. P. & Blitz, L. 1993, ApJ 405, L75

Williams, D. M., Comeron, F., Rieke, G. H. & Rieke, M. J. 1995, ApJ 454, 144

Yoshii, Y. & Saio, H. 1985, ApJ 295, 521

Yoshii, Y. & Saio, H. 1986, ApJ 301, 587

Zinnecker, H., 1984, MNRAS 210, 43

Zinnecker, H., McCaughrean, M.J., Wilking, B.A. 1993, in Protostars and Planets III, eds. E. H. Levy & J. I. Lunine (Tucson: University of Arizona Press), 429

NEAR INFRARED HIGH ANGULAR RESOLUTION IMAGING OF YOUNG STELLAR OBJECTS

N. Ageorges
European Southern Observatory, Karl-Schwarzschild-Strasse 2
D-45748 Garching b. München, Germany

Abstract

The use of high angular resolution (HAR) techniques to observe young stellar objects (YSOs) corresponds to the wish to resolve disk-like structures around these objects. Such structures are well expected features of young stars. The near infrared is well suited to the study of the circumstellar environment (at these wavelengths, the optical depth is much smaller than in optical). Here I present near infrared HAR imaging methods. I will point out the advantage of each observing mode and will comment, on the basis of few examples, the results of such observations. Among others, the impact of the discovered high degree of multiplicity of YSOs will be discussed.

1 Introduction

The background problem considered here is the one of star formation. High angular resolution (HAR) is used to determine multiplicity of stars (i.e. invoking different scenarios of star formation), to study the distribution and properties of circumstellar matter, to pick out objects in a crowded field (like in the Galactic center), to do high sensitivity searches for faint sources (e.g. detection of disks, or faint companions). The use of HAR techniques to observe young stellar objects (YSOs) corresponds to the wish to resolve disk-like structures around these sources. Such structures are well expected features of young stars (see e.g. review from C.M. Walmsley in these proceedings p.177). The near-infrared (NIR) is well-suited to the study of the circumstellar environment of YSOs since, at these wavelengths, the optical depth is ten times smaller than in the visible. Moreover, dust reemits the stellar light in the infrared.

Some of the techniques available to realise such studies are presented hereafter, beginning with lunar occultations and adaptive optics. Then, speckle techniques and speckle polarimetry will be further detailed.

2 Lunar occultation

This technique has initially been used for binarity surveys (mostly in Taurus & Ophiuchus; see e.g. Simon et al. 1987). But other information can also be extracted: for example, extended matter has been discovered around one of the components of Haro 6-10 (Richichi et al. 1994). It is important to emphasize that lunar occultation is the only technique presently available providing milli-arcsecond resolution and thus probing the surroundings of YSOs on an AU-scale. This is the most powerful method for HAR in the NIR. The major restrictions of this method are that you have to wait until your target is on the Moon path, the observations are very weather dependent and not very sensitive to scale structures $\geq 6''$, and you can resolve the object in only one direction.

3 Adaptive optics: The ADONIS system

This method performs on-line correction of atmospheric perturbations. It needs a reference star for the wavefront sensor, which, with the presently available systems, represents the major problem. In the case of ADONIS (the ESO adaptive optics system), the reference star must be at maximum $30''$ from the science object and be bright in the visible ($m_V \geq 13$ to get a Strehl ratio ≥ 0.1). The main problem of this system is the use of an optical detector for the wavefront sensor. Note that coronographs are also used on adaptive optics systems (see e.g. Malbet 1996). The best reachable resolution corresponds to the diffraction limit of the telescope, i.e. $0.15''$ at 2.2μm for a 4m class telescope (see e.g. McArthur et al. 1996). The promising future of this technique lies in laser guide star systems where the reference star is simulated by a laser beam (see e.g. Fugate et al., 1996).

4 Speckle techniques: SHARP at the NTT

This is the most reliable HAR technique providing diffraction limited images for all possible types of sources. On average speckle observations of stars were characterised by a resolution of $0.2''$ under average seeing conditions ($0.7''$) (Ageorges et al. 1996, in preparation). This resolution corresponds to what has been obtained with the MPE SHARP (System for High Angular Resolution Pictures, Hoffman et al., 1995) camera at the ESO New Technology Telescope (NTT, 3.5 m). Associated with shift-and-add (Bates & Cady, 1980) it corresponds to a perfect tip-tilt correction without servo-system noise propagation effects. This kind of observation is restricted to objects of magnitude $m_K \geq 14.5$ (due to sky contribution) and actually $m_K \geq$ 12-13 for the SHARP camera. Another general restriction to speckle observations is linked with the necessity to have a bright (speckle) core of extension $\leq 1''$. Speckle observations represent nowadays the only solution for observations of 'objects' like the Galactic center, i.e. where infrared sources ($m_K \geq 12$) are the only bright reference. Stecklum et al. (1995) is a good illustration of what can be achieved while combining speckle techniques and adaptive optics.

As an example, let us consider V536 Aql. This K7 variable classical T Tauri star, situated at 200 pc, is known to have a degree of optical polarization varying between 6 and 8 %. The only indication of 'young star' activity known before 1995 was the fact that the center of the blueshifted emission in optical forbidden lines is shifted by $\approx 1''$ east with respect to the continuum. This fact is indicative of the presence of an outflow and has been confirmed by Hirth (1994).

NIR speckle observations (Ageorges et al., 1994) resolved this object in a binary system of 0.52″ separation at a position angle of 17°. These observations also point out the existence of extended matter around this system.

5 Polarimetry

What I present here is actually restricted to speckle polarimetry techniques associated with the SHARP camera at the NTT. This technique furnishes two-dimensional diffraction limited polarization maps. A warm wire grating has been installed in front of the SHARP camera. Data are acquired in a speckle mode for 6 positions of the polarizer (30° from each other). Then a cosine function is fitted through the data. For details on the observational techniques and data reduction see Ageorges (1995).

Here the Infrared Nebula in Chamaeleon serves as an illustration.

The Chamaeleon Infrared Nebula (Cha IRN) is a candidate for the class of objects that are in an intermediate state between deeply embedded protostars and young star–disk systems. It presents the typical morphology of a bipolar nebula, i.e. two lobes separated by a dark lane of obscuration. High angular resolution imaging polarimetry of this source has been performed in the J and H bands. These new measurements together with previously published polarization data have been interpreted using a Monte Carlo code for radiative transfer (Fischer et al., 1994). Simulations with various envelope configurations have been performed to get polarization maps similar to the observed ones. As a result of these calculations, properties of the circumstellar dust configuration of Cha IRN have been derived (Ageorges et al., 1996).

First of all, 3 new knots (B,C,D in Figure 1) have been discovered in the high spatial resolution maps, which have been interpreted as the result of scattering in the clumpy circumstellar environment.

The best correspondence between the model and the observational data has been obtained for a Toomre disk (Toomre, 1982) in a free falling molecular cloud core with bipolar outflow cavities at the edge of a molecular cloud. This disk is characterised by a radius of 1000 AU. The grains used are composed of 2/3 graphites and 1/3 silicates. The repartition of grains favours the small ones ($n(a) \propto a^{-4}$). As a result of the simulations we found that the inclination of the disk is $70° \pm 6°$.

A larger disk would obscure the western lobe but not ‘fit’ the polarization maps and distribution of intensity very well. A smaller disk allows a better modelling of contour maps but demands additional obscuring material in front of the western part of the observed configuration. This hypothesis is reasonable when we recall that some $C^{18}O$ as well as CS (2-1) has been detected on the source (Haikala, private communication). Moereover this explains the asymmetry of this nebula. Indeed the western lobe is much less prominent than the eastern one. Details and complete results can be found in Ageorges et al. (1996).

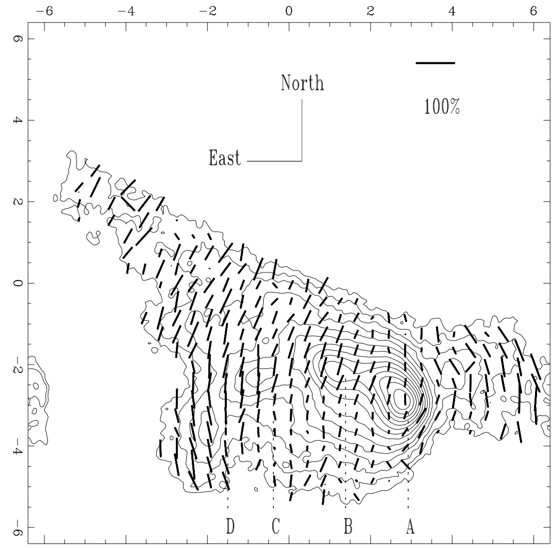

Figure 1: Two-dimensional H band polarization map of the Cha IRN (12.8″ × 12.8″). Intensity contours are spaced by a factor of 1.32 what corresponds to brightness steps of 0.3 mag.

6 Final remarks

The future of HAR NIR observations is to be found in interferometric techniques. One such project under construction is the ESO VLTI (see e.g. Von der Lühe et al., 1995). In the next century space interferometric missions will then open new horizons.

Acknowledgements

I would like to thank the group of Prof. R. Genzel (MPE-Garching) as well as the people in Jena, N. Hubin and O. Von der Lühe without whom this presentation would never have been possible. Many thanks also go to F. Paresce for constructive remarks.

References

Ageorges N., 1995, PhD thesis, University Paris VII

Ageorges N., Ménard F., Monin J.L., Eckart A., 1994, A&A 283, L5

Ageorges N. et al., 1996, ApJL 463, L101

Bates R.H.T., Cady F.M., 1980, Opt. Comm. 32, 365

Fischer O., Henning Th., Yorke H.W., 1994, A&A 284, 187

Fugate R.Q. et al., 1996, ESO Conf. Proc. 54, M. Cullum ed., p.287

Hirth G.A., 1994, PhD thesis, University Heidelberg

Hoffman et al., 1995, SPIE international Symposium, Orlando, in press

Mc Arthur S., Rigaut F., Arsenault R., 1996, CFH Bull. 35, 10

Malbet F., 1996, A&ASS 115, 161

Richichi A., Leinert Ch., Jameson R., Zinnecker H., 1994, A&A 287, 145

Simon M. et al., 1987, ApJ 320, 344

Stecklum B., Eckart A., Henning Th., Loewe M., 1995, A&A 296, 463

Toomre A., 1982, ApJ 259, 535

Von der Lühe O. et al., 1995, SPIE Vol. 2566, 124

X-RAY EMISSION IN STAR-FORMING REGIONS

R. Neuhäuser and M. Sterzik
Max-Planck-Institut für Extraterrestrische Physik, 85740 Garching, Germany

Abstract

We report on the discovery of hundreds of new T Tauri stars (TTS) in several star forming regions like Taurus–Auriga and Orion. Our target selection for ground-based optical follow-up observations of X-ray sources is based on the large sample of ROSAT All-Sky Survey sources. Most of the newly discovered TTS are weak-line TTS, one of their main characteristics is strong X-ray emission. Based on the spatially complete ROSAT All-Sky Survey, we can confirm that weak-line TTS outnumber classical TTS by a factor between 3 and 10.

1 Introduction

The study of T Tauri stars (TTS) is a main step towards the understanding of star formation in the Galaxy and early phases of low-mass stellar evolution. Early definitions (e.g. Herbig 1962, Bastian et al. 1983) describe TTS as low-mass pre-main sequence (PMS) objects showing in their spectrum emission from the Balmer lines and the CaII H and K lines, reflecting the fact that TTS were discovered in Hα-surveys of nearby molecular clouds (classical TTS, cTTS). PMS stars are young stars with ages between $\sim 10^5$ and $\sim 10^7$ yrs. One of the best studied regions of on-going low-mass star formation is the Taurus–Auriga area, a T association at ~ 140 *pc* distance (Elias 1978, Kenyon et al. 1994).

The spatial extension of star forming regions (SFR) is usually studied by CO surveys, e.g. Ungerechts & Thaddeus (1987) for the Taurus–Auriga area. Almost all TTS known prior to the ROSAT mission were situated in areas where molecular gas had been detected. Herbig (1977) found that TTS share the clouds' radial velocity. Also, members of a T association share the same proper motion (Jones & Herbig 1979), so that kinematic membership of a TTS in an association can be studied by determining its space motion.

The advent of the ROSAT All-Sky Survey (RASS) has enabled to extend the search for X-ray active, low-mass stars to the complete sky with a flux limit comparable with typical EO pointed observations. By studying X-ray spectra of RASS detected well-known TTS and unidentified RASS sources in the Taurus-Auriga SFR, Neuhäuser et al. (1995a) have proposed that several hundred coronally active TTS are hidden in the RASS database. So far, 76 TTS have been discovered in the central parts of the Taurus–Auriga T association (Wichmann et al. 1996). A few more TTS have been discovered with optical follow-up observations of sources found in deep ROSAT pointed observations in Taurus–Auriga (Strom & Strom 1994, Carkner et al. 1996, Wichmann et al. 1996). Based on ROSAT observations, many new TTS have been discovered in other star forming regions as well, namely in Chamaeleon (Feigelson et al. 1993, Huenemoerder et al. 1994, Alcalá et al. 1995, Lawson et al. 1996), ρ Ophiuchi (Casanova et al. 1995), Lupus (Krautter et al. 1997), and Orion (Alcalá et al. 1996). Almost all the X-ray discovered TTS are wTTS.

As the set of unidentified RASS sources is very large, Sterzik et al. (1995) have proposed an efficient way of pre-selecting TTS candidates just from ROSAT and Hubble Space Telescope Guide Star Catalog (GSC) data alone. They use data which are easily accessible for all unidentified RASS sources having a nearby GSC counterpart. Surprisingly, Sterzik et al. (1995) did not find a gradient in the space density of TTS candidates at the edges of the Orion SFR, and they proposed to extend the search for TTS even outside the cloud complexes. The strength of RASS as being spatially unbiased allows us to survey for TTS also outside of regions previously known to be populated by TTS.

2 Search for new T Tauri stars

ROSAT has surveyed the complete sky with a detector sensitive in the 0.1 to 2.4 keV range. In the Taurus–Auriga region, from among 66 cTTS only ten have been detected with RASS (15%), while 42 out of 63 wTTS (67%) have been detected. Their X-ray luminosities can be used to construct X-ray luminosity functions. For several SFR such X-ray luminosity functions have been published, e.g. for Taurus–Auriga (Neuhäuser et al. 1995b), Lupus (Krautter et al. 1996), Orion (Alcalá et al. 1996), and Chamaeleon I (Feigelson et al. 1993, Huenemoerder et al. 1994, Alcalá et al. 1995). X-ray luminosity functions show that wTTS emit intrinsically more X-rays than cTTS, mainly because wTTS rotate faster than cTTS.

Following the extrapolation on the size of the wTTS population by Walter et al. (1988) based on Einstein Observatory (EO) observations, there should be up to $\sim 10^3$ wTTS in Taurus–Auriga. There are almost 2000 unidentified RASS sources in Taurus–Auriga and its vicinity, among which hundreds of hitherto unknown TTS are expected (Neuhäuser et al. 1995a). However, it would take many years to perform optical follow-up observations for all unidentified sources. Therefore, the multi-parameter discrimination analysis (Sterzik et al. 1995) is applied to the RASS data base in order to separate non-TTS from unknown, but real TTS.

This method is useful in two ways: One can concentrate on the most likely TTS candidates when searching for new TTS with optical follow-up observations in order to find many new TTS fast. However, in this way one can find almost only typical TTS; this disadvantage can be by-passed by observing rejected RASS sources (i.e. less likely TTS candidates), too. The results of the pre-selection can also be used to investigate the large-scale spatial distribution of TTS candidates (e.g. Sterzik et al. 1995).

3 The new PMS population south of Taurus

We have surveyed a ~ 300 square degree wide area south of the Taurus molecular clouds. Having selected TTS candidates using the method introduced by Sterzik et al. (1995), we have performed both medium-resolution spectroscopy to identify TTS among the objects and high-resolution spectroscopy to measure their radial velocity to investigate their kinematics. These studies are reported by Neuhäuser et al. (1995c), Magazzú et al. (1997), and Neuhäuser et al. (1996).

Many of our newly discovered low-mass PMS stars appear to lie up to several tens of parsecs away from regions of on-going star formation. Yet, their (often large) lithium equivalent widths are suggestive of young ages, just typical for wTTS. Radial velocities for some of them have been presented in Neuhäuser et al. (1995c) and show that about half of their 15 new wTTS are kinematic members of the Taurus–Auriga T association. A full discussion of the kinematic status of all stars studied here will be given in Neuhäuser et al. (in preparation) together with radial velocities (for almost all stars studied here) and proper motions for several stars identified here as new PMS stars.

Some of our new PMS stars (with the Li I $\lambda 6708$Å line clearly detected but moderately deep) may not be *very* young and may be near the ZAMS. Hence, they may well be the long sought post-TTS which have been dispersed out of the region of on-going star formation. If star formation has been on-going in Taurus–Auriga for $\sim 10^7$ years, there should be numerous post-TTS all around the CO clouds, even if the velocity dispersion in Taurus–Auriga is only a very few km/s.

However, given the Li I $\lambda 6708$Å strength as youth indicator, there seem to be very young new wTTS in our sample. If they are less than 10^6 years old, it appears to be impossible for them to have moved the distance between their present location and central Taurus–Auriga, if one assumes a velocity dispersion typical of a SFR, i.e. 1 to 2 km/s (Jones & Herbig 1979). If they have been formed in central Taurus–Auriga, they must have moved to their present location with high velocities. Such TTS are called 'run-away' TTS (Sterzik et al. 1995, Neuhäuser et al. 1995c).

Many such "RATTS" are expected in the vicinity of other SFR as the preselection of TTS candidates indicates (e.g. Sterzik et al. 1995). Sterzik & Durisen (1995) suggest that RATTS can be ejected by three-body encounters in multiple protostellar systems. By direct numerical simulations of such events, they can predict properties of RATTS, which can be tested by observation. These predictions include the velocity and mass distribution of RATTS and the fact that there should be less wide binaries among RATTS as compared to other TTS. Interestingly, Brandner et al. (1996) have searched for binaries among RASS discovered TTS in and near the Chamaeleon SFR as identified by Alcalá et al. (1995). Brandner et al. (1996) have found indications for a smaller binary fraction among off-cloud wTTS than among on-cloud ones, which support the RATTS hypothesis.

Feigelson (1996) proposes a different explanation for the existence of TTS outside regions of on-going star formation (as traced by cloud gas). He argues that TTS can form in small, high-velocity, short-lived cloudlets within and around a turbulent giant molecular cloud complex (like Taurus–Auriga and Chamaeleon). If this scenario is correct, there should exist many cTTS outside the regions with CO gas, too. They can hardly be found by X-ray observations, as cTTS are X-ray faint. However, with infrared surveys such as DENIS and 2MASS one should be able to find them. Additional cloud gas surveys with high sensitivity and sufficient spatial resolution should also be performed in the vicinity of any SFR in order to search for small cloudlets.

The RASS has revealed hundreds of hitherto unknown wTTS in any SFR studied. Even outside regions of on-going star formation, wTTS have been discovered. However, almost no new cTTS have been discovered – neither by EO nor ROSAT. As the RASS is flux-limited and ROSAT pointed observations are spatially biased towards 'interesting' regions, many wTTS have still not been discovered. From the RASS detection rate of wTTS and the discovery rate of new wTTS using RASS, we can expect that there should be as many as ~ 850 wTTS in and around the Taurus–Auriga region (Neuhäuser et al. 1995a). This implies a larger star formation efficiency in Taurus–Auriga than estimated so far.

Also, one can estimate the typical disk life-time from the number of wTTS and cTTS, if one assumes that wTTS usually do not have disks and cTTS do have disks. With ~ 850 wTTS and only ~ 80 cTTS and a typical PMS life-time of about $\sim 10^7$ years, one obtains a typical disk life-time of only $\sim 10^6$ years. However, the large spread in ages of wTTS shows, that the disk life-time can vary significantly from star to star.

Our sample of new low-mass PMS stars found south of the Taurus–Auriga dark cloud complex may contain relatively old dispersed post-TTS, young wTTS formed locally in small short-lived cloudlets, and young wTTS ejected from the central areas of on-going star formation. With kinematic data (both radial velocities and proper motions) and age estimates (e.g. from placing the stars into the HR-diagram or from precise Li I λ6708Å abundances) one may be able to distinguish between these different contributions in the future. The high Li I λ6708Å abundance in a large number of stars in the general direction of any known SFR studied is an observational fact that certainly needs further explanation.

References

Alcalá, J.M., Krautter, J., Schmitt, J.H.M.M., et al., 1995, A&AS 114, 109

Alcalá, J.M., Terranegra, L., Wichmann, R., Chavarria, C., Krautter, J. 1996, A&AS 119, 7

Bastian, U., Finkenzeller, U., Jaschek, C., Jaschek, M., 1983, A&A 126, 438

Brandner, W., Alcalá J.M., Kunkel M., Moneti A., Zinnecker H., 1996, A&A 307, 121

Carkner, L., Feigelson, E.D., Koyama, K., Montmerle, T., Reid, N., 1996, ApJ 464, 286

Casanova, S., Montmerle, T., Feigelson, E.D., André, P., 1995, ApJ 439, 752

Elias, J.H., 1978, ApJ 224, 857

Feigelson, E.D., 1996, ApJ 468, 306

Feigelson, E.D., Casanova, S. Montmerle T., Guibert J., 1993, ApJ 416, 623

Herbig, G.H., 1962, Adv. Astron. Astrophys. 1, 47

Herbig, G.H., 1977, ApJ 214, 747

Huenemoerder, D.P., Lawson, W.A., Feigelson, E.D., 1994, MNRAS 271, 967

Jones, B.F. and Herbig, G.H., 1979, AJ 84, 1872

Kenyon, S.J., Dobrzycka, D., Hartmann, L.W., 1994, AJ 108, 1872

Krautter, J., Wichmann, R., Schmitt, J.H.M.M., Alcalá, J.M., Neuhäuser, R., Terranegra L., 1997, A&AS 123, 329

Lawson, W.A., Feigelson, E.D., Huenemoerder, D.P., 1996, MNRAS 280, 1071

Magazzú, A., Martín, E.L., Sterzik, M.F., Neuhäuser, R., Covino, E., Alcalá J.M., 1997, A&AS, 124, 449

Neuhäuser, R., Sterzik, M.F., Schmitt, J.H.M.M., Wichmann, R., Krautter, J., 1995a, A&A, 295, L5

Neuhäuser, R., Sterzik, M.F., Schmitt, J.H.M.M., Wichmann, R., Krautter, J., 1995b, A&A 297, 391

Neuhäuser, R., Sterzik, M.F., Torres, G., Martín, E.L., 1995c, A&A 299, L13

Neuhäuser, R., Torres, G., Sterzik, M.F., 1996, A&A, to be submitted

Sterzik, M.F. and Durisen, R., 1995, A&A 304, L9

Sterzik, M.F., Alcalá, J.M., Neuhäuser, R., Schmitt, J.H.M.M., 1995, A&A 297, 419

Strom, K.M. and Strom, S.E., 1994, ApJ 424, 237

Ungerechts, H. and Thaddeus, P., 1987, ApJ Suppl. 63, 645

Walter, F.M., Brown, A., Mathieu, R.D., Myers, P.C., Vrba, F.J., 1988, AJ 96, 297

Wichmann, R., Krautter, J., Schmitt, J.H.M.M., Neuhäuser, R., Alcalá, J.M., Zinnecker, H., Wagner, R.M., Mundt, R., Sterzik, M.F. 1996, A&A 312, 439

Main Sequence and Post–Main Sequence stars

LOW MASS STARS INTERACTING WITH THEIR ENVIRONMENT: THE FORMATION OF PLANETARY NEBULAE

Garrelt Mellema
Stockholm Observatory, S-133 36 Saltsjöbaden, Sweden

Abstract

This review gives a brief introduction to the subject of the formation of planetary nebulae. I describe the PN phase and the phases leading to it, concentrating on mass loss and circumstellar material. Next I describe the mechanism by which PNe are thought to form, the interacting stellar wind model. I end with a discussion of the origin of the aspherical shapes seen in the majority of PNe.

1 Introduction

In this review I describe the current understanding of the formation of planetary nebulae. Although PNe have been studied for over a century, it is only in the last 20 years that a dynamical description for the formation of nebulae of different shapes has been developed. We now have a good idea about how a nebula forms from the material lost while the star was a red giant on the asymptotic giant branch (AGB) and how it acquires its shape. This last aspects makes the study of PNe also interesting for other branches of astrophysics since physically similar circumstances are responsible for the formation of nebulae around Wolf–Rayet stars and stars such as the precursor of SN1987a. The study of the formation of PNe also helps in solving the problem of mass loss processes in different types of stars, since the formation depends on the mass loss history of the star both before and during the PN phase. PNe are good objects to study these things since they are often isolated and symmetrical systems.

I start by describing the three phases of stellar evolution which are important for the formation of PNe, the AGB, post-AGB, and PN phase. Then I describe the current understanding of the formation process of PNe, and end with some remarks on the biggest remaining problem: the real physical origin of the asphericity seen in most PNe.

2 Stellar evolution

PNe are thought to form around stars with main sequence (MS) masses of $8M_\odot$[1] or less. After the MS evolution, they increase their energy production

---

[1] This upper limit is not very certain, some people put it as low as $6M_\odot$.

and expand their outer layers, as nuclear burning moves from the core to a shell, and the star turns into a red giant. This redward evolution is temporarily halted by the ignition of Helium burning in the core, but after a degenerated C-O core has formed the star turns into a red giant once more. This phase is called the asymptotic giant branch (AGB).

2.1 The AGB phase

I can only give a very brief overview of the properties of AGB stars and their CSM. An excellent and very thorough review on this subject was written by Habing (1996). This paper covers almost every aspect of the observations and theory of AGB stars. Other good reviews on the circumstellar envelopes around AGB stars are those by Olofsson (1993, 1994, 1996).

An AGB star consists of a degenerate C-O core, a He-shell, a H-shell and a H-envelope. The size of the core and the shells is only a few Earth-radii, whereas the stellar radius is of the order of an AU, so these stars differ radically from MS stars. Initially the He-shell produces most of the energy, the so-called Early AGB, but later the bulk of the stellar energy is produced by the H-shell, occasionally switching back to the He-shell during short events called thermal pulses or He-shell flashes. This phase is referred to as the thermal-pulsing AGB (TP-AGB), and often when people speak about AGB stars they mean this latter phase.

AGB stars have luminosities in the range 3000 to 20,000 $L_\odot$ and effective temperatures lower than 3000 K, making them M- or C-giants depending on whether they are O or C-rich. They are also often variable stars, such as Miras, OH-IR stars, and semi-regular variables.

Stars on the TP-AGB lose mass, which may be observed in a number of ways: thermal emission from the dust that forms, observable in the infrared (often called the IR-excess), emission lines of rotational transitions of molecules in the outflow (the most easily observable one being CO), and maser emission lines from some molecules (OH, H_2O, SiO).

Estimates for the mass loss rates range from 10^{-6} to 10^{-4} $M_\odot \mathrm{yr}^{-1}$. One should keep in mind that the mass loss determinations for individual objects are uncertain by a factor of ~ 10. From the molecular rotational and maser lines one can find the velocity of the outflow, which is typically of the order of 10 kms^{-1}.

The process thought to be responsible for the mass loss is radiation pressure on dust. The stellar pulsations lift off material from the star. At some distance from the star dust forms, which is then pushed away by radiation pressure, dragging the gas along. The main uncertainty here is the process of dust formation. The formation rate and the distance at which it forms are still unresolved issues. This uncertainty makes it impossible to relate mass loss rates to the physical properties of the star.

The geometry of the mass loss, derived for instance by mapping the CO emission or the OH maser shells, appears to be largely spherical but clumpy. There are some cases in which deviations from asphericity are observed, but these are not the majority. The study of the geometry is often hindered by resolution problems and the fact that different emission processes measure different parts of the CSM. For instance SiO masers are found at distances of about 10^{14} cm from the star, whereas the OH masers shells have sizes of $\sim 10^{16}$ cm.

Since nuclear burning only reduces the envelope mass at a rate of about $10^{-7}\ M_{\odot}/\mathrm{yr}$, the evolution of these stars is dominated by the mass loss. The AGB phase ends when the mass loss has reduced the envelope to a mass of about $10^{-3}\ M_{\odot}$ at which point the envelope starts to contract onto the core (which has a mass of 0.5–0.9 $M_{\odot}$). Stellar evolution calculations for the AGB are uncertain because of this strong dependence on mass loss and the imperfect theoretical description of the mass loss process. Compare for instance the calculations of Vassiliadis & Wood (1994) and Blöcker (1995).

Another complication is the phase in the thermal pulse cycle at which the star leaves the AGB. A fraction of stars is expected be in the middle of a thermal pulse at the end of the AGB, and they will continue their evolution as helium-burners. The current opinion is that most post-AGB stars are hydrogen-burners.

2.2 The post-AGB phase

In this phase the star contracts, its effective temperature increasing at constant luminosity. The source of energy is still nuclear fusion of either H or He. During this phase (lasting 100–10,000 years) the star moves through spectral types K to B at a constant luminosity in the range 2000 to 20,000 $L_{\odot}$. These parameters are mainly mass dependent, the more massive stars evolving faster at higher luminosities.

A post-AGB star is surrounded by CSM consisting of material lost during the AGB. This CSM is observable as reflection nebulae (such as Frosty Leo, the Egg Nebula, and the Red Rectangle), or in thermal molecular line emission (mostly CO), or as thermal dust continuum emission. Some of this material expands at velocities similar to those on the AGB, but in some cases velocities up to a few hundred km s^{-1} are found. This indicates ongoing mass loss, at a higher velocity than on the AGB. Velocities like these are expected because the terminal velocity of a stellar wind is typically of the order of the escape velocity from the surface of the star, and post-AGB stars are smaller than AGB stars. Other indications of ongoing mass loss are observations of a hot dust component, implying the presence of dust close to the star. But mass loss rates are extremely uncertain and we lack theoretical understanding of the mass loss during this phase.

The observed morphologies of the reflection nebulae and the molecular line emission are generally aspherical, showing a high degree of axisymmetry. The transition from a more or less spherical to a clearly aspherical morphology appears to coincide with the end of the AGB.

2.3 The PN phase

The PN phase is said to start when a substantial amount of material gets ionized by the central star. This normally implies an effective temperature of 20,000 K or higher. Initially the effective temperature keeps increasing at constant luminosity, reaching values as high as 200,000 K. When the nuclear burning stops (after 50–5,000 years depending on mass) the star becomes fainter and cooler turning into a white dwarf.

During the PN phase the CSM can be observed as the PN in the optical, especially in the prominent forbidden lines of O^{2+} and the Balmer lines, but also in some cases in molecular line emission (mainly from CO, see for example Huggins et al. 1996) and in the IR dust continuum. All this material is the remnant of the AGB and maybe post-AGB mass loss.

In a number of cases P Cygni profiles are found in the stellar spectrum, indicating current mass loss with rates of about 10^{-9} to 10^{-7} $M_\odot$ yr^{-1}, and velocities in the range of 1000 to 3000 km s^{-1} (Perinotto 1993). This fast wind is well explained by models using radiation pressure on lines (Pauldrach et al. 1988).

PNe show a wide range of morphologies, and only 20% or less can be described as circular. Some look like hourglasses (this type is normally referred to as 'bipolar'), some are elliptical. Most show a high degree of cylindrical symmetry, but cases of point-symmetry also exist. See the narrow band image catalogues in Balick (1987), Schwarz, Corradi & Melnick (1993), and Manchado et al. (1996) for many examples. A number of PNe show additional structures such as detached and attached haloes (see e.g. Stanghellini & Pasquali 1995), dense fast moving knots (see e.g. Balick et al. 1993), and jets (Mellema 1996a). Essentially nothing is known about the geometry of the fast wind.

3 Formation of the Nebula

One of the big questions of the late stages of stellar evolution is how a PN is shaped from the CSM. Early work on this was done by Mathews (1966), who assumed that the PN was just the AGB material streaming away and getting ionized. The problem with this model was that it could not explain why so many PNe have sharp inner and outer boundaries, and why no material was streaming back to the star.

3.1 Interacting Stellar Winds

The change came when Kwok, Purton & Fitzgerald (1978) suggested that the formation process might be more violent than gentle free expansion. They came up with the interacting stellar winds (ISW) model in which the fast wind from the central star sweeps up the nebula from the surrounding AGB material.

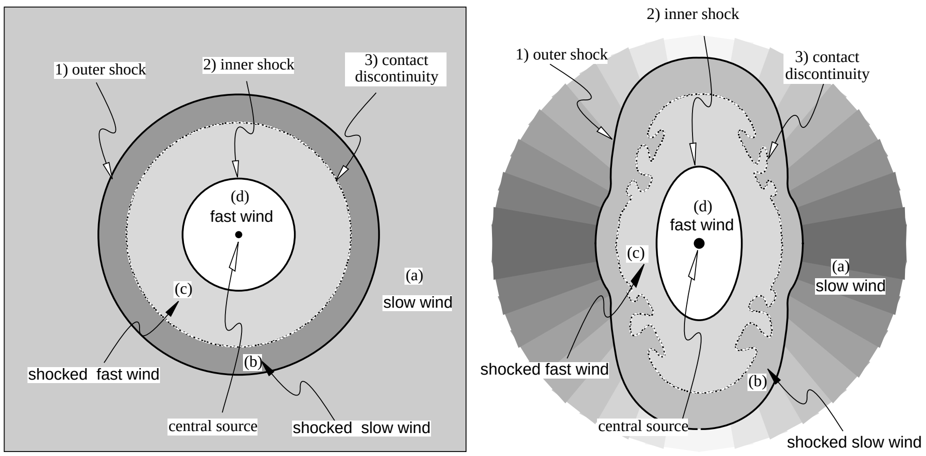

Figure 1: A schematic view of the interacting stellar wind model for the formation of PNe. On the left the bubble configuration for a homogeneous AGB wind, on the right for an inhomogeneous AGB wind.

This configuration leads to a structure containing three discontinuities: an outer shock running into the AGB material, an inner shock running into the fast wind, and a contact discontinuity separating the two, see Fig. 1a. Inside the inner shock the stellar fast wind is freely expanding. Beyond it lies the shocked fast wind which has a high temperature (10^7 K) and low density (~ 1 cm^{-3}). This region accounts for the central hole of the nebula, it is the high pressure of this hot bubble which pushes into the surrounding material and stops the nebula from flowing back to the star. The actual nebula is material that was swept up from the AGB wind. It is separated from the shocked fast wind by a contact discontinuity which means a jump in density and temperature, but not in pressure and velocity. This material has high density (10^3–10^5 cm^{-3}) and nebular temperatures (10^4 K). Beyond the outer shock lies the undisturbed AGB wind.

The main reasons for introducing this model were the sharp outer edges and central cavities seen in most PNe, as well as the first observations of fast wind P Cygni profiles in the stellar spectrum. However, it was soon realized that this model also provides a good description for the formation of PNe of different shapes. If the slow wind is not distributed spherically symmetrically but is instead concentrated towards the equatorial plane, the nebula will get an aspherical shape because the outer shock will travel more slowly into regions of higher density. The expansion velocity goes as $\sqrt{(P_\mathrm{i}/\rho_\mathrm{o})}$, with P_i the pressure of the hot bubble and ρ_o the outer slow wind density. See also Fig. 1b. This configuration was first explored by Kahn & West (1985), and later by Balick (1987).

Table 1: Relation between PN morphology and AGB mass loss properties.

PN Morphology	AGB Mass loss
Bipolar	highly concentrated towards the equator with high density contrast / low expansion velocity
Elliptical	less concentrated towards the equator and/or lower density contrast / higher expansion velocity
Point-Symmetric	not reproduced

It is mainly the density distribution in the slow wind which in this model determines the shape of the nebula; see Table 1. The reason for choosing the asphericity to be associated with the slow wind is that the fast wind does not interact with the surrounding medium directly but via the pressure of the hot bubble. The fast sound waves in this high temperature gas will quickly smooth out asphericities, making it at best an inefficient mechanism to create aspherical nebulae.

3.2 Other effects

Two further factors can influence the formation of the nebula. The first is the flux of ionizing photons from the star. This flux is time-dependent, since the average central star is evolving on about the same time scale as the nebula forms. If this flux is powerful enough, it may send an ionization front through the AGB wind before the fast wind has swept up a proper nebula. This front can modify the density distribution in the slow wind, creating an attached halo (see e.g. Mellema 1994). It may also modify the asphericity of slow wind, smoothing out the equatorial density enhancement (Mellema 1995; Mellema 1996b). In this case the simple relation between AGB mass loss geometry and PN morphology shown in Table 1 no longer holds.

The other factor which may be important for the shaping of the nebula is the clumpiness of the medium. There is abundant evidence of clumpiness in PNe, especially from the Hubble Space Telescope data. How this influences the formation of the nebula is not clear. Arthur, Dyson & Hartquist (1994) studied the case of spherical nebulae and their haloes, but the influence of clumpiness on the formation of aspherical nebulae has not been investigated. The success of the modelling (see below) seems to imply that it is not necessary to take into account clumpiness.

3.3 Modelling

The ISW process for the formation of PNe has been intensively studied using both analytic and numerical methods in varying degrees of complexity. Reviews containing references to the many papers on this subject can be found in Mellema & Frank (1995), Mellema (1996b), and Balick & Frank (1997).

All the models confirm the powerfulness of the ISW model for the explaining the majority of observed PNe. Models containing detailed micro-physics can be compared to observed narrow-band images and long slit spectra. These comparisons show a very good match between the models and the observations (Frank et al. 1994, Frank & Mellema 1994). Models which include the effects of an evolving star reproduce the observed attached haloes and also show that the ISW model works on the right time scale (Marten & Schönberner 1991, Mellema 1994, Mellema 1995).

Not all kinds of morphologies and micro-structures have been reproduced in models (e.g. point-symmetric nebulae and ansae), but these aspects can be explained by slightly modified versions of the model, such as using a warped geometry for the AGB mass loss.

4 Origin of the asphericity

Now of course the ISW model replaces one puzzle (the shape of PNe) with another (aspherical mass loss on the AGB). This aspherical mass loss is assumed, and this assumption can be justified by both the theoretical considerations (essentially the argument presented at the end of Sect. 3.1), and from observations of the outer parts of PNe. However, as we saw in Sect. 2.1 it is very hard to *observe* traces of aspherical mass loss on the AGB. Furthermore it is not entirely clear which process is responsible for the asphericity.

4.1 Observations of aspherical mass loss on the AGB

A recent review on this subject is by Olofsson (1996). The observational evidence points to an increase in the asphericity of the mass loss towards the end of the AGB and non-spherical shapes are the rule rather than the exception once the star has left the AGB. Most observational techniques lack the resolution to observe the most recent mass loss characteristics of an AGB star, and favour the larger scales and therefore earlier phases. It is also relatively easy to hide asphericities in projection effects.

An intriguing suggestion is put forward by Olofsson (1996). A high degree of clumpiness might hide an intrinsically aspherical mass distribution during the AGB phase, and only when the clumps start to be destroyed in the post-AGB and PN phases, does the asphericity become apparent

4.2 Cause of asphericity

The actual cause of the asphericity is still not clear. If one accepts the ISW model one needs to identify a reason for aspherical mass loss on the AGB. Several suggestions have been made:

1. proto-stellar disk
2. rotation
3. magnetic field
4. non-radial pulsations
5. deformation by a nearby companion star, brown dwarf, or massive planet.

The first suggestion has not been seriously explored, but is unlikely because of the long MS phase of most of these stars. Numbers 2, 3 and 4 can produce aspherical mass loss, but all three require a certain amount of stellar rotation. The amount of angular momentum contained in a MS star is not enough to produce appreciable effects in an AGB star. If rotation, magnetic fields or non-radial pulsations are to be important the star needs to gain angular momentum during its evolution.

One of the sources of momentum could be a companion star, or another fairly massive companion. In this sense the recent discoveries of Jupiter mass planets in close orbits around other stars are significant. As was shown by Soker (1996, and references therein) even massive planets might spin up an AGB envelope to make it rotate fast enough to produce aspherical mass loss. This is done most efficiently if the companion object enters the atmosphere of the AGB star, an event normally called the common-envelope phase. As the companion spirals in, it injects angular momentum into the AGB star's envelope. Other ways in which companions influence the formation of PNe are described in Soker & Harpaz (1992) and Soker (1994).

A further indication that companions are influencing the formation of PNe comes from the cases in which we see fast moving knots, jet-like phenomena, and warped geometries, all associated with changes in the outflow direction, suggesting precession in a binary system.

If one restricts oneself to companion *stars*, one can show that 40% of the AGB stars should be influenced by a companion star (Han et al. 1995). This percentage is too low to explain all the aspherical PNe, since about 80% of PNe are aspherical. If one only considers the extreme cases, 40% might be enough. If massive planets in close orbits prove to be quite common occurrences, they can account for the other cases.

5 Conclusions

- Most PNe can be explained with the ISW model. A fraction of PNe (10–20%) shows features which are not readily explained by it. They are bright fast moving knots, jet-like phenomena and a warped/quadrupolar geometry. These features are all associated with changes in the outflow direction, suggesting precession in a binary system.
- The CSM and mass loss during the post-AGB phase is not well understood.
- Aspherical mass loss around AGB stars can be difficult to observe due to lack of resolution and clumpiness.
- The actual origin of the asphericity is still a problem. None of the mechanisms can explain all of the cases. A solution is to use combinations. One example would be to that stellar companions produce the more extreme morphologies (bipolars), while the milder cases (ellipticals) are caused by massive planets.

References

Arthur, S.J., Dyson, J.E., Hartquist, T.W. 1994, MNRAS 269, 1117

Balick, B. 1987, AJ 94, 671

Balick, B., Perinotto, M., Maccioni, A., Terzian, Y., Hajian, A. 1993, ApJ 424, 800

Balick, B., Frank, A. 1997, IAU symposium 180: Planetary Nebulae, H.J. Habing, H.J.G.L.M. Lamers (eds.). Kluwer, Dordrecht, in press

Blöcker, T. 1995, A&A 299, 755

Frank, A., Balick, B., Icke, V., Mellema, G. 1994, ApJ 404, L25

Frank, A., Mellema, G. 1994, ApJ 430, 800

Habing, H.J. 1996, A&AR 7, 97

Han, Z., Podsiadlowski, P., Eggleton, P.P. 1995, MNRAS 272, 800

Huggins, P.J., Bachiller, R., Cox, P., Forveille, T. 1996, A&A 315, 284

Kahn, F.D., West, K.A. 1985, MNRAS 212, 837

Kwok, S., Purton, C.R., Fitzgerald, P.M. 1978, ApJ 219, L125

Manchado, A., Guerrero, M.A., Stanghellini, L., Serra-Ricart, M. 1996, The IAC Morphological Catalogue of Northern Galactic Planetary Nebulae, Instituto Astrofisico de Canarias, Tenerife.

Marten, H., Schönberner, D. 1991, A&A 248, 590

Mathews, W.G. 1966, ApJ 143, 173

Mellema, G. 1994, A&A 290, 915

Mellema, G. 1995, MNRAS 277, 173

Mellema, G. 1996a, in: Jets from Stars and Galactic Nuclei, W. Kundt (ed.), Springer, Berlin, p. 149

Mellema, G. 1996b, ApSS 238, 113

Mellema, G., Frank, A. 1995, Annals of the Israel Phys. Soc. 11, 229

Olofsson, H. 1993, in: *Mass loss on the AGB and beyond*, H.E. Schwarz (ed.). ESO, Garching, p. 330

Olofsson, H. 1994, in: *Circumstellar Media in the Late Stages of Stellar Evolution*, R.E.S. Clegg, I.R. Stevens, W.P.S. Meikle (eds.), CUP, Cambridge, p. 246

Olofsson, H. 1996, ApSS in press

Pauldrach, A., Puls, J., Kudritzki, R.P., Méndez, R.H. Heap, S.R. 1988, A&A 207, 123

Perinotto, M. 1993, in: IAU symposium 155: *Planetary Nebulae*, R. Weinberger, A. Acker (eds.). Kluwer, Dordrecht, p. 57

Schwarz, H.E., Corradi, R.L.M., Melnick, J. 1993, A&AS 96, 23

Soker, N. 1994, MNRAS 270, 774

Soker, N. 1996, ApJ 469, 734

Soker, N., Harpaz, A. 1992, PASP 104, 923

Stanghellini, L., Pasquali, A. 1995, ApJ 452, 286

Vassiliadis, E., Wood, P.R. 1994, ApJS 92, 125

ABSORPTION SPECTRA OF CIRCUMSTELLAR DISKS

J. Krełowski
Institute of Astronomy, Nicholas Copernicus University
Chopina 12//18, PL-87-100 Toruń, Poland
e-mail: jacek@astri.uni.torun.pl

Abstract

The young objects, being still closely related to the relic, circumstellar matter are known as Be stars, characterized by the emission in the Fraunhofer D3 HeI (5876 Å) line and the specific profiles of the hydrogen Balmer lines containing emission cores originating in rotating, circumstellar disks. Such circumstellar shells are capable of producing quite a substantial reddening, as well as the infrared emission. However, the extinction law, derived from their spectra is far not the same as in the general interstellar medium. The disks also apparently do not contain the carriers of the diffuse interstellar bands (DIBs) as the latter are either absent or very weak in spectra of Be stars.

1 Introduction

Diffuse Interstellar Bands (DIBs) are the features which, being known since the publication of Heger (1922), still remain unidentified. It is now evident that the optical properties of individual clouds differ substantially, i.e. that the pattern of the DIBs can change substantially from cloud to cloud. Moreover, their behaviour seems to be related to that of other interstellar absorptions.

The latter are usually observed in spectra of early type, reddened OB stars, because of their high luminosity and the lack of stellar lines in their spectra which allows to observe a variety of interstellar features such as:

- continuous extinction – which affects the broad-band colors of stars by the selective attenuation of starlight; for review see e.g. Mathis (1990);
- polarization of starlight, caused by the same grains, which must be at least partially aligned by some mechanism, most probably magnetic field;
- spectral lines of rarified atomic gases (especially in far-UV) – many resonant lines of several elements (Morton 1975);
- absorption features of simple molecular species (CH, CH^+, CN, C_2, H_2, CO); their pattern varies strongly from cloud to cloud (Crawford, 1992; Krełowski *et al.*, 1992; Snow, 1992);
- DIBs – the rapidly growing set of spectral features. Some of them are so broad that they can affect the local continuum levels; sometimes they

are so shallow that it is difficult to separate them from the continua; for review see Herbig (1995).

All the above features are mutually related and form absorption spectra of interstellar clouds (Krełowski et al. 1992). None of them can be changed without affecting all other ones. Let's consider some examples of interstellar features in spectra of Be stars which are classified as a Be object if any of the strong stellar lines (usually H_α) is observed in emission. In this paper we will not consider the P Cygni profiles but only the broad emission components with some absorption in their centers suggesting the presence of opaque circumstellar disks. The disk, rotating much slower than the star itself, can be assumed to be the remnant of the star parent cloud in contrast to the circumstellar matter producing P Cygni profiles which reveal a fast expansion of the matter from the stellar atmosphere. We can assume that such media differ considerably in their histories and the current physical conditions. The circumstellar disks produce continuous extinction. The recent atlas of extinction curves (Papaj et al., 1991) shows several "peculiar" extinction curves derived from spectra of Be stars. Such curves have been described for the first time by Sitko et al. (1981). The paper of Krełowski et al. (1992) suggests that DIB intensity ratios are strongly related to the shapes of extinction curves.

2 Setting the problem

The high resolution, high S/N spectra acquired in 1993 at the McDonald Observatory and in 1995 at the Pic du Midi Observatory allow to observe many of the DIBs together with the stellar lines of hydrogen and helium. We have selected the objects, listed in Table 1, to illustrate the behaviour of DIBs in spectra of "normal" and Be stars.

The recent review of Krełowski and Papaj (1993) suggests that the intrinsic flux distributions of both B and Be stars are identical, however altered by different extinction laws. The extinction curves, observed towards Be stars, suggest that circumstellar disks are populated by bigger grains than diffuse interstellar clouds. Perhaps the DIB carriers are incorporated into these big grains in the course of the cloud evolution leading to the star formation.

3 The observations

The targets, listed in Table 1, have been observed with the aid of two echelle spectrographs. One of them is installed at the Cassegrain focus of the McDonald Observatory 2.1m telescope and permits to cover in a single exposure the range ~5600 – ~7000 Å. For the data acquiring and reduction see Krełowski & Sneden (1993). The second one is the MISICOS – the optical fibre spectrograph, attached to the 2.03m Bernard Lyot Telescope of the Pic du Midi Observatory. The latter permits to cover the range ~3800 Å – ~8750 Å in two exposures

Table 1: Basic stellar data

HD	Sp/L	V	B−V	E(B−V)
2905	B1 Ia	4.19	0.14	0.33
23180	B1 III	3.82	0.05	0.26
24534	O9.5pe	6.10	0.29	0.56
42087	B2.5 Ib	5.75	0.21	0.35
164284	B2 Ve	4.64	−0.03	0.18
184915	B0.5 III	4.95	−0.05	0.22

(Baudrand & Böhm, 1992).

The observed stars are listed in Table 1.

Figure 1 shows the wavelength range containing the 5876 Å strong helium line, usually observed in atmospheres of hot stars. Both our targets belong to the same stellar association. However, they differ by more than a factor of 2 in the colour excess E_{B-V}. The HeI line profile, observed in HD 24534, clearly indicates the presence of a circumstellar disk around this object in contrast to the second star.

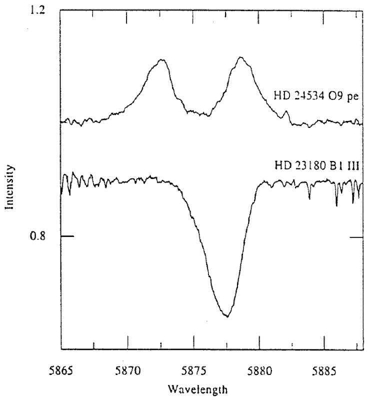

Figure 1: The profiles of the stellar HeI lines in the spectra of HD 23180 and HD 24534 – the stars from the Per $OB2$ association. Note the difference in reddening.

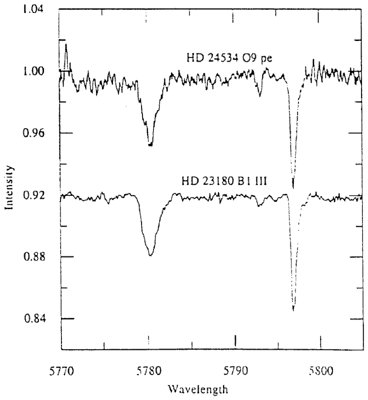

Figure 2: The 5780 and 5797 diffuse interstellar bands in the spectra of HD 23180 and HD 24534. Their intensities are identical in both spectra despite the difference in reddening.

Figure 2 shows the prominent DIBs: 5780 and 5797 in the same two spectra. It is evident that in both cases the intensities of the features are identical in spite of the evident difference of the E_{B-V}'s. This phenomenon can be interpreted in terms of the absence of the diffuse band carriers in the circumstellar disk which, however, contains the dust grains, responsible for the reddening.

Another pair of stars selected for our project is HD 2905 and HD 42087. Both objects are B supergiants of very similar reddening. However, the former is classified as a Be star. Are the DIBs also weaker in its spectrum? Figure 3 presents the range of the two spectra containing the strong stellar H_α line. Apparently HD 2905 is classified as a Be star due to this emission. However, the neighbour 6614 DIB looks very similar in both spectra.

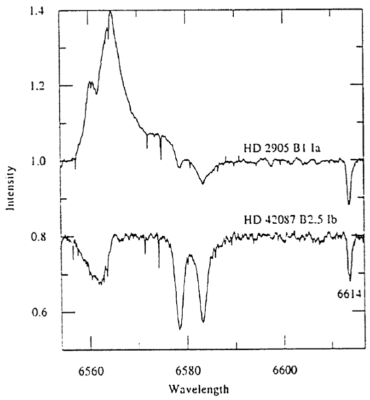

Figure 3: The spectral range containing H_α stellar line and the interstellar 6614 feature in the spectra of HD 2905 and HD 42087 – two supergiants of very similar reddening

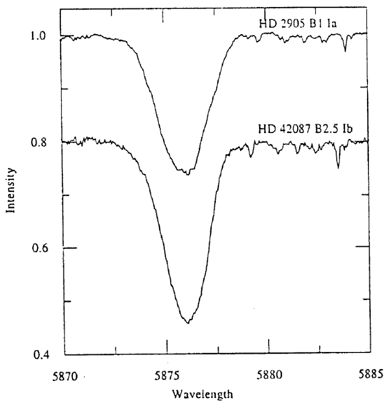

Figure 4: The spectral range containing HeI 5876 Å stellar line in the spectra of HD 2905 and HD 42087.

Figure 4 shows the stellar HeI 5876 Å line in both spectra. Apparently it is a very similar, absorption feature in both cases. No signs of a circumstellar disk around any of our targets can be found here.

Figure 5 proves that the prominent DIBs are of the same intensities in both spectra as well as the reddenings of both stars. This suggests that the emission in only H_α lines does not alter the diffuse interstellar spectrum.

The circumstellar disks, causing some extinction but not containing the DIB carriers, may be indicated also by the presence of special hydrogen line profiles. Our last pair of targets is presented in the following figures. Figure 6 shows the profile of the H_γ stellar line in the spectra of HD 164284 and HD 184915. Both targets are of similar reddening. However, the former is apparently encircled with a disk, rotating slower than the star itself.

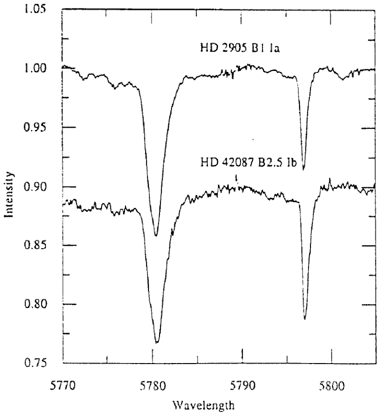

Figure 5: The spectral range containing the prominent 5780 and 5797 diffuse bands in the spectra of HD 2905 and HD 42087.

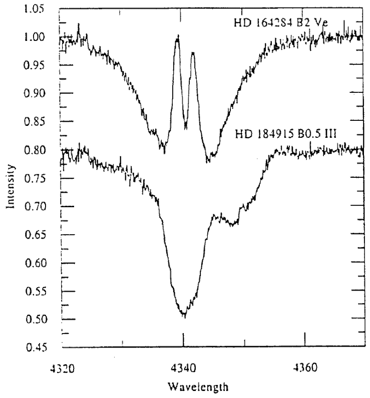

Figure 6: The profiles of the H_γ line in the spectra of HD 164284 and HD 184915.

The last figure (Figure 7) compares the major DIBs in the same spectra. It is clear that both features are weaker in the target where the disk is present. Apparently also in this case a part of the reddening towards HD 164284 originates in the disk.

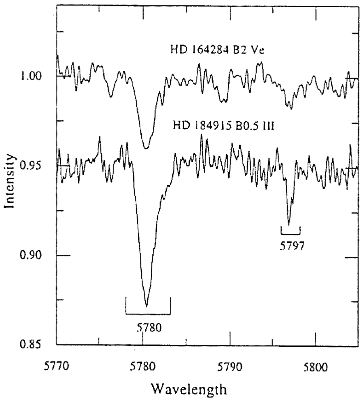

Figure 7: The spectral range containing the prominent 5780 and 5797 diffuse bands in the spectrum of HD 164284 and HD 184915.

4 Discussion

The existing spectra suggest that the opaque, circumstellar disks, most probably rotating slower than their central stars, can create extinction. The latter should be accompanied by some infrared emission as the dust particles, situated around a hot star, must be hotter than typical interstellar grains. This may lead to the observed, incredibly high ratios of total to selective extinction.

However, the same disks, in which the E_{B-V}'s as large as 0.3 mag may origin, apparently do not contain the carriers of the unidentified diffuse interstellar bands. In all observed cases the presence of emission lines originating in a circumstellar disk, the DIBs are very weak in comparison to other objects of the same E_{B-V} in which we observe no emission lines at all or the only emission line is H_α.

As it seems quite difficult to build the dust grains in the matter just being shed from a very hot star we expect these circumstellar disks to be made of the relic matter – formed together with central stars in the course of gravitational collapse. Thus the grains are very likely to be relatively large which may be reflected in the shapes of the usually observed extinction curves without the prominent 2200 Å feature. In the course of the collapse the DIB carriers stick to grain surfaces and loose their identities. This makes the grains larger and changes the shape of the extinction curve. The DIB carriers, incorporated into the grains, do not produce the bands any more.

Acknowledgements

This project was supported by the Polish National Committee for Scientific Research under the grant PB–0913/P3/94/07. The author wishes to express his gratitude to the McDonald and Pic du Midi Observatories where the spectra have been acquired.

References

Baudrand, J. & Böhm, T. 1992, Astr. Astrophys., 259, 711.

Crawford, I.A. 1992, Mon. Not R. Astr. Soc., 254, 264.

Heger, M.L. 1922, Lick Obs. Bull. 10, 146.

Herbig, G.H. 1995, ARA&A, 33, 19.

Krełowski, J., Snow, T.P., Seab, C.G., & Papaj, J. 1992, Mon. Not R. Astr. Soc., 258, 693.

Krełowski, J., Papaj, J. 1993, PASP 105, 1209.

Krełowski, J. & Sneden, C. 1993, Publs. Astr. Soc. Pacific, 105, 1141.

Mathis, J. 1990, ARA&A, 28, 37.

Morton, D.C. 1975, ApJ, 197, 85.

Papaj, J., Wegner, W., and Krełowski, J. 1991, MNRAS, 252, 403.

Sitko, M.L., Savage, B.D., Meade, M.R. 1981, ApJ, 246, 161.

Snow, T.P. 1992, Australian J. Phys., 45, 543.

POSSIBLE INTERACTION OF SOME RS CVn-TYPE BINARIES WITH THEIR ENVIRONMENT

F.F. Özeren, B. Albayrak, F. Ekmekçi and O. Demircan
Ankara University, Faculty of Sciences
Department of Astronomy and Space Sciences
Tandoğan, Ankara 06100, Turkey
e-mail: ozeren@dione.astro.science.ankara.edu.tr

Abstract

Long-term period variation of seven RS CVn type eclipsing binaries (RT Lac, RT And, CG Cyg, SV Cam, WY Cnc, SZ Psc and WW Dra) are presented and interpreted in terms of possible interaction of these binaries with their environment.

1 Introduction

RS Cvn-type binaries mostly exhibit both period increases and decreases (Hall and Kreiner 1980), and they are known to be detached binaries with late type components whose mass ratios are remarkably close to unity (e.g. Hall 1978, Demircan 1990). It is thus difficult to explain their alternating period changes in terms of mass transfer and mass loss. DeCampli and Baliunas (1979) proposed the anisotropic wind (the so called rocket effect) as the cause of alternating period changes in RS CVn systems and Hall and Kreiner (1980) applied this model to 34 RS CVn systems. Later observations proved the invalidity of this model (Hall 1990). Among the existing models proposed to explain cyclic period variations of eclipsing binary stars three mechanisms have seemed plausible for our sample of the RS CVn systems :

i) apsidal motion of the elliptical orbit,

ii) period modulation due to magnetic activity cycle of a component star

iii) light time effect due to additional objects in the system.

The apsidal motion hypothesis is not valid for the circular orbits of these systems. The cyclic magnetic activity effect seems quite possible, since the components of these systems are late type and they display spin-orbit coupling. Unfortunately due to insufficient data, the predictions of this theory could not be checked properly. We noted however that the period estimates of the O$-$C variations are all too long in comparison to magnetic cycles in solar type single and close binary stars, as compiled by Maceroni et al. (1990) and Bianchini (1990).

In the present work we collected, for seven RS CVn systems, additional times of minima after Hall and Kreiner's compilation, and analysed the period variations in terms of possible interaction with their environment.

Table 1: Summary of the collected moments of minima

	RT Lac	RT And	CG Cyg	SV Cam	WY Cnc	SZ Psc	WW Dra
n_{pe}	31	111	40	129	21	6	3
n_{ph}	82	12	2	-	4	21	31
n_v	-	-	1	147	1	11	43
n_{total}	113	131	43	276	26	38	77
T_0	40382.891	41141.888	44528.5351	34988.483	26352.3895	42308.946	28020.3481
P	5.074015	0.6289298	0.63114347	0.593071	0.82937121	3.965866	4.629617
$\overline{T_0}$	40382.84	41141.8888	22967.4248	41212.763	26352.40467	42308.946	28020.3481
$\overline{P}$	5.073985	0.6289313	0.63114347	0.5930718	0.82937034	3.9658663	4.6296166

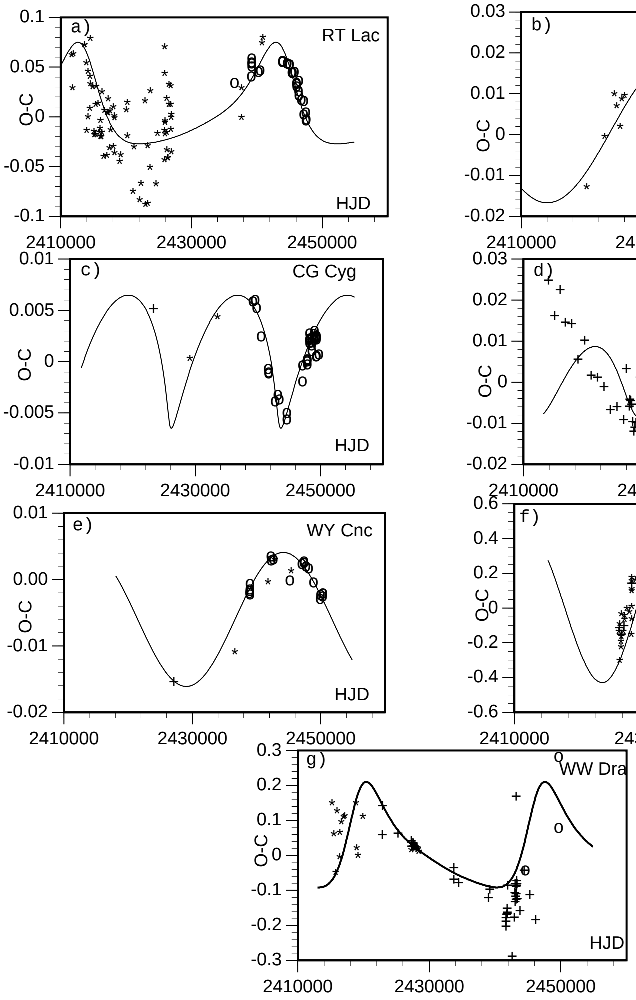

Figure 1: The O−C diagrams of RT Lac, RT And, CG Cyg, SV Cam, WY Cnc, SZ Psc and WW Dra (n_e=o, n_v=+, n_p=*)

Table 2: Some parameters (extracted from the CABS catalog of our sample RS CVn systems)

Star No	Star	Sp	m_{hot}	m_{cool}	M_v(hot/cool)	i(deg)	d(pc)
189	RT Lac	G5:+G9IV	0.78	1.66	2.9/3.4	89	205
201	RT And	F8V+K0V	1.5	0.99	5.5/3.9	88.9	95
177	CG Cyg	G9.5V+K3V	0.52	0.52	[5.8/6.65]	81.8	[≈63]
65	SV Cam	G2-3V+K4V	0.93	0.67	5.0/6.74	89.5	74
82	WY Cnc	G5V+M2	0.93	0.53	3.5/3.2	[≈90]	160
202	SZ Psc	F8IV+K1IV	1.28	1.62	2.8/2.3	76	125
136	WW Dra	G2IV+K0IV	1.36	1.34	3.0/3.2	81.4	180

Table 3: The preliminary third body solution of seven RS CVn systems

	RT Lac	RT And	CG Cyg	SV Cam	WY Cnc	SZ Psc	WW Dra
A(d)	0.052	0.025	0.0058	0.0085	0.01	0.37	0.15
$P_s(yr)$	83	108	48	44	83	58	74
a_{12}	9	3.1	1.0	1.5	1.8	66	26
$f(m_3)(M_\odot)$	0.106	0.0025	0.0004	0.0017	0.0008	78	3.48
$M_3(M_\odot)$	1.1	0.3	0.1	0.2	0.1	-	-
$M_{12}(M_\odot)$	2.44	2.49	1.04	1.6	1.46	2.9	2.7
Δm	2^m	6^m	7^m	6^m	9^m	-	-
$V_{max}(km/s)$	2.79	0.84	0.58	0.85	0.63	33	14.0

2 Data

The collected moments of minima including Hall and Kreiner's compilation for seven RS CVn systems are summarized in Table 1, where n_{pe}, n_{ph} and n_v stand for the number of photoelectric, photographic, and visual times of minima. The new data are available on request from the authors. Some of the system parameters (spectral type, mass, and the visual absolute magnitude of component stars, inclination of the orbit and the distance) are listed in Table 2.

3 O−C diagrams

The collected times of minima, 704 altogether, for seven systems, are used in forming the O−C residuals. The initial C values are obtained by using the light elements listed in Hall and Kreiner (1980). They are also given in Table 1. By adjusting the initial period, we estimated the mean value of the period and epoch (see Table 3). The O−C diagrams of seven RS CVn systems are plotted in Figure 1 where the values of C are calculated by using the mean values of P and T_0 from Table 1.

It is seen in Figure 1 that the O−C diagrams are not formed by linear segments. They represent continuous oscillatory variations, although only about one cycle is covered in each case by the present data.

4 Interpretation and discussion

The periodic O−C curves in Figure 1 display asymmetries indicating the effect of motion in eccentric orbit. We thus analysed the present data assuming the light time effect due to unseen component stars in the systems. Assuming initially coplanar third body orbits we obtained the preliminary masses for the hypothetical main sequence third stars in these systems. The preliminary third body parameters are listed in Table 3, where A is the amplitude and P_s is the period of O−C variation, a_{12} is the radius of the binary's orbit around the common mass center of the triple system, M_{12} is the total mass of the binary from CABS catalog, Δ_{max} is the brightness difference between binary and third star, and V_{max} is the maximum orbital velocity of the binary around the common centre of mass of the triple system.

Theoretical O−C curves are shown in Figure 1 as continuous lines. In the case of SZ Psc and WW Dra the unseen component masses are so high that the light time effect explanation should be unrealistic for these systems.

Although only about one cycle is covered by the present data, the cyclic nature of the O−C variation of other systems can be explained in terms of the gravitational interaction of binaries with the unseen third component stars. The asymmetric variation of the O−C curves for RT Lac, CG Cyg, and SV Cam indicate eccentric orbits around the common center of mass of the triple systems. The hypothetical third stars are too faint and the orbital velocities are too small to check the existence of these stars by other means. Future eclipse timing is thus highly valuable for these systems.

Acknowledgements

The authors thank to Dr. Z. Müyesseroğlu for his kind help.

References

Applegate, J.H., 1992, ApJ 385, 621

Bianchini, A., 1990, AJ 99, 1941

DeCampli, W.M., Baliunas, S.L., 1979, ApJ, 230, 815

Demircan, O., 1990, in *Active Close Binaries*, ed. C. Ibanoglu, Kluwer, p.431

Hall, D.S., 1978, AJ, 83, 146

Hall, D.S., 1990, in *Active Close Binaries*, ed. C. Ibanoglu, Kluwer, p.95

Hall, D.S., Kreiner, J.M., 1980, Acta A. 30, 387

Maceroni C., Bianchini, A., Rodono M., Van't Veer F., Vio, R., 1990, A&A, 237, 395

INTERACTION OF ECLIPSING BINARIES WITH THEIR ENVIRONMENT

O. Demircan
Ankara University, Faculty of Sciences
Department of Astronomy and Space Sciences
Tandoğan, Ankara 06100, Turkey
e-mail: demircan@astro1.science.ankara.edu.tr

Abstract

The interaction of eclipsing binary star systems with the mass around (in the form of star, planet, envelope or disk) affects the orbital period of these systems. Thus, the long-term orbital period changes of eclipsing binaries which can be deduced by using the observed times of eclipse minima provide a good tool in understanding the interaction of eclipsing binaries with their environment. In the present contribution many examples of the orbital period changes of different eclipsing binaries are presented and interpreted in terms of the interaction with their environment.

1 Introduction

The most easily detectable parameter of the eclipsing binaries is the photometric period (the period of the light variation), which in most cases, becomes equal to the orbital period of the systems. The O$-$C diagrams formed by the observed times of eclipse minima provide the basis for studying time dependent period variations. Thus, the long-term monitoring of the eclipse timing in these systems revealed actual period changes, in some cases indicative of the gravitational interaction of binaries with the unseen third component stars around (e.g. Frieboes-Conde and Herczeg 1973, Mayer 1990). If there is a third star in the system, simply the binary orbits around the common mass center of the triple system, thus changes its distance from us periodically and due to light time effect the times of minima shift also periodically. The pertinent formula was given e.g. by Irwin (1959).

2 Problems with the observational data

The present data forming the O$-$C diagrams rarely permit deducing definite periodic character giving observational evidence of the gravitational interaction of binaries with unseen component stars.

- First, the long-term monitoring of the eclipse timing in most cases covers less than one cycle in the periodic O$-$C diagrams.
- The large gaps, particularly during the two world wars raise difficulties in deducing the character of O$-$C variation.

- Observational scatter of the data (which for visual and photographic estimates may sometimes reach ± 0.02 day or more) makes it difficult to recognize a small amplitude light-time effect. Thus, if the binary has not deep eclipse minima and/or the amplitude of O−C variation is less than about 0.01 day, then much of the earlier visual and photographic observations are of limited usefulness.
- In many cases the expected regularity in the O−C diagram could be obliterated by some other effects such as episodic mass loss, mass transfer, magnetic activity etc., or the O−C variation could be formed by the summation of many effects. In this case the periodic light-time effect can be restored by taking the other effects into proper consideration.
- In some cases even the photoelectric times of minima may be markedly influenced by distortions in the light curves, notably by asymmetries of the eclipse minima. Available evidence seems to indicate that such asymmetries cause only a scatter in the O−C diagrams but do not deform large genuine variations (see e.g. Geyer 1977, Olson 1985).
- Unfavorable choice of the period used for calculating the C epochs may also cause difficulty in discussion of a possible light time effect.

3 Eclipsing binaries with light-time effect

It is known that the light time effect produces periodic O−C curve whose shape depends only on the eccentricity and the longitude of periastron of the eclipsing binary orbit with respect to a distant third component. However periodic O−C variations are also caused by the apsidal motion of the elliptical motion of the eclipsing pair or by little understood cyclic changes in the internal structure of one or both of the eclipsing components. Therefore, only the periodic O−C variation is insufficient for the light-time effect interpretation. Some other necessary criteria have been listed by Frieboes-Conde and Herczeg (1973): The secondary minima should behave identically with primary minima in the O−C diagram; the resulting mass function for the unseen third component should be reasonable. The corresponding third light should appear in the light curve solutions. The theoretical estimates of the systemic radial velocity difference in brightness and the angular separation between the binary and third star should all be acceptable. Interferometric and spectroscopic detection of the third bodies in binary systems are relatively easy under certain conditions. A list of such binaries is given by Fekel (1981) and Chambliss (1992). At present, there are only nine cases of definite light time effects observed in the long term O−C diagrams for which the triplicity of the system is supported by some other technique (see Table 1).

Table 1: Eclipsing binaries with periodic O−C diagrams caused by the additional component stars.

	Sp	P_1(d)	P_2(yr)	M_3 sin i	Reference
Algol	B8V+G8IV	2.87	1.86	1.6	Eggen 1948
EE Peg	A3+F5	2.63	4.01	≈0.5	Lacy & Popper 1984
IM Aur	B7V+A	1.25	3.78	1.6	Bartolini & Zoffoli 1986
IU Aur	B0pV+	1.81	0.88	12.8	Mayer 1983
44 i Boo	GIV+G	0.27	225	-	Hill et al. 1989
FZ CMa	B2.5V+	1.27	1.48	14.0	Moffat et al. 1983
XY Leo	K0V	0.28	20	0.85	Hrivnak 1985, Barden 1987
ER Ori	F8V	0.42	63	0.9	Geocking et al. 1994
V505 Sgr	A2V+G5IV	1.88	105	-	Chambliss 1993, Tomkin 1992

4 Eclipsing binaries with possible light-time effect

Increasing number of accurate photoelectric minima timings, in recent years revealed many possible light time effects or strengthened the suspected cases. Such eclipsing binaries with possible additional component stars are listed in Table 2. The list is by no means complete, and in no case in this list, the existence of third star is confirmed yet by other techniques.

Moreover, the early very incomplete observations of the following eclipsing binaries show the signature of cyclic O−C variation. They are TW And, RY Aqr, KO Aql, W Del, Z Dra, SX Dra, S Equ, UX Her, RX Hya, Y Leo, RV Lyr, RW Mon, SW Oph, TY Peg, Z Per, Y Psc, RW Tau and X Tri. With the up to date observations, some of these binaries may turn out to be triple systems.

The O−C diagrams of four interesting systems are presented in Figures 1-4. Theoretical best fit third body effects are also drawn. The O−C diagram of U Cep in fact oscillates around a parabola caused by the episodic mass transfer from the less massive to more massive component. Figure 1 presents the residuals from this parabola. It is seen that the O−C diagrams of U Cep, XZ And and TX UMa are representable by the summation of two (or three) different sine curves, each. The O−C diagram of SS Ari is represented by a single sine curve. Triplicity of SS Ari is almost definite. The interacting third body should be around 1.0 $M_\odot$, which should be bright enough to be detected if it is a normal star. It can also be a binary, just as in the case of XY Leo (cf. Barden 1987). We think that at least one or two sine curves forming the O−C diagrams of U Cep, XZ And and TX UMa should be real and caused by the light time effect due to gravitational interaction of additional objects in these systems. The sine curves with the largest amplitudes in the O−C curves of U Cep and XZ And require bright component stars (only ≈1 mag fainter than the binary). They can also be binaries. However, in the case of Y Cam and SW Cyg (see Table 2) if the periodic O−C curves (which have been observed for only about one cycle) are due to light time effects, then the third component stars should be at least 6 and 11 $M_\odot$, respectively. Binarity assumption of these stars does not solve the problem of their invisibility. In this case, they can only be black holes! At

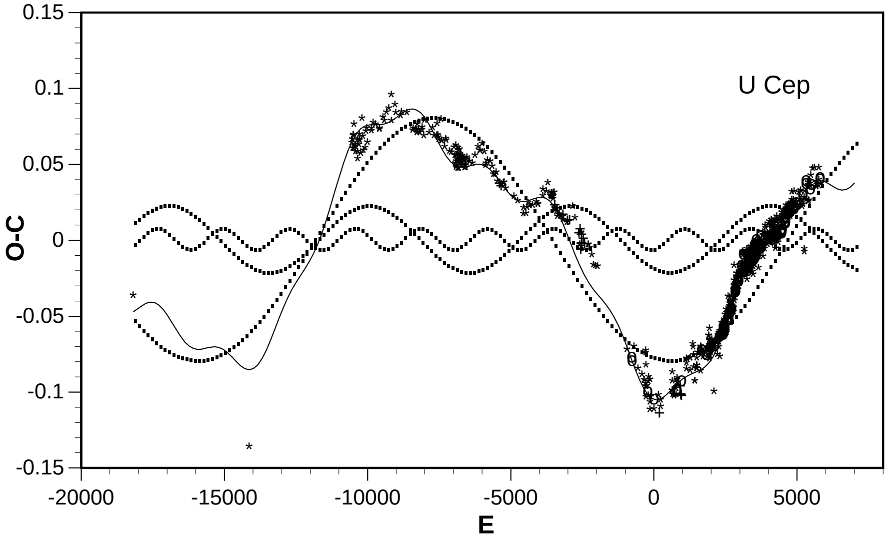

Figure 1: Representation of residuals from the mean parabolic variation of the O−C diagram of U Cep by the summation of three different sine curves (after Selam and Demircan 1996)

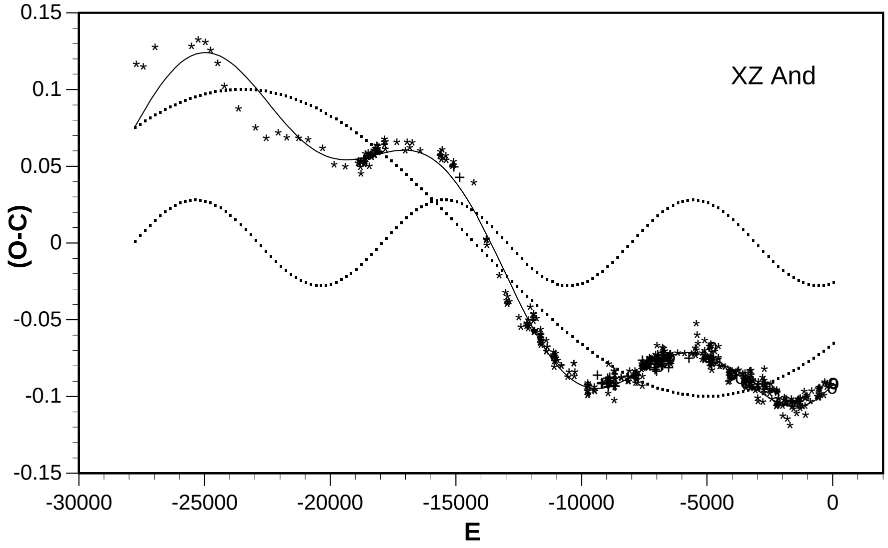

Figure 2: Represantion of the O−C diagram of XZ And by the summation of three different sine curves (after Demircan et al. 1995)

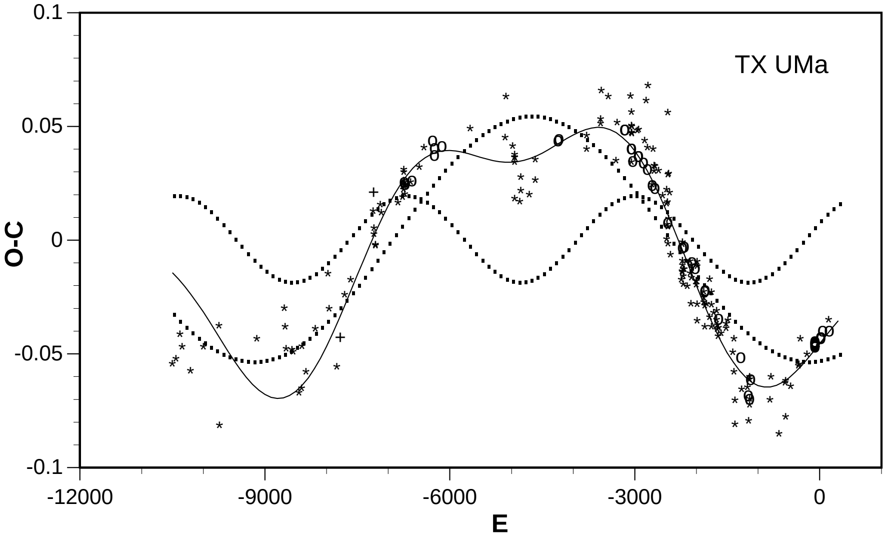

Figure 3: Represantion of the O−C diagram of TX UMa by the summation of two different sine curves (after Demircan et al. 1995)

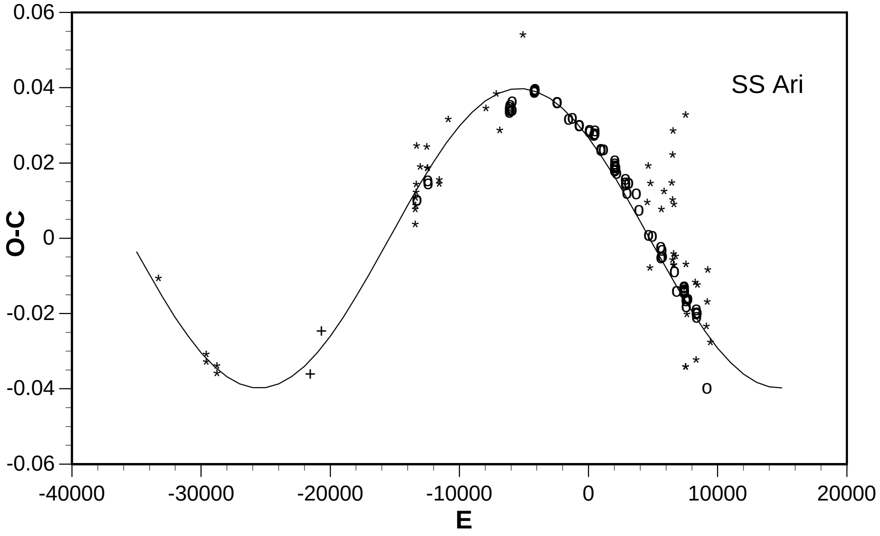

Figure 4: Represantion of the O−C diagram of SS Ari by a sine curve (after Demircan et al. 1995)

present, there is nothing against this hypothesis. In fact, this is the only way to detect remote black hole components of eclipsing binaries.

Table 2: Eclipsing binaries with possible light-time effect

Name	Sp	P_1(d)	P_2(yr)	$M_3(M_\odot)$	References
RT And	F8V+K0V	0.63	108	0.3	Özeren et al. 1997
XZ And	A4IV-V+G5IV	1.36	11	0.4	Demircan et al. 1995
			37	1.2	
			138	1.9	
AB And	G5V+G5V	0.33	88	0.9	Demircan et al. 1994
BX And	F2V	0.61	71	0.3	Demircan et al. 1993
OO Aql	G5V	0.51	89	0.8	Demircan & Gürol 1996
SS Ari	F8V	0.41	45	1.0	Demircan & Selam 1993a
AR Aur	B9V+A0V	4.14	27	0.5	Chochol et al. 1988
Y Cam	A9IV+K1	3.31	86	6.0	Mossakovskaya 1993
SV Cam	G2-3V+K4V	0.59	44	0.2	Özeren et al. 1997
R CMa	F2V	1.14	91	0.5	Radhakrishnan et al. 1984
RZ Cas	A3V	1.20	5	0.2	Hegedüs et al. 1992
			6	0.2	
			18	0.2	
			37	0.2	
TV Cas	B9V+F7IV	1.81	56	0.6	Erdem 1996
V444 Cas		2.22			Kurochkin 1979
BH Cen	B5V	0.79	50	4.0	Herczeg 1984
U Cep	B7V+G8III-IV	2.49	16	0.7	Selam & Demircan 1997
			48	1.0	
			113	2.3	
GK Cep	A2V+A2V	0.94	18	1.7	Derman & Demircan 1992a
WY Cnc	G5V+M2	0.83	83	0.1	Özeren et al. 1997
U CrB	B6V+F8IV	3.45	75		Van Gent 1982
SW Cyg	A2 +K0	4.57	100	11	Todoran & Agerer 1994
CG Cyg	G9.5V+K3V	0.63	48	0.1	Özeren et al. 1996
V463 Cyg	A0V	2.12			Vetesnik & Papousek 1968
V512 Cyg	A0V	2.42			Häussler 1968
V1580 Cyg		1.81	22		Hoffleit 1977
TW Dra	A8V+K0III	2.81			Abhyankar & Panchatsaram 1984
YY Eri	G5V+G5V	0.32	24	0.2	Kim 1992
TX Her	A5 +F0	2.06	48	0.45	Vetesnik & Papousek 1973
AK Her	F2V	0.42	78	0.2	Barker & Herczeg 1979
RT Lac	G5:+G9IV	5.07	83	1.1	Özeren et al. 1997
SW Lac	G3V+G3V	0.32	20	1.0	Panchatsaram & Abhyankar 1981
			70	1.0	
AM Leo	F8V	0.37	33	0.1	Demircan & Derman 1992
AP Leo	G0V	0.43	43		Zhang et al. 1989
T LMi	A3V	3.02	66	1.1	Busch 1982
RU Mon	B7V	3.59	68	2.2	Khaliullina et al. 1985
U Oph	B5V+B5V	1.68	39	0.8	Kamper 1986
V502 Oph	G2V+F9V	0.45	35	0.3	Derman & Demircan 1992b
V839 Oph	F8V	0.41			Wolf et al. 1996
RT Per	F2V	0.85	42	0.7	Panchatsaram 1981
RW Per	A5III+G0III	13.20	64	3.5	Demircan et al. 1996
			100	0.6	
ST Per	A3V+K1-2IV	2.65	23	0.9	Demircan & Selam 1993b
			83	0.9	
V471 Tau	K2V+WD	0.52	25	0.05	Ibanoglu et al. 1994
TX UMa	B8V+G0III-IV	3.06	31	1.5	Demircan et al. 1996
			76	2.5	
XY UMa	G2-5V+K5V	0.48	25	0.3	Pojmanski & Geyer 1990
AH Vir	K0V+K0V	0.41	10	0.5	Demircan et al. 1991
DR Vul	B0V	2.25	18	3.4	Khaliullina 1987
			47	5.4	

5 Conclusion

Component stars around binary systems based on the spectroscopic and astrometric data have been reviewed by Fekel (1981) and Chambliss (1992). As the examples in this work demonstrate, the oscillatory nature of the O−C diagrams of eclipsing binaries deserves further consideration in terms of the hypothesis of simple geometrical light time effects due to unseen objects in the systems. The number of systems where the presence of light time effect in the O−C diagrams is still low and does not allow any statistical conclusions to be drawn. This is because of the problems in handling the insufficient observational data (see Section 2). It is expected that further efforts on this line will rapidly increase the number of eclipsing binaries with additional component stars around. Invisible black hole components as well as the planet size objects may also be detected in this way.

References

Abhyankar, K.D., Panchatsaram, T., 1984, MNRAS 211, 75

Barden, S.C., 1987, ApJ 317, 333

Barker, L.A., Herczeg, T., 1979, PASP 91, 247

Bartolini, C., Zoffoli, M., 1986, A&A 168, 377

Busch, H., 1982, Hartha Mitt. 17, 12

Chambliss, C.R., 1992, PASP 104, 663

Chambliss, C.R., 1993, AJ 106, 2058

Chochol, D., Juza, K., Mayer, P., Zverko, J., Ziznovski, J., 1988, BAC 39, 69

Demircan, O., Akalın, A., Derman, E., 1993, A&AS 98, 583

Demircan, O., Akalın, A., Selam, S.O., Derman, E., Müyesseroğlu, Z., 1995, A&AS 114, 167

Demircan, O., Derman, E., 1992, AJ 103, 593

Demircan, O., Derman, E., Akalın, A., 1991, AJ 101, 201

Demircan, O., Derman, E., Akalın, A., Selam, S.O., Müyesseroğlu, Z., 1994, MNRAS 267, 19

Demircan, O., Derman, E., Müyesseroğlu, Z., Selam, S.O., Akalın, A., 1996, unpublished

Demircan, O., Gürol, B., 1996, A&AS 115, 333

Demircan, O., Selam, S.O., 1993a, A&A 267, 107

Demircan, O., Selam, S.O:, 1993b, A&AS 98, 513

Derman, E., Demircan, O., 1992a, AJ 103, 599

Derman, E., Demircan, O., 1992b, AJ 103, 1658

Eggen, O.J., 1948, ApJ 108, 1

Erdem, A., 1996 PhD Thesis, Ege Univ. Izmir, unpublished

Fekel, F.C., 1981, ApJ 246, 879

Frieboes-Conde, H., Herczeg, T., 1973, A&AS 12, 1

Geocking, K.D., Duerbeck, H.W., Plewa, T., Kaluzny, J., Schertl, D., Weigelt, G., Flin, P., 1994, A&A 289, 827

Geyer, E.H., 1977, Ap&SS 48, 137

Häussler, K., 1968, Hartha Mitt. 1.

Hegedüs, T., Szatmáry, K., Vinkó, J., 1992, Ap&SS 187, 57

Herczeg, T., 1984, IBVS No. 2477

Hill, G., Fisher, W.A., Holgren, D., 1989, A&A 211, 81

Hoffleit, D., 1977, IBVS No. 1252.

Hrivnak, B.J., 1985, ApJ 290, 696

Ibanoglu, C., Tunca, Z., Evren, S., Keskin, V., Akan, C., 1994, A&A 281, 811

Irwin, J.B., 1959, AJ 64, 149

Kamper, B.C., 1986, Ap&SS 120, 167

Khaliullina, A.I., 1987, MNRAS 225, 425

Khaliullina, A.I., Khaliullin, K.F., Martynov, D.Y., 1985, MNRAS 216, 909

Kim, C.H., 1992 in *Evolutionary processes in interacting binary stars*, eds. Y. Kondo et al., Kluwer p.383.

Kurochkin, N.E., 1979, Astron. Circ. No. 1065

Lacy, C.H., Popper, D.M., 1984, ApJ 291, 268

Mayer, P., 1983, BAC 34, 335

Mayer, P., 1990, BAC 41, 231

Moffat, A.F.J., Vogt, N., Vaz, L.P.R., Gronbech, B., 1983, A&A 120, 278

Mossakovskaya, L., 1993, IBVS No. 3902

Olson, E.C., 1985 in *Interacting Binaries*, NATO ASI Ser. C Vol.150 p.127

Özeren, F.F., Albayrak, B., Ekmekçi, F., Demircan, O., 1997 in these proceedings, p. 393

Panchatsaram, T., 1981, Ap&SS 77, 179

Panchatsaram, T., Abhyankar, K.D., 1981, PAS India 9, 31

Pojmanski, G., Geyer, E.H., 1990, AcA 40, 245

Radhakrishnan, K.R., Sarma, M.B.K., Abhyankar, K.D., 1984, Ap&SS 99, 229

Selam, S.O., Demircan, O., 1997, will be submitted to A&A

Todoran, I., Agerer, F., 1994, AN 315, 349

Tomkin, J., 1992, ApJ 387, 631

Van Gent, R.H., 1982, A&AS 48, 457

Vetesnik, M., Papousek, J., 1968, BAC 19, 123

Vetesnik, M., Papousek, J., 1973, BAC 24, 57

Wolf, M., Sarounova, L., Molik, P., 1996, IBVS No. 4304

Zhang, J.T., Zhang, R.X., Zhai, D.S., Li, Q.S., Jin, T.L., 1989, IBVS No. 3302

VISCOUS TRANSONIC OUTFLOW IN EQUATORIAL DISCS OF Be STARS

A. T. Okazaki
Institute of Astronomy 'Anton Pannekoek', University of Amsterdam
Kruislaan 403, 1098 SJ Amsterdam, The Netherlands
and
College of General Education, Hokkai-Gakuen University
Toyohira-ku, Sapporo 062, Japan
e-mail: okazaki@elsa.hokkai-s-u.ac.jp

Abstract

We discuss the characteristics of the outflow in discs of Be stars, based on the viscous decretion disc scenario. Solving the wind equation, we find that a transonic solution exists for any α. The sonic point is located at $r > 100R$ for plausible values of parameters, where R is the stellar radius. The sonic radius is smaller for higher temperature and/or larger radiative force. We also find that the topology of the sonic point is nodal for $\alpha \gtrsim 0.95$, while it is saddle type for $\alpha \lesssim 0.9$. In the subsonic region, the outflow velocity increases as r and the surface density decreases as r^{-2}. The angular velocity of the disc decreases as $r^{-1/2}$ in the inner subsonic region, while it decreases as r^{-1} in the outer subsonic region.

1 Introduction

Be stars are non-supergiant early-type stars with Balmer emission lines, whose spectral types range from late O- to early A-type. Extensive studies have revealed that a Be star has a two-component extended atmosphere, a polar region and a cool disc-like region. The polar region consists of a low-density, fast outflow emitting UV radiation. The mass loss rate of this region inferred from the UV lines is about $10^{-11} - 10^{-9}\, M_{\odot}\,\mathrm{yr}^{-1}$ (Snow 1981).

In contrast to the polar region, the disc region consists of a high-density plasma whose outflow velocity is small. The optical emission lines and the IR excess arise from this region. Unfortunately, the nature of this region is not well understood, despite that large observational efforts have been devoted to the study of Be stars.

Lee et al. (1991) constructed a disc model, in which matter rotates at Keplerian speed but gradually drifts outward because of the effect of viscosity. Assuming Keplerian rotation and neglecting the advective term in the equation of momentum conservation, they obtained steady structure of viscous decretion discs around Be stars. The purpose of this paper is to study the characteristics of the outflow in viscous decretion discs around Be stars.

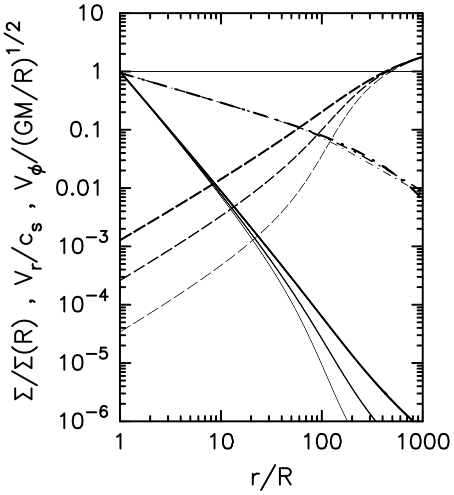

Figure 1: Structure of the viscous transonic decretion disc for $T_\mathrm{d} = \frac{2}{3}T_\mathrm{eff}$ and $(\eta, \epsilon) = (0.1, 0.1)$, where T_d is the disc temperature. Solid, dashed, and dash-dotted lines denote $\Sigma/\Sigma(R)$, V_r/c_s, and $V_\phi/(GM/R)^{1/2}$, respectively. Thick lines, lines with intermediate thickness, and thin lines are for $\alpha = 1$, $\alpha = 0.1$, and $\alpha = 0.01$, respectively

2 Basic equations for viscous decretion discs

We assume that the circumstellar disc of a Be star is steady, geometrically thin, and symmetric about the rotational axis and the equatorial plane. Moreover, we assume for simplicity that the disc is isothermal, and adopt the Shakura-Sunyaev viscosity prescription. Since the deviation from a point mass potential due to the rotational distortion of the star is small in general, we neglect the quadrupole contribution to the gravitational potential. We assume that the radiative acceleration arises from the absorption of stellar continuum by an ensemble of optically-thin weak lines, and adopt the parametric form for the radiative force proposed by Chen & Marlborough (1994).

From the vertically integrated equations describing the mass, momentum, and angular momentum conservation in a disc around a star of mass M and radius R, together with the equation of state and the Shakura-Sunyaev viscosity prescription, we obtain the following equations which describe the stationary viscous flow.

$$\left(V_r - \frac{c_\mathrm{s}^2}{V_r}\right)\frac{\mathrm{d}V_r}{\mathrm{d}r} = -\frac{GM}{r^2}\left[1-\eta\left(\frac{r}{R}\right)^{\epsilon}\right] + \frac{\ell^2}{r^3} + \frac{5}{2}\frac{c_\mathrm{s}^2}{r}, \tag{1}$$

$$\ell = \ell_\mathrm{s} + \alpha c_\mathrm{s}^2\left(\frac{r_\mathrm{s}}{c_\mathrm{s}} - \frac{r}{V_r}\right), \tag{2}$$

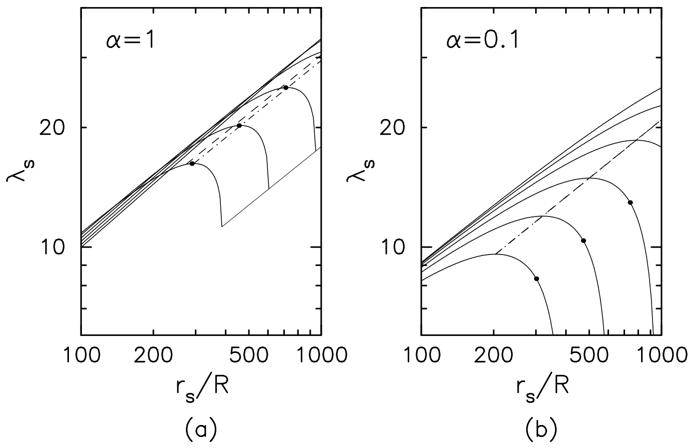

Figure 2: Diagram showing the location of the sonic points in the $(r_\mathrm{s}, \lambda_\mathrm{s})$-plane for (a) $\alpha = 1$ and (b) $\alpha = 0.1$, where $\lambda_\mathrm{s} = \ell_\mathrm{s} + \alpha c_\mathrm{s} r_\mathrm{s}$ is normalized by $(GMR)^{1/2}$. Each curve denotes the relation between r_s and λ_s for a constant sound speed. From the bottommost curve upwards $T_\mathrm{d}/T_\mathrm{eff} = 1.0$, 0.82, 0.64, 0.46, 0.28, and 0.10. The filled circle on each curve indicates the position of the sonic point. The dashed line separates the spiral-type sonic point region (upper side of the line) from the nodal-type sonic point region (lower side of the line), and the dash-dotted line separates the nodal-type region (upper side) from the saddle-type region (lower side). In Figure 2(b) the nodal-type region is so narrow that it is indistinguishable in the figure. The thin line on Figure 2(a) indicates the boundary in the parameter space below which the circular orbit at the sonic radius is unstable

where c_s is the isothermal sound speed, α is a viscosity parameter, η and ϵ are parameters which characterize the radiative force, and V_r and ℓ are the vertically-averaged radial velocity and specific angular momentum, respectively. The subscript ‘s’ denotes the quantities at the sonic point.

It is important to note that, in the current problem, the angular momentum distribution of the flow is not given a priori but obtained as the solution of Eqs. (1) and (2); r_s and ℓ_s are the eigenvalues of these equations. Note also that Eq. (2) indicates that a tiny deviation from the Keplerian rotation can cause a drastic change in the radial velocity distribution.

3 Viscous transonic solutions

In the following examples, the central star is a B0 main-sequence star with $M = 17.8 M_\odot$, $R = 7.41 R_\odot$, and $T_\mathrm{eff} = 2.80 \cdot 10^4\,\mathrm{K}$ (Allen 1973). Since, the disc is assumed to be isothermal, the structure of the viscous transonic outflow is independent of the mass decretion rate (see Sec. 3 of Abramowicz & Kato, 1989).

3.1 Structure of the viscous transonic outflow

Figure 1 shows a typical structure of the viscous transonic decretion disc. From Figure 1, we find that the sonic point is located far from the star and the outflow is highly subsonic for $r \ll 10^2\,R$. This is because it is basically the pressure force which accelerates the flow up to a supersonic speed. Consequently, the sonic radius is smaller for higher disc temperature and/or larger radiative force.

We also find that, in the subsonic part of the disc, V_r increases as r and Σ decreases as r^{-2}. In the inner subsonic region, V_ϕ decreases as $r^{-1/2}$, while in the outer subsonic region it decreases as r^{-1}. It should be noted that these radial dependences hold in general in viscous decretion discs.

Our results, together with the observed range of the base density for Be star discs (Dougherty et al. 1994), suggest that the mass loss rate in the equatorial region is at most comparable with that in the polar region.

3.2 Topology of the sonic point

It is well known that the stability of the transonic accretion with Shakura-Sunyaev viscosity prescriptions is related to the topology of the sonic point (e.g., Abramowicz & Kato 1989, and references therein). For α greater than a critical value, the sonic point is nodal and the transonic accretion is unstable. On the other hand, for α smaller than the critical value, the sonic point is saddle type and the stable transonic accretion exists. The instability arises as a result of work done by viscous force (see Kato et al., 1988, for detailed analysis).

In Figure 2, we present an example showing the location of the sonic points in the $(r_\mathrm{s}, \lambda_\mathrm{s})$-plane. As shown in Figure 2, in our model, the topology of the sonic point is nodal for $\alpha \gtrsim 0.95$, while it is saddle type for $\alpha \lesssim 0.9$. This means that the stationary transonic decretion in discs of Be stars exists if $\alpha \lesssim 0.9$, whereas the transonic decretion cannot be stationary if $\alpha \gtrsim 0.95$.

References

Abramowicz, M.A., Kato, S., 1989, ApJ 336, 304

Allen, C.W., 1973, Astrophysical Quantities, 3rd ed. The Athlone Press, London, pp.206, 209

Chen, H., Marlborough, J.M., 1994, ApJ 427, 1005

Dougherty, S.M., Waters, L.B.F.M., Burki, G., et al., 1994, A&A 290, 609

Kato, S., Honma, F., Matsumoto, R., 1988, MNRAS 231, 37

Lee, U., Saio, H., Osaki, Y., 1991, MNRAS 250, 432

Snow, T.P., 1981, ApJ 251, 139

Supernova Remnants

COSMIC RAY ACCELERATION IN SNRs

Luke O'C Drury
Dublin Institute for Advanced Studies, 5 Merrion Square, Dublin 2, Ireland
e-mail: ld@cp.dias.ie

Abstract

The possibility of confirming current ideas on particle acceleration in supernova remnants by means of gamma-ray and other obervations are discussed.

1 Introduction

Most astronomers regard cosmic rays as nothing more than a nuisance, an annoying and unwanted effect which disturbs their delicate photon detectors in unpredictable and irritating ways. However, looked at as an astronomical phenomenon, the origin of the cosmic rays is one of the oldest major unsolved problems in modern astrophysics. Victor Hess discovered the existence of a very penetrating ionizing radiation coming from above the atmosphere, which we now call the cosmic rays, back in 1912 and the problem of understanding the nature and origin of this radiation has been a well-defined question since then. The only other open question which is equally specific and of similar antiquity is that of identifying the carrier(s) of the diffuse interstellar bands. Furthermore it should be noted that we are not talking about some relatively insignificant effect; the energy density of the cosmic rays in the Galaxy is comparable to that of the magnetic field, and their pressure comparable to that of the thermal gas.

In this review I will consider three related questions. Why do we currently think cosmic ray acceleration may occur in supernova remnants? If it does, how might it work? And finally, and perhaps most importantly, what evidence is there that it actually happens? Obviously a short article such as this cannot be an objective and detailed review of the field. Rather it should be read as a personal view of some aspects which I find fascinating. Similarly I only refer to some of the more recent interesting papers without any claim to completeness; my apologies to the many others who should have been cited.

2 The inverse problem of cosmic ray astronomy

It is helpful to think of the cosmic ray origin problem as an inverse problem, where we start with what we actually observe at and near the Earth, and try to work backwards to the mysterious source or sources of the cosmic rays. There is a conventional terminology for the different processes thought to be involved along this chain. At the far end, in the mysterious sources, there is an "injection" process which takes ordinary matter and feeds it into an "acceleration" process which produces a spectrum of accelerated particles over a wide range of energies. After leaving the sources the particles are subject to "propagation effects" associated with transport in the Galactic disc and, probably, an extended halo region surrounding the disc. Those which reach the neighbourhood of the solar system are then subject to "modulation" by the magnetic structures in the solar wind before finally being detected, either directly by instruments on spacecraft and balloons in the upper stratosphere, or from the ground by the secondary effects they cause in the atmosphere.

A serious difficulty in experimental cosmic ray physics is that the signal we measure can only be related to the processes we really want to study, namely those of injection and acceleration, by applying corrections for the effects of Galactic propagation and solar modulation. In addition we have virtually no directional information. In photonic astronomy one can at least be sure that photons travel along straight lines (strictly space-time geodesics; the distinction is only relevant in the context of gravitational lensing), and if one measures the arrival direction of a photon that is also the direction in which the source of that photon lies. Charged particles, in contrast, are deflected by magnetic fields so that, except at very high energies, their passage through the Galaxy resembles a random walk rather than rectilinear propagation. A charged particle detected coming from one direction may have originated in a source located in some completely different part of the sky.

2.1 What is observed

The cosmic rays detected at and near the Earth consist mainly of fully stripped atomic nuclei along with some electrons and a few positrons and antiprotons. Concentrating on the dominant nuclear component, all species are observed to have energy spectra which are very close to power-laws of the form $N(E) \propto E^{-2.7}$ for energy per nucleon in the range $1\,\mathrm{GeV}$ to about $10^{14}\,\mathrm{eV}$. Below $1\,\mathrm{GeV}$ measurements show large variations which clearly correlate with solar activity. This solar modulation effectively wipes out any information about the interstellar spectrum at lower energies and in addition the measurements are contaminated by particles locally accelerated in the heliosphere; these effects are authoritatively discussed at this meeting in the reviews by Szegő (not published) and Király (these proceedings, p.277).

However above a few GeV per nucleon particle energy the effects of solar modulation are essentially negligible.

At around $1\,\mathrm{GeV}$ per nucleon it is relatively straightforward to determine the composition of the cosmic rays. The chemical composition turns out to be quite similar to the "local galactic abundances" of the elements, but with one major difference. The deep valleys which occur in the standard galactic abundances, most notably those associated with the light elements Li, Be and B but also the region just below Fe, are partially filled in in the cosmic ray abundances. This can be easily explained as a propagation effect. In travelling through the interstellar medium (ISM) at essentially the speed of light the cosmic ray nuclei will occasionally collide with the nucleus of an ISM atom. Many of these collisions result in what are called spallation reactions in which a fragment is chipped or spalled off the incident nucleus. In this way a relatively abundant C, N or O nucleus can be converted to a rare Li, Be or B nucleus and the sub-Iron region can be partially filled in by spallation products from the Iron peak.

In addition to providing a simple explanation for the gross features of the cosmic ray composition this idea, that in the cosmic rays we see a mixture of primary cosmic rays and secondary spallation products, is of vital importance because it enables us to experimentally determine some of the effects of Galactic propagation. The key point is that we can determine the true production spectrum of the secondary spallation products. The primary cosmic ray flux in the solar vicinity can be measured, the interaction cross-sections are in principle known from nuclear physics, and the mean density of the ISM and its composition is known; from these the production spectrum of spallation products can be calculated. By comparing the observed spectrum of secondary nuclei with this deduced source spectrum we can determine the effects of Galactic propagation on the secondary nuclei, and thus by inference also on the primary nuclei.

In the region around a few GeV per nucleon where we have sufficiently accurate composition data for this comparison, the observed energy spectrum is substantially steeper than the production spectrum; the production spectrum of the secondaries essentially mirrors the power-law of the primary energy spectrum (the cross-sections are only weakly energy dependent) at $E^{-2.7}$ whereas the observed spectrum of secondaries is much softer and more like $E^{-3.3}$. The natural explanation for this is in terms of energy-dependent escape from the Galaxy. At low energies the particles are more tightly coupled to the magnetic field and take longer to diffuse out of the Galaxy, whereas at higher energies the confinement time in the Galactic field is less. The compositional data are consistent with a confinement time of order 10^8 yr at around a GeV per nucleon falling as $E^{-0.6}$. This in turn implies that to produce an observed primary spectrum of $E^{-2.7}$ we need a production process which results in a harder spectrum more like $E^{-2.1}$.

Strictly this argument can only be made over a rather small energy range, say 1–30 GeV, but the fact that the observed primary spectrum is a very close approximation to a single power-law out to 10^5 GeV suggests that the same relationship between production spectrum, observed spectrum and confinement time holds over this extended energy range. However it must be admitted that not only is this a very dangerous extrapolation, but also there are then some difficulties in understanding the very small anisotropy (of order 10^{-4}) of the cosmic rays at 10^{13} eV.

There is a feature, usually called the "knee" in the energy spectrum at about 10^{15} eV beyond which the observed spectrum steepens to roughly E^{-3} and there may be a flattening (predictably called the "ankle") at around $10^{18.5}$ eV. Unfortunately it has not been possible to determine the composition at these energies and thus almost nothing is known about the propagation characteristics. In particular it is not known whether the "knee" reflects a change in the production spectrum or a change in propagation. The very high energy cosmic rays, from say 10^{16} eV to at least 10^{20} eV are a fascinating topic, but one which I do not have space to discuss here.

Returning to more modest, but still relativistic, energies there is one further important piece of evidence which has to be discussed. This comes from gamma-ray astronomy. In addition to spallation reactions nuclear collisions at energies above a GeV typically produce large numbers of pions. The neutral π^0 particles then decay rapidly into two gamma-rays which, as uncharged photons, do travel in straight lines. Thus observations of diffuse gamma-ray emission above 100 MeV can be used to trace the product of the cosmic ray intensity and the ISM gas density. Of course this is not entirely trivial; the additional gamma-ray emission from the cosmic ray electrons through bremsstrahlung and inverse Compton processses has to be disentangled from the π^0 component and the interstellar gas density is somewhat uncertain. Analysis of the Compton Gamma-Ray Observatory EGRET, and also earlier COS-B and SAS-2 observations, indicates that the cosmic rays are distributed rather smoothly throughout the Galactic disc, but with a radial gradient from higher values near the centre to lower values in the outer Galaxy. This is a clear indication that the cosmic rays, at least in this energy range, are of Galactic origin. Further confirmation comes from observations of the Magellanic clouds which show that the cosmic ray intensity in the small cloud cannot be more than one quarter of that observed in the solar neighbourhood.

The local energy density in the cosmic rays is of order $0.4\,\mathrm{eV\,cm^{-3}}$ and the associated pressure $0.17\,\mathrm{eV\,cm^{-3}}$, comparable to other energy densities and pressures in the ISM. However the number density of the cosmic rays is very low, of order $5 \times 10^{-10}\,\mathrm{cm^{-3}}$. Assuming a Galactic origin, and using the information obtained from the compositional data to constrain propagation, the power needed to maintain the cosmic rays at this level is about $10^{41}\,\mathrm{erg\,s^{-1}}$.

This brings us to the main piece of circumstantial evidence suggesting a rôle for supernovae (SNe) in the acceleration of cosmic rays. The mechanical energy input into the Galaxy from SNe is estimated as $10^{42}\,\mathrm{erg\,s^{-1}}$ and it is hard to think of anything else which could plausibly drive the cosmic ray accelerator. In addition we have a theoretical picture of how the acceleration (and injection) might actually work; this is through a version of Fermi acceleration operating at the strong shock waves associated with the supernova remnants (SNRs) produced by the SN explosions. It is worth noting that the so-called "adiabatic loss problem" rules out any model in which the cosmic rays are generated directly in the SN explosion itself; thus if there is a link to SNe it must be indirect and through the resulting remnants. As the SNRs can be thought of as the dynamical structures which process the mechanical energy of the explosion into other forms they are also the most natural places to locate an acceleration process.

3 Elements of diffusive shock acceleration

The shock waves which form in a low density plasma are very different (at the microscopic level) from the gas-dynamic shocks we are used to. The dissipative processes which convert the mechanical energy of the upstream plasma flow into "random" or "thermal" motion of the constituent particles of the plasma downstream are not, as in gas-dynamic shocks, two-body collisional processes but collective plasma processes. These collision-less shocks work by exciting high-frequency plasma modes in the shock front which then scatter and isotropize the particle distributions. However although the resulting distributions may be close to Maxwellian there is no reason to expect them to be exactly Maxwellian. Indeed theoretical arguments, computer simulations and in situ observations of heliospheric shocks all agree that the "shock heated" ion distribution functions do not drop off with increasing energy as fast as a pure Maxwellian, or, to put it another way, there is in general a high-energy tail to the distribution function. A simple, but quite subtle, theory can be developed for the asymptotic form of this "tail" based on the use of a diffusion model for particle transport (hence the name "Diffusive Shock Acceleration") which predicts that the tail will in fact take the form of a power-law in momentum with an exponent determined purely by the shock compression. Remarkably, not only does this process naturally predict power-law spectra extending over large ranges of energy (which is a severe problem for all alternative acceleration mechanisms) and simultaneously solve the "injection problem", but also the exponent in the power-law is close to that which the observations appear to require.

In fact the simple theory gives a differential energy spectrum $N(E) \propto E^{-2}$ for relativistic particles and a shock compression ratio of four. However because this corresponds to equal energy per decade in the spectrum the results are very sensitive to slight changes in the spectral exponent, nonlinear modifications of the simple theory, location of the upper cut-off energy etc. Thus a detailed nonlinear theory is very difficult although significant progress has been made. Probably the best recent results are those described in Berezhko et al (1996) which also contains references to earlier work. Remarkably it has turned out that it is actually easier to understand time-dependent expanding spherical shocks than steady planar ones! The latter are plagued with various mathematical pathologies which turn out to be much less serious in the real world (Drury et al, 1995).

The hypothesis that cosmic rays are produced by this process operating at the strong shocks associated with supernova remnants works quite well in terms of the general composition, energy and spectrum up to the "knee" region. Unfortunately it fails catastrophically thereafter. Without going into detail the maximum energy that can be reached by shock acceleration in a remnant of radius R, velocity R' and magnetic field strength B is of order (as might be guessed on dimensional grounds) charge times BRR'. If we substitute $R \approx 10\,\mathrm{pc}$, $R' \approx 10^3\,\mathrm{km\,s^{-1}}$ and $B \approx 3\,\mu\mathrm{G}$ we find that protons cannot be accelerated to more than 10^{15} eV whereas the observed cosmic ray spectrum goes on for at least another five decades! Furthermore the transition is extremely smooth although there is a change of slope (the "knee" in the spectrum). Although most unsatisfactory, it seems that if we wish to use SNRs to generate the particles below the "knee" we must then invoke a second source for the particles above the "knee". But the circumstantial evidence is quite strong, the mechanism is plausible, and there is no other rival theory, so we should look for direct observational evidence.

4 Observational evidence

There is actually good evidence for the acceleration of electrons in SNRs. The most convincing case comes from radio and X-ray studies of young remnants like those of Tycho's SN and SN1006 which have simple spherical morphology (presumably reflecting a type Ia supernova origin). These have non-radiative shocks, therefore modest compression, and thus the radio emission cannot be simple van der Laan compression but must result from relativistic electron acceleration. The extreme sharpness of the radio rims (Achterberg et al, 1994) is a strong indication of locally generated wave turbulence, small diffusion coefficients and ongoing injection and acceleration in the shock front. The mainly radial magnetic field structure revealed by polarization studies also indicates strong turbulence. The spectral indices seen in the radio can be interpreted in terms of acceleration at shocks modified by an accelerated ion component, and this may be weak evidence for ion acceleration; otherwise the radio observations, while convincing proof of electron acceleration to GeV energies, say nothing about acceleration of ions. The exciting new result in this field is the detection (Koyama et al 1995) by the ASCA satellite of nonthermal X-ray emission in parts of the remnant of SN1006 which is interpreted as synchrotron emission from TeV electrons (Reynolds, 1996; Mastichiadis and de Jager, 1996).

Of course one can always argue that if electrons are being accelerated to GeV and TeV energies, then the ions should also be accelerated. But it is desirable to have some more direct evidence than hints from the radio spectral indices. One obvious possibility is to use gamma-ray observations. If SNRs are filled with freshly accelerated protons (and other ions) these will interact with the ejecta and the sweptup interstellar medium to produce, among other products, π^0 particles which then decay to produce gamma-rays. It is relatively straightforward to estimate the expected fluxes of gamma-rays from SNRs in the GeV and TeV regions with the result that at least some of the nearby SNRs should indeed be detectable sources (Dorfi, 1990, 1991; Drury et al, 1994; Naito and Takahara, 1994). However while there do appear to be real detections in the GeV region from the EGRET instrument on the Compton gamma-ray observatory satellite (Esposito et al, 1996) searches in the TeV region and above have so far only yielded upper limits (G E Allen et al, 1995; W H Allen et al, 1995; Lessard et al, 1995; Prosch et al, 1995).

In conclusion there is very good evidence for electron acceleration in SNRs, and some evidence for ion acceleration although the absence of TeV gamma-ray detections is beginning to be worrying. However at best this is only half the story. We still need to explain the remaining six decades or so of the spectrum beyond the "knee". If, as seems probable, the ultra-high energy cosmic rays are of extragalactic origin it is interesting to note that they are the only sample of extra-galactic matter which is ever likely to reach the solar system.

Acknowledgements

I would like to express my appreciation of the warm Hungarian hospitality in Visegrad and the stimulating scientific discussion at the meeting. To all involved, a sincere *köszönöm*!

References

Achterberg A., Blandford R.D., Reynolds S.P., 1994, A&A 281, 220

Allen G. E. et al. 1995, ApJ 448, L25

Allen W. H. et al, 1995, Proc 24th ICRC (Rome) 2, 447

Berezhko E. G., Elshin V. K. and Ksenofontov L. T., 1996, Zh. Eksp. Teor. Fiz. 109, 3 (English translation in JETP 82 1)

Dorfi E. A., 1990, A&A 234, 419

Dorfi E. A., 1991, A&A 251, 597

Drury L. O'C., Aharonian F. and Völk H. J., 1994, A&A 267, 959

Drury L. O'C., Völk H. J. and Berezhko E. G., 1995, A&A 299, 222

Esposito J. A., Hunter S. D., Kanbach G. and Sreekumar P., 1996, ApJ 461, 820

Koyama K., Petre R., Gotthelf E. V., Matsuura M., Ozaki M. and Holt S. S., 1995, Nature 378, 255

Lessard R. W. et al., 1995 Proceedings of the 24th. Int. Cosmic Ray Conf, Rome, 2, 475

Mastichiadis A. and de Jager O. C., 1996, A&A 311, 5

Naito T. and Takahara F., 1994, J Phys G 20, 477

Prosch C. et al., 1995, Proc 24th ICRC (Rome) 2, 405

Reynolds S. P., 1996, ApJ 459, L13

PULSAR – SUPERNOVA REMNANT INTERACTION: A SIMPLE MODEL

D.M.G.C. Luz[1] and D.L. Berry[2]
[1]Departamento de Física, Universidade de Lisboa
Campo Grande, Ed. C1, Piso 4, 1700 Lisboa, Portugal
[2]Departamento de Física, Universidade de Évora
Rua Romão Ramalho, 59, 7000 Évora, Portugal

Abstract

A model for the expansion of the ejecta following a supernova explosion is presented. If a pulsar remains at the site of the explosion, it emits magnetodipole radiation which is trapped inside the ejecta and contributes to its expansion through radiation pressure. If rotational effects are also included, outbursts of gas may occur at the poles of the remnant, possibly leading to a barrel-shaped supernova remnant.

1 Introduction

During the past fifteen years the number of supernova remnants (SNRs) proposed to be associated with pulsars (PSRs) has increased (Caraveo 1993) by an amount that leaves no room for doubt that the problem of the PSR–SNR interaction should be addressed. Most approaches to this interaction problem are concerned with the emission of either particles or synchrotron radiation from the PSR magnetosphere, while possible effects resulting from magnetodipole radiation are often neglected. A simple approach to this different aspect of the interaction is described here.

The evolutionary process after a type II supernova explosion involves various stages. First, a strong shock is generated that ejects and ionizes most of the mass of the progenitor star. The ejecta then expands subject to an interior radiation dominated pressure, until the temperature of the gas drops and it recombines. This allows radiation to escape so that the material then moves ballistically. However, the presence of a pulsar at the site of the explosion may change this evolutionary process. The PSR emits very low frequency magnetodipole radiation which is trapped inside the ejecta. A radiation pressure then gradually builds up and will eventually act upon it, changing its evolution through momentum transfer. Thus, it is possible that the rate of ejecta expansion and the shape of the resulting SNR will be modified.

2 Modelling the supernova remnant

The supernova explosion can be modelled simply as a pointlike release of energy, which generates a strong shock that goes through the body of the progenitor star. The energy released in the explosion is about $E = 10^{51}$ erg, some

1000 times the gravitational energy of the stellar envelope, which allows gravitational effects to be neglected. Furthermore, the density distribution in the progenitor star as a function of radius r can ideally be considered to be of the form

$$\rho_0(r) = \Omega r^{-n} \tag{1}$$

where Ω is a scale factor and n is a real number in the range 0–3. The ionization produced by the passing of the shock liberates enough radiation that the resulting radiation pressure dominates the expansion. This means that the ejecta gas can be treated as ideal with an adiabatic index $\gamma = 4/3$.

The pointlike character of the energy release along with the power law character of the density distribution allows for similarity to be assumed in the flow. This means that the shock radius, r_s, as well as all the physical variables in the shocked gas depend only on time and on the initial conditions — the energy E released in the explosion and density parameters Ω and n.

The assumption of similarity asserts certain conclusions about these physical variables, just by applying the equations of mass, energy and momentum conservation to the sphere bounded by the shock (Sedov 1959). The principal conclusion is that the density of the shocked gas depends strongly on the value of n, unlike the other variables which are insensitive to it. For n in the range 0 to 9/4, the density grows from zero at the site of the explosion to a maximum ρ_s at radius r_s, but if n is between 9/4 and 17/7 it decreases from infinity at the origin to ρ_s at radius r_s. For n greater than 17/7, the solution is significantly different — an evacuated cavity forms within the shocked region. All the shocked gas is therefore contained in a region extending from the cavity radius to the shock. In this region the density grows from zero at the cavity radius to ρ_s at radius r_s, if n ranges from 17/7 to 18/7, and it decreases from infinity at the boundary of the cavity to ρ_s at radius r_s, if n is between 18/7 and 3. The cavity radius grows as a function of n from zero for $n = 17/7$ to about $0.7r_s$ for $n = 3$.

It should be stressed that the similarity solution is just an approximation to the real flow in a supernova explosion, while the shock sweeps through the progenitor star. It is bound to fail in a small region near the site of the explosion because there neither the explosion can be considered as pointlike, nor the initial density can behave as r^{-n}. But both the behaviour of the physical variables outside this region and the creation of a cavity within the shocked sphere are physically valid for the initial density distribution considered.

However, in order that Equation 1 can be taken even as a rough representation of a stellar atmosphere, it has to be modified beyond the stellar radius $R_\star$, to account for the fact that the progenitor star is surrounded by a medium, for example the ISM or a stellar wind. Such a modification will introduce a discontinuity in the flow and forbid the assumption of similarity after the shock has reached the edge of the star. Then a numerical model is required for solving directly the set of coupled partial differential equations of hydrodynamics (HD).

Such a computational hydrodynamic model is being developed to follow the evolution of the ejecta from the disruption of the progenitor star by the shock to later stages where the ejecta are being acted on by radiation from the central pulsar. The model implements a conservative, finite volume, time explicit scheme for solving the equations of HD. It uses a two dimensional, axially symmetric grid, allowing for simulation of any spherically or axially symmetric initial conditions (Bowers and Wilson 1991), such as the density profile of Equation 1 cutoff at the stellar radius and embedded in some surrounding medium. It also takes account of the possibility of rotation of the progenitor star.

The explosion is simulated as the release of 10^{51} erg of kinetic energy at the centre of the density distribution described by Equation 1. Such conditions allow for a direct comparison of the numerical model with various solutions of the similarity model, as long as the shock has travelled a radial distance great enough for the explosion to be considered as pointlike.

3 Modelling the pulsar – SNR interaction

The simplest model for the PSR is that of a spinning magnetic dipole tilted by some angle relative to the spin axis. Other multipole magnetic moments are negligible because they decay away as higher powers of radial distance from the PSR. Under these conditions, a radiation field is observed at distances $r \gg r_{lc}$, where r_{lc} is the radius of the light cylinder. A spherical electromagnetic wave is produced with the spin frequency ω, typically 30 s^{-1}. Then both the wavelength and r_{lc} are of the order of 10^7 m, which is much smaller than the shock radius just a few hours after the explosion.

Radiation from the PSR is trapped inside the hot expanding ejecta due to Thomson scattering, and builds up a pressure P_{rad}. This accelerates the gas from the inside, forcing it into a shell whose surface density depends on two opposing factors: the rate of expansion due to radiation pressure and the rate at which material is picked up from the ejecta. Thus the evolution is ultimately governed by the energy output from the PSR, which determines P_{rad}, and the initial conditions E, Ω and n, which determine the flow of the ejecta.

Therefore, the interaction of radiation from a central PSR on an expanding SNR can lead to a greater expansion rate of the SNR. Furthermore, some magnetic field enhancement may also result because of compression, as long as the energy output from the PSR is sufficiently great.

Another interesting consequence follows if rotation of the progenitor star is considered. Rotation produces some oblateness of the expanding ejecta, while the cavity created by the action of P_{rad} is spherical. If the cavity expands at a greater rate than the ejecta, then the resulting shell will be thicker in the equatorial region than at the poles. Continued momentum transfer from P_{rad} can thus lead to shell disruption at these thinner regions, with material bursting outwards at the poles. The resulting young SNR shell would be observed with a variety of shapes depending on the line of sight orientation: from a barrel-like shape, if observed from the equatorial direction, to a ring-like shape, seen from the direction of the polar axis.

4 Summary

A simple model has been presented to account for the interaction of radiation from a central PSR on an expanding SNR. The most important effect resulting from the PSR is that the young SNR shell will expand at a greater rate due to the contribution of the PSR radiation pressure. If rotation of the progenitor is included, the expanding material will present some oblateness and the polar regions will be more sensitive to the interior radiation pressure than at the equatorial region. This may lead to gas bursting outwards at the poles, resulting, in later stages, in a barrel-shaped SNR.

Observation of barrel-shaped young SNRs associated with PSRs could thus provide evidence that the interaction here described may be an important one on the initial stages of the evolution of remnants of type II supernovae.

Acknowledgement

The authors would like to thank Prof. F.D. Kahn, Department of Physics and Astronomy, Manchester University, UK, for his invaluable guidance and advice. D.M.G.C.L. acknowledges JNICT for support of his work by grant PRAXIS XXI BM/18/94.

References

Bowers R.L., Wilson J.R., 1991, Numerical Modeling in Applied Physics and Astrophysics. Jones and Bartlett, Boston

Caraveo P.A., 1993, On The Pulsar/SNR Associations. In: Alpar M.A., Kiziloğlu Ü., van Paradijs J. (eds.) The Lives of the Neutron Stars. Kluwer Academic Publishers, Dordrecht, p.39

Luz D.M.G.C., 1996, MSc. Thesis, in preparation

Sedov L.I., 1959, Similarity and Dimensional Methods in Mechanics. Cleaver Hume Press, London

PHOTOMETRIC OBSERVATIONS OF SMALL-AMPLITUDE VARIATIONS IN CRAB PULSAR LIGHT-CURVE ON SHORT TIME-SCALES

Mirjam Galičič and Andrej Čadež
University of Ljubljana, Department of Physics FMF
Ljubljana, Slovenia
e-mail: mirjam.galicic@uni-lj.si

Abstract

During the last three years, we developed an optical stroboscopic observing device which enables us to precisely measure the possible variations in Crab pulsar optical light-curve. We observed Crab with our apparatus and Asiago 1.82m telescope twice (in December 1994 and 1995), and analysed the Hubble Space Telescope *High Speed Photometer* Crab pulsar data (obtained in October 1991). Results show a 0.006±0.002 magnitude periodic modulation at the period of 60 seconds. Further observations are needed to confirm the periodicity which may be explained by the free precession of a neutron star.

1 Introduction

Crab is among the most frequently observed pulsars and is the brightest of the few optical pulsars. Its integrated pulse shapes at different wavelengths are remarkably similar (Smith 1977). Its radio emission is variable on a wide range of time scales (Lyne et al. 1993, Jones 1988), which is possibly related to the emission mechanism and the interstellar scattering (Smith 1977). Its optical intensity is essentially constant, and the shape of optical pulse is surprisingly stable (Kristian 1971, Smith 1977). The shortest time-scales were examined by Kristian (1971) who writes that Crab's optical signal is constant over time-spans from 10 minutes to several hours, with the accuracy of 5%. In these or shorter time ranges, no other observers, to our knowledge, report on Crab's optical light-curve variability.

We considered that a weak modulation might be observed in Crab's optical light-curve. Its cause would be geometrical: free precession of a neutron star. A simple estimate gave us a value around 100s for Crab's free precessional period. We were well aware of the fact that this periodic modulation, if present, would be very weak (less than 5%). We carefully designed the observing device which enables us to search for small variations in the optical light-curve on a time scale from about 40 seconds to several minutes. We applied it at the Asiago 1.82m telescope in Italy (Asiago and Padua Observatories, University of Padua). In addition to our data, we analysed the Hubble Space Telescope (HST) Crab data.

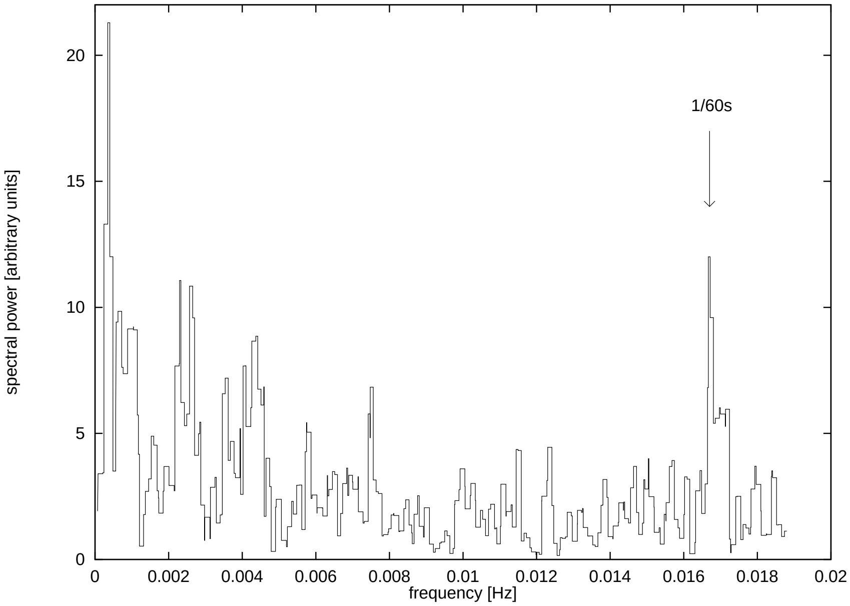

Figure 1: The sum of Fourier power spectra from Asiago 1994 and 1995, and HST 1993 data.

Both results give a weak modulation at the frequency of 1/60s.

2 Stroboscopic observing method and analysis of Asiago and HST data

Our photometric observational method includes a stroboscope. Its main advantages are twofold: **a)** we can select the pulse phase at which we observe, and **b)** we reduce the noise by letting light to reach the CCD chip only through a part of the whole pulse. The theoretical accuracy of photometric observation is limited by the number of detected photons. Since the background Crab nebula is very bright while we are looking for a weak signal, point b) above is of greatest importance for us. By choosing the shape of the stroboscope wheel which passes the light through only for about ten percent of the pulse period (main pulse), we were able to reduce the photon noise substantially. For example, the actual noise level – the statistical average amplitude in Fourier spectrum over the frequency range 1/40s to 1/150s – in a two hour long observational run was 0.001 magnitude (Galičič 1995). With this noise-level, and a suitably accurate stroboscope timing, we were able to observe the 0.006 magnitude periodic modulation.

The photometric stroboscopic light-curves as well as the HST data[1] were analysed by the Fourier transform method. In the three corresponding spectra we observe a peak[2] at the modulation frequency 1/60s. To compare them, we add the three power spectra. The sum is shown in Figure 1.

3 Possible explanation of the observed periodicity: free precession of a neutron star

The question of neutron star's free precession was first addressed in the seventies when Pines and Shaham (1974) and Goldreich (1970) discussed the existence of the phenomenon and its possible driving mechanisms. They estimated that free precession damps while the neutron star ages so that it would be observable only with young pulsars. Later Alpar and Ögelman (1987) estimated the the typical damping time as a consequence of dissipative exchange of angular momentum between different parts of the star would around 1000 years. Pines and Shaham compared possible neutron star free precession to the Earth Chandler wobble, and estimated Crab pulsar's free precessional period. They expressed the ratio of free precessional to rotational period by the ratio of gravitational and elastic energy stored in the star (Baym and Pines 1971). Observationally, the lack of strong evidence and the unclear knowledge of neutron star interior structure led different authors to connect a wide range of Crab pulsar's light-curve variabilities to free precession (Huguenin and Taylor 1973, Helfland and Fowler 1977, Richards et al. 1970, Jones 1988, Thompson 1993).

Similar to Earth Crab pulsar most probably has a solid crust and a liquid mantle. Chandler wobble period has been measured for Earth, and its value can well be estimated by the Euler formula (Goldstein 1981) for the rigid body free precession, where we estimate the inertial eccentricity by the Maclaurin formula (Lang 1978). The latest relates the rotational velocity and inertial eccentricity for the rotating homogeneous fluid. Since pulsar glitches which considered as starquakes which release internal stress (Lyne et al. 1993), we might consider that Crab pulsar interior matter is not far from hydrostatic equilibrium which can be described by a rotating polytrope of a polytropic index n. Thus we obtain 100 seconds for its free precessional period.

Neutron stars were considered in the context of slowly rotating relativistic polytropic stars in early seventies (Cohen 1971). Neutron stars are considered also by Tassoul (1978) in his theory of rotating stars. Thorne and Gürsel (1983) showed that relativistic free precession can be described by the same relation as the free precession of a rigid body, yet they exposed the question of the degree of neutron star rigidity which could sustain the free precessional motion. On the

---

[1] Data were obtained by the HST's instrument *High Speed Photometer* in 1991, and belong to *Space Telescope Science Institute*, contract NAS 5-26555, AURA Inc., and were mailed to us by J. Dolan and P. Boyd, GSFC, NASA.

[2] The analysis is described and the modulation amplitude determined in Galičič (1995), Čadež and Galičič (1995), and Čadež and Galičič (1996).

basis of the theory of rotating polytropes, Schwarzenberg-Czerny (1992) derives that the ratio of precessional frequency to rotational frequency is proportional to ω_{rot}^2/ρ, where ρ is the density of the neutron matter. This relation can be applied in the cases of neutron stars for which we know rotational periods and a periodicity in their light-curves, as in the case of our 60-second Crab pulsar periodicity, or the Her X-1 as a free precession. Thus we can estimate their masses which come very close for the two pulsars, just as Lipunov (1992) notes that pulsar masses might be spread over a very narrow interval.

4 Conclusions

We explain the observed 60s periodic modulation in Crab light-curve as free precession of the neutron star. The measured period coincides well with a simple estimation. New observations over a longer time span are necessary to confirm the modulation and its connection to the free precession. The advantage of the young Crab pulsar is that it slows down substantially. Thus the time-dependence of the modulation can be observed in a couple of years. The undoubtful determination of Crab pulsar free precessional period would put important constraints on the mass and the interior structure of the pulsars.

References

Alpar, A., Ögelman, H., 1987, A&A, 185, 196

Baym, G., Pines, D., 1971, Annals of Physics, 66, 816

Čadež, A., Galičič, M. 1995, poster presented at *Science with Hubble Space Telescope*, Paris, 4th to 8th Dec. 1995

Čadež, A., Galičič, M. 1996, A&A, 306, 443

Cohen, J. M., 1971, in *"The Crab nebula"*, Proc. IAU Symp. No. 46, ed. R. D. Davis, F. G. Smith, D. Reidel, Dordrecht, pp.334-340

Galičič, M. 1995, *Observation of optical variability of pulsar PSR0531+21 on short time-scales*, M.Sc. thesis (in Slovene), University of Ljubljana

Goldreich, P., 1970, ApJ, 160, L11

Goldstein, H., 1981, *Classical Mechanics* (Reading Massachusetts: Addison-Wesley Publishing Company)

Helfland, D.J., Fowler, L.A., 1977, AJ, 82, 701

Huguenin, G.R., Taylor, J. H. 1973, ApJ, 181, L139

Jones, P. B., 1988, MNRAS, 235, 545

Kristian, A. 1971, in *The Crab nebula*, IAU Symp. No. 46, Ed. R.D. Davies, F.G. Smith, D. Reidel Publishing Company: Dordrecht

Lang, K.R., 1978, *Astrophysical Formulae* (Berlin: Springer-Verlag)

Lipunov, V.M., 1992, *Astrophysics of Neutron Stars* (Berlin: Springer Verlag)

Lyne, A.G., et al., 1993, MNRAS, 265, 1003

Percival, J.W., et al., 1993, ApJ, 407, 276

Pines, D., Shaham, J., 1974, Nature, 248, 483

Richards, D.W., et al. 1970, ApJ, 160, L1

Schwarzenberg-Czerny, A. 1992, A&A, 260, 268

Smith, F.G., 1977, *Pulsars*, Cambridge Univ. Press, Cambridge

Tassoul, J.-L., 1978, *Theory of rotating Stars* (Princeton: Princeton Univ. Press)

Thompson, D.J., 1993, in *Isolated Pulsars*, ed. van Riper, K.A., Epstein, R., Ho, C. (Cambridge: Cambridge University Press)

Thorne, K.S., Gürsel, Y., 1983, MNRAS, 205, 809